
ETD Archive

2011

Free Space Optical Communications with High Intensity Laser Power Beaming

Daniel Edward Raible
Cleveland State University

Follow this and additional works at: <https://engagedscholarship.csuohio.edu/etdarchive>

 Part of the [Electrical and Computer Engineering Commons](#)

How does access to this work benefit you? Let us know!

Recommended Citation

Raible, Daniel Edward, "Free Space Optical Communications with High Intensity Laser Power Beaming" (2011). *ETD Archive*. 251.
<https://engagedscholarship.csuohio.edu/etdarchive/251>

This Dissertation is brought to you for free and open access by EngagedScholarship@CSU. It has been accepted for inclusion in ETD Archive by an authorized administrator of EngagedScholarship@CSU. For more information, please contact library.es@csuohio.edu.

**FREE SPACE OPTICAL COMMUNICATIONS WITH HIGH
INTENSITY LASER POWER BEAMING**

DANIEL EDWARD RAIBLE

Bachelor of Science in Electrical Engineering

Cleveland State University

May 2006

Master of Science in Electrical Engineering

Cleveland State University

May 2008

submitted in partial fulfillment of requirements for the degree

DOCTOR OF ENGINEERING

at the

CLEVELAND STATE UNIVERSITY

June 2011

This dissertation has been approved
for the Department of Electrical and Computer Engineering
and the College of Graduate Studies by

Dissertation Committee Chairperson, Taysir H. Nayfeh

Department/Date

Nigamanth Sridhar

Department/Date

Ana V. Stankovic

Department/Date

Petru S. Fodor

Department/Date

John F. Turner

Department/Date

This work is dedicated to the memory of my dearest friends, Michael Matthews and Jason Adams. It would have been great, and I miss you.

ACKNOWLEDGEMENTS

There are many people that I would like to express my gratitude towards, starting with my advisor Dr. Taysir Nayfeh, for affording me the opportunity to pursue my education through working at the Industrial Space Systems Laboratory, and for helping me develop my skills as a researcher.

I would like to graciously thank my committee for their time and review starting with Dr. Nigamanth Sridhar for providing his background in wireless systems, Dr. Ana V. Stankovic for offering her knowledge in power electronics and systems, Dr. Petru S. Fodor and Dr. John F. Turner for supplying their expertise in optics and general physics, and finally Dr. Joseph A. Svestka for serving as a non-voting member and for sharing his expertise in systems engineering and mathematical programming.

I am ever grateful for the technical guidance that I received from Bernie Sater of Photovolt, Inc. His lifelong pursuit of the VMJ technology is the enabler of this project.

Special thanks to Ken Edwards and the Eglin AFRL for believing in and supporting this research. I am looking forward to what the future will bring with HILPB.

Thanks to Hobson Lane, Bob Rice and NGST, as well as Colin Burke and LIMO for providing their facilities and invaluable expertise.

Great thanks to Ray Beach, Fred Wolff and Jim Soeder of the NASA John H. Glenn Research Center for their support of the ISSL and our work over the years.

I would also like to thank several graduate students and employees with whom I have had the honor of working with at the Industrial Space Systems Laboratory: Brian Fast, Dragos Dinca, Nick Tollis, Andrew Jalics, Sagar Gadkari, Scott Darpel, Maciej

Zborowski, Harry Olar, Tom DePietro, Michael Wyban, Ishu Pradhan, Anita Wiederholt and David Avanesian. They made many great contributions to this research, and it has been a pleasure serving on the team with them.

Thanks to Adrienne Fox and Jan Basch for all of their hard work behind the scenes, the rest of the Electrical and Computer Engineering Department, the Industrial and Manufacturing Engineering Department, and Pam Charity, Gregg Schoof and Joanne Hundt in the Dean's office for their support and guidance given to me while at the Fenn College of Engineering.

Also, thanks to my NASA colleagues James Nessel, Alan Hylton and Robert Manning for lending a hand and giving me sanity checks during this work.

I wish to particularly thank my wife, Jamie, for her eternal patience and love. I am grateful to my parents Elaine and Dennis, sister Janice, Uncle Richard, Uncle Fred and Aunt Anna Rae for their continual support and for encouraging me to always take the Giant Steps in life.

FREE SPACE OPTICAL COMMUNICATIONS WITH HIGH INTENSITY LASER POWER BEAMING

DANIEL EDWARD RAIBLE

ABSTRACT

This research demonstrates the feasibility of utilizing high intensity laser power beaming (HILPB) systems as a conduit for robust free-space optical communications over large distances and in challenging atmospheric conditions. The uniqueness of vertical multi-junction (VMJ) photovoltaic cells used in HILPB systems in their ability to receive and to convert at high efficiency, very high intensity laser light of over 200 W/cm^2 , presents a unique opportunity for the development of the robust free space optical communication system by modulating information signals onto the transmitted high intensity photonic energy.

Experiments were conducted to investigate and validate several optical communications concepts. A laser modulator was implemented to exhibit the excellent transient response of the VMJ technology at very high illumination intensities, and thus show its applicability to optical communications. In addition, beam polarization optic stages were employed to demonstrate a secure multi-channel communications scheme. The off-axis response of the receiver and the beam profile were characterized in order to

evaluate the feasibility of developing acceptable pointing and tracking geometries. Finally, the impact of signal modulation on the total converted energy was evaluated and shown to have minimal effect on the overall power transmission efficiency. Other aspects of the proposed communication system are studied including: quantifying beamwidth and directivity, signal-to-noise-ratio, information bandwidth, privacy, modulation and detection schemes, transmission channel attenuation and disturbances (atmospheric turbulence, scintillation from index of refraction fluctuations, absorption and scattering from thermal and moisture variation) and beam acquisition tracking and pointing influence on the performance metrics of optical transmission technologies.

The result of this research demonstrates the feasibility of, and serves as a comprehensive design guide for the implementation of a HILPB communication system. Such a system may be applied to mission architectures requiring generous amounts of link margin, critical privacy in battle field environment, and/or where the channel characteristics are dynamic and unknown. In addition, the developed mathematical models and empirical data support the ongoing wireless power transmission efforts by expanding the fundamental knowledge base of the HILPB technology.

TABLE OF CONTENTS

	Page
NOMENCLATURE	XV
LIST OF TABLES	XX
LIST OF FIGURES	XXI
CHAPTER I: INTRODUCTION.....	1
1.1 A Brief History of Free Space Optical Communications	1
1.2 The HILPB System	10
1.3 Future Potential for a High Intensity Laser Communications System	16
1.4 Document Organization.....	19
CHAPTER II: LITERATURE REVIEW OF LASER COMMUNICATIONS	20
2.1 Advantages of Optical Communications	20
2.2 Beam Polarization.....	27
2.3 Modulation and Demodulation Techniques.....	35
2.3.1 Direct Detection Receiver.....	36
2.3.2 Coherent Detection Receiver	42
2.4 Terrestrial and In-Space Issues	44
2.4.1 Terrestrial Links.....	45
2.4.2 Spatial Crosslink	52

2.4.3	Waveguide Medium.....	57
2.5	Beam Acquisition, Tracking and Pointing.....	59
CHAPTER III: EXPERIMENT SETUP AND RESEARCH METHODOLOGY		63
3.1	System Description – Optical Receivers.....	63
3.2	System Description – Laser and Optics Bench.....	69
3.3	System Description – Data Acquisition System	72
3.4	Photovoltaic Array Cell Back-feeding.....	76
3.5	Comparison of Receiver Geometries	78
3.6	Optical Frequency Optimization.....	86
3.7	Beam Homogenization Optics	96
CHAPTER IV: EXPERIMENT PROCEDURE AND ANALYSIS		102
4.1	Beam Profile Characterization.....	102
4.2	Off-Axis Illumination	108
4.3	Pulse Modulation	114
4.4	Pulsed Power.....	132
4.5	Multi-Channel Polarization Optics	137
4.6	Link Budget and Applicable Systems.....	143
CHAPTER V: RESULTS AND CONCLUSIONS		150
CHAPTER VI: RECOMMENDATIONS		156

REFERENCES	158
APPENDICES	166

NOMENCLATURE

ABL	Airborne Laser
AFGL	Air Force Geological Laboratory
AFRL	Air Force Research Laboratory
AFTS	Airborne flight test system
AOS	Adaptive optics system
APD	Avalanche photodiode
AR	Anti-reflective
ARTEMIS	Advanced relay and technology mission
ASK	Amplitude shift keying
ATC	Air Traffic Control
BER	Bit error rate
CAD	Computer aided design
CCD	Charge coupled device
CDF	Cumulative distribution function
COTS	Commercial off the shelf
CSU	Cleveland State University
CW	Continuous wave
DATAQ	Data acquisition

DSCS-2	Defense Satellite Communications System
EO	Electro-optic
ER	Extinction ratio
ESA	European Space Agency
FAA	Federal Aviation Administration
FFT	Fast Fourier transformation
FOV	Field of view
FPGA	Field programmable gate array
FSK	Frequency shift keying
FSO	Free space optical
FWHM	Full width half maximum
GEO	Geosynchronous orbit
GOPEX	Galileo optical experiment
GPS	Global Positioning System
GRC	John H. Glenn Research Center
GSFC	Goddard Space Flight Center
GUI	Graphical user interface
HEL	High energy laser
HILPB	High intensity laser power beaming

I-V	Current-voltage
IBE	Integrated beamed energy
IC	Integrated circuit
IR-A	Infra-red (near)
ISSL	Industrial Space Systems Laboratory
ITU	International Telecommunications Union
JAXA	Japan Aerospace Exploration Agency
JPL	Jet Propulsion Laboratory
LASER	Light Amplification by Stimulated Emission of Radiation
LaWS	Laser weapons system
LCP	Left circular polarized
LEO	Low Earth orbit
LIMO	Lissotschenko Mikrooptik GmbH
LLNL	Lawrence Livermore National Laboratory
MEMS	Microelectromechanical systems
MITLL	Massachusetts Institute of Technology's Lincoln Laboratory
MLA	Mercury laser altimeter
MODTRAN	MODerate spectral resolution atmospheric TRANSmittance algorithm
MRR	Modulated retro-reflector

MTO	Mars telecommunications orbiter
MUAV	Micro unmanned aerial vehicles
Nd:YAG	Neodymium yttrium aluminum garnet
NIR	Near infra-red
NRL	Naval Research Laboratory
NTIA	National Telecommunications and Information Administration
OICETS	Optical intersatellite communications engineering test satellite
OOK	On-off keying
PAPI	Precision approach path indicator
PAT	Pointing acquisition and tracking
PCB	Printed circuit board
PDF	Probability density function
PGBM	Pulse-gated binary modulation
PMAD	Power management and distribution
PPBM	Pulse polarization binary modulation
PPM	Pulse position modulation
RCP	Right circular polarized
RF	Radio frequency
RMS	Root mean square

RTT	Round trip time
SILEX	Semiconductor laser intersatellite link experiment
SNR	Signal-to-noise ratio
SOR	Starfire optical range
SPB	Signal power budget
SWaP	Size, weight and power
TASC	Triple junction advanced solar cell
TEM ₀₀	Transverse electro-magnetic Gaussian
UART	Universal asynchronous receiver/transmitter
UAV	Unmanned aerial vehicles
VMJ	Vertical multi-junction
WPAFB	Wright Patterson Air Force Base
WPT	Wireless power transmission

LIST OF TABLES

Table	Page
TABLE I: GEO to LEO acquisition time sequence [reproduced from source 23]	23
TABLE II: Laser transmittance through rainfall [reproduced from source 34]	50
TABLE III: Cloudburst Scattering Coefficients [reproduced from source 35]	50
TABLE IV: Weather parameter attenuation [reproduced from source 36, 37]	51
TABLE V: Tabulated SPB calculations for two proposed spatial link systems.....	55
TABLE VI: HILPB Receiver Construction Log.....	68
TABLE VII: 940 nm Wavelength Results.....	91
TABLE VIII: 976 nm Wavelength Results.....	91
TABLE IX: 808 nm Wavelength Results	91
TABLE X: Measured off-axis power generated by the receiver	110
TABLE XI: VMJ Responsivity at increasing irradiance levels	131
TABLE XII: Ambient and Dark Current Measurements.....	134
TABLE XIII: Polarization rotation at both optic stages	140

LIST OF FIGURES

Figure		Page
Figure 1:	Claude Chappe's optical telegraph	2
Figure 2:	Photophone transmitter and receiver set	2
Figure 3:	Left: Naval signal lamp for transmitting Morse code, Right: PAPI indicating glide slope of approaching aircraft	3
Figure 4:	Advertisement for the Zenith optical remote control.....	4
Figure 5:	SILEX signal strength and noise components [reproduced from source 8]	6
Figure 6:	ARTEMIS and OICETS optically linked	7
Figure 7:	FSO communications system deployed in an urban environment.....	8
Figure 8:	Novasol bistatic lasercomm terminal aboard the USS Denver	9
Figure 9:	Solar concentrator installation utilizing VMJ photovoltaic cells at NASA GRC [reproduced from source 14]	10
Figure 10:	VMJ cell with attached silver ribbon electrical leads	11
Figure 11:	Spectral response plot for VMJ cell.....	12
Figure 12:	Silicon VMJ cell thermal efficiency de-rating curve.....	13
Figure 13:	Integrated HILPB system into an Air Force Pointer UAV	14
Figure 14:	Boeing 747 ABL with laser turret [reproduced from source 15].....	15
Figure 15:	Navy LaWS [reproduced from source 16].....	15

Figure 16:	Airship optical link delivering power and/or communications.....	17
Figure 17:	Data returned from UAV with a MRR to interrogating laser station [reproduced from source 18].....	17
Figure 18:	Flight model of the laser boosted lightcraft [reproduced from source 19]	18
Figure 19:	Optical vs. RF ground intercept area [reproduced from source 23]	21
Figure 20:	Laser and microwave privacy comparison [reproduced from source 23].	24
Figure 21:	Atmospheric opacity across the electromagnetic spectrum [reproduced from source 24]	25
Figure 22:	Trajectory of electric-field vector [reproduced from source 25]	28
Figure 23:	Linear polarization [reproduced from source 25]	29
Figure 24:	Circular polarization [reproduced from source 26]	30
Figure 25:	Grid polarizer [reproduced from source 26]	31
Figure 26:	The law of Malus [reproduced from source 26]	31
Figure 27:	Series Brewster angle plates [reproduced from source 26]	32
Figure 28:	Example of a half-wave plate [reproduced from source 27].....	33
Figure 29:	Birefringent wave plate [reproduced from source 27].....	34
Figure 30:	Illustration of a Wollaston prism [reproduced from source 26]	34
Figure 31:	System block diagram for a direct detection laser receiver	38
Figure 32:	OOK and PPBM waveforms.....	39
Figure 33:	Pulse-gated binary modulation waveform progression.....	40

Figure 34:	BEP plot for PGBM [reproduced from source 30]	41
Figure 35:	Diagram of a coherent optical communication receiver system.....	42
Figure 36:	Aerosol absorption extinction [reproduced from source 33]	49
Figure 37:	Calculation of the received power [reproduced from source 39]	54
Figure 38:	Spatial link power budget [reproduced from source 23]	56
Figure 39:	Noise background calculations [reproduced from source 23]	57
Figure 40:	Depiction of total internal reflection of light	58
Figure 41:	Bundled fiber delivery system [reproduced from source 42]	58
Figure 42:	OOK bit error rate [reproduced from source 47]	62
Figure 43:	Cross-sectional stack-up of the power receiver	64
Figure 44:	Zalman heat pipe unit.....	65
Figure 45:	Thermal analysis of the power receiver	66
Figure 46:	Two views of a complete HILPB receiver.....	67
Figure 47:	LIMO water-cooled turnkey laser diode system.....	69
Figure 48:	HILPB test facility at CSU	70
Figure 49:	Transmittance curve and coating on the protective fiber window	71
Figure 50:	Design and construction of the gimbaled yoke target mechanism	72
Figure 51:	Gimbal rig with receiver, power electronics and MUAV	72
Figure 52:	Top level block diagram of the receiver electronics system.....	73

Figure 53:	Flight ready power management and data handling system	74
Figure 54:	DATAQ – functional block diagram	75
Figure 55:	The data acquisition system GUI with example power curve	75
Figure 56:	Cell back-feeding with small overfill	77
Figure 57:	Cell back-feeding with medium overfill	77
Figure 58:	Cell back-feeding with large overfill	77
Figure 59:	Nine-cell square receiver	79
Figure 60:	Square receiver at 30% beam overfill, $23 \text{ W } P_{\text{mp}}$	79
Figure 61:	CAD layout of the radial orientation receiver design	80
Figure 62:	Top cell I-V curve, $7.471 \text{ W } P_{\text{mp}}$	81
Figure 63:	Right cell I-V curve, $7.467 \text{ W } P_{\text{mp}}$	81
Figure 64:	Bottom cell I-V curve, $7.485 \text{ W } P_{\text{mp}}$	82
Figure 65:	Left cell I-V curve, $7.385 \text{ W } P_{\text{mp}}$	82
Figure 66:	Center cell I-V curve, $6.852 \text{ W } P_{\text{mp}}$	82
Figure 67:	Four cell I-V curve, $19.976 \text{ W } P_{\text{mp}}$	83
Figure 68:	Five cell I-V curve, $23.935 \text{ W } P_{\text{mp}}$	83
Figure 69:	48.09% illumination, $25.206 \text{ W } P_{\text{mp}}$ at $26.2\% \eta$	84
Figure 70:	37.72% illumination, $23.479 \text{ W } P_{\text{mp}}$ at $31.12\% \eta$	85
Figure 71:	25.24% illumination, $22.488 \text{ W } P_{\text{mp}}$, at $44.39\% \eta$	85

Figure 72:	9-cell radial array in the Northrop Grumman laser facility	86
Figure 73:	Silicon spectral response.....	87
Figure 74:	Optical absorption for various semiconductor materials	89
Figure 75:	Single VMJ cell laser power beaming test rig	90
Figure 76:	Wavelength maximum power I-V curves	92
Figure 77:	Wavelength input versus output.....	93
Figure 78:	Wavelength conversion efficiencies	93
Figure 79:	Wavelength efficiency comparison.....	94
Figure 80:	Wavelength output comparison	94
Figure 81:	H and V profile cuts of the conditioned flat-top beam profile.....	97
Figure 82:	Mechanical illustration of the enclosed beam tube.....	97
Figure 83:	Picture of the unenclosed beam homogenization optic stages.....	98
Figure 84:	Nine cell water cooled receiver illuminated with a flat-top beam	99
Figure 85:	Results of the flat-top beam with a 9-cell parallel array	99
Figure 86:	Nine cell receiver illuminated with a Gaussian beam.....	100
Figure 87:	Results of the Gaussian beam with a 9-cell parallel array	100
Figure 88:	Peak power density test with a single VMJ cell	101
Figure 89:	Peak power density I-V curve with a single VMJ cell.....	101
Figure 90:	LIMO laser system and diode module	102

Figure 91:	TEM ₀₀ model of the beam profile	103
Figure 92:	Beam profiling setup.....	104
Figure 93:	Scanning to the extents of the beam profile.....	105
Figure 94:	Surface plot of the beam at 200 W of radiant power	106
Figure 95:	Contour plot of the beam at 200 W of radiant power	106
Figure 96:	10 th order polynomial beam distribution.....	107
Figure 97:	Experiment setup for the off axis tests.....	108
Figure 98:	Progression of a horizontal axis rotation	109
Figure 99:	Progression of a vertical axis rotation.....	109
Figure 100:	Horizontal and vertical off axis responses at 150 W radiant power	110
Figure 101:	Horizontal and vertical off axis responses at 200 W radiant power	111
Figure 102:	Horizontal and vertical off axis responses at 250 W radiant power	111
Figure 103:	Horizontal and vertical off axis responses at 300 W radiant power	112
Figure 104:	Horizontal and vertical off axis responses at 350 W radiant power	112
Figure 105:	Direct illumination at 350 W	113
Figure 106:	Horizontal axis rotation of 45 degrees	113
Figure 107:	Vertical axis rotation of 45 degrees	113
Figure 108:	Single (mono) crystalline photovoltaic cell	114
Figure 109:	1 kHz clocking (top) of the laser diodes (bottom)	115

Figure 110:	10kHz clocking (top) of the laser diodes (bottom)	115
Figure 111:	Mono-crystalline silicone photovoltaic cell output under 10 W illumination exhibiting significant noise but good transient responsivity	116
Figure 112:	Triple Junction TASC under pulsed illumination.....	117
Figure 113:	Triple junction photovoltaic cell output under 50 W illumination exhibiting significant signal distortion.....	118
Figure 114:	Quantum efficiency versus wavelength for a triple junction cell	119
Figure 115:	VMJ photovoltaic cell under pulsed illumination.....	119
Figure 116:	VMJ photovoltaic cell output under 30 W illumination	120
Figure 117:	VMJ photovoltaic cell output under 75 W illumination	121
Figure 118:	VMJ photovoltaic cell output under 120 W illumination	122
Figure 119:	VMJ photovoltaic cell output under 165 W illumination	123
Figure 120:	VMJ photovoltaic cell output under 210 W illumination	124
Figure 121:	VMJ photovoltaic cell output under 255 W illumination	125
Figure 122:	VMJ photovoltaic cell output under 300 W illumination	126
Figure 123:	VMJ photovoltaic cell output under 345 W illumination	127
Figure 124:	Discrete Fourier Transformation of the VMJ output	129
Figure 125:	Optically-coupled switched-mode DC/DC power convertor abstraction for the HILPB communications system.....	132

Figure 126: Clockwise from left: breadboard DC/DC convertor, data collection electronics and active variable load	133
Figure 127: Full duty cycle with 11.3327 W output	134
Figure 128: Half duty cycle with 4.8078 W output.....	135
Figure 129: Quarter duty cycle with 2.6789 W output.....	135
Figure 130: Receiver output versus duty cycle	135
Figure 131: Source optics for the polarization experiment	137
Figure 132: Rotating the linear source optic to characterize the dominant linear beam polarization angle.....	138
Figure 133: Introduction of the receiver optic for the polarization experiment	139
Figure 134: Stage 1 (source) linear polarization rotation	141
Figure 135: Stage 2 (receiver) linear polarization rotation	141
Figure 136: Optical communications link budget	144
Figure 137: Modulating retro reflector.....	146
Figure 138: Optical multi-function architecture schematic	147
Figure 139: Potential integrated beamed energy representation	154

CHAPTER I: INTRODUCTION

The heritage of optical communications extends back much farther than that of RF technology, yet there is still a wide tradespace to explore in terms of exploiting the capabilities offered in the optical domain. This chapter will highlight some of the major advances in optical communication systems, and identify potential synergies with the developed wireless power transmission system.

1.1 A Brief History of Free Space Optical Communications

The history of optical communications starts with using light for the dissemination of news through what we could decipher with our own eyes, and over time technology was developed to allow us to transmit and receive signals from increasing distances. Some of the early incarnations included beacon fires, smoke signals, signal markers and light houses. The achievable range was greatly increased through the use of relay stations, such as with Chappe's optical telegraph system for the French military during the early 1800's (*Figure 1*). Here, a series of mechanical lighted structures spaced 11 km apart could relay a message over 135 km in one minute, and reproduce 196 distinct symbols.



Figure 1: Claude Chappe's optical telegraph

Later during the 1800's the optical telegraph system was widely adopted in both the European and US railway systems in the form of semaphore signaling. In 1880, Alexander Graham Bell patented what he referred to as his greatest invention, the photophone (*Figure 2*). This system modulated human conversations onto visible light, and demonstrated transmission across distances up to 200 m. This achievement may be thought of as a very early predecessor to our modern fiber optic communications systems, and legs of the system are still operational today.

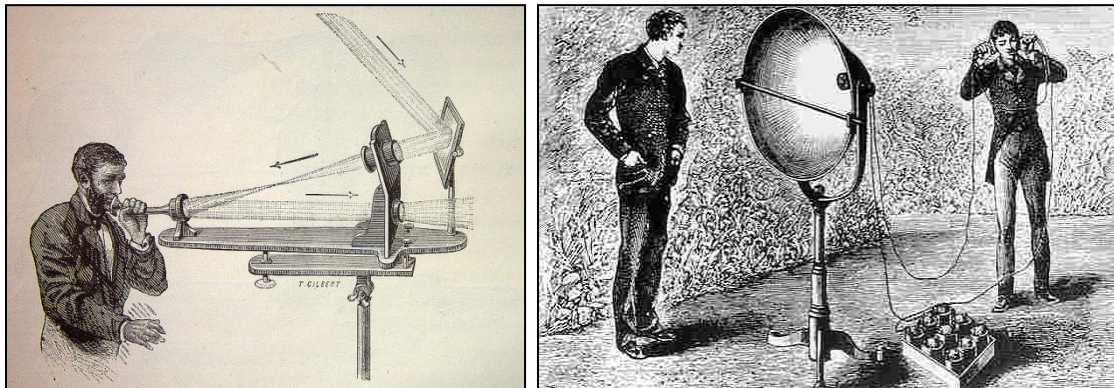


Figure 2: Photophone transmitter and receiver set

Similar variations of the simple essence of these early forms of optical

communication still exist today. The Navy has long used a signal lantern intermittently covered with a shutter as a way to pass Morse code messages between vessels during periods of radio silence [1]. Modern Air Traffic Control (ATC) towers still maintain a multi-colored light gun as a backup device in case of radio failure, and all pilots are versed in these procedures to accomplish safe queuing and landing in such an event. In addition, the Federal Aviation Administration (FAA) employs a series of brightly colored Fresnel lens instruments called Precision Approach Path Indicators (PAPI) which provide a landing pilot visual feedback for the position of their aircraft relative to the optimal 3 degree glide slope [2]. These instruments are especially useful during night and carrier operations where visual distortion is at its highest, and may be visible for several nautical miles away depending on the atmospheric conditions.



Figure 3: Left: Naval signal lamp for transmitting Morse code, Right: PAPI indicating glide slope of approaching aircraft

In the consumer electronics area, the first wireless remote control for television was introduced by Zenith as the Flash Matic system in 1955 (*Figure 4*). This system used four corner photocells to control the functionality of the set, and later evolved into

the infrared remote control systems that are commonly used today.



Figure 4: Advertisement for the Zenith optical remote control

The advantages of high energy density and narrow beamwidth of the laser make it a natural candidate for free space optical communication applications. These properties allow for the propagation path of a laser communications link to extend farther than with conventional lamps, favorably suggesting space-based communications applications. After years of developing a direct detection system for the neodymium yttrium aluminum garnet (Nd:YAG) laser operating at 1064 nm, the U. S. Air Force formalized an agenda to develop and demonstrate a space-based laser crosslink in the early seventies. One of the early stepping stones in developing the space-qualified laser communications hardware for this directorate was the Airborne Flight Test System (AFTS), or the Air Force 405B program, which was funded out of Wright Patterson Air Force Base (WPAFB) in Dayton, Ohio. The 405B experiments consisted of an EC-135 test aircraft using a Nd:YAG laser to prove the feasibility of transmitting information over a turbulent atmospheric channel to a ground station. The program was successful in demonstrating up to 1 Gbps of

optical data transfer rate, and achieved slant range distances to 100 km [3].

Following the success of the WPAFB 405B program, many investigations were made into developing and refining the component technologies of the laser communications system. Some of these advances were the emergence of avalanche photodiode detectors, laser-diode pump sources, optical alignment techniques and radiation hardening and optical coatings for system components. One notable achievement made by the Massachusetts Institute of Technology's Lincoln Laboratory (MITLL) was the development of a coherent optical communications system [4-6]. The coherent system employed frequency shift keying (FSK) to modulate the transmitted energy, and the receiver utilized a local oscillator laser source mixed with the received signal to decode the message. Gallium-Arsenide photodiodes were used to detect the energy, and data rates up to 220 Mbps were demonstrated in the lab.

In 1992, a breakthrough demonstration called the Galileo Optical Experiment (GOPEX) demonstrated the ability to point ground-based lasers precisely to objects in deep space, and to sense long-distance optical pulses. Both the Jet Propulsion Laboratory's (JPL) Table Mountain Facility and the Starfire Optical Range (SOR) at Kirtland Air Force base in Albuquerque, New Mexico were used to illuminate the charge coupled device (CCD) camera on board the Galileo spacecraft at a range of six million kilometers [7]. The optical pulses were successfully detected and then retransmitted back to the ground for validation using the conventional spacecraft RF downlink.

A demonstrated study into atmospheric propagation effects has been made with the European Semiconductor Laser Intersatellite Link Experiment (SILEX), in which one link leg consisted of a 148 km horizontal terrestrial path along the sea between the

Canary Islands [8]. The program utilized 0.79, 0.87, 1.064, 1.3 and 10.2 μm laser wavelengths with up to 50 Mbps data rates, and measurements of absorption, scattering, scintillations and turbulence were made. The signal strength and noise components from the SILEX experiments across a 148 km terrestrial link are plotted simultaneously in *Figure 5*, and it can be seen that the signal-to-noise ratio (SNR) when the sun is in the field of view (FOV) of the receiver is approximately 25 dB, for the case when atmospheric attenuation is at 4.5 dB.

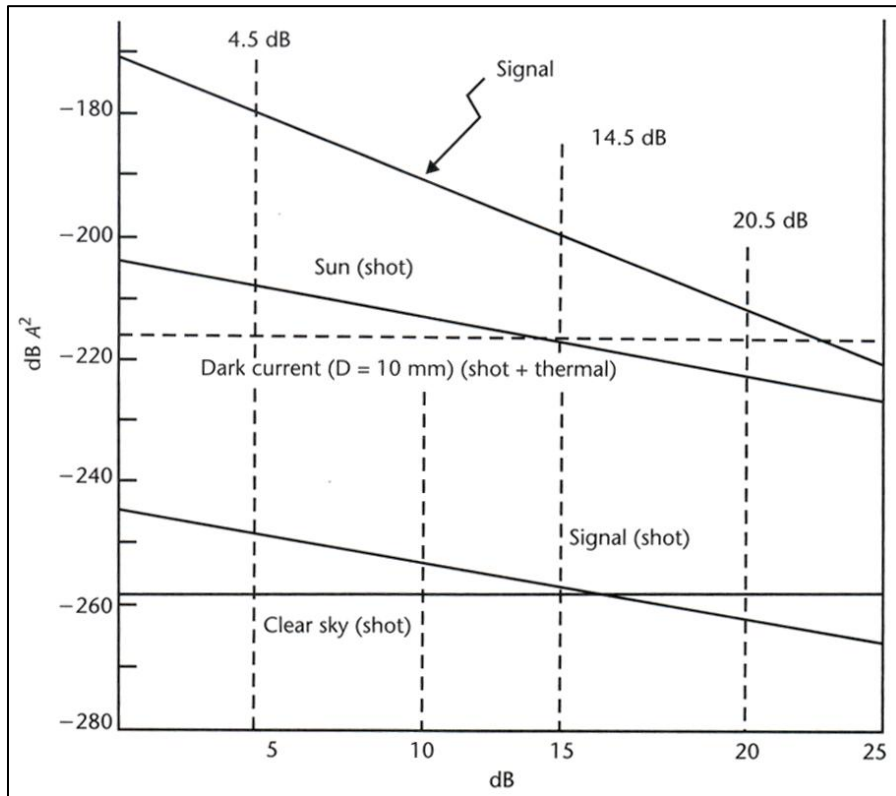


Figure 5: SILEX signal strength and noise components [reproduced from source 8]

In a more recent measurement program conducted by the Lawrence Livermore National Laboratory (LLNL), a 28 km laser link employing an adaptive optical system was operated in Northern California [9]. Measurements of the wavefront distortion were made at the receiver, and deformable mirror elements actuated by

microelectromechanical systems (MEMS) corrected for the turbulence in the atmosphere. This approach achieved a reduction in the bit-error-rate (BER) of the signal, and a data rate of 20 Gbps was achieved.

In 2005, the Japan Aerospace Exploration Agency's (JAXA) Optical Intersatellite Communications Engineering Test Satellite (OICETS) 'KIRARI' in LEO and the European Space Agency's (ESA) Advanced Relay and Technology Mission (ARTEMIS) satellite in GEO successfully established an optical intersatellite communications link [10]. Since then, the optical service has operated regularly and accumulated more than 1100 links totaling 230 hours to date, achieving 2 Mbps forward and 50 Mbps return links.



Figure 6: ARTEMIS and OICETS optically linked

The maximum distance record for laser communications transmission was set in 2006 by NASA Goddard Space Flight Center's (GSFC) Geophysical and Astronomical Observatory in Maryland, which successfully communicated with the Messenger

spacecraft across a distance of approximately 25 million km [11]. Messenger was outfitted with a Mercury Laser Altimeter (MLA), an instrument designed to map Mercury's surface, and this was used to exchange laser pulses with the observatory to demonstrate two-way deep space optical communication. The success of this technology demonstration laid the groundwork for a proposed Mars Telecommunications Orbiter (MTO) spacecraft to serve as a high speed optical data link for relaying scientific information back to Earth from the other Mars orbiter and lander assets, but unfortunately the program was cancelled due to funding problems [12].

In a more terrestrial accomplishment, within a few days of the World Trade Center collapse in New York which severed many crucial fiber optic systems, high speed communication services were reestablished to surrounding businesses clients through deploying rooftop FSO systems from Lightpointe Communications, Inc. The systems feature multi-Gb/s service across 1 km or better, depending on the atmospheric conditions. The ability to quickly establish a backup network in an emergency situation demonstrates the flexibility and rapid deployment capability of the FSO system, and its ability to reduce downtime during periods of construction and repair.



Figure 7: FSO communications system deployed in an urban environment

Finally, during the Navy's Trident Warrior 2006 sea trial experiment, ship-to-ship laser communications was demonstrated as a way to evaluate the utility of the capability and quantify the performance of the systems. During the trial the 2 W 1550 nm lasercomm terminals were able to demonstrate fast Ethernet (125 Mbps) transmission to successfully send large data, movie and audio files, as well as enable live ship-to-ship video teleconferencing between the USS Denver and the USS Bonhomme at ranges from 2.5 to 11 nm [13]. A two level PAT system nulled out the ship's motion, and provided lock onto the other terminal. This was the first demonstration of ship-to-ship laser communications on operational US Navy ships at sea, and resulted in over 10 hours of successful 300 Mbps audio and video links at ranges up to 9.5 nm in the rain. Improvements based on lessons learned from this exercise should allow links to the horizon (\leq 20 nm).



Figure 8: Novasol bistatic lasercomm terminal aboard the USS Denver

1.2 The HILPB System

A novel optical wireless power transmission system has been developed by a cadre of researchers in the Industrial Space Systems Laboratory (ISSL) at Cleveland State University (CSU) under contract (grant) from the Air Force Research Laboratory (AFRL) Revolutionary Munitions Directorate at Eglin Air Force Base. This system utilizes specially designed photovoltaic cells to receive and convert high radiant laser light into electrical energy at appreciable efficiencies and substantial energy densities at the receiver. The nominal optical-to-electrical conversion efficiency and output power density at the cell level that has been achieved thus far are on the order of 44% and 20 W/cm².

While typical photovoltaic devices may only handle broadband irradiances up to 100 mW/cm², special photovoltaic cells developed by NASA John H. Glenn Research Center (GRC) scientists at Lewis Field in the early 1990s, known as vertical multi-junction (VMJ) cells, have demonstrated high conversion rates of 25% at up to 70 W/cm² broadband solar irradiance. The primary application for the VMJ technology has been for terrestrial solar concentration applications, such as the 1.5 kW integrated solar power plants currently being deployed by Greenfield Solar Corporation [14].



Figure 9: Solar concentrator installation utilizing VMJ photovoltaic cells at NASA GRC
[reproduced from source 14]

The silicon based VMJ cells differ fundamentally from conventional photovoltaic devices, in that each individual chip contains multiple junctions of semiconductor material, arranged to rest on its edge. This creates an edge-illuminated device, where the electrical power may be easily routed through the low resistance junctions and delivered on the outer edges of the cell. A typical 0.8 cm VMJ cell is constructed with 40 junctions as shown in *Figure 10*, thus offering a nominal 24 V output, but this may easily be tailored at the manufacturing stage to accommodate different bus voltages.

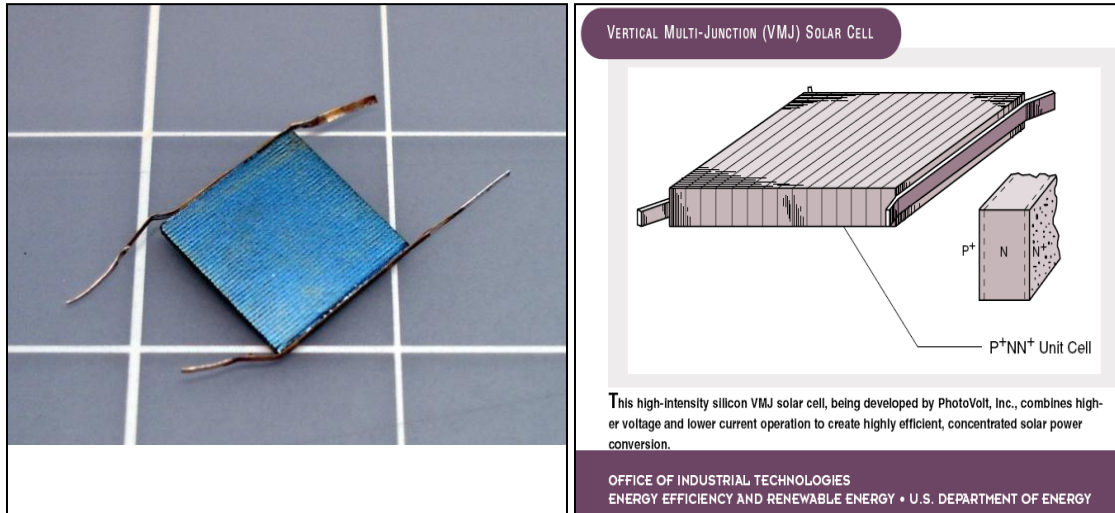


Figure 10: VMJ cell with attached silver ribbon electrical leads

The 25% optical-to-electrical efficiency figure for the VMJ cell is an average value across all frequencies in the solar spectrum. The frequency dependent conversion efficiency is the result of the silicon construction of the cell, and exhibits a peak at the band gap (around 1.125-1.2 eV) of the silicon crystalline structure corresponding to the near infrared region (IR-A) in *Figure 11*. It is this peak that may be exploited with narrowband laser illumination, and it is expected that with further optimization, the optical-to-electrical energy conversion efficiency of the cells may reach close to 60% for incident laser light in the IR-A range.

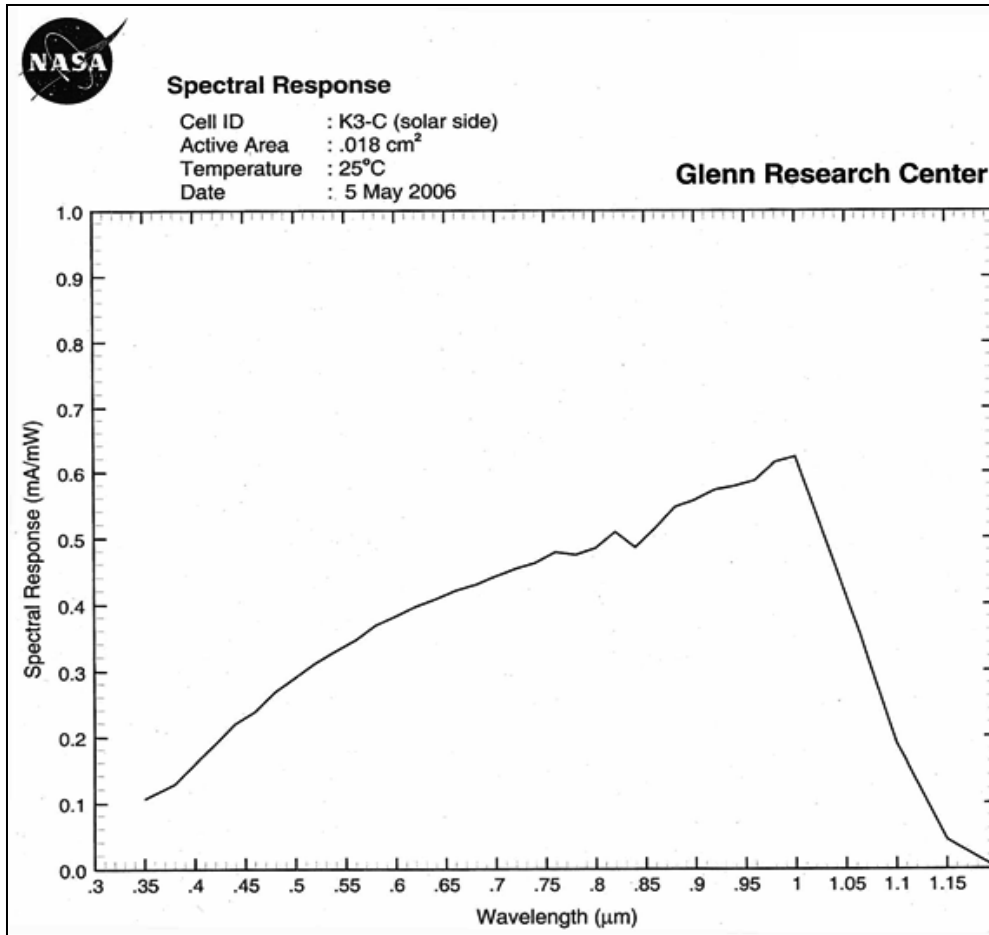


Figure 11: Spectral response plot for VMJ cell

The VMJ cells are extremely robust and are able to withstand large thermal loads because they are fabricated from high-grade silicon, and do not utilize the planar contacts found in conventional solar cell topologies that trap heat under high irradiance levels. By receiving the photonic energy through junction edges rather than on conventional wired surfaces, the VMJ cell also maximizes the convertible photovoltaic surface area, and eliminates exposing the contact wires to the high intensity light. As such, the cells are able to operate continuously at high temperatures (with corresponding reduction in efficiency-*Figure 12*) and are also able to survive and recover from exposure to temperatures as high as 600° C.

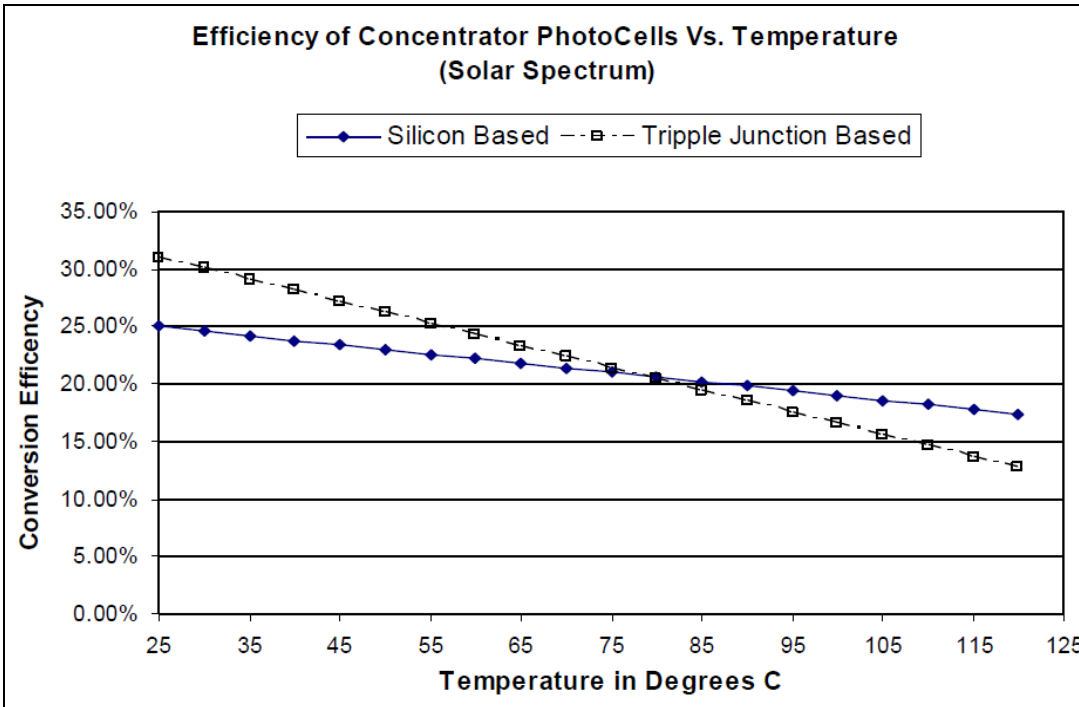


Figure 12: Silicon VMJ cell thermal efficiency de-rating curve

The integration of the VMJ cell technology into a thermal receiver, combined with high wall plug efficiency semiconductor laser sources, high energy optics, digital high speed pointing acquisition and tracking (PAT) systems and power management and distribution (PMAD) electronics creates the high intensity laser power beaming (HILPB) system. The HILPB system can wirelessly deliver large amounts of electrical energy from distant sources to aerial vehicles, satellites and remote robotic platforms, among many other applications where energy may not be obtained by conventional means. The performance of the VMJ photovoltaic cells for these applications is a breakthrough technology for the development of a revolutionary in-air, long range, remote laser refueling system that will provide unprecedented 24/7 area dominance capability by constellations of micro unmanned aerial vehicles (MUAV's).



Figure 13: Integrated HILPB system into an Air Force Pointer UAV

The ability to acquire and track a target, such as the UAV shown above, is a critical system element to enabling the HILPB system. Synergies with the munitions directorates may be identified, such as with the flagship megawatt class Airborne Laser (ABL) research and development platform (*Figure 14*). Techniques such as on-line sensing of the beam propagation through the atmosphere and adaptive optics have successfully been employed to insure the integrity of the beam propagation and to reduce jitter and compensate for air turbulence. The 600 km range of the ABL is a testament to the maturity of the current HEL technologies, and these military successes can be capitalized on with laser power beaming. The high-profile ABL program is an ongoing effort, and new advances in laser control will be continually developed to increase the range and accuracy of the beam.



Figure 14: Boeing 747 ABL with laser turret [reproduced from source 15]

HEL laser tracking systems since the ABL have been progressively downsized, resulting in a more portable source. The Navy laser weapons system (LaWS) is a ship defense system currently under development. LaWS has been able to successfully engage airborne targets in a marine environment, considering the atmospheric effects of aerosols and dynamic platform motion. Such a system will see further downsizing and tracking control capability in the future, realizing a more attractive deployable solution for a HEL system.



Figure 15: Navy LaWS [reproduced from source 16]

1.3 Future Potential for a High Intensity Laser Communications System

The current application for the Air Force HILPB program is to provide optical in-air ‘refueling’ of electric aircraft, which will allow indefinitely extended mission flight times for 24/7 aerial domination. Beyond the immediate AFRL program, the HILPB system can be used for many applications where power is needed but conventional transmission lines are impracticality prohibitive. Examples may include deep space exploration vehicles, reconfigurable power grids on the Moon and Mars, and establishing ad-hoc emergency power to terrestrial areas in distress. By utilizing the VMJ cells as a detector for communications, forward command and control information may be send concurrently with the power transmission, resulting in a dual use system.

For example, the recent renewed interest in long duration, high altitude and heavy-lift airship designs offers another opportunity for HILPB to extend mission capability [17]. One of the primary applications for these proposed airships is to serve as a stratospheric surveillance and communications relay platform that may be deployed for a year at a time, and then be recovered for servicing and payload technology updating. Among the propulsion sources considered for this application are electric motors, which would operate off of onboard lithium-ion storage batteries and thin film photovoltaic devices to supply the recharging energy. This type of platform may benefit from the addition of a HILPB receiver to offset a portion of the photovoltaic array, which would give it the ability to quickly recharge its power system from a remote location, or to provide a transient enhanced capability.

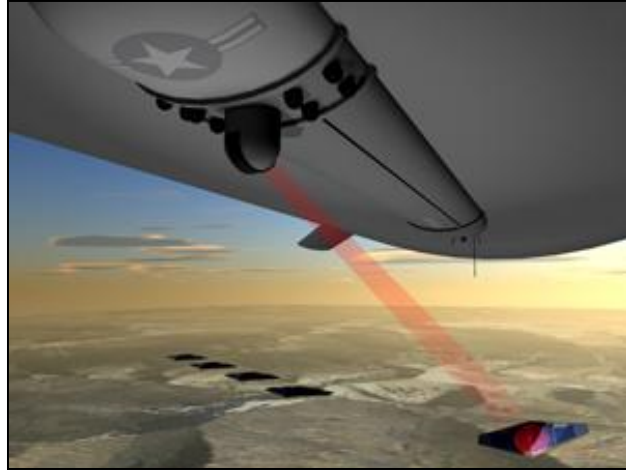


Figure 16: Airship optical link delivering power and/or communications

By incorporating a communications signal into the optical energy delivery path, enormous amounts of data may be securely and covertly uplinked to the airship, and by employing a modulated retro-reflector (MRR) on the airframe, comparable amounts of data may be equally retrieved from the platform during the transmission [18]. Such a link has been demonstrated by the Naval Research Laboratory (NRL) using a small UAV helicopter as the flight platform to successfully return near-real time compressed video information back to the interrogating ground station.

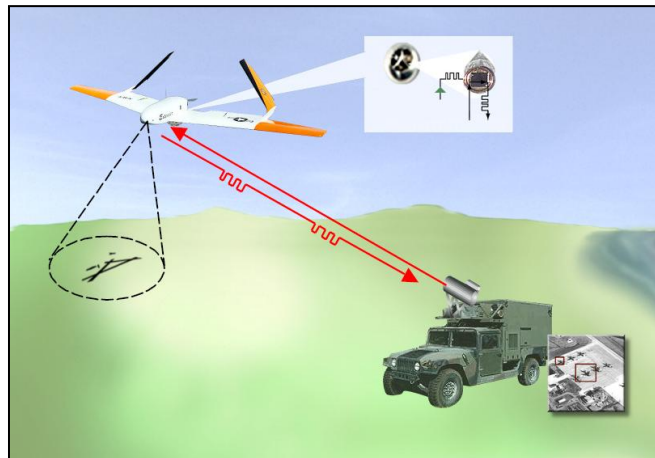


Figure 17: Data returned from UAV with a MRR to interrogating laser station
[reproduced from source 18]

Beamed energy propulsion is a concept where directed energy is utilized to propel a craft through a variety of means such as a thermal engine, or by generation of a plasma-induced detonation wave (*Figure 18*). These types of beamed energy vehicles are being developed as a low cost alternative way to achieve hypersonic velocities in the atmosphere, and to launch payloads to orbit. The beam riding properties of the lightcraft under conditions of intense directed illumination lend themselves favorably to utilizing high energy photovoltaic devices that could enable both energy harvesting and communications capability to the craft.

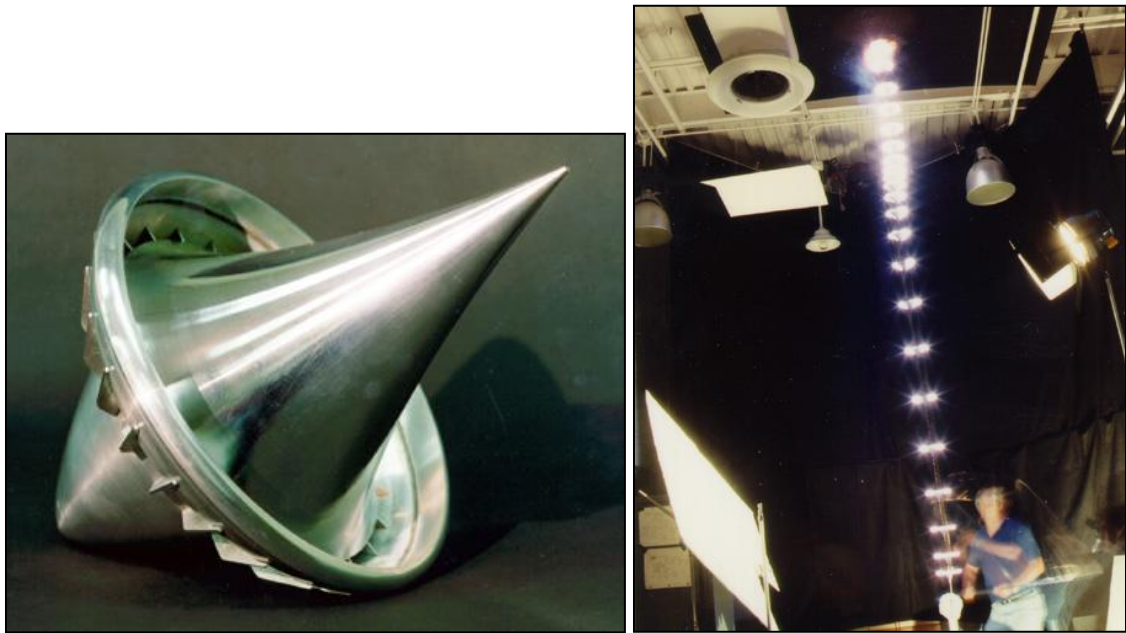


Figure 18: Flight model of the laser boosted lightcraft [reproduced from source 19]

In each of these scenarios, the ability to integrate communications capability with wireless power transmission offers a high value added technology with a minimal amount of modification to the existing system infrastructure. Uplinks, downlinks and crosslinks to a satellite backbone system could be augmented with HILPB to develop a virtual power and communications grid network that could deliver both information and power

anywhere in the world and beyond. The performance metrics of such a system will be discussed in the following chapters, along with design recommendations and avenues for future research.

1.4 Document Organization

A literature review of optical communications systems including comparisons with RF based systems, performance metrics, system trades and design parameters appears in Chapter 2. The experimental setup and research methodology is described in Chapter 3, and the experiments conducted and data analysis appears in Chapter 4. Finally, the results and conclusions are stated in Chapter 5, with recommendation for future work in Chapter 6.

CHAPTER II: LITERATURE REVIEW OF LASER COMMUNICATIONS

2.1 Advantages of Optical Communications

As early as the first successful implementation of Light Amplification by Stimulated Emission of Radiation, or LASER, in 1960, optical communications has been one of the principal considered applications for the technology [20]. Lasers lend themselves favorably to the field of communications because of several unique characteristics inherent in the technology. The extreme directivity of the transmitted photonic energy in the optical regime, when compared to that of conventional microwave technology, results in several systems level benefits. The directionality of a beam exhibiting a Gaussian energy profile is described by the angle of beam divergence θ , subject to the diffraction limit, and as a function of the wavelength of the beam λ_{laser} and the diameter of the beam waist (D_{laser}) at the aperture of the transmitting telescope. [21]

$$\theta \cong 2.24 \times \frac{\lambda_{laser}}{D_{laser}} \quad (1)$$

As an example, for a 1.0 micron laser with an aperture diameter $D_{laser}=10$ cm the resulting the beamwidth would be 22.4 μ rad. *Expression 1* may also be used to approximate the directionality of a pattern transmitted from a microwave antenna with a

diameter $D_{\text{microwave}}$ and radiating at a wavelength of $\lambda_{\text{microwave}}$. By comparing both of these calculations, the first benefit of laser optical communications is revealed. For the X-band antenna dish onboard the workhorse Defense Satellite Communications System (DSCS-2) satellite the resulting beamwidth would be 3° [22]. At the point of ground intercept on the Earth's surface at the equator from a geosynchronous orbit (approximately 35,786 km (22,236 mi) above mean sea level altitude at the equator), the example laser beam would illuminate a circular area 800 m in diameter, while the microwave footprint would encompass a diameter of 1,880 km as illustrated in *Figure 19*. This is a best case scenario comparison of the two technologies, in the sense that as the selected ground intercept area moves away from the equator longitudinally the circle of illumination will elongate into an ellipse, and the ratio between the two intercept areas will change. The difference in footprints will have privacy implications with securing a monitored intercept area on the ground, and as previously shown in *Equation 1* this is wavelength driven.

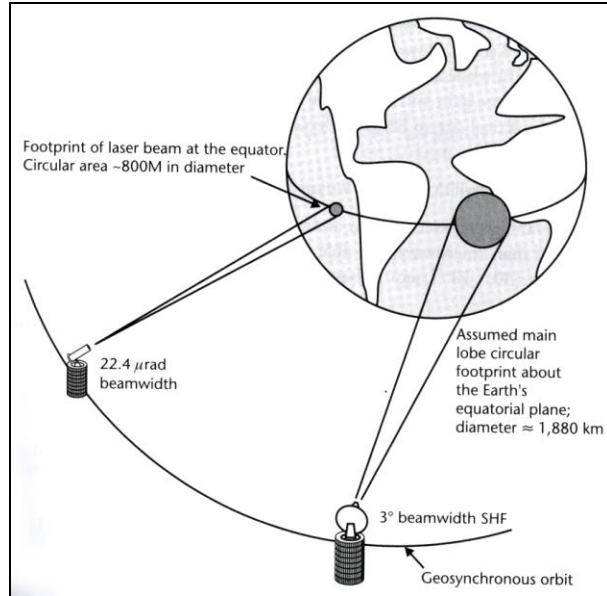


Figure 19: Optical vs. RF ground intercept area [reproduced from source 23]

With the comparably short optical wavelengths, high directivity may be achieved even through relatively small apertures. This is demonstrated by:

$$(\lambda_{laser}/D_{laser})^2 \div (\lambda_{microwave}/D_{microwave})^2 = \theta^2_{laser}/\theta^2_{microwave} \quad (2)$$

The antenna/aperture directivity ratio may be expressed as:

$$G_{laser}/G_{microwave} = 4\pi/\theta^2_{laser} \div 4\pi/\theta^2_{microwave} \quad (3)$$

In the aforementioned example for $\lambda_{laser}=1.0$ micron with aperture $D_{laser}=10$ cm and beamwidth $\theta_{laser}=22.4$ μ rad, the resulting antenna/aperture gain $G_{laser}=104$ dB. To achieve that same amount of gain utilizing X-band RF ($\lambda_{microwave}=3$ cm) the antenna surface would have to be 3 km across. Clearly this is a prohibitive size for operation in space, even for lightweight deployable and inflatable apertures. In a general sense on the receiving side, the microwave antenna needs to be much larger than the optical aperture in order to appreciably encompass the transmitted energy. This creates a fundamental constraint on the physical architecture of an RF based system design.

The narrow beamwidth of the optical system does impart a challenge to the pointing, acquisition and tracking (PAT) system across long distances. By utilizing other technologies such as GPS satellites, star trackers and inertial guidance instruments to obtain attitude and position information, the acquisition process may be accomplished in a timely manner. In addition a beacon may also be used to aid in the acquisition process, in a similar manner to RF communications. *Table I* depicts a scenario in which a GEO satellite accomplishes acquisition and closes the link with a LEO satellite to begin the communications transmission within 7.5 seconds.

TABLE I: GEO to LEO acquisition time sequence [reproduced from source 23]

Function	Duration (sec)	Elapsed Time (sec)
1. Sequence starts at GEO	—	—
2. Beam travel to LEO	0.12	0.12
3. Acquisition of beacon on LEO (without scanning)	5.0	5.12
4. Beam travel to GEO	0.12	5.24
5. Acquisition of communication beam on GEO	0.5	5.74
6. Change beacon mode from acquisition to track	0.5	6.24
7. Beam travel to LEO	0.12	6.36
8. Check beam code, stop acquisition, and begin communication	1.0	7.36
9. Beam travel to GEO	0.12	7.48
Total time from start of beacon acquisition to receiving of communication stream: 7.48 sec		

Considering privacy comparisons between the interception of laser and microwave footprints, *Figure 20* shows a contrast of the relative received power with respect to perpendicular distance from the beam's central axis. In the case of a 1 arcsec (290 μ rad) beamwidth laser, at 0.4 miles from the central axis the power is 40 dB down from the peak at the aperture. With the 35 GHz microwave signal at $1/4^\circ$ beamwidth, the -40 dB point would not occur until approximately 100 miles from the center of the beam. This indicates a substantial loss of privacy in the microwave case.

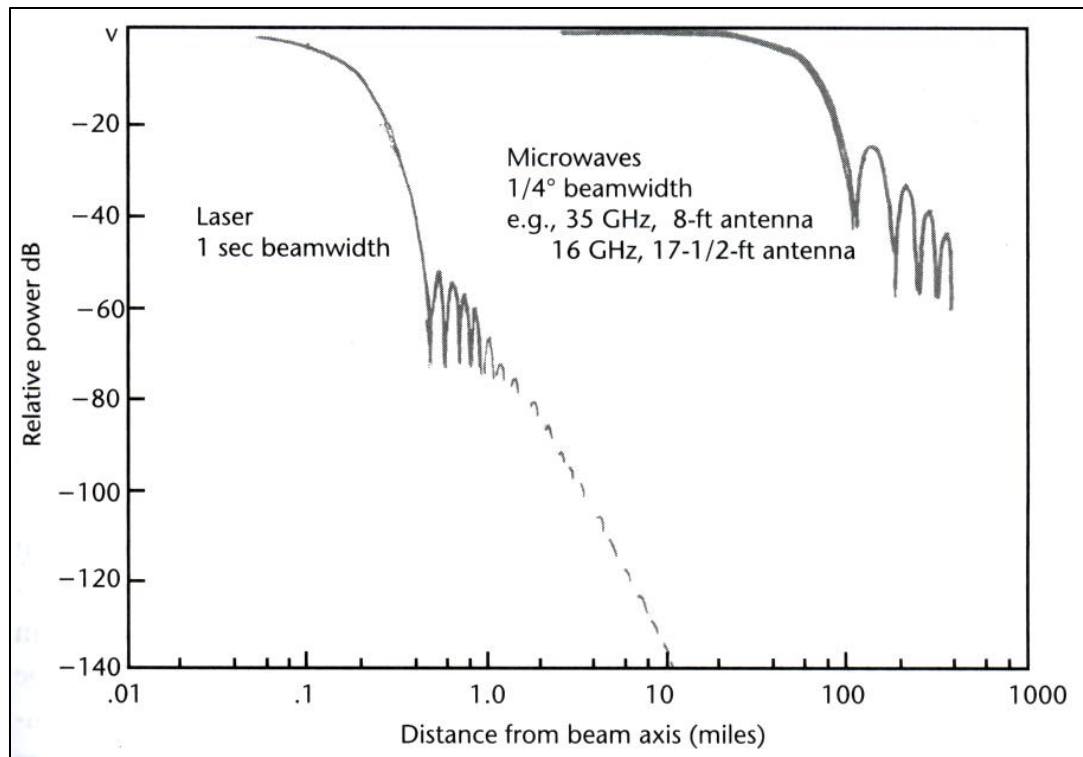


Figure 20: Laser and microwave privacy comparison [reproduced from source 23]

When comparing the atmospheric propagation implications of optical versus RF bands electromagnetic radiation, it can be seen in *Figure 21* that transmittance windows exist across both spectral regions. Within the microwave RF regime the opacity is relatively constant, while the optical bands vary greatly depending on wavelength. This variability places a constraint on the design of an optical system, in that the frequency must be carefully selected to optimize the overall system capability. At 1550 nm, substantial investment has been made by the telecommunications industry to advance the development of supporting components for fiber optic systems, and a significant transmission window through the earth's atmosphere at this frequency also exists.

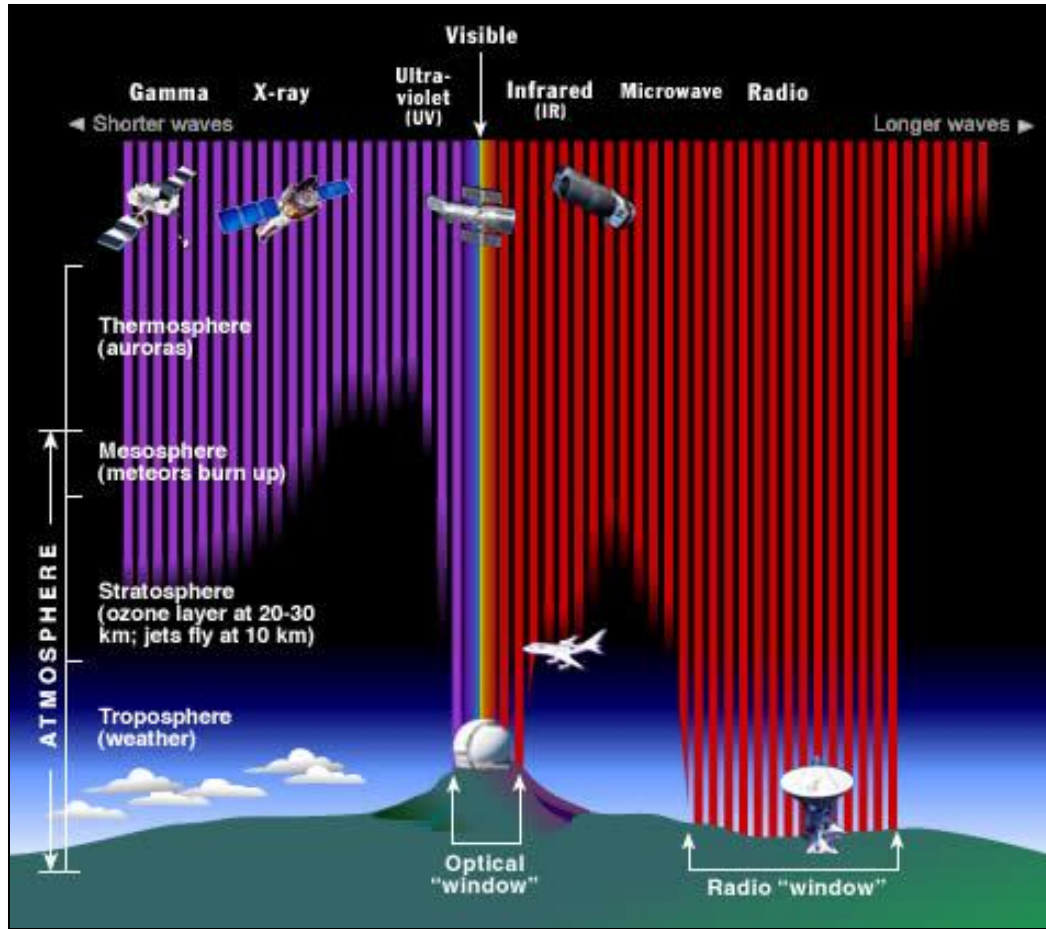


Figure 21: Atmospheric opacity across the electromagnetic spectrum [reproduced from source 24]

Another advantage that laser optical communications has over conventional RF is the enormous amount of information carrying potential in the Terahertz carrier beam. For example, a mode locked laser operating near $1 \mu\text{m}$ ($2.86 \times 10^{14} \text{ Hz}$) and producing 30 ps repetition rate pulses will have a bandwidth of at least 30 GHz. It is important to note that the high rate of repetition is necessary to achieve the information bandwidth, and this may be challenging to accomplish with current single laser implementations. One way to achieve high repetition rates is to employ a system similar to that of a Gatlin gun, where multiple laser sources, each producing picosecond pulses (offset from each other), are fed

into a common aperture. This technique relaxes the pulse repetition requirement on any one laser, and may be used to accomplish an information bandwidth of 30 GHz. In that case, the bandwidth-to-frequency ratio would be:

$$\Delta v/v = 30 \times 10^9 / 3 \times 10^{14} = 10^{-4} \quad (4)$$

In this example the optical carrier could accommodate 1,000 channels that are each 30 GHz wide at a carrier capacity of 10% as given by:

$$(1000 \times 30 \text{ GHz}) / (3 \times 10^{14}) = 10\% \quad (5)$$

This amount of bandwidth can be used to carry an enormous amount of information, but the usefulness of this bandwidth will be limited by factors such as the ease with which information can be imposed upon the beam, the ability for the channel to support it and the capability of the receiver to detect and decode it. These factors will be described in subsequent sections on modulation and demodulation techniques and channel effects.

Finally, in comparing the future growth potential of RF versus optical systems, it is important to note the diminishing available spectrum allocation for certification and licensing in the RF domain from the International Telecommunications Union (ITU) and the National Telecommunications and Information Administration (NTIA), while the entire optical region still remains unregulated and free of license fees, beyond nominal hazard zone restrictions. This currently frees optical technology from the frequency allocation issues and interference problems encountered with RF counterparts.

2.2 Beam Polarization

Before venturing into modulation and detection techniques, a discussion first must be made into the polarization of light since this may serve as a unique optical tool to aid in modulation process. At a given point in space and instant in time the electric-field of a light wave points to a particular direction, and is described by a vector $\boldsymbol{\epsilon}$. This electric-field lies in the x-y plane, and the vector is perpendicular to both the direction of travel of the wave and the instantaneous direction of the magnetic-field of the wave. The direction of the electric field-vector is described as the direction of polarization of light, and since lasers produce light with highly oriented electric-fields, it follows that a degree and form of polarization will also exist. Given a plane wave of frequency ν and an angular frequency $2\pi\nu$, and travelling in the z direction with a velocity c , the electric-field may be represented as:

$$\boldsymbol{\epsilon}(z, t) = \operatorname{Re} \left\{ \mathbf{A} \exp \left[t - \frac{z}{c} \right] \right\} \quad (6)$$

Where the complex envelope \mathbf{A} has components A_x and A_y :

$$\mathbf{A} = A_x \hat{x} + A_y \hat{y} \quad (7)$$

By tracing the endpoint of the vector $\boldsymbol{\epsilon}(z, t)$ at each position z as a function of time t , the direction and type of polarization may be described. For example, the complex components can be represented in terms of their magnitude and phase, given by:

$$A_x = a_x \exp(j\varphi_x) \quad (8)$$

$$A_y = a_y \exp(j\varphi_y) \quad (9)$$

Substituting into the electric-field equations obtains:

$$\boldsymbol{\epsilon}(z, t) = \epsilon_x \hat{x} + \epsilon_y \hat{y} \quad (10)$$

Where the x and y components are described by the periodic functions:

$$\varepsilon_x = a_x \cos \left[\omega \left(t - \frac{z}{c} \right) + \varphi_x \right] \quad (11)$$

$$\varepsilon_y = a_y \cos \left[\omega \left(t - \frac{z}{c} \right) + \varphi_y \right] \quad (12)$$

These equations serve as the parametric equations of an ellipse given by:

$$\frac{\varepsilon_x^2}{a_x^2} + \frac{\varepsilon_y^2}{a_y^2} - 2 \cos \varphi \frac{\varepsilon_x \varepsilon_y}{a_x a_y} = \sin^2 \varphi \quad (13)$$

where $\varphi = \varphi_y - \varphi_x$ describes the phase difference between the two components.

By tracing the electric-field vector, the type of polarization can be revealed as illustrated in *Figure 22*. For fixed positions of z , the electric-field vector rotates in the x-y plane tracing an ellipse in which the field never goes to zero, creating a Lissajous figure. For fixed times t , the electric-field vector tracks a helical trajectory due to one of the components leading the other, which spatially follows the surface of an elliptical cylinder. As the electric-field rotates elliptically the wave advances forward, describing the general polarization ellipse.

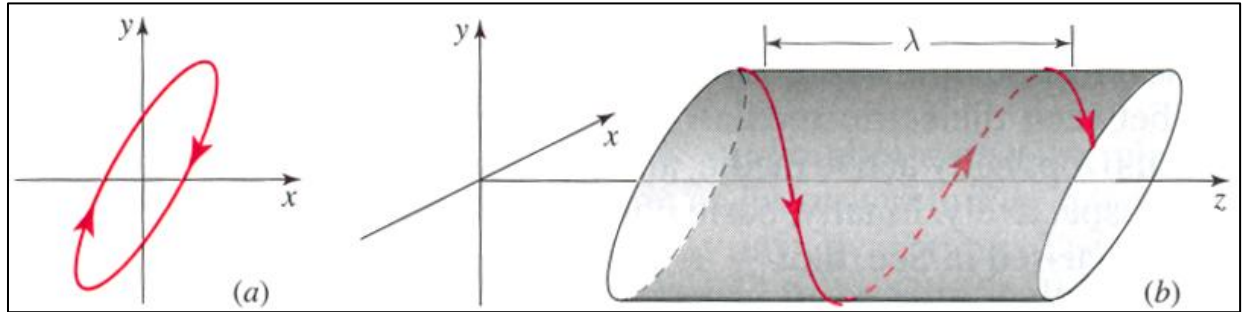


Figure 22: Trajectory of electric-field vector [reproduced from source 25]

In the simplest case if the phase difference $\varphi = 0$ or π , the light is linearly polarized (LP) since (X) gives:

$$\varepsilon_y = \pm \left(\frac{a_y}{a_x} \right) \varepsilon_x \quad (14)$$

Which describes a straight line of slope $\pm a_y/a_x$, where the + and - signs correspond to $\varphi = 0$ or π . Here the polarization is planar, and the electric-field oscillates in the direction of the slope as illustrated in *Figure 23*.

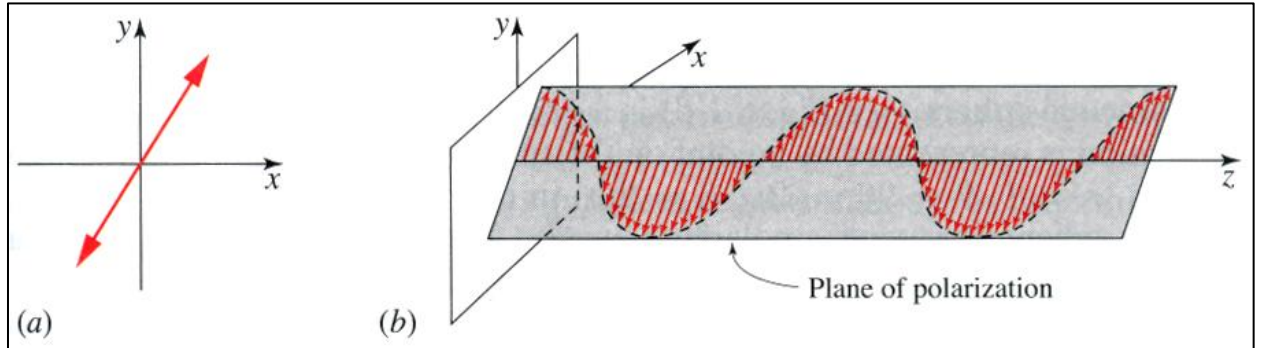


Figure 23: Linear polarization [reproduced from source 25]

If the phase difference $\varphi = \pm\pi/2$, and the components are equivalent in magnitude where $a_x = a_y = a_0$, then the electric-field components can be written:

$$\varepsilon_x = a_0 \cos \left[\omega \left(t - \frac{z}{c} \right) + \varphi_x \right] \quad (15)$$

$$\varepsilon_y = \pm a_0 \cos \left[\omega \left(t - \frac{z}{c} \right) + \varphi_x \right] \quad (16)$$

From which:

$$\varepsilon_x^2 + \varepsilon_y^2 = a_0^2 \quad (17)$$

...describing the equation of a circle, due to the equivalent component magnitudes. When $\varphi = +\pi/2$, at a fixed position z the electric-field rotates in a clockwise direction and this case is called right circular polarized (RCP). Conversely when $\varphi = -\pi/2$, at a fixed position z the electric-field rotates in a counter-clockwise direction and this case is called left circular polarized (LCP), as illustrated in *Figures 24a and 24b*.

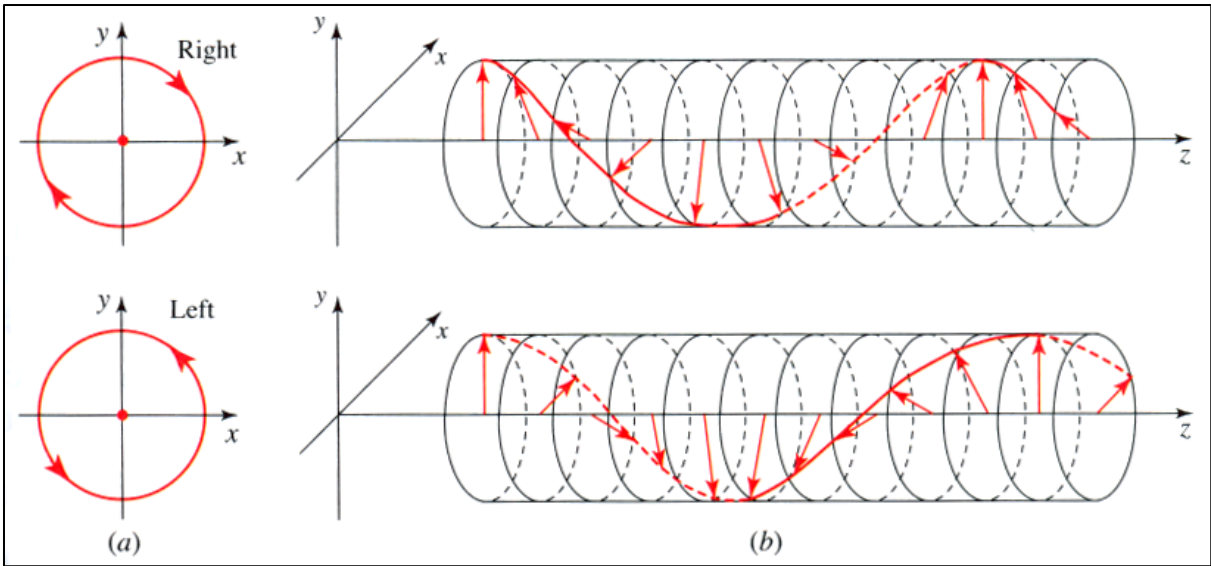


Figure 24: Circular polarization [reproduced from source 26]

There are several ways to manipulate the polarization of light. One of the most familiar methods is through polarization by absorption, which is generally how polarization is achieved in sunglasses for eye protection. Such an optical material consists of elongated molecules oriented in a similar grid direction, which provides a path for electrons to move. When an electromagnetic wave of random polarization passes through the material, the electric field components that are aligned parallel to the material grid will be absorbed and reflected. The resulting transmitted light will be LP at an axis perpendicular to the molecular grid as shown in *Figure 25*, and will consist of roughly one-half of the original light, minus any transmission losses in the optics. This axis is called the polarizer axis.

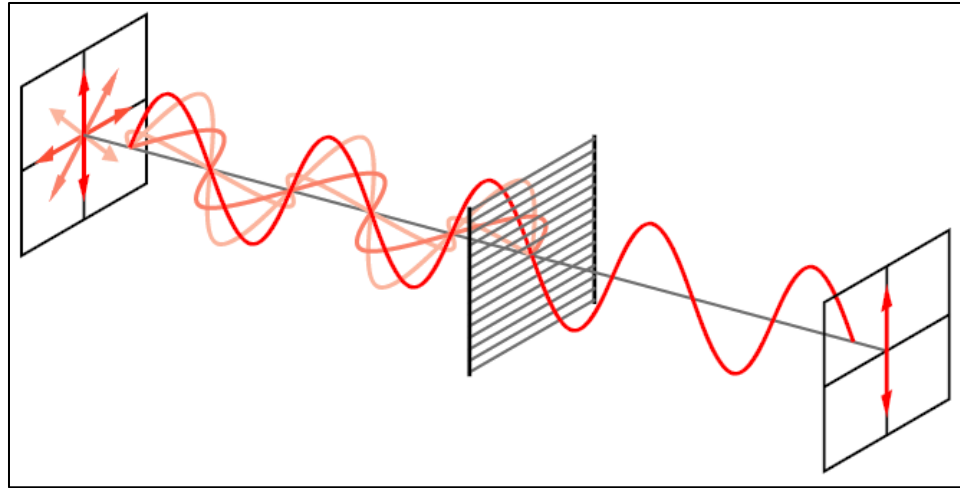


Figure 25: Grid polarizer [reproduced from source 26]

In the case that the impinging light is already linearly polarized, the amount of transmitted light is dependent on the angle θ between the electric field vector of the original light wave and the polarizer axis. The Law of Malus describes the resulting irradiance function as:

$$I_{transmitted} = I_{initial} \cos^2 \theta_i \quad (18)$$

as illustrated below in Figure 26. At $\theta_i = 0$, I_0 is at its maximum transmitted irradiance.

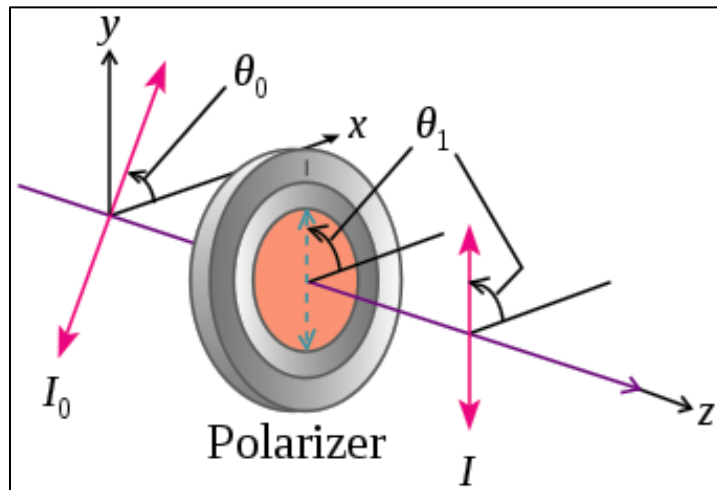


Figure 26: The law of Malus [reproduced from source 26]

In polarization by reflection, the interaction of the light wave with the surface of a material will allow for a manipulation of the beam. In this case the light component with a polarization vector parallel to the surface face is preferentially reflected, while the remaining light is refracted due to the refractive indices at a critical angle. The key is to obtain an angle that allows for the maximum amount of transmission, while reflecting out the undesired polarization components. This angle is referred to as the Brewster angle, as given by:

$$\theta_B = \tan^{-1} \left(\frac{n_2}{n_1} \right) \quad (19)$$

where n_1 and n_2 are the refractive indices of the two respective transmission media. Brewster's Law is illustrated using several stages in Figure 27. In this example, a series of optical stages are used to separate the s-polarized (light polarized perpendicular to the plane of incidence) and p-polarized (light polarized in the plane of incidence) components of the light. For a Brewster angle where no p-polarized light is reflected, only a portion of the s-polarized light is depleted. Hence, it is necessary to use multiple optical stages in order to avoid reducing the p-polarized light while simultaneously removing the s-polarized light.

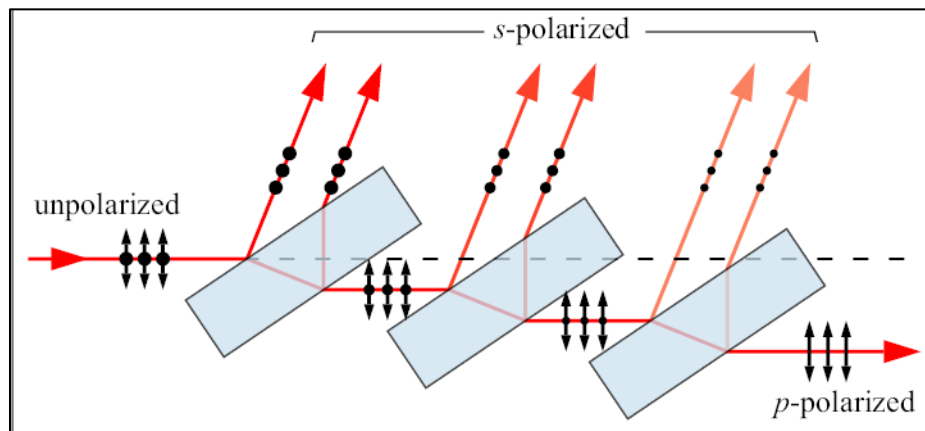


Figure 27: Series Brewster angle plates [reproduced from source 26]

Another way to manipulate the beam polarization is with birefringent crystals. Within the crystal there are two perpendicular axes known as the fast axis and the slow axis. The difference in these axes means that light with different polarizations will travel through the crystal at different refractive indices. Light with polarization parallel to the fast axis will travel through the crystal faster than light with polarization parallel to the slow axis. Such a crystal can be used as a retarder to a polarization component, and this allows for a manipulation of the overall wave polarization as illustrated in *Figure 28*. When used in this fashion the birefringent crystal is referred to as a wave plate.

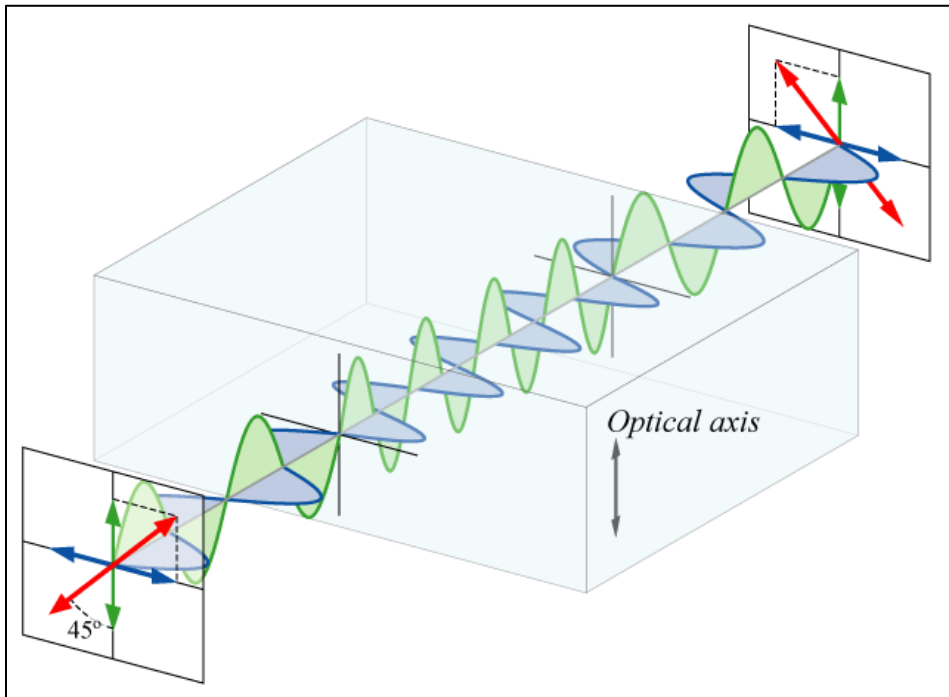


Figure 28: Example of a half-wave plate [reproduced from source 27]

The amount of relative phase shift Γ imparted on the polarization is dependent on the birefringence Δn and the length of the crystal L as given by:

$$\Gamma = \frac{2\pi\Delta n L}{\lambda} \quad (20)$$

The above example illustrates a half-wave plate, resulting in a transmitted wave

that is orthogonal to the orthogonal polarization. Additionally, a quarter-wave plate creates a quarter wavelength phase shift, and this can be used to change linearly polarized light into circularly polarized light and vice-versa.

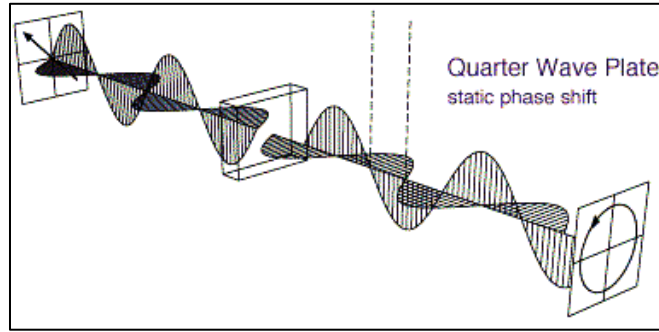


Figure 29: Birefringent wave plate [reproduced from source 27]

Extending the birefringent crystal further, the index of refraction of the fast axis n_{fast} is not equal to the index of refraction of the slow axis n_{slow} . Therefore a beam of light incident on the crystal may be partitioned into two component polarization waves through selective refraction. By cutting the crystal at an oblique angle as shown in *Figure 30*, the two linearly polarized rays leave the prism at separate diverging angles. Such a device functions as a polarizing beam splitter, and is known as a Wollaston prism. The device consists of two triangular Calcite prisms cemented together with orthogonal crystal axes.

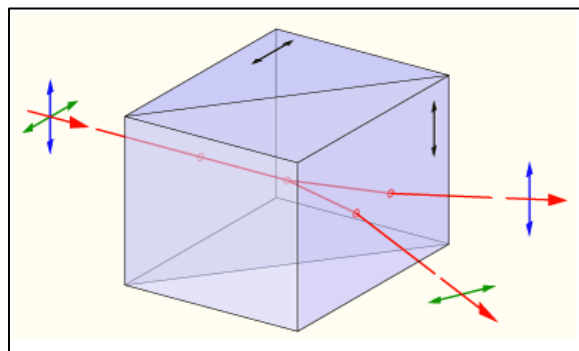


Figure 30: Illustration of a Wollaston prism [reproduced from source 26]

There are many other methods for manipulating the polarization of the beam. The output of many laser systems is predominantly linearly polarized, with a high degree exceeding 1000:1 between the light polarized in one direction and the orthogonal component. This is due to factors such as Brewster surfaces that may be employed within the laser construction for efficiency, or birefringence associated with the optical components. These techniques may be employed to further condition the beam for communications purposes through optical multiplexing, as will be discussed in the next section.

2.3 Modulation and Demodulation Techniques

The process of imposing an information signal on a laser beam carrier is known as modulation, and this is achieved with a device called a modulator. Modulators may vary in complexity from simple external electromechanical shutters to solid state electro-optic (EO) devices positioned within the laser cavity. In total, there are five characteristics of a laser beam that may be altered for the purpose of sending a message: power, frequency, phase, polarization and direction. In practice, phase and direction modulation are seldom used due to system complexity.

The detection process in an optical communication system is required to convert the variations in received light to variations in signal voltage, in order to decode the message. Historically, laser detectors have been divided into either thermal or quantum detectors. Although thermal detectors cover a wide range of wavelengths due to their response of the total absorbed energy, they are neither as fast nor as sensitive as quantum detectors, such as with photomultiplier tubes and semiconductor photodiodes.

Photomultiplier tubes are an appropriate detector in cases of low light levels and high bandwidths, but they are generally bulky, not especially rugged, and require supply voltages from hundreds to thousands of volts. Photodiodes also have a rapid response time, but are generally limited to maximum radiant power levels of 1 to 100 mW, beyond which permanent thermal damage may occur [28]. In addition, they also require a power supply to operate, although the voltages are far lower than that of the photomultiplier tube. The VMJ photovoltaic cells employed in HILPB share the same charge carrier properties of the photodiode lending to high sensitivity, but they additionally offer continuous operation under intense illumination, and do not require external biasing.

2.3.1 Direct Detection Receiver

The nature of the detection operation at the receiver is determined by the type of modulation scheme chosen at the source. Whenever the message information is contained through variations in the irradiance of the light, a direct detection scheme is used at the receiver. Direct detection provides electrical variations proportional to the light variations, and these signals can be processed by appropriate demodulation algorithms. The direct detection receiver offers design simplicity, uses few components and does not depend on the phase of the signal. Its main function is to identify when more than a few photons have been collected per bit, indicating a binary 1. When fewer photons are received, a 0 is indicated. By minimizing background noise, the differentiation between a 0 and a 1 can be made more successfully. The signal-to-noise ratio (SNR) for a direct detection receiver can be calculated by starting with the ratio of optical power received P_C to the energy per photon $h\nu$, resulting in the collected number

of photons per second:

$$P_C/h\nu \quad (21)$$

Considering charge q , and the quantum efficiency of the receiver Q (ratio of output photoelectron rate to input photon rate), the signal current may be represented by:

$$i = q * (\text{photoelectron rate}) = q * Q * (\text{photon rate}) = qQP_C/h\nu \quad (22)$$

By feeding the signal into a load resistor R_L and considering the photoelectric current gain G , the signal power P_s is expressed through:

$$P_s = G * R_L = (G_q Q P_C / h\nu) * R_L \quad (23)$$

The noise components at the receiver will consist of the shot noise (due to the signal current i_{SS} , the background current i_{BS} and the dark current i_D) and the thermal noise i_{nT} . The total squared noise current is given by the following summation of components:

$$i_{total}^2 = i_{SS}^2 + i_{BS}^2 + i_D^2 + i_{nT}^2 \quad (24)$$

Where the components are defined as:

$$i_{SS}^2 = (2qQ\{G\}P_C B_n)/h\nu \quad (\text{signal current}) \quad (25)$$

$$i_{BS}^2 = (2qQ\{G\}P_B B_n)/h\nu \quad (\text{background current}) \quad (26)$$

$$i_D^2 = 2qi_D B_n \quad (\text{dark current}) \quad (27)$$

$$i_{nT}^2 = N_o B_n \quad (\text{thermal noise current}) \quad (28)$$

B_n = noise bandwidth

N_o = electronic thermal noise spectral density (watts/Hz)

The previous equation is multiplied by the load resistance, and divided into the signal power to form the SNR ratio:

$$\frac{S}{N} = G_q Q P_C / h\nu R_L / \{2qGQ B_n R_L (P_C + P_B) + 2qi_D B_n R_L + 4kTB\} \quad (30)$$

The simplicity of the architecture of the direct detection receiver can be seen in *Figure 31*. The primary reason for this simplicity is that the receiver is designed to collect photons without any respect for the signal phase.

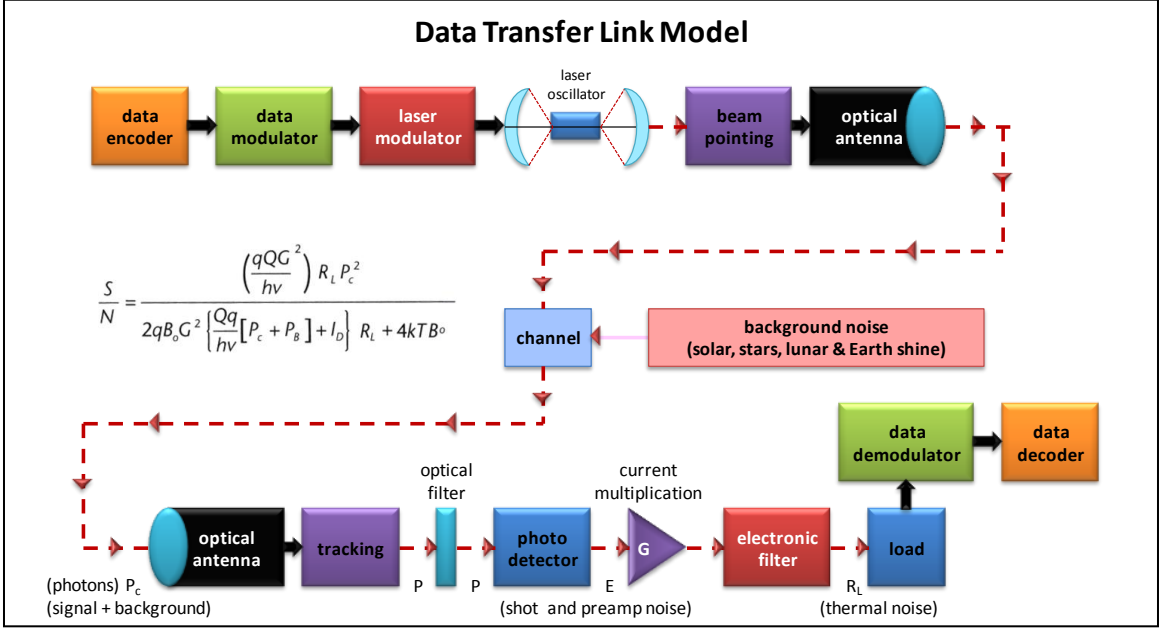


Figure 31: System block diagram for a direct detection laser receiver

On-off key (OOK) modulation of the laser beam is one of the most commonly employed schemes with direct detection communications [29]. OOK is a simplification of the amplitude shift keying (ASK) method, in that the source transmits a large amplitude carrier when it wants to send a binary value of '1', and no carrier when it wants to send a '0'. As illustrated in *Figure 32a*, a typical OOK waveform is shown representing the binary string '10110'. A modification to this scheme would be pulse polarization binary modulation (PPBM) which may incorporate two orthogonal polarization states for the laser beam to represent a binary value of 1 or 0, as shown in *Figure 32b*. For example, these two polarization states could be horizontal and vertical linear, or left and right circular, and this would offer an improved average received

energy for the HILPB case, along with allowing easy detection for loss of signal, since the receiver is expecting a pulse at each time interval. PPBM also has the advantage of operating in a noisy environment without substantially increasing the BER, when compared with other modulation schemes. The implementation of a PPBM system requires a dual channel polarized receiver.

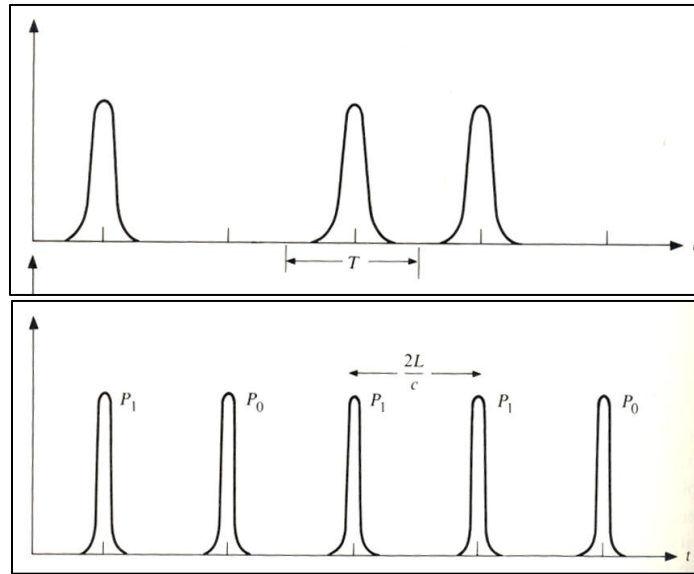


Figure 32: OOK and PPBM waveforms

Pulse-gated binary modulation (PGBM) is a one-bit-per-pulse stream that is well suited for a mode-locked laser with a high speed EO modulator, and when used in conjunction with a pulse-gated receiver the system achieves high noise discrimination. An illustration of the individual wave components that construct a PGBM system are shown in *Figure 33*.

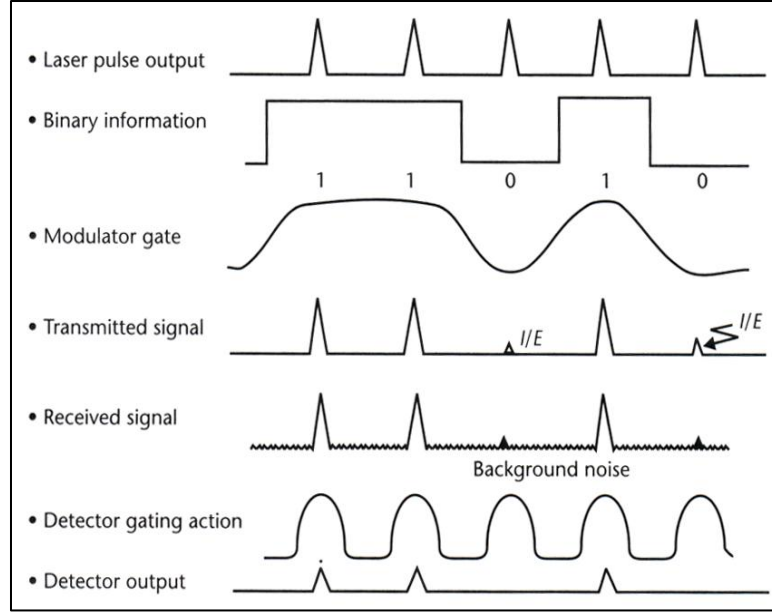


Figure 33: Pulse-gated binary modulation waveform progression

Given a number of signal and background (noise) photoelectrons and extinction ratio E (ratio between number of received signal photoelectrons during a desired pulse to the total number of photoelectrons when no pulse is desired), an expression for the probability of error is given:

$$P_E = pP_{nd} + (1 - p)P_{fd} \quad (31)$$

Where the components are defined as:

p = probability of transmitting a pulse

$(1 - p)$ = probability of not transmitting a pulse

P_{nd} = probability of no detection for a transmitted pulse

P_{fd} = probability of false detection for no pulse

The signal and noise follow a Poisson distribution, and the probability of a false detection of no pulse is described by [30]:

$$P_{fd} = \sum_{k=T}^{\infty} (\bar{m}_B)^k E^{-\bar{m}_B} / k! \quad (32)$$

Where the components are defined as:

T = optimum threshold (maximum likelihood ratio detection)

\bar{m}_S = mean number of signal photoelectrons per decision period

\bar{m}_B = mean number of background (noise) photoelectrons per period

Likewise the expression for the probability of no detection of a transmitted pulse is described by:

$$P_{nd} = 1 - \sum_{k=T}^{\infty} (\bar{m}_S + \bar{m}_B)^k e^{-(\bar{m}_S + \bar{m}_B)} / k! \quad (33)$$

The probability of a false detection by the receiver for a finite extinction ratio E is:

$$P_{fd}' = 1 - \sum_{k=T}^{\infty} (\bar{m}_S/E + \bar{m}_B)^k e^{-(\bar{m}_S/E + \bar{m}_B)} / k! \quad (34)$$

For the PGBM modulation scheme, the error rates are plotted for different numbers of photoelectrons with a constant extinction ratio $E= 100$ in *Figure 34*. The average number of signal photoelectrons \bar{m}_S ranges from 0 to 100, and the resulting BER ranges from near 1.0 to 10^{-8} . These values will be used later to demonstrate a laser signal power budget.

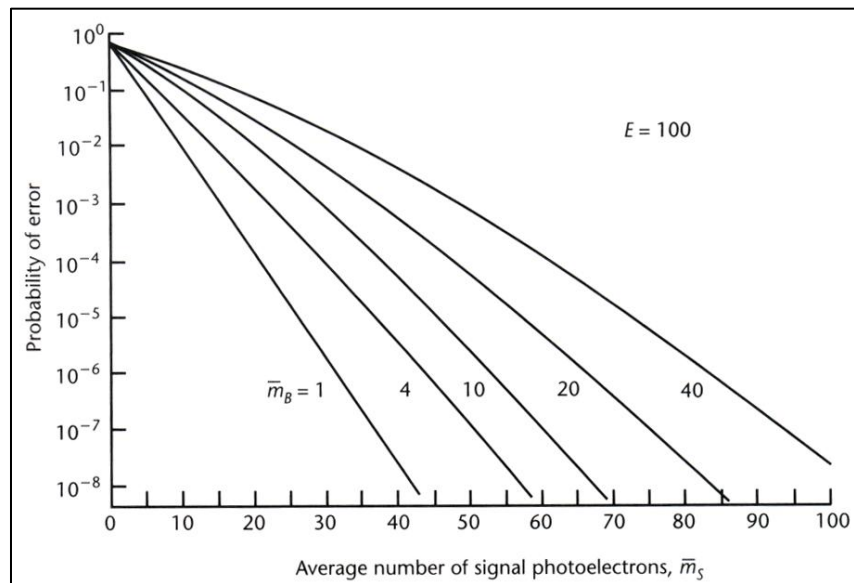


Figure 34: BEP plot for PGBM [reproduced from source 30]

2.3.2 Coherent Detection Receiver

Although many optical communications systems employ direct detection, it is also possible for variations in the phase or frequency of the laser field to contain the message information. A coherent detection method is used in these cases to measure the variations using superposition, by comparing them with the stable phase or frequency from a local coherent reference field using interferometric techniques as shown in *Figure 35*. In this arrangement, the detector receives the signal-bearing laser beam combined with energy from a local oscillator source, and the resulting interference between the two fields will contain information about both the amplitude and the phase of the signal. The coherent optical reception method is analogous to the superheterodyne radio receiver, and likewise it offers a reduction of the accumulated noise effects.

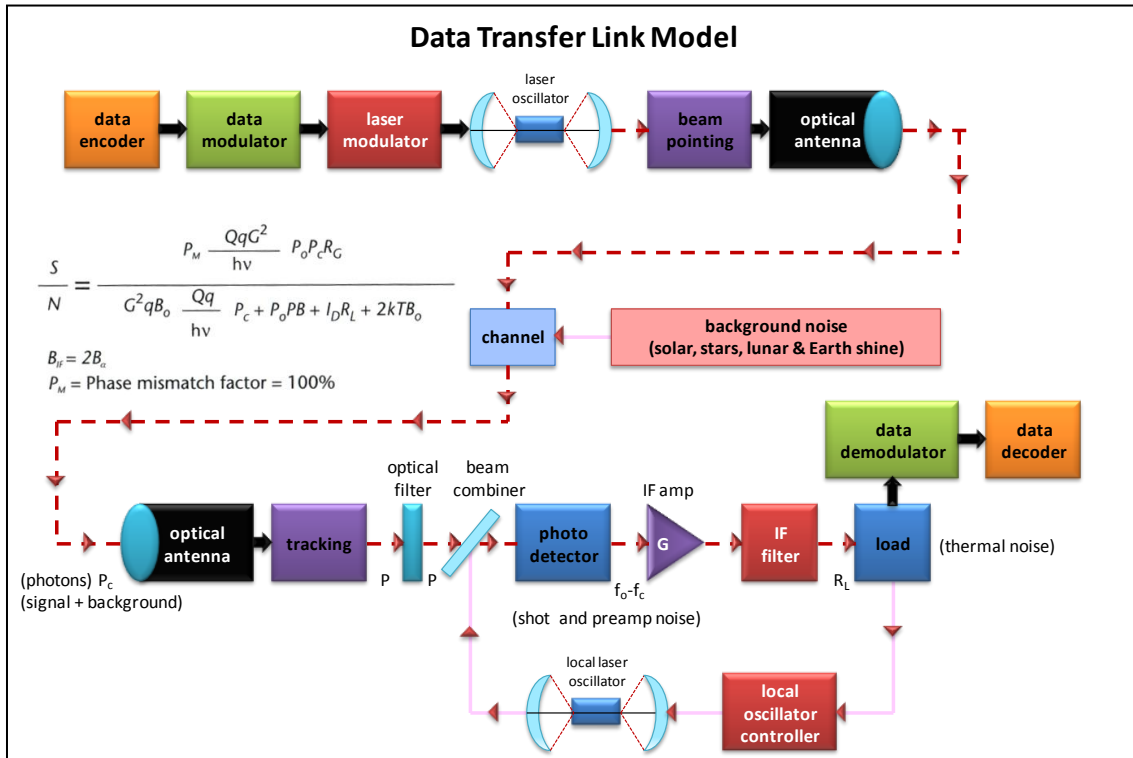


Figure 35: Diagram of a coherent optical communication receiver system

Considering ω_S as the optical carrier frequency (on the order of 10^{13} to 10^{15} depending on the laser source) and the signal bearing modulation $\varphi(t)$, then the electric field of the incident signal waves can be described by:

$$A_S \times \cos[\omega_S t + \varphi(t)] \quad (35)$$

In the case of frequency modulation $d\varphi/dt$ is proportional to the message signal, and in the case of phase modulation $\varphi(t)$ is proportional to the message signal. Considering ω_R as the local oscillator frequency at the receiver (not necessarily the same as ω_S), then the electric field of the local oscillator can be described by:

$$A_R \times \cos[\omega_R t] \quad (36)$$

By superposition, the composite of these two waves arriving at the detector can be described by the total wave field:

$$E(t) = A_S \times \cos[\omega_S t + \varphi(t)] + A_R \times \cos[\omega_R t] \quad (37)$$

The two optical frequencies, ω_S and ω_R are much too high to be sensed by the detector. Instead, the detector generates a voltage proportional to the total photon flux, which is the time average of the square of the electric field. This expression is essentially the mixer output and is proportional to:

$$A_S^2 + A_R^2 + 2A_S A_R \cos[\omega_D t + \varphi(t)] \quad (38)$$

In this expression, $\omega_D = \omega_S - \omega_R$, and this difference can be chosen to be well within the response performance of the detector. In the case $\omega_D = 0$, the local oscillator equals the carrier frequency and the operation is described as homodyne detection. If $\omega_D \neq 0$, then the local oscillator is different than the carrier frequency and the operation is described as heterodyne detection. The output signal is converted back into the original message information using conventional phase or frequency demodulation

techniques, depending on which method was used at the transmitter.

In general, the coherent optical detection method has some critical issues concerning practical implementation. The heterodyne receiver requires a high surface quality optical coupler that can precisely align the mixed signals to prevent distortion of the interference term. Many laser oscillators do not exhibit the necessary frequency stability to make the communications scheme successful. Laser light, although narrowband, is not truly monochromatic and thus small variations in $\varphi(t)$ would not be able to be distinguished from ω_D in practice unless some degree of signal degradation can be accepted. At the time of this writing frequency tunable lasers generally do not approach the average power levels typically encountered with HILPB. In addition, induced phase distortion in the received optical signal will introduce a higher BER when compared with a direct detection scheme. Finally, the added system complexity of a coherent system will limit its potential application to larger platforms.

2.4 Terrestrial and In-Space Issues

Clearly directionality and bandwidth are two inherent advantages of a laser based communication system, but there are also a few unique challenges when considering the channel. The optical path may be disturbed by turbulent atmospheric conditions, and rain or fog may create significant signal attenuation. Additionally, a link across a considerable distance such as one established in space will experience an appreciable range loss.

2.4.1 Terrestrial Links

Long range transmission of a laser signal beam through the atmosphere offers an array of challenges. For a terrestrial communication link there are a number of components that can cause signal loss such as absorption and scattering by airborne molecules and aerosols. Wavefront distortion by atmospheric turbulence resulting from variations of the index of refraction along the beam's path can create problems for successful demodulation at the receiver, especially in the case of coherent detection. An understanding of these channel effects may be used to correct such distortions with tools such as an adaptive optics system (AOS), and this warrants a venture into describing the phenomena.

The atmospheric turbulence parameters may be calculated by first starting with the Hufnagle-Valley-Bufton model [31] for the atmospheric index of refraction structure parameter across the range of visible frequencies:

$$\begin{aligned} C_N^2(h) = & \\ 0.00594(W/27)^2(10^{-5}h)^{10} \exp(-h/1000) + 2.7 \times 10^{-16} \times \exp(-h/1500) + \\ A \exp(-h/100) \end{aligned} \quad (39)$$

Where the components are defined as:

h = altitude in meters

W = RMS windspeed in m/sec

A = nominal value of $C_N^2(0)$ at the ground in $m^{-2/3}$

(approximately $1.7 \times 10^{-4} m^{-2/3}$ during daytime and $8.4 \times 10^{-15} m^{-2/3}$ at

night)

In general, C_N^2 varies from $10^{-13} \text{ m}^{-2/3}$ for strong turbulence to $10^{-17} \text{ m}^{-2/3}$ for weak turbulence, with $10^{-15} \text{ m}^{-2/3}$ often defined as a typical average value [32]. The 0th turbulence moment μ_0 , for a 0° zenith angle is evaluated from:

$$\mu_0(L) = \int_0^L dz C_N^2(h) \quad (40)$$

The coherence diameter r_0 is obtained from:

$$\rho_0 = \{0.423k^2\mu_0\}^{-3/5} \quad (41)$$

The turbulence signal coupling efficiency Γ_T is given by:

$$\Gamma_T \sim 1/\{1 + (D/\rho_0)^2\} \quad (42)$$

The need for an AOS is determined from the expression for Γ_T . If the ratio of $D/p_0 \ll 1$, this indicates little distortion and thus does not require an AOS. Conversely, in instances when $D > p_0$, an AOS should be employed. In this case, the SPB should be multiplied by the Γ_T factor in order to remain an effective measure of photoelectrons per bit during turbulent atmospheric conditions.

The basic attenuation constant for beam propagation through the atmosphere is made up of the molecular and aerosol scatter and absorption constants as given by:

$$\gamma = \alpha_M + \beta_M + \alpha_A + \beta_A \quad (43)$$

Where the components are defined as:

α_M = molecular absorption constant

β_M = molecular scattering constant

α_A = aerosol absorption constant

β_A = aerosol absorption constant

The attenuation is expressed using Beer's Law with:

$$T_R = I_Z/I_0 = \exp(-\gamma z) \quad (44)$$

Where the components are defined as:

T_R = transmittance

I_0 = initial beam intensity

I_Z = beam intensity at distance z from the aperture

The total molecular absorption constant α_M is computed by summing over each of the prevalent absorber components, such as H_2O and CO_2 , when the wavelength of the beam is greater than the size of the molecules.

The molecular scattering constant is derived from a harmonic field inducing a dipole as discussed by Hugo Weichel [33], and it is described as the Rayleigh Scattering:

$$\sigma = f' e^4 \lambda_0^{-4} / 6\pi \epsilon_0^{-2} m^2 c^4 \lambda^4 \quad (45)$$

Where the components are defined as:

f' = effective number of electrons per molecule that oscillate at the natural frequency ω_0

e = charge of an electron

λ = wavelength of the laser beam

λ_0 = wavelength related to ω_0

When the laser beam wavelength is similar to the size of the particles, and interaction of Mie Scattering with small water droplets and aerosols occurs [34]. The fractional decrease in laser intensity when passing through an elementary volume is given by

$$-dI/I = K\pi a^2 N A dz/A \quad (46)$$

Where the components are defined as:

I = laser intensity

A = cross sectional area of element

dz = length of element

$a^2 dz$ = volume of element

$NAdz\pi a^2$ = total cross section of the particles

N = total number of particles in the elementary volume interacting with the laser beam

K = attenuation factor from scattering and absorption of similarly-sized particles as λ

By substitution, *equation 46* may be rewritten as:

$$-dI/I = N\sigma(a, \lambda)dz \quad (47)$$

Where the components are defined as:

$N\sigma(a, \lambda)dz$ = Mie attenuation coefficient

$\sigma = K\pi a^2$ = Mie attenuation cross-section

Many empirical measurements of aerosol scattering coefficients as a function of laser wavelength have been made across the world. Hugo Weichel [33] related the scattering coefficient to both Mie and Rayleigh scattering by:

$$\beta(\lambda) = C_1\lambda^{-\delta} + C_2\lambda^{-4} \quad (48)$$

In this relation, the C_1 , C_2 and δ constants are determined by the aerosol density and the size distribution of the particle sizes. The second term may be effectively neglected for most wavelengths exceeding the UV region.

The transmittance may be calculated by knowing the visible range and the relative humidity. An example plot for the coefficient of extinction is shown in *Figure 36* for a

23 km visibility. In this example it can be seen that at $1.0 \mu\text{m}$, the total aerosol extinction is about $10^{-1}/\text{km}$.

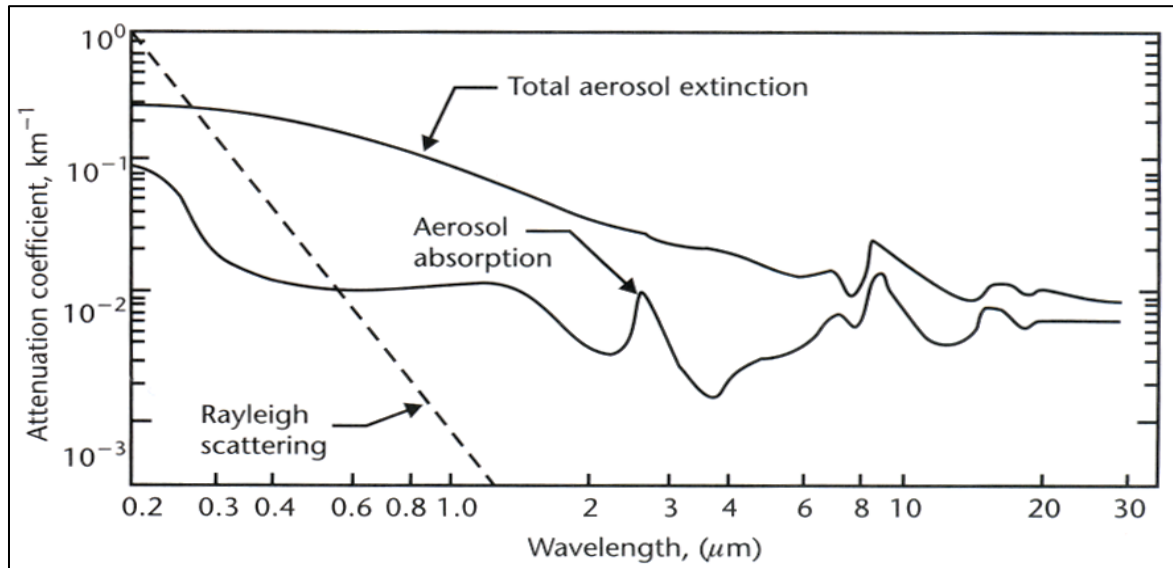


Figure 36: Aerosol absorption extinction [reproduced from source 33]

When calculating the beam propagation through weather particulates whose physical size is beyond that of the laser wavelength, such as with haze, fog and rain, there is a negligible dependency on wavelength and the scattering coefficient may be expressed as:

$$\beta = 1.25 \times 10^{-6} (\Delta x / \Delta t) a^3 \quad (49)$$

Where the components are defined as:

$\Delta x / \Delta t$ = rate of rainfall in centimeters of depth/sec

a = raindrop size in centimeters

An example with raindrop radii between 0.025 and 0.325-cm and a laser path-length of 1.8-km is shown in *Table II*, with a transmittance ranging from 0.88 to 0.38 depending on the intensity of the rainfall.

TABLE II: Laser transmittance through rainfall [reproduced from source 34]

Condition	Rainfall	Transmittance of 1.8-km Path
$\Delta x/\Delta t$ in cm/hr		
Light rain	0.25	0.88
Medium rain	1.25	0.74
Heavy rain	2.5	0.65
Cloudburst	10.0	0.38

For a similar cloudburst condition yielding a rainfall rate of 10-cm/hour, a range of scattering coefficients as a function of drop radii and concentration of drops per square cm are tabulated in *Table III*. These values may be used in the Beer's Law expression to estimate the signal attenuation.

TABLE III: Cloudburst Scattering Coefficients [reproduced from source 35]

Drop Radius (cm)	Number of Drops per cm ² of Horizontal Area in 100 Seconds	Rainfall Rate cm/sec	Scattering Coefficient (cm ⁻¹)
0.025	43	$2.78 \cdot 10^{-5}$	$2.24 \cdot 10^{-6}$
0.05	21.4	$1.11 \cdot 10^{-4}$	$1.11 \cdot 10^{-6}$
0.075	14.3	$2.5 \cdot 10^{-4}$	$7.43 \cdot 10^{-7}$
0.10	9.3	$3.89 \cdot 10^{-4}$	$4.87 \cdot 10^{-7}$
0.125	5.8	$4.72 \cdot 10^{-4}$	$3.02 \cdot 10^{-7}$
0.150	3.6	$5.00 \cdot 10^{-4}$	$1.865 \cdot 10^{-7}$
0.175	1.8	$4.07 \cdot 10^{-4}$	$9.59 \cdot 10^{-8}$
0.200	0.75	$2.50 \cdot 10^{-4}$	$3.91 \cdot 10^{-8}$
0.225	0.35	$1.67 \cdot 10^{-4}$	$1.83 \cdot 10^{-8}$
0.250	0.13	$8.36 \cdot 10^{-5}$	$6.76 \cdot 10^{-9}$
0.275	0.064	$5.56 \cdot 10^{-5}$	$3.34 \cdot 10^{-9}$
0.300	0.024	$2.78 \cdot 10^{-5}$	$1.29 \cdot 10^{-9}$
0.325	0.019	$2.78 \cdot 10^{-5}$	$1.02 \cdot 10^{-9}$
$\Sigma = 100.54$		$\Sigma = 5.234 \cdot 10^{-6}$	

Table IV is a collection of experimental measurements of signal attenuation due to absorption and scattering in a range of environments, from clear weather to snow at distances from 1- to 100-km [36, 37]. Extending the table, a 0.53 μm laser beam penetrating a cumulus cloud containing a liquid water concentration of 1.77 gm/m³ and a thickness of 230-m will produce an attenuation of 17-dB. At a thickness of 677-m the attenuation becomes 50-dB, and at 2,100-m the attenuation becomes 156-dB [36]. These losses were calculated from a number of software tools developed by the Air Force Geological laboratory (AFGL), and can be used to determine repeater station placement and give a measure for BER.

TABLE IV: Weather parameter attenuation [reproduced from source 36, 37]

Weather	Wavelength, λ	Attenuation in dB at L Distance		
		1 km	10 km	100 km
Conditions	microns			
Clear weather (at sea level)	0.53, 1.06	0.06	0.6	6
	10.6	0.54	5.4	54
CO ₂ absorption	0.53, 1.06	—	—	—
	10.06	0.25	2.5	25
Haze	0.53, 1.06	1.4	14	140
Size; 0.1 mg/m ³	10.6	0.66	6.6	66
Light Fog (0.5-10 μ size; 0.5 mg/m ³ ; visibility ~2 km)	0.53, 1.06	0.1-5	1-50	10-500
	10.6	0.9	9	90
Fog (0.5-10 μ size; 1 mg/m ³ visibility ~0.5 km)	0.53, 1.06	0.2-10	2-100	20-1000
	10.6	1.9	19	190
Rain:	5mm/hr	0.53, 1.06	1.6	16
	25mm/hr	0.53, 1.06	4.2	42
	75mm/hr	0.53, 1.06	7.0	70
Light rain (1000 μ size; 50 mg/m ³)	10.6	1.6	16	160
Snow:	Light	0.53, 1.06	1.9	19
	Heavy	0.53, 1.06	6.9	690

The Air Force Research Laboratory (AFRL) Space Vehicle Directorate, in collaboration with Spectral Science, Inc. has developed MODerate spectral resolution atmospheric TRANSmittance algorithm and computer modeling (currently MODTRAN) software that can calculate atmospheric transmittance and radiance for wavelengths from 200 nm to 100 μm with a spectral resolution of 1.0 cm^{-1} [38]. This code covers spherical refraction geometry, solar and lunar background sources, Rayleigh, Mie and multiple-scattered radiance, variable aerosol profiles such as clouds & rain, gas molecule compositions and climatological descriptions such as tropical, midlatitude, summer, winter, etc. For point design atmospheric laser communication system engineering and analysis, MODTRAN may be used make predictions under most weather conditions.

2.4.2 Spatial Crosslink

For communications between two satellites orbiting in space, a laser signal power budget (SPB) may be constructed to achieve a desired BER for a particular modulation scheme. The generalized SPB assumes that the acquisition, tracking and pointing (ATP) process is capable of firmly locking the optical pattern onto the receiver. In reality factors such as systemic and random vibrations will require additional terms in the SPB, which may be nullified by the ATP system.

The laser SPB is different than its RF counterpart, in that it considers the ratio of signal to noise in terms of the number of photons per cycle (or bit). This is obtained by:

$$n = P_R/hvf \quad (50)$$

Where the components are defined as:

n = number of photons per bit

P_R = received optical power (watts)

$h = 6.625 \times 10^{-34}$ watt-second (joule) per photon per Hz (Plank's constant)

ν = laser light frequency (Hz)

f = signal data rate (bits per second)

Therefore, the expression hv represents the energy (joules) per photon. This is illustrated in *Figure 37*, and the received power is described by:

$$P_R = P_T \Omega_R / \Omega_T \quad (51)$$

$$\Omega_R = \pi(a_R)^2 / R^2 \quad (52)$$

$$\Omega_T = \lambda^2 / \pi(a_t)^2 \quad (53)$$

Where the components are defined as:

R = distance between the transmitter and the receiver aperture

a_R = radius of receiver aperture

a_T = radius of transmitter aperture

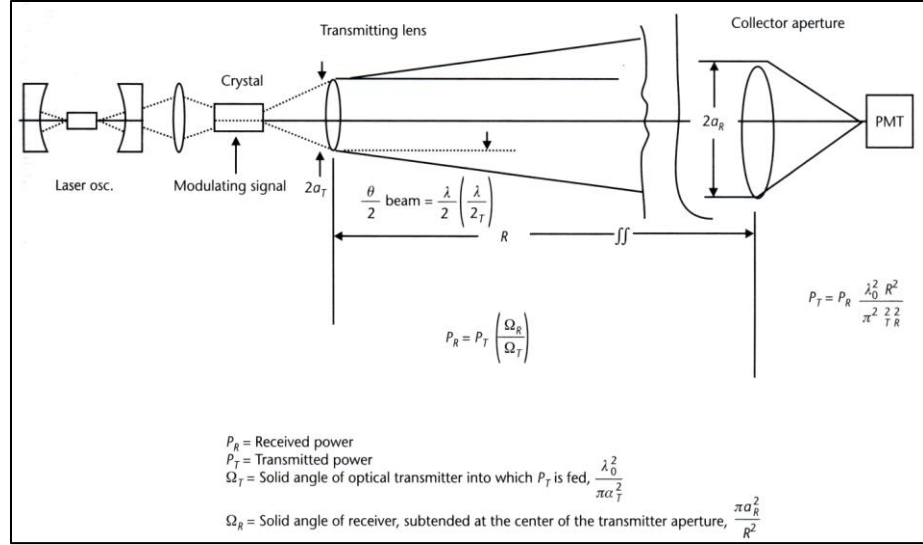


Figure 37: Calculation of the received power [reproduced from source 39]

By substitution:

$$P_R = P_T \pi^2 (a_R)^2 (a_T)^2 / (R^2) (\lambda^2) \quad (54)$$

The received optical power P_R is equivalent to the number of received photons per bit:

$$P_R = n(hv)f \text{ or } n = P_R / (hv)f \quad (55)$$

To obtain only the number of signal photoelectrons n' , the quantum efficiency Q (ratio of output photoelectrons to input photons) of the detector is used:

$$n' = Q P_R / (hv)f \quad (56)$$

Equations 54 and 55 are combined, and extra terms are added to obtain the full expression:

$$n' = P_T (D_R)^2 (FQ) / M (R^2) (\theta^2) (hv)f \quad (57)$$

Where the components are defined as:

F = combined efficiencies of transmitter and receiver subsystems ($L_T^* L_R$)

M = margin (safety factor)

Θ = optical beamwidth of the transmitter

D_R = diameter of the receiver aperture

R = range between the transmitter and the receiver

P_T = transmitted power

An numerical example of the SPB can be made with a 1.064 μm Nd:YAG laser [40]m at a distance of 45,000 mi (81,000 km). For a PGBM modulation scheme, in order to achieve a 10^{-8} error rate with an extinction ratio of 20 dB, the required n' photoelectrons per bit is 40 (or 16 dB). Consider a detector's quantum efficiency of 30% (5.2 dB), and n' becomes 133 required photons per bit (21.2 dB). For $\lambda=1.064 \mu\text{m}$ ($v=3\times 10^{14} \text{ Hz}$), $h\nu=187.2 \text{ dB}$ joules per photon. For the required BER, -187.2 dB (joules per photons) + 21.2 dB (photons per bit) = -166 dB (joules per bit). For a signal data rate of 10^9 bits per second, the power is computed from -166 dB (watt-sec per bit) + 90 dB (bits per second) = -76 dBw (or 2.5×10^{-8} watts per bit). These values are tabulated in *Table V* and *Figure 38*, along with similar calculations for a 0.780 μm GaAlAs semiconductor laser with a data rate of 12.6 megabits per second.

TABLE V:Tabulated SPB calculations for two proposed spatial link systems

	Nd:YAG	GaAlAs diode laser
• Required photoelectrons/BIT	dB 16 (40)	16 (40)
• Detector quantum efficiency	dB 5.2 (30%)	5.7 (0.27)
• Required photons per BIT	dB 21.2 (133)	21.7 (148)
• $h\nu$ = watt-sec/photon	dB -184.2	-185
	dBj -163.	-163.3
• Joules per BIT = $21.2 - 184.2$	dB $90.(10)^9$	$70.9(12.6 \cdot 10^6)$
• Bit rate (assume 1 GBPS); 10^9 bit/sec	- 73 dBW	-92.4 dBw ($5 \cdot 10^{-8}$ watts) ($5.75 \cdot 10^{-10}$ watts)
• Watts required at detector, P_{RD}		
• 10^{-7} BER, 1 Background pe/decision period, PGBM; extinction ratio -20 dB		
• $h = 6.625 \cdot 10^{-34} \text{ watt-sec/Hz}$		
• $v = c/\lambda = 3 \cdot 10^8 / 0.53 \cdot 10^{-6} = 6 \cdot 10^{14} \text{ Hz}$		

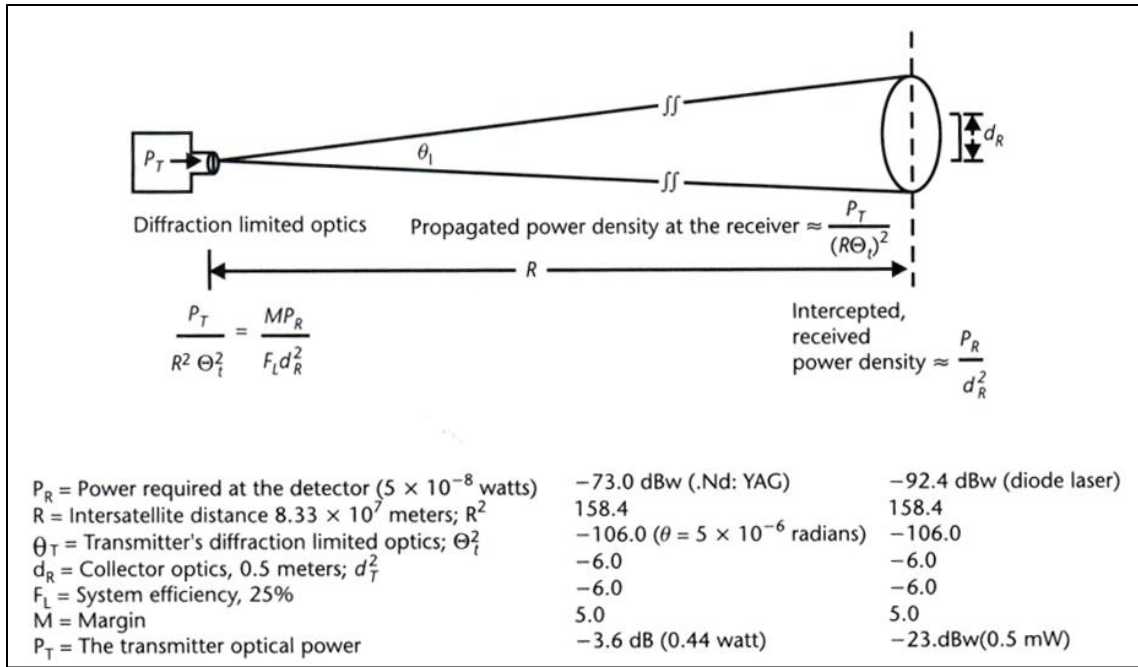


Figure 38: Spatial link power budget [reproduced from source 23]

Background irradiance (noise) will interfere with the photonic signal, and therefore needs to be quantified. Sources may include the moon, stars, sky and earthshine, but these are typically 40 dB below the solar radiance and thus not a factor. The background power due to the sun may be computed by:

$$P_B = (\text{Solar Irradiance})x(\text{Area of Receiver Aperture})x(\text{Filter BW})x(\text{Solar FOV}) \quad (58)$$

Where the components are defined as:

$$\text{Solar Irradiance} = 7 \times 10^{-2} \text{ watts/cm}^2/\mu\text{m} @ 1.06 \mu\text{m}$$

$$\text{Receiver Aperture} = \pi/4 d^2$$

$$\text{Filter Bandwidth} = 1.0 \text{ nm}$$

$$\text{Solar Field of View} = 870,000 \text{ miles (diameter of sun)/distance from sun}$$

An example computation is shown in *Figure 39* for a Gb/sec system 93 million miles away from the sun, resulting in a background power $P_B = 1.08 \times 10^{-8}$ watts. At this rate, during one bit period lasting 10^{-9} seconds there will be 1.08×10^{-17} joules of background energy.

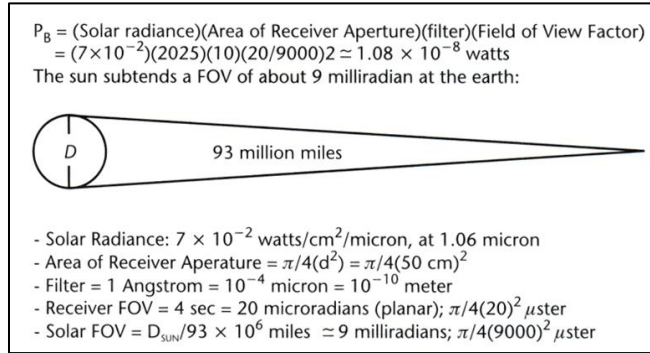


Figure 39: Noise background calculations [reproduced from source 23]

2.4.3 Waveguide Medium

Although the basis of this research is on free-space systems, it is worth mentioning an alternative medium for propagation. An optical waveguide may be employed as a way to avoid the system considerations and detrimental effects of atmospheric transmission. The waveguide consists of a flexible glass or plastic cable called an optical fiber, which confines the beam through the property of total internal reflection. The core material has a refractive index n_c , and is surrounded by a cladding material with a lower refractive index n_a . As demonstrated in *Figure 40*, all rays of light incident on the cladding from the core with a normal angle greater than θ_c remain in the core due to total internal reflection, with θ_c given by [41]:

$$\theta_c = \sin^{-1} \frac{n_a}{n_c} \quad (59)$$

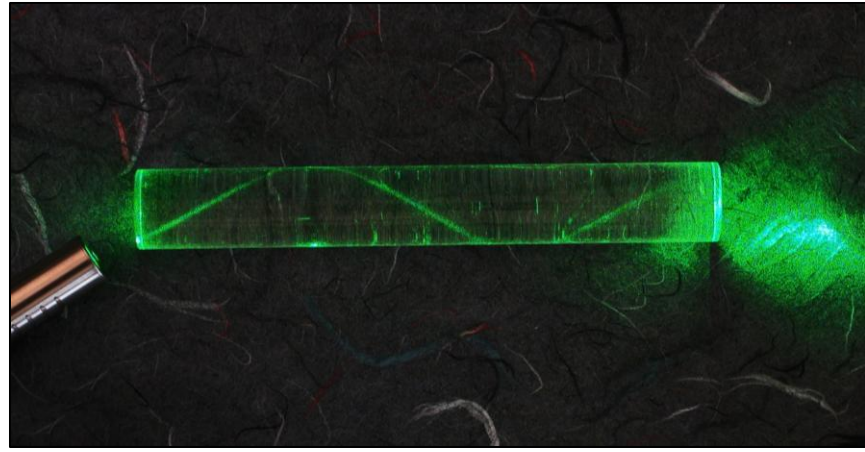


Figure 40: Depiction of total internal reflection of light

Since optical fibers can easily be bundled together, a laser power beaming and communications system may be developed in which the total transmitted energy is distributed throughout the bundle, and individual fibers may carry unique modulations as a way to capitalize on bandwidth multiplexing. Related work has been achieved in the area of combining incoherent high-power fiber-laser beams, and the demonstrated results are reaching a 90% propagation efficiency at a kilometer of free-space range [42].

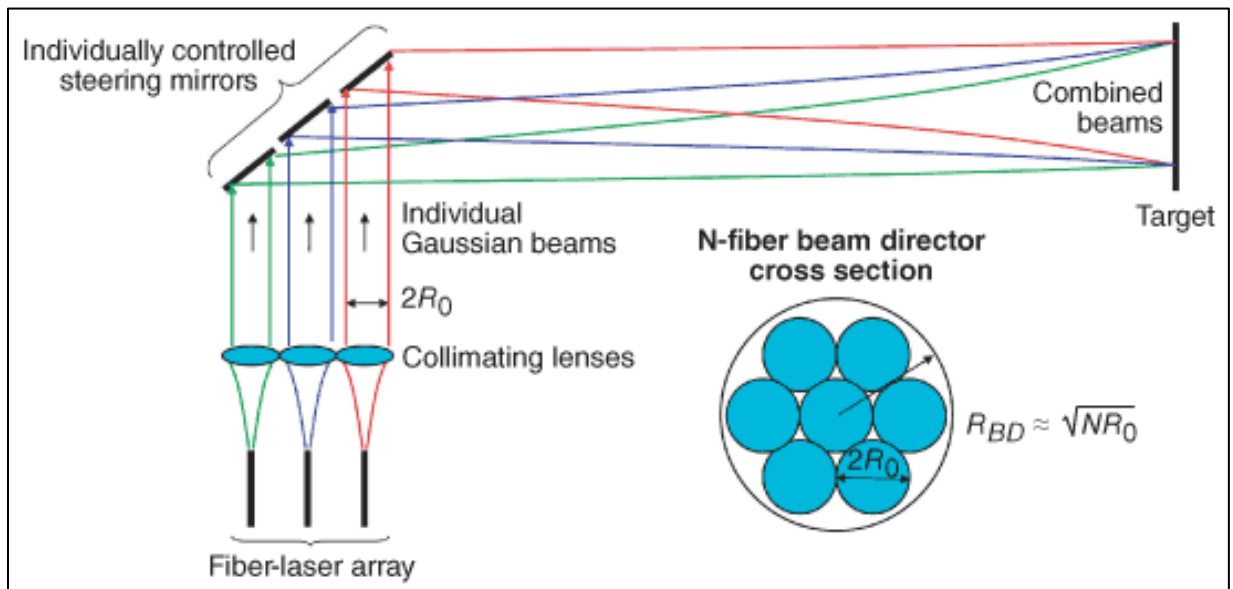


Figure 41: Bundled fiber delivery system [reproduced from source 42]

Additionally, the HILPB system to date has employed a fiber optic beam deliver system from a semiconductor laser module [43]. The compact laser diode modules may be power added together through a variety of beam combining techniques such as frequency or time division multiplexing to easily realize a multi-kW source using COTS hardware.

2.5 Beam Acquisition, Tracking and Pointing

For the case of spatial links between satellites, the SPB equation may be modified to accommodate the effect of the platform's physical vibrations on the pointing quality and the noise in the acquisition and tracking circuitry. The vibrations will cause the transmit beam to move away from the center of the receiver's aperture. The frequency and amplitude of these vibrations will have an effect on the achievable BER of the communication link, and this is expressed with:

$$n' = P_T L_T G_T L_R Q(L_{P-T})(L_{P-R})/L_S(hv)f \quad (60)$$

Where the components are defined as:

n' = number of photoelectrons per bit

P_T = transmitted optical power

L_T = total signal losses in the transmitter

G_T = gain of the transmitter antenna $(\pi D_T/\lambda)^2$

D_T = diameter of the transmitter aperture

G_R = gain of the receiver antenna $(\pi D_R/\lambda)^2$

D_R = diameter of the receiver aperture

L_T = total signal losses in the receiver system

f = signal data rate (bits per second)

L_S = free space losses $((4\pi R)^2/\lambda^2)$

R = range between the transmitter and the receiver

$h = 6.625 \times 10^{-34}$ watt-second (joule) per photon per Hz (Plank's constant)

ν = laser light frequency (Hz)

hv = energy per photon

Q = quantum efficiency

L_{P-T} = pointing error (loss) of the transmitting beam

L_{P-R} = pointing error (loss) of the receiver's optical aperture beam

The pointing losses L_{P-T} and L_{P-R} may be derived from detailed research and analysis of laser space communications performance in environments with physical vibrations [44-50] and from engineering simulation work performed in this area at the Jet Propulsion Laboratory (JPL) [51]. It is first assumed that the pointing error angle θ_R is composed of both a steady-state pointing error and a random pointing error component. The random portion is further composed of a pointing error angle along the azimuth axis θ_{az} , and the pointing error angle along the elevation axis θ_{EL} . Both of these angles are assumed to be independent of each other and normally distributed. The probability density function (PDF) of θ_{az} is written as:

$$f(\theta_{az}) = 1/\{(2\pi)^{1/2} \sigma_{az}\} \exp^{-\{(\theta_{az}-\mu_{az})^2/2\sigma_{az}^2\}} \quad (61)$$

$$f(\theta_{EL}) = 1/\{(2\pi)^{1/2} \sigma_{EL}\} \exp^{-\{(\theta_{EL}-\mu_{EL})^2/2\sigma_{EL}^2\}} \quad (62)$$

Where the components are defined as:

σ_{az} = standard deviation of the random component of the error angle along the azimuth axis

μ_{az} = mean value of the random component of the error angle along the azimuth axis

σ_{EL} = standard deviation of the random component of the error angle along the elevation axis

μ_{EL} = mean value of the random component of the error angle along the elevation axis

Since the random error angles components are independent, the case is defined for symmetry and no bias, therefore the radial angle error square may be expressed as:

$$\theta_R^2 = \theta_{az}^2 + \theta_{EL}^2 \quad (63)$$

Due to the symmetry assumption, the according variances of the error angles are equivalent:

$$\sigma_R = \sigma_{az} = \sigma_{EL} \quad (64)$$

From the previous equations the Rayleigh distribution functions for the transmitter and the receiver pointing error angles may be expressed, considering a case of zero bias in the jitter environment:

$$f(\theta_T) = \theta_T / \sigma_T^2 \exp\{-\theta_T^2 / 2\sigma_T^2\} \quad (65)$$

$$f(\theta_R) = \theta_R / \sigma_R^2 \exp\{-\theta_R^2 / 2\sigma_R^2\} \quad (66)$$

The key parameters influencing the pointing error are the optical antenna gains G_T

and G_R , and the square of the radial pointing errors for the transmitted and received beam θ_T^2 and θ_R^2 . Provided a Gaussian beam, the signal losses are given by:

$$L_{P-T} = \exp(-G_T \theta_T^2) = \exp\{-(\pi D_T/\lambda)^2 \theta_T^2\} \quad (67)$$

$$L_{P-R} = \exp(-G_R \theta_R^2) = \exp\{-(\pi D_R/\lambda)^2 \theta_R^2\} \quad (68)$$

These two equations can be substituted back into the laser SPB equation 60. A plot by Arnon [47] of the BER as a function of the ratio of RMS amplitude of the vibration σ to the laser beamwidth (λ/D) for the OOK modulation is shown in *Figure 42*. For this scheme, it is shown that when the RMS amplitude of the pointing jitter is within 7% of the transmitter beamwidth, then the BER will not exceed 10^{-9} .

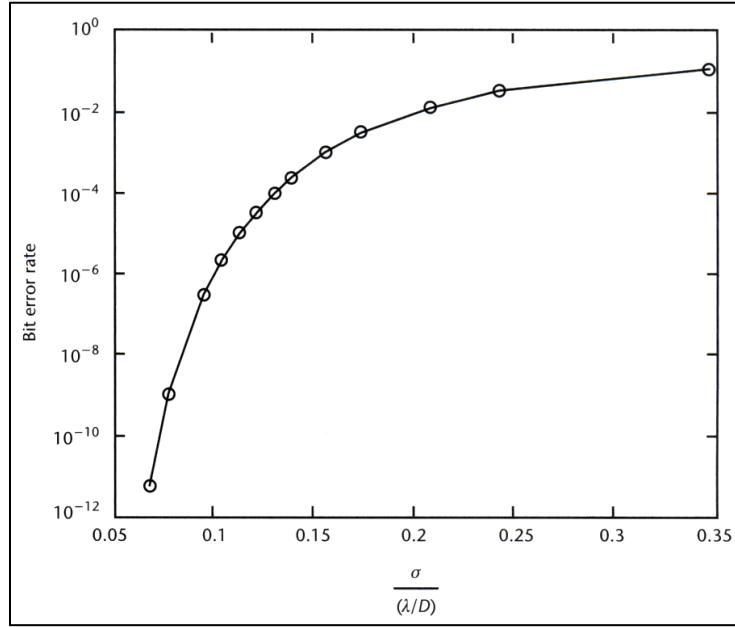


Figure 42: OOK bit error rate [reproduced from source 47]

A general acquisition sequence begins with a scanning algorithm within a cone of uncertainty, eventually narrowing to achieve lock between the terminals. During the fine pointing process, a quadrant detector may be employed at the receiver to assist in the tracking process.

CHAPTER III: EXPERIMENT SETUP AND RESEARCH METHODOLOGY

3.1 System Description – Optical Receivers

The design and construction of the power receiver addresses four main issues. First, the receiver needs to provide sufficient thermal dissipation in order to handle the excess electrically unconvertible energy. Second, the materials in the power receiver must have similar coefficients of thermal expansion to avoid stress fracturing during thermal cycling. Third, the electrical paths and connections in the receiver must feature low resistivity in order to maintain good end-to-end power efficiency. Lastly, the receiver must provide electrical isolation for the VMJ cells as well as the electrical routing and the interconnections.

The prototype of the HILPB receiver includes a high performance thermal management system. One of the primary challenges with HILPB is how to efficiently remove the undesirable thermal energy from the VMJ cell. The first part of the thermal management system was determining how to mechanically attach the cell to the rest of the receiver while providing good thermal conductivity along with electrical isolation. The current design is constructed from a series of epoxies and substrate materials. A cross-sectional illustration of the optical receiver is shown in *Figure 43*. The VMJ cell is

mounted to a substrate with a boron nitride filled epoxy resin [52]. The resin features a good thermal conductivity ($1.5 \text{ W/m}^\circ\text{K}$) and a relatively high operating temperature (approximately 200°C). In the center of the stack up is the polished aluminum nitride substrate. Aluminum nitride offers very good thermal performance ($175 \text{ W/m}^\circ\text{K}$), low coefficient of thermal expansion and good dielectric strength. Aluminum nitride is commonly used as a substitute for the standard FR4 fiberglass in printed circuit board (PCB) construction for better thermal conductivity in high power circuits. These characteristics render it ideal for the power receiver application. The substrate is mounted to the copper heat pipe unit using another layer of the boron nitride epoxy resin.

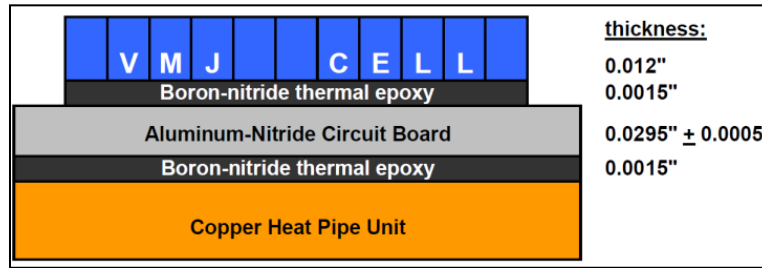


Figure 43: Cross-sectional stack-up of the power receiver

The electrical paths between the photovoltaic cells were routed with a ferrite-nickel-cobalt alloy wire known as KovarTM [53]. KovarTM is a material commonly used for bond wires within integrated circuit (IC) semiconductor constructions, since its coefficient of thermal expansion is similar to that of silicon. A layer of 6% silver plating was added to the KovarTM wire, resulting in a low electrical resistance of 31.9Ω per 1000 ft. The routing wires are electrically attached to the outer two junctions of each VMJ cell with a silver-filled adhesive paste, called SPI Silver Paste PlusTM [54]. The conductive adhesive paste has a very high melting temperature (962° C) and exhibits low electrical resistivity ($3 \times 10^{-5} \Omega\text{-cm}$), which meets the demands of the power receiver.

The current prototype receiver focuses on a terrestrial application of providing remote in-air refueling capability to an electric MUAV, and therefore the size and weight constraints of the thermal control system are a significant consideration for the prototypes. The initial anticipated maximum input radiance was to be less than 220 W of optical energy with a desired receiver operating temperature of 60°C. A small commercial off the shelf (COTS) Zalman microprocessor heat pipe unit, shown in *Figure 44*, was employed as the primary means of thermal conduction, and modified to maximize surface cooling effect by utilizing the airflow from the MUAV propeller. The top mating surface of the unit is finely lapped to provide for maximum thermal transfer. The unit is constructed out of copper, and features three heat pipes that are partially filled with phase change fluid. The heat pipes traverse from the surface plate through a radial array of fins, where airflow is supplied by a small DC fan. This original fan has been replaced by a more powerful motor and propeller commonly used for propulsion on military MUAVs, supplied by the AFRL, in order to increase the amount of cooling beyond the manufacturer's specifications.

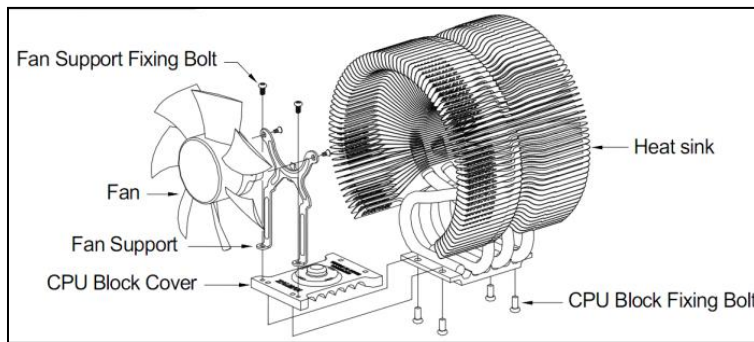


Figure 44: Zalman heat pipe unit

A heat transfer analysis may be performed on the receiver to obtain the theoretical operating temperature at the surface of the VMJ cell during test. This is accomplished by

calculating the thermal resistance for each material in the stack, considering the ambient temperature, surface air velocity generated by the propeller, conversion efficiency and the total optical input energy.

Material Stack (top-to-bottom)	Thermal Resistance $\Theta_i = (\Delta\text{C} / \text{W})$
VMJ Cells	$\Theta_1 = 0.02$
Boron-Nitride Epoxy	$\Theta_2 = 0.1905$
Aluminum-Nitride Substrate	$\Theta_3 = 0.0027$
Boron-Nitride Epoxy	$\Theta_4 = 0.0119$
Heat Sink (stock fan at 2,600 RPM)	$\Theta_5 = 0.12$
Heat Sink (stock fan at 1,350 RPM)	$\Theta_5 = 0.16$
Surface Temperature Equals:	
$\text{Ambient Temp} + \text{Input Power} * (\Theta_1 + \Theta_2 + \Theta_3 + \Theta_4 + \Theta_5)$	

Figure 45: Thermal analysis of the power receiver

With an ambient laboratory temperature of 20° C, the original manufacturer's cooling fan running at 2,600 RPM, an estimated 30% optical-to-electrical conversion efficiency for the VMJ cells (70% thermal load assuming zero reflectivity with AR coatings) and an input radiance of 130 W, the above equation yields a theoretical surface temperature of 51.4° C. With an input radiance equal to 220 W, the resulting theoretical surface temperature is 73.15° C. This is well within the operating limitations of the prototype power receiver materials for the initial range of tests to be conducted.

A constructed prototype HILPB receiver featuring a parallel array of nine photovoltaic VMJ cells is shown below in *Figure 46*. The red ring is manufactured from GPO-3 electrical grade fiberglass, and serves as a mounting surface for the stainless hardware. Optical mounting blocks have been machined to interface with standard 7/8" optical rods, and have been bolted to the heat pipe unit. 1/32" channels were milled into the top face of the copper plate, where several thermocouples have been embedded to characterize the thermal profile of the interface between the copper and the aluminum-

nitride substrate. There have been a few variations in the geometry of the receivers, each featuring a different number and arrangement of VMJ cells to vary the total convertible surface area to support a variety of experiments.

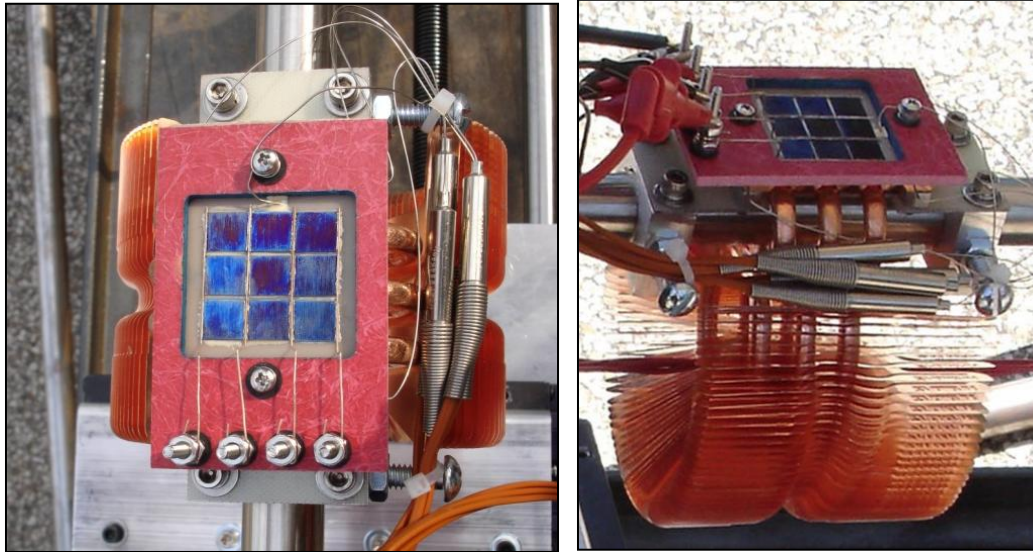


Figure 46: Two views of a complete HILPB receiver

As of 2010, a total of seventeen photovoltaic receiver prototypes have been designed and constructed to undergo HILPB experiments in support of the AFRL funded research program. Each of the receivers was designed to investigate a particular aspect of the wireless power transmission system, in an effort to explore the performance capabilities in the photonics, optics, materials and geometries.

In addition, a water-cooled receiver was also employed on several experiments. This variation replaced the copper heat pipe unit and aluminum-nitride substrate material with a custom machined aluminum cold plate, through which water recirculation channels have been machined. A thin anodized coating was applied to the exterior surfaces of the aluminum unit before mounting the VMJ cells to provide electrical isolation to the face of the receiver.

TABLE VI: HILPB Receiver Construction Log

Construction Log		
Designator	Cells	Notes
MK-I	H3-14	single, consistant side down, lead ripped off during testing
	H3-11	obscured during assembly
MK-II	E12-11	rebuild double, consistant side up
	H3-33	rebuild double, consistant side down
MK-III	E12-4	single, consistant side up, lead ripped off during testing & repaired at Northrop
	K3-5	experienced a burn to the AR coating from the Gaussian laser set to 110W rebuild single consistant side up
MK-IV	K1-C	double, IR coating, thick cell
	SCA9-A	double, IR coating, small cell
MK-V	K3-23	double, IR coating
	SCA9-B	double IR coating, small cell
MK-VI	E12-10	top left corner
	E12-13	top right corner
	H3-7	bottom right corner
	F1-5	bottom left corner
MK-VII	K1-B	top left corner
	K3-3	top center
	K3-4	top right corner
	K3-15	right center
	K3-20	bottom right corner
	K3-19	bottom center
	K3-17	bottom left corner
	K3-8	left center
	K3-12	center
MK-VIII-A (radial)	K3-1	top left corner
	K3-27	top center
	E12-8	top right corner
	E12-20	right center
	K3-11	bottom right corner
	E12-17	bottom center
	E12-18	bottom left corner
	K3-10	left center
	F3-13	center
MK-IX (radial) water-cooled	H3-5	top left corner
	K5-19	top center
	H1-14	top right corner
	K12-13	right center
	H1-29	bottom right corner
	K7-16	bottom center
	H1-31	bottom left corner
	K12-3	left center
	K11-9	center
	SCA9-D	top-right small cell
	SCA9-E	bottom-left small cell
	K9-3 S1	top
MK-X water-cooled	K11-3 S1	left center
	K5-20 S1	center
	K3-29 S2	right center
	K12-9 S1	bottom
	K5-8	top left corner
MK-XI water-cooled	D5-2	top center
	K12-12	top right corner
	K12-7	right center
	K12-11	bottom right corner
	K11-5	bottom center
	K9-2	bottom left corner
	K12-4	left center
	K11-11	center
MK-XII beam-profile, air-cooled	no-number	top (thin cell)
	no-number	bottom (thick cell)
MK-XIII flight-unit air cooled	E12-7	center
	D2-2	top left corner
	unmarked	top center
	unmarked	top right corner
	unmarked	right center
	D3-2	bottom right corner
	C5-10	bottom center
	D1-10	bottom left corner
	K12-10 S1	left center center

3.2 System Description – Laser and Optics Bench

To support the variety of HILPB experiments, a laser facility was established at CSU consisting of a fiber-coupled 350 W continuous wave (CW) semiconductor laser (*Figure 47*), 4'x10' optical bench, custom six-axis gimbaled target and variable air and liquid chiller capabilities. The ability to conduct these experiments in house was crucial to accomplishing the research objectives within the project timeframe by maintaining complete control over the experimental process. The overall laboratory is depicted in *Figure 48*.



Figure 47: LIMO water-cooled turnkey laser diode system



Figure 48: HILPB test facility at CSU

In order to protect the end of the laser fiber from dust and disturbance, a shroud was placed over it containing an optical window. This is a common manufacturing practice in laser welding applications, and it increases the life expectancy of the cleaved

fiber. The window is Melles Griot part 02WBK044 with HEBBAR AR coating /077. There is a minor efficiency loss in using the optical window, and this is taken into account in the analysis of the experimental results.

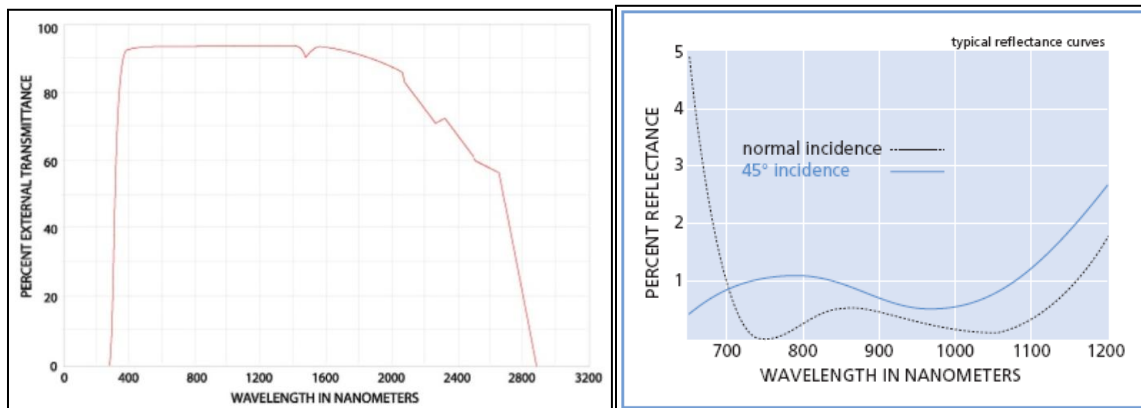


Figure 49: Transmittance curve and coating on the protective fiber window

The target range hardware was designed to perform a variety of functions. First, it allows for a manual translation of the HILPB receiver in three axes to fine tune the alignment of the laser beam and the range distance. Second, the gimbaled yoke performs programmable rotations in three axes up to 75 degrees, to investigate the off-normal performance and radial position of a receiver design within the field of illumination. This capability is used to simulate the pitch, roll and yaw of an aircraft in flight during the conduction of a laser test. Lastly, the target unit provides a quick-change mounting surface and thermal interface for the prototype receivers, and offers a controllable high-flow water-cooling option.

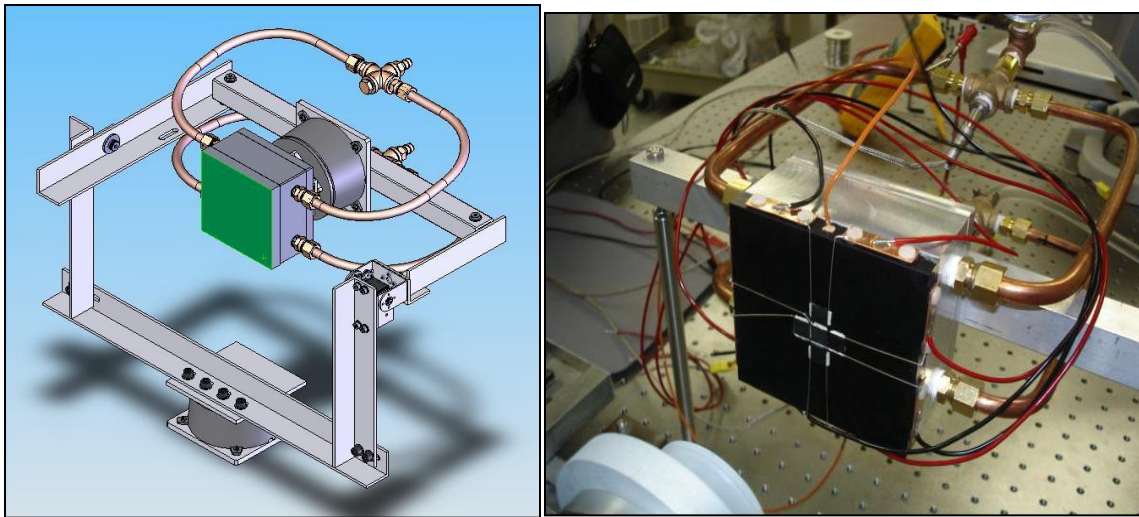


Figure 50: Design and construction of the gimbaled yoke target mechanism



Figure 51: Gimbal rig with receiver, power electronics and MUAV

3.3 System Description – Data Acquisition System

A high speed data acquisition system was developed by the multi-disciplinary ISSL team to sense the various temperatures, currents and voltages in the receiver and load during the testing of the HILPB system, as well as provide a power management and distribution (PMAD) system to sink the power generated by the receiver through either a variable resistive load or through a battery charging circuit. The analog sensing circuitry

has been designed to maximize accuracy while minimizing measurement noise and parasitic impedance, and all of the digital logic control and functionality is achieved through a Xilinx Spartan-3 FPGA. The electronics also provides remote data logging capability of the performance parameters of the system for later analysis.

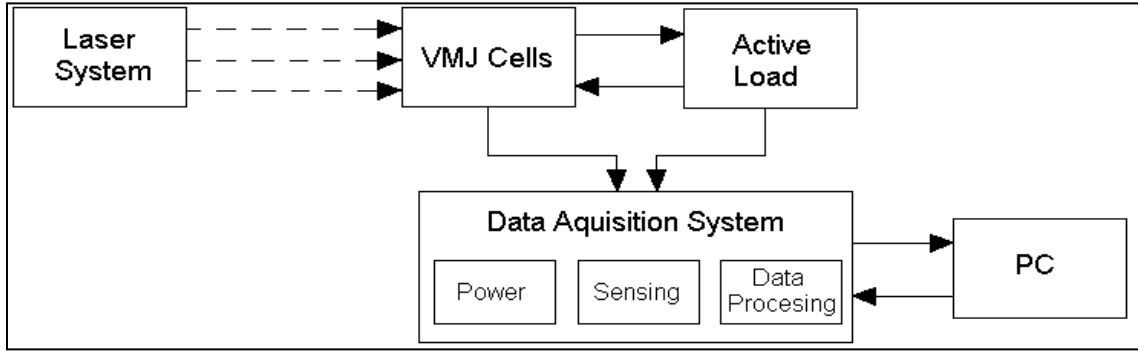


Figure 52: Top level block diagram of the receiver electronics system

The PMAD system is capable of handling input voltage swings from 9-28 V and controllable current limits of 3-7 A, while delivering regulated power to the load (motor) and charging the batteries. The individual Li⁺ cell voltages, currents and temperatures are monitored, and the PMAD system provides for power shunting (cell balancing) and charge rate control. All of the sensed data is sent through a wireless UART interface to a custom graphical user interface (GUI) written using the C# language coupled with the .NET framework, and the server was written in C under the Cygwin environment. The GUI runs on the remote computer terminal for on-line system monitoring and data analysis. Overall, the prototype electronics system stack weighs approximately 160 grams, making it appropriate for >5 lb MUAV's. Although some initial design work was performed to minimize the form factor of the electronics, a major miniaturization redesign may be performed in the future when a reduced functionality and form factor is specified. In its current state, the electronics system may be used to conduct an initial

flight experiment, and is easily reconfigurable to accommodate additional data collection channels and operating ranges.

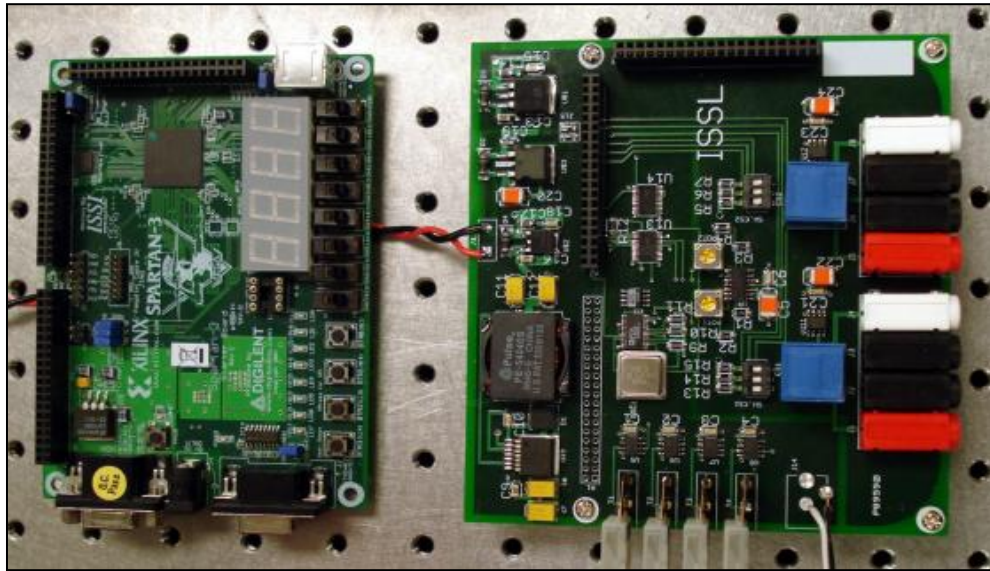


Figure 53: Flight ready power management and data handling system

In order to characterize the performance of the receiver, an automated, high performance data acquisition (DATAQ) system was designed and constructed to record voltage, current, and temperature information simultaneously. The DATAQ system is made up of three individual subsystems: an active variable load that can be adjusted from open-circuit to short-circuit in order to trace the characteristic I-V curve, sensing circuitry and data processing. The focus during the design of the DATAQ system was to achieve high data integrity and reliability. Many design decisions were made to improve the accuracy and quality of the measured states, such as using open-loop/Hall-Effect current sensors to minimize noise interference. For accuracy purposes, the information is represented by 16-bit words (19 bits effective). In addition, to improve the overall system reliability, the DATAQ has been divided into two separate printed circuit boards (PCB), with special attention given to the board layout phase of the design. Data logging

and processing is achieved by utilizing a Xilinx Spartan-3 development board, which includes a field programmable gate array (FPGA) that contains a total of 200k gates.

Figure 54 illustrates the functional block diagram of the DATAQ system. The data transmits via the RS-232 interface to a personal computer at a rate of 6 Hz. Lastly, a custom Graphical User Interface (GUI) was designed to plot and display the I-V characteristic curve of the receiver in real-time.

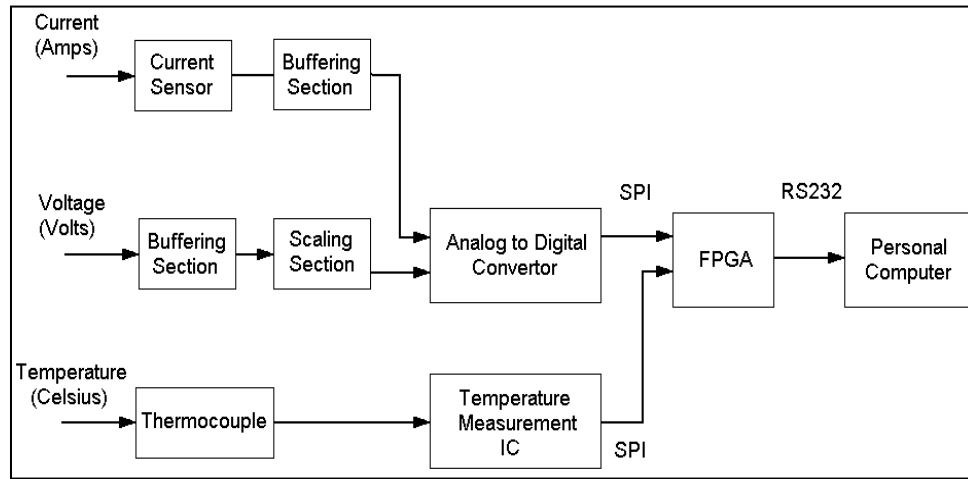


Figure 54: DATAQ – functional block diagram

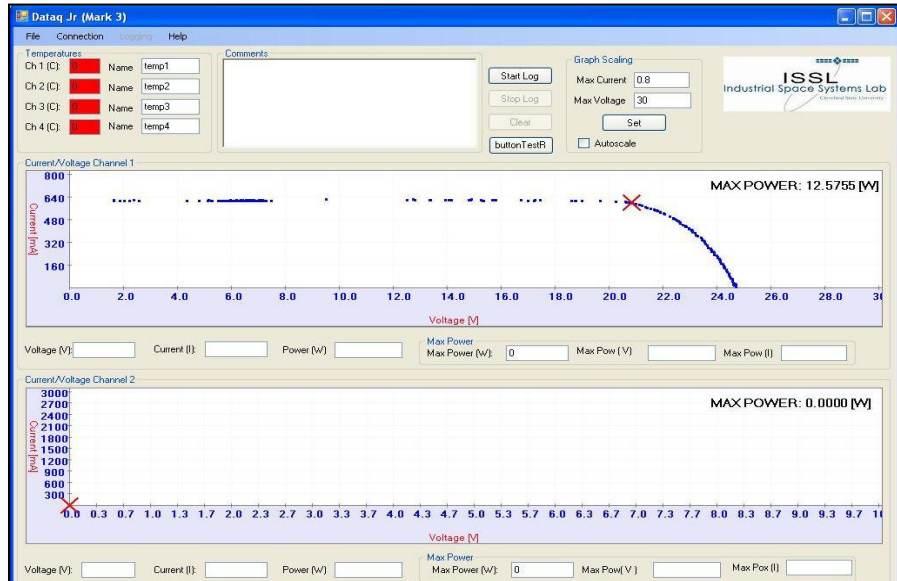


Figure 55: The data acquisition system GUI with example power curve

The HILPB receivers, together with the laser and optics bench and supporting electrical and mechanical systems have been utilized to conduct several notable experimental achievements. The results of this research are being chronicled in several forthcoming reports and publications.

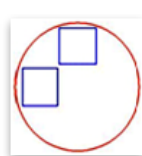
3.4 Photovoltaic Array Cell Back-feeding

The purpose of these experiments was to investigate the potential for current back-feeding of VMJ cells when they are wired in a parallel arrangement. This effect is encountered in a conventional solar array under conditions where the photovoltaic cells are subjected to non-uniform illumination (such as from partial shading or debris on the panel), and this is commonly solved by inserting blocking diodes between each cell and the array bus to prevent the current flow from back-feeding into a weaker cell. The downside of doing this is that a voltage drop will occur across the diodes during normal operation of the array, resulting in slightly lower output power.

Since the beam profile of the laser is non-uniform, this phenomenon could be encountered when using a parallel array of VMJ cells for HILPB. To investigate this, an experiment was conducted on a multi-cell receiver, using two of the available VMJ cells (referred to as the top and left cell) connected in parallel. These particular cells were chosen because they represent two different grades of VMJ cells, with one offering consistently better performance than the other in the NASA GRC flash lamp range. This would establish the conditions for the imbalance to occur, even if both cells received equal illumination. Low-loss diodes were selected for the blocking application, and these could be introduced into the circuit to observe their effects. Ammeters were used to

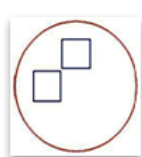
measure the amount and polarity of the individual branch current contributions from both cells.

The tests were conducted using a 200 W continuous wave 980 nm laser, with the beam illuminating the two cells in a manner as to allow for each to receive a similar profile. Both of the cells were oriented with the direction of their junctions aligned towards the center of the beam, so that they both received equivalent amounts and profile of illumination. The test was conducted with three different amounts of beam overfill to vary the overall profile illuminating the cells, and was repeated both with and without the blocking diodes in the circuit. The receiver temperature was maintained within 50–60°C for the duration of the experiment using a variable speed cooling fan flowing air across the heat pipe unit. The results of these tests are shown below in *Figures 56-58*, and the relative diameter and placement of the beam overfill is illustrated.



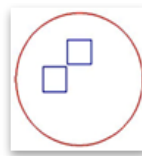
Position	Without Diodes	With Diodes
	Current (amps)	Current (amps)
Top cell	0.233 A	0.147 A
Left cell	-0.097A	0.0 A

Figure 56: Cell back-feeding with small overfill



Position	Without Diodes	With Diodes
	Current (amps)	Current (amps)
Top cell	0.151 A	0.129 A
Left cell	-0.003A	0.0 A

Figure 57: Cell back-feeding with medium overfill



Position	Without Diodes	With Diodes
	Current (amps)	Current (amps)
Top cell	0.189 A	0.122 A
Left cell	-0.087A	0.004 A

Figure 58: Cell back-feeding with large overfill

The negative currents may be observed in the above figures when the blocking diodes are not present, and represent the back-feeding of the current from the strong cell (top) into the weak cell (left). The addition of the blocking diodes does correct the backflow, but at the expense of the inherent power loss through the diodes, to the extent that the diodes did not improve the overall output power of the receiver for any of the experimental results, and it was observed in these instances that their presence was more detrimental than beneficial. This is due to the diode losses exceeding the branch current gains, leading to a decrease in bulk output power.

It is therefore concluded that for HILPB applications, the use of blocking diodes as typically employed in photovoltaic arrays is not necessary. Furthermore, the detrimental receiver output power losses due to the inclusion of the blocking diodes exceeds the parasitic losses induced from cell back-feeding. The omission of the diodes yields a receiver design with fewer components, and permits a further investigation into receiver geometries as presented in the next section.

3.5 Comparison of Receiver Geometries

To explore the hypothesis of an alternate cell configuration and quantify the degree of its improvement, two receiver geometries are considered, a 9-cell square array and a 9-cell radial orientation array. The 9-cell square array simply orients all of the p+nn+ junctions for each cell in the same direction, which optimizes packing density but generates the maximum possible junction-to-junction output variation when illuminated with a Gaussian laser beam. The receiver is constructed in a similar manner to the initial HILPB prototype [55], and is hard-wired to provide three separate stacks of three

paralleled cells (*Figure 59*). For the purposes of these tests each stack is electrically connected together to produce a total of nine parallel cells.

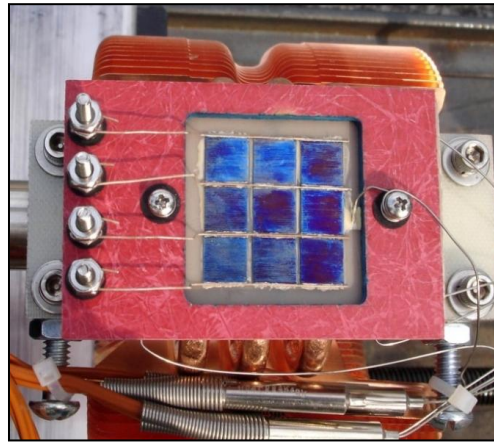


Figure 59: Nine-cell square receiver

The first objective of the experiment was to establish a baseline maximum power measurement for the subsequent tests. The 9-cell square receiver was illuminated with a 980 nm fiber-coupled laser. The receiver position was adjusted in three axes to obtain the maximum output power with the laser's radiant power set to 200 W, and the crest of this procedure resulted in a 30% illumination as depicted in the *Figure 60*. The peak output of the receiver in this configuration was measured to be 23 W, and the temperature at the heat pipe face was regulated within 50–60 °C during the test.

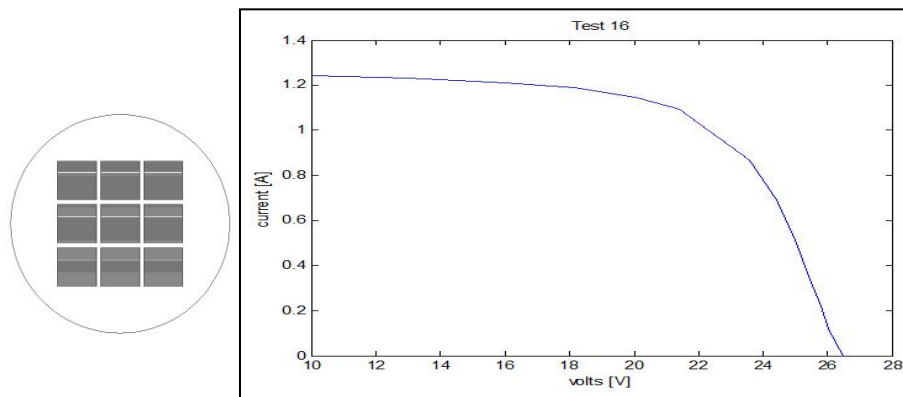


Figure 60: Square receiver at 30% beam overfill, 23 W P_{mp}

The 23 W output result represents a receiver with the maximum photovoltaic cell packing density, and with no regard for accommodating the non-uniform profile of the impinging beam. Next, an alternative receiver geometry will be compared with this baseline figure.

The 9-cell radial orientation array places all of the junctions in eight of the cells on a radial to the center-point of the receiver (*Figure 61*). When centered with the laser beam, the Gaussian profile will extend down the length of each p+nn+ junction, rather than appear across the junctions. In this way, the junction-to-junction delta is minimized, resulting in an equal average illumination per cell. A compromise to this rule is made by placing a single cell at the center of the array, for the purpose of maximizing packing density.

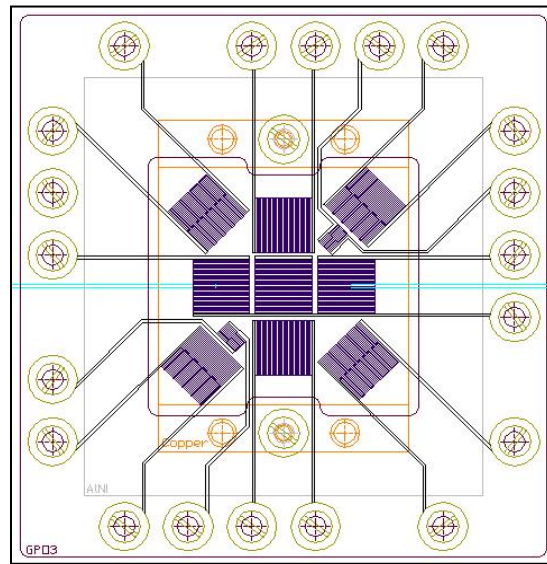


Figure 61: CAD layout of the radial orientation receiver design

In this design each cell has its own dedicated pair of electrical leads, and as a design tradeoff to implement the radial concept it can be seen that the packing density is much lower than 9-cell square array. This receiver also features two additional miniature

VMJ cells mounted in the vacant triangular corners, which were not used for this test.

For this part of the experiment, the radial orientation receiver was used with all 9 of the 40-junction VMJ cells connected in a parallel arrangement. The same conditions were used as with the previous test to align the receiver at full (200 W) laser radiant power, starting with the inner grouping of five cells. The z-axis was adjusted to achieve a range that would maximize the overall power converted by the receiver array, resulting in a peak overfill condition. Each of the individual cells in the array were then disconnected and characterized in order to determine their contribution to the overall output of the receiver. The resulting output I-V curves are shown below in *Figures 62-66*, and the relative diameter and placement of the beam overfill is illustrated.

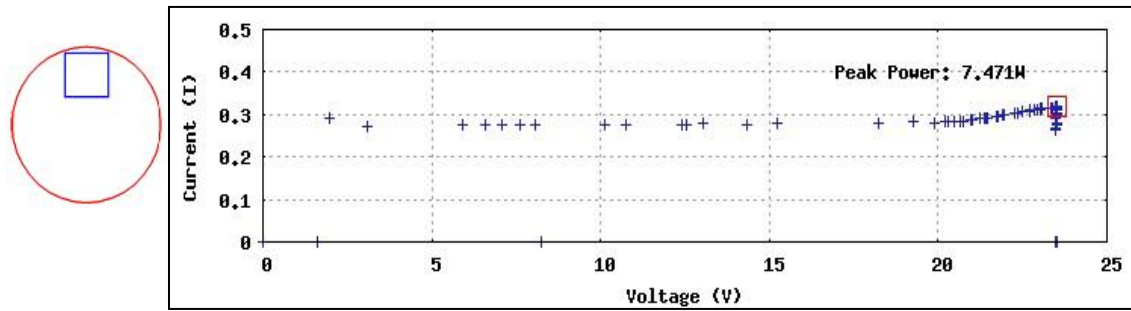


Figure 62: Top cell I-V curve, 7.471 W P_{mp}

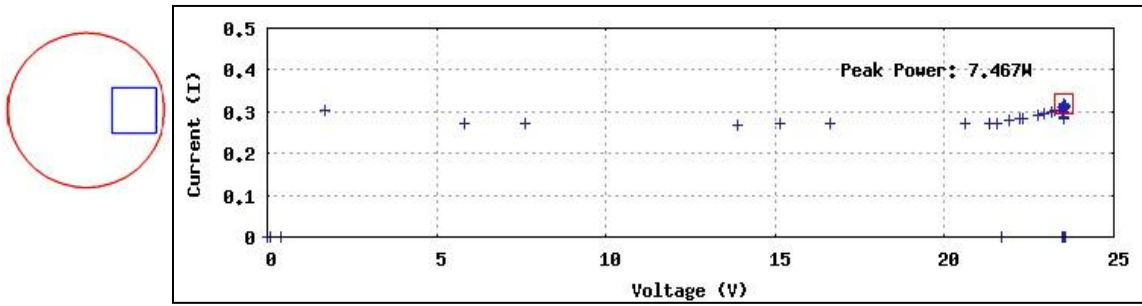


Figure 63: Right cell I-V curve, 7.467 W P_{mp}

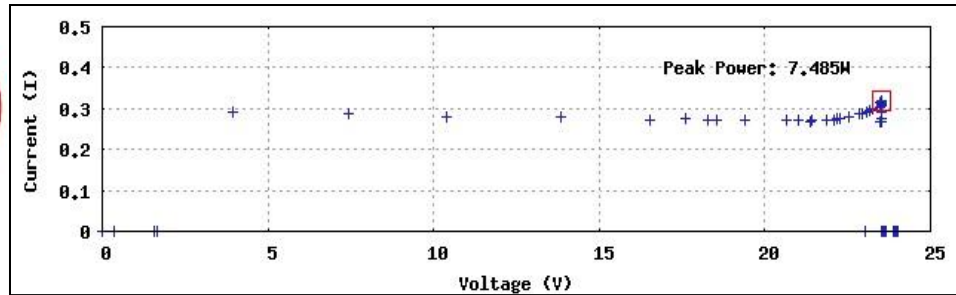
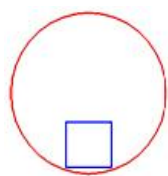


Figure 64: Bottom cell I-V curve, 7.485 W P_{mp}

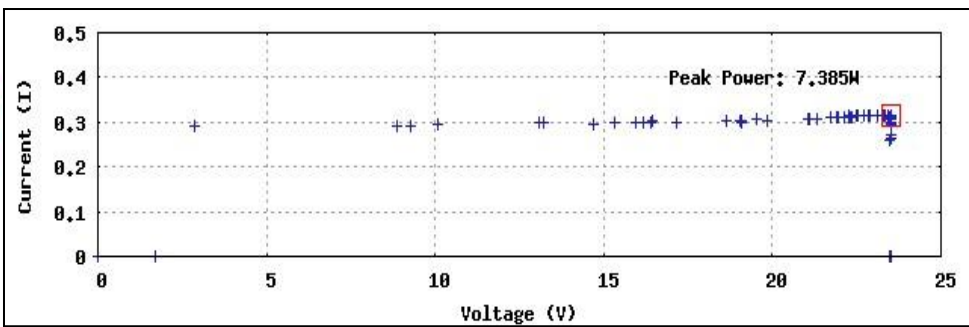
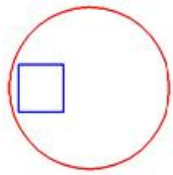


Figure 65: Left cell I-V curve, 7.385 W P_{mp}

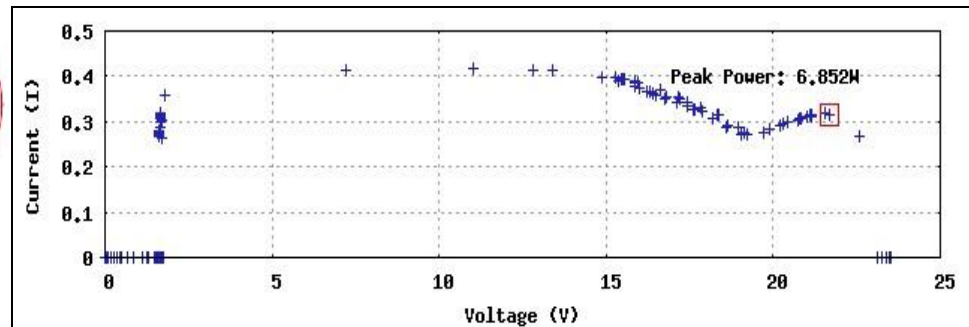
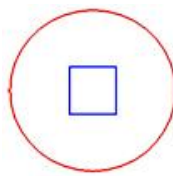


Figure 66: Center cell I-V curve, 6.852 W P_{mp}

It is interesting to note that the center cell, where the beam profile contains the most amount of energy, did not have a higher output power than the four immediately surrounding cells. This may be attributed to the fact that unlike the surrounding cells, the center cell does not comply with the radial configuration, and even though it is receiving the highest intensity portion of the laser beam, it is unable to convert the energy efficiently since it is seeing an uneven power distribution across its p+nn+ junctions.

This is an indication into the magnitude of the detrimental effect of uneven power distribution across the p+nn+ junctions, and is also a first glimpse into the validity of the radial arrangement of the surrounding cells.

For the next part of the experiment, data sets were collected from both the inner four and five cell arrangements wired in parallel. These tests were performed with an optical alignment illuminating the five inner cells and at the 200 W laser output. The resulting output I-V curves are shown below in *Figures 67 & 68*, and the relative diameter and placement of the beam overfill is illustrated.

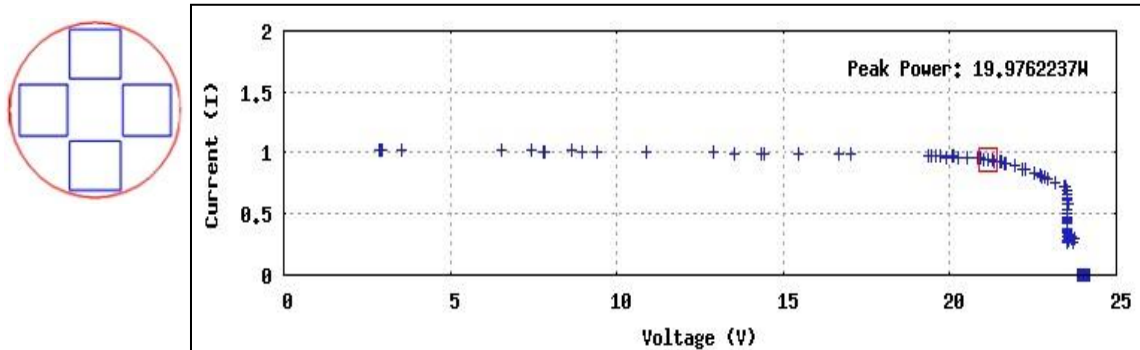


Figure 67: Four cell I-V curve, 19.976 W P_{mp}

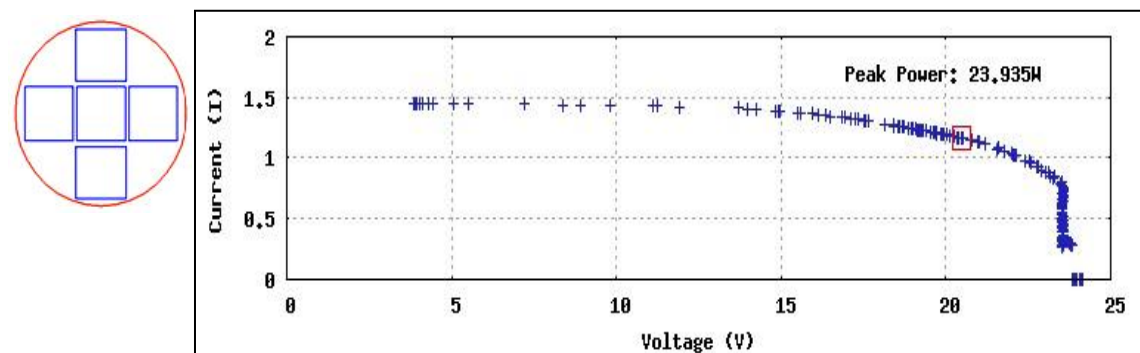


Figure 68: Five cell I-V curve, 23.935 W P_{mp}

A comparison of the results obtained in the grouped cell tests with the single cell tests shows that the four inner cells are again contributing the majority of the radial

receiver's total output. Although the center cell is illuminated by the most intense part of the laser beam, it is converting less energy than its four individual neighboring cells. As stated earlier, this may be attributed to the center cell not complying with the radial configuration.

The five-cell output power of 23.935 W was calculated to have an optical-to-electrical conversion efficiency of 22.75% based on the overfill level of the beam. Comparing these results with those of the square array demonstrates that five cells in the radial orientation can outperform nine cells in the square orientation, even with the packing density losses, providing further validation of the radial array concept.

For the final portion of the test, the overfill level of the receiver was incrementally increased to involve more of the corner cells in the overall output. As with all of the previous parts of this experiment the laser was operated at 200 W, and the receiver temperature was regulated within 50–60° C. The results may be observed in *Figures 69-71*.

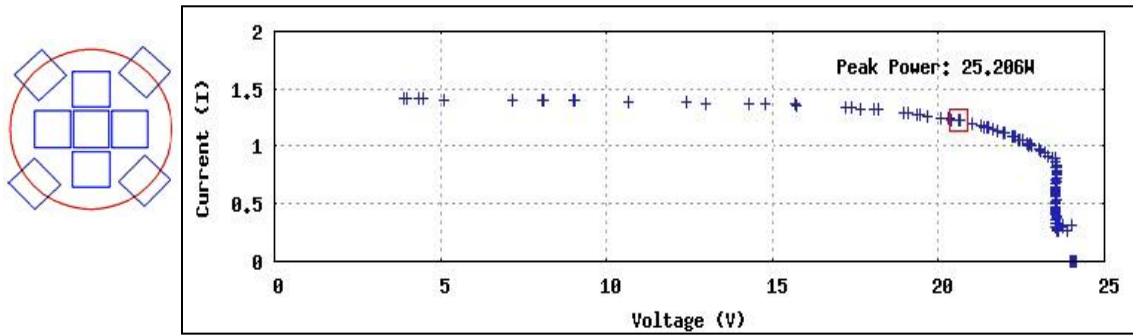


Figure 69: 48.09% illumination, 25.206 W P_{mp} at 26.2% η

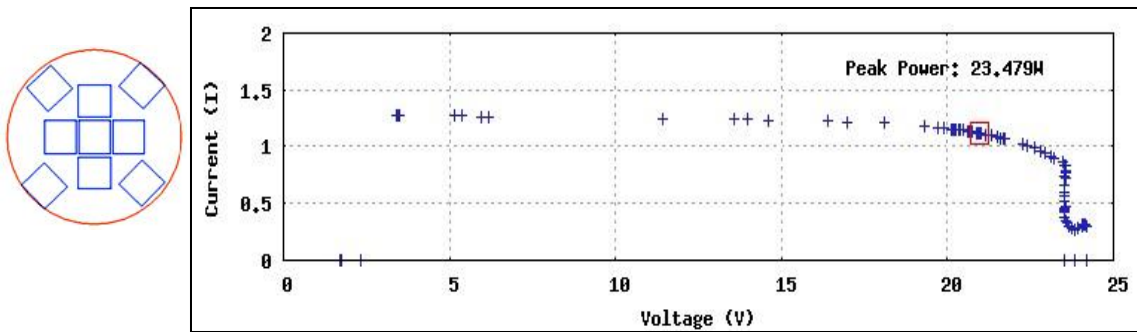


Figure 70: 37.72% illumination, 23.479 W P_{mp} at 31.12% η

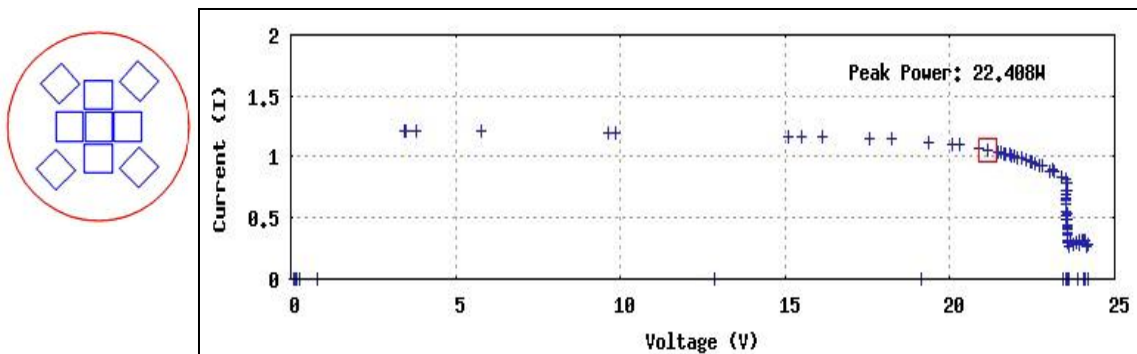


Figure 71: 25.24% illumination, 22.488 W P_{mp} , at 44.39% η

The smallest beam overfill level (*Figure 69*) yielded the highest output power generated by a receiver during the experiment, at 25.206 W. At this level of overfill, the optical-to-electrical conversion efficiency was calculated to be 26.2%. The highest optical-to-electrical conversion efficiency was found to be with the largest beam overfill level, at 44.39%, but this occurred at the expense of total receiver output power dropping to 22.488 W. The receiver setup used to achieve these experiments is shown in *Figure 72*.

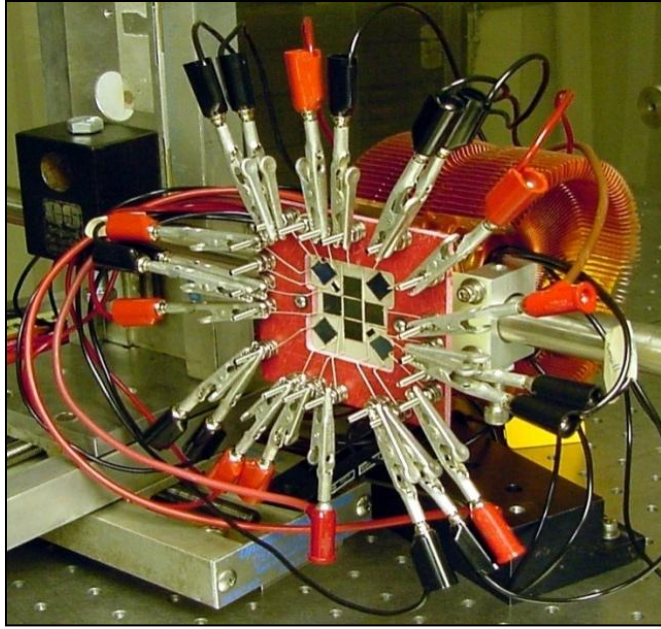


Figure 72: 9-cell radial array in the Northrop Grumman laser facility

In summary, the radial orientation of the p+nn+ junctions was able to generate over 25 W of continuous output power from only 9 small VMJ cells, and under different overfill levels the same receiver was able to achieve 44.39% optical-to-electrical conversion efficiency. This demonstrates one potential solution to the Gaussian distribution issue, by outperforming the peak performance obtained from the conventional 9-cell square receiver array.

3.6 Optical Frequency Optimization

Maximizing the conversion efficiency and power density of the HILPB system is directly depended on matching the wavelength of the source laser with the frequency response of the VMJ cell under high levels of illumination. The band-gap of the VMJ cell can be determined directly from the semiconductor material used in the

manufacturing process. These particular VMJ cells were constructed using silicon wafers, and the characteristic frequency response of the cell is depicted in Figure X as obtained from NASA GRC's Large Area Pulsed Solar Simulator. The silicon spectral response of the VMJ cell clearly illustrates that a near infra-red (IR-A) laser with a wavelength in the vicinity of 1000 nm would maximize the output performance of the power receiver.

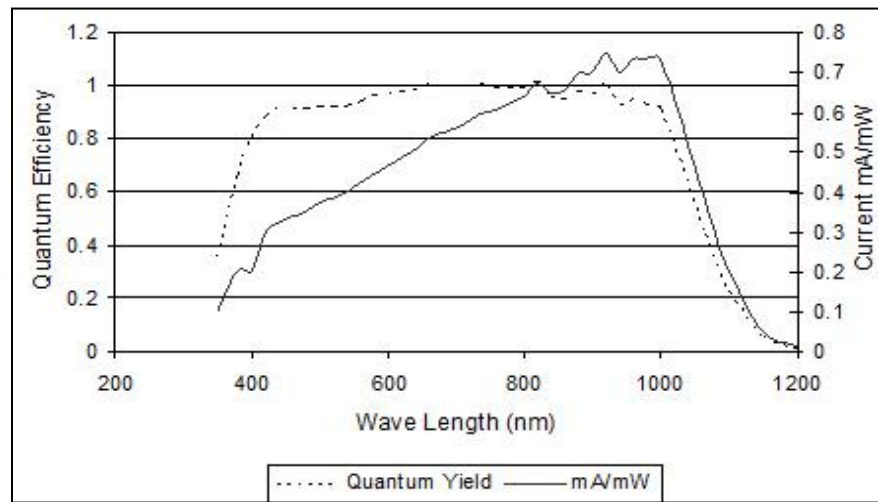


Figure 73: Silicon spectral response

One key aspect that is illustrated by the quantum efficiency plot shown in *Figure 73* is the specific optimal conversion frequency of a VMJ cell. The quantum efficiency and thus the conversion efficiency of a VMJ cell increases as the wavelength of the incident photons approaches the band gap for silicon. The band gap for silicon ranges from 1.125 to 1.2 eV, depending on its crystalline structure, in this particular case the peak response is approximately 1000 nm. Based on the quantum efficiency peak range of *Figure 73*, if incident laser energy in the vicinity of 800-1000 nm is used with a VMJ cell, its theoretical conversion efficiency may approach 50-60%.

The linear transient and steady state behavior of a typical silicon based VMJ cell

theoretically should be maintained even at high laser power concentrations. The peak conversion efficiency at high intensities may be affected since high injection levels may cause the band gap to narrow due to the change in the carrier generation and recombination process, where the Shockley equations describing the current-voltage relationship of p-n junctions become less applicable. Hence, in order to maintain high conversion efficiency at high intensity levels the energy wavelength must be within this nonlinear band gap [56, 57].

It must be noted here that for semiconductor materials, the coefficient of absorption decreases significantly beyond the cutoff wavelength of the impinging energy, as illustrated by the knee curves of *Figure 74*. At high injection levels the narrow band-gap of silicon may be affected as there is a possibility that the knee of the silicon curve may shift, further affecting the conversion efficiency of the VMJ cells. In addition, there are two scenarios that may limit the overall conversion efficiency and creating additional thermal stress due to the excess heat byproduct. First, the thickness of the semiconductor material may lead to saturation by limiting the total depth of penetration for the impinging energy, thus limiting the efficient photoelectric conversion. Another scenario that may limit the overall conversion efficiency is the increase in wavelength of the impinging light due to the oblique collisions in the capture cross section as the light penetrates through the silicon material. Empirical investigation of the optimal frequency under high levels of steady-state illumination is necessary to validate the transient response.

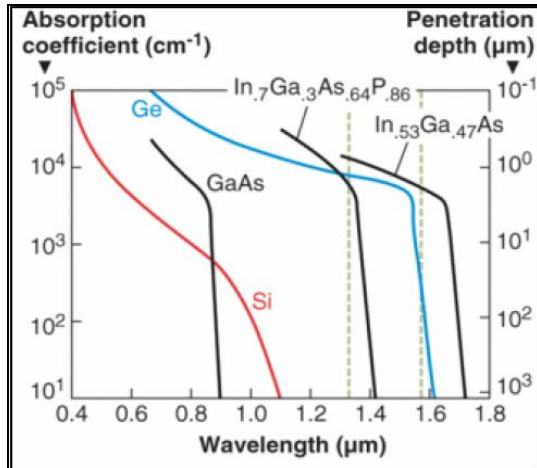


Figure 74: Optical absorption for various semiconductor materials

The best range of narrow band illumination for the VMJ cell was identified based on the quantum efficiency plot shown in *Figure 73*. The particular peak frequency must be verified experimentally to ensure that saturation does not occur at continuous high intensities. The experimental set-up consists of a single VMJ cell receiver and three similar continuous-wave, fiber-coupled semiconductor lasers with distinct operating frequencies. Since the current technology does not offer a tunable laser at the wavelength range of interest, three standard high intensity lasers were selected from Lissotschenko Mikrooptik GmbH (LIMO) Laser Applications Laboratory in Dortmund, Germany. The wavelengths of the three lasers were selected to be in close range of the VMJ narrow band gap: 808 nm (LIMO70-F200-DL808), 940 nm (LIMO70-F200-DL940), and 976 nm (LIMO70-F200-DL976). All three LIMO lasers are complete systems that include power, control, water chiller, and a laser diode module.

The experimental rig consists of the following components: a single VMJ cell receiver mounted to a 3-axis translational positioned system, laser source, adjustable mechanical stage for the optical fiber, cooling fan, custom data acquisition electronics

(DATAQ), and a logging personal computer. A pictorial representation of the experimental set-up is illustrated in *Figure 75*.

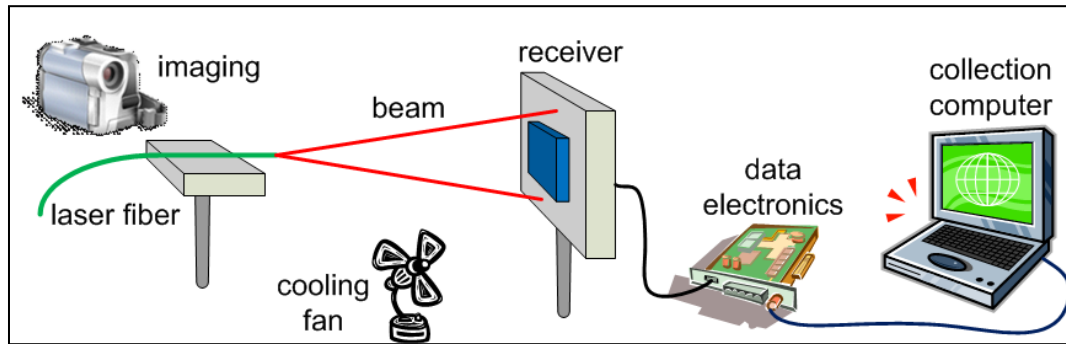


Figure 75: Single VMJ cell laser power beaming test rig

For experimental consistency purposes, all three lasers have a 70 W capacity and the fiber is 200 μm in diameter. All optical equipment was fastened down to the work surface, and only one laser fiber was used for all experiments; this way the laser diode module became the only hardware variable during each test trial. An initial alignment was performed prior to conducting all tests, by using the laser pilot beam to visually align the laser beam at the center of the VMJ cell. At low laser intensities the receiver was adjusted using the 3-axis translational stage positioners for peak output power generation. For all tests, the laser power was increased to cover the full power range of each LIMO laser system. The point of maximum output power was achieved when 26 W of laser energy directly illuminated the VMJ cell, overfilling its surface area.

The experimental results from the conducted tests are illustrated in *Tables VII, VIII, and IX*, and the maximum output power attained is highlighted in each corresponding table.

TABLE VII: 940 nm Wavelength Results

LIMO70-F200-DL940				LIMO70-F200-DL940			
Current Setpoint Amps (A)	Rated Optical Power Watts (W)	Operating Optical Power Watts (W)	Adj. Optical Window Transmittance Watts (W)	Impinging Optical Power Watts (W)	VMJ Peak Power Watts (W)	Conversion Efficiency (%)	Receiver Temp. (°C)
10	9.9	9.207	8.608545	3.6586	1.5198	41.54	24.4
20	25.7	23.901	22.347435	9.4977	3.5398	37.27	25
30	40.9	38.037	35.564595	15.1150	5.0675	33.53	27.6
40	55.1	51.243	47.912205	20.3627	6.1611	30.26	30.1
50.8	70	65.1	60.8685	25.8691	6.8263	26.39	32

TABLE VIII: 976 nm Wavelength Results

LIMO70-F200-DL976				LIMO70-F200-DL976			
Current Setpoint Amps (A)	Rated Optical Power Watts (W)	Operating Optical Power Watts (W)	Adj. Optical Window Transmittance Watts (W)	Impinging Optical Power Watts (W)	VMJ Peak Power Watts (W)	Conversion Efficiency (%)	Receiver Temp. (°C)
10	9.8	9.114	8.52159	3.6217	1.5481	42.74	24.1
20	25.4	23.622	22.08657	9.3868	3.5402	37.71	24.7
30	40.9	38.037	35.564595	15.1150	5.1722	34.22	27.5
40	56	52.08	48.6948	20.6953	6.4459	31.15	30.1
50	70	65.1	60.8685	25.8691	7.2430	28.00	32.6

TABLE IX: 808 nm Wavelength Results

LIMO70-F200-DL808				LIMO70-F200-DL808			
Current Setpoint Amps (A)	Rated Optical Power Watts (W)	Operating Optical Power Watts (W)	Adj. Optical Window Transmittance Watts (W)	Impinging Optical Power Watts (W)	VMJ Peak Power Watts (W)	Conversion Efficiency (%)	Receiver Temp. (°C)
10	1.7	1.581	1.478235	0.6282	0.3131	49.83	22.5
20	20.3	18.879	17.651865	7.5020	1.8050	24.06	28.7
30	38.9	36.177	33.825495	14.3758	3.0695	21.35	35.4
40	56.4	52.452	49.04262	20.8431	3.9837	19.11	41.8
49.4	70	65.1	60.8685	25.8691	4.6798	18.09	47.2

Furthermore, the output power characteristic I-V curves corresponding to each LIMO laser system are illustrated in Figure X. Corresponding images of the experiments are also shown in *Figure 76*, and if viewing this document in color please note that the images are shown in three different colors even though all three laser beams are in the NIR region, which is invisible to the human eye. The coloring effect is due to the digital camera used during the experiment aliasing the IR-A frequencies in the experimental hardware rig.

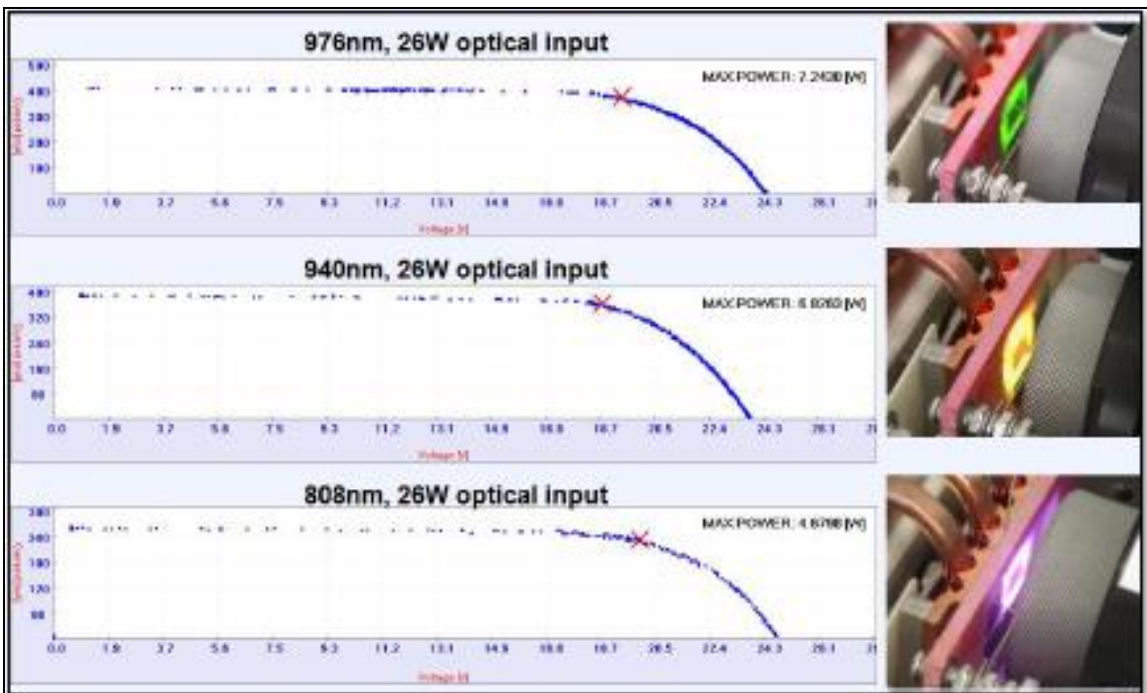


Figure 76: Wavelength maximum power I-V curves

Figures 77 and 78 illustrate the response at each frequency as a function of input intensity, and conversion efficiency. It is shown here that the response across varying irradiance is fairly linear, while the efficiency curve for the 808 nm test exhibits a strong decrease above nominally low optical inputs.

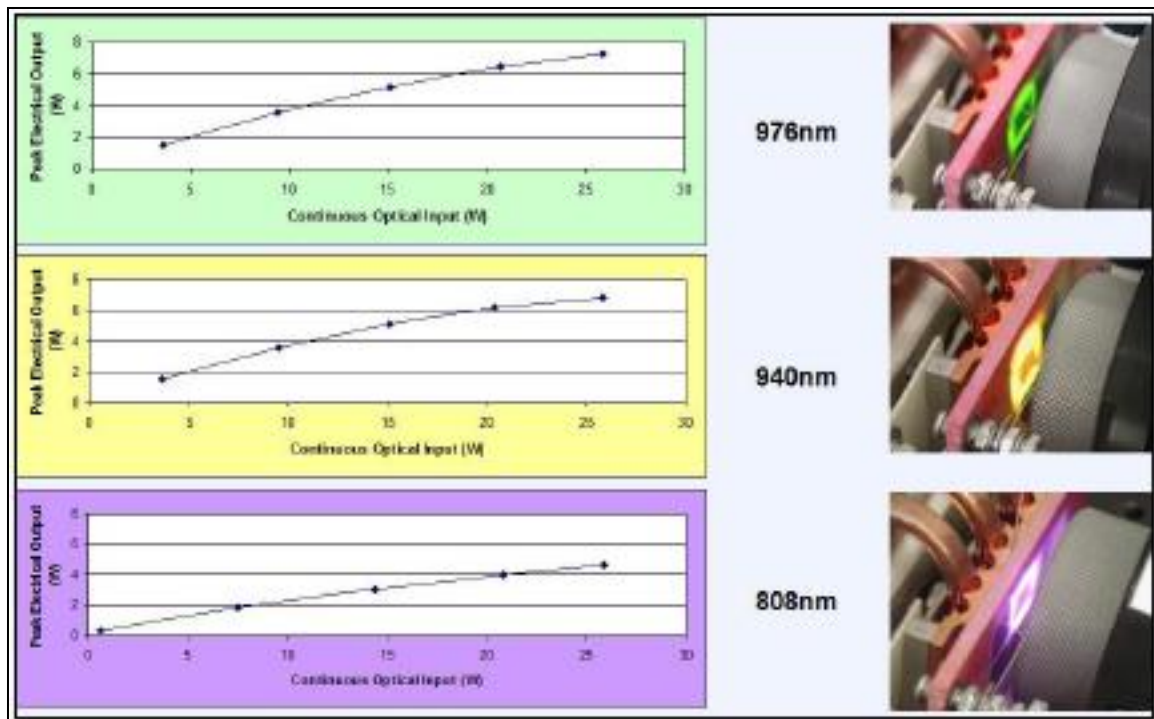


Figure 77: Wavelength input versus output

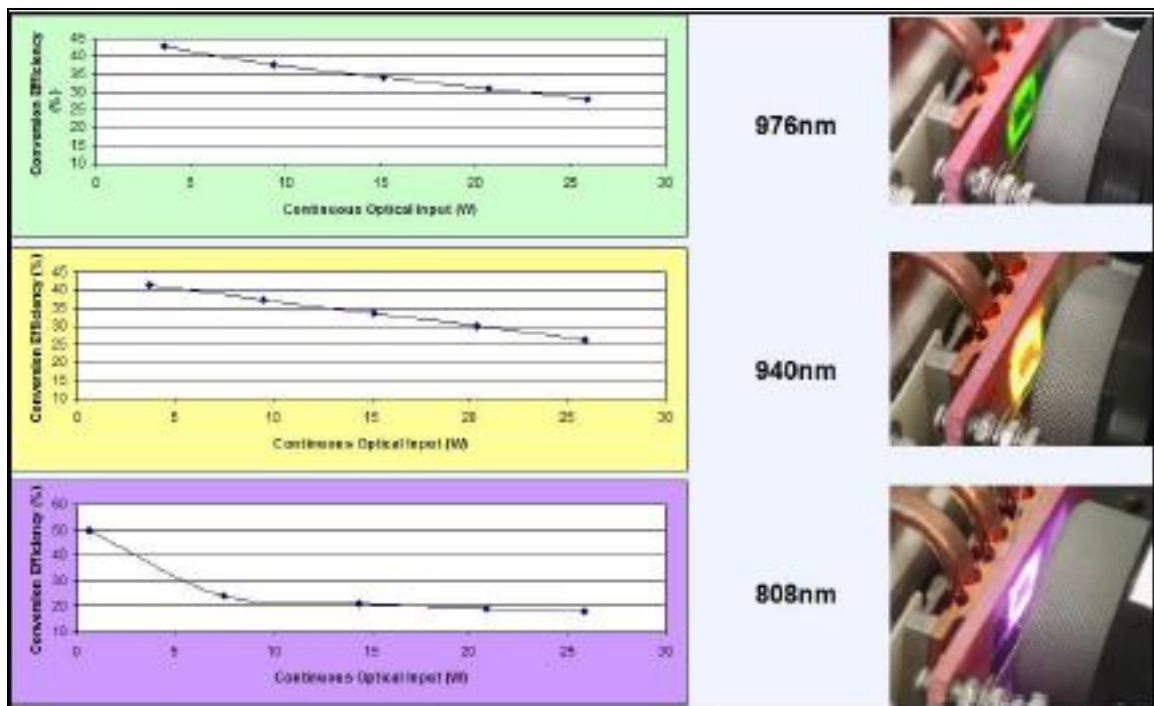


Figure 78: Wavelength conversion efficiencies

The experimental results illustrated in *Tables VII, VIII, IX* and *Figures 76-78*

illustrate that the 976 nm wavelength laser offers the optimal performance when used with the silicon based VMJ cells. Furthermore, the 976 nm wavelength laser offers better efficiency and higher electrical output as depicted in *Figure 79* and *Figure 80* comparisons, respectively.

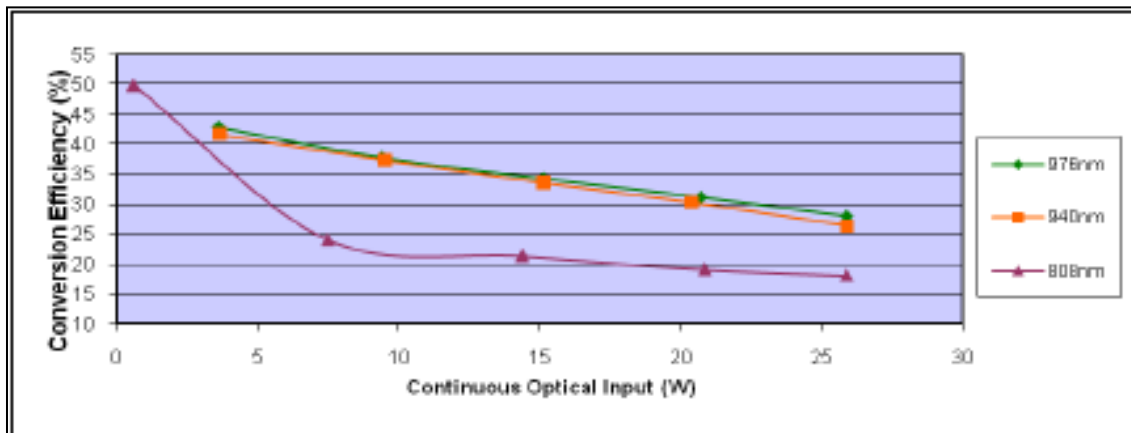


Figure 79: Wavelength efficiency comparison

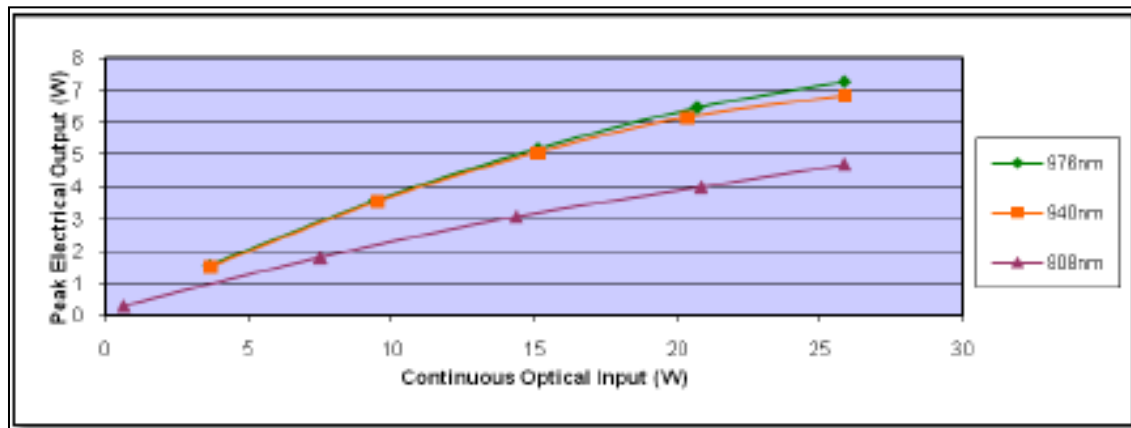


Figure 80: Wavelength output comparison

An interesting phenomenon is illustrated in *Figure 79*. The 808 nm wavelength laser is shown to achieve 50% efficiency at lower laser intensities, followed by a drop in efficiency with increasing levels. At first, this may indicate that the VMJ cell reached saturation. However, that may not be the case since the sharp drop is only associated

with the 808 nm wavelength. The associated hardware pictures also depict a high level of scattering for the 808 nm tests, which may indicate that some of the laser energy is reflected back and away from the surface of the VMJ cell, and is thus not contributing to the electrical output of the cell.

These data sets may be compared with an earlier experiment conducted with a very similar test setup, but utilizing a LIMO 1064 nm source laser. In that experiment, the laser source was similarly operated at a peak optical output power of 70 W (with 25.86 W illuminating the receiver), and after fine tuning the alignment of the receiver the single illuminated VMJ cell was able to deliver 4.08 W of electrical power. This performance indicates a 15.8% optical-to-electrical efficiency, which is below the performance achieved with either the 808, 940 or 976 nm sources. This is because the 1064 nm source is beyond the band gap of the silicon VMJ cell, as illustrated in *Figure 73*.

Lastly, a separate experiment was conducted while at the LIMO laser laboratory in Dortmund, Germany, to determine the highest power density achievable with a single VMJ photovoltaic cell. Using the selected 976 nm laser system, one VMJ cell produced 10.74 W from 44.72 W of impinging laser energy, which is equivalent to an output power density of 13.6 W/cm^2 from 56.6 W/cm^2 of total laser energy. Hence, the total optical-to-electrical conversion efficiency was approximately 24%. This represents the highest output power density achieved to date in HILPB, with a single VMJ silicon-based photovoltaic cell.

In conclusion the optimal frequency of the laser source to be used with the current HILPB receiver should be in the vicinity of 976 nm, which corresponds favorably to

commercially available laser systems. Appreciative responses may be realized at adjacent frequencies including 808, 940 and 1064 nm, but they are significantly reduced when compared with the performance results obtained near 976 nm. This capability may be utilized in a multi-beam/multi-wavelength system, in which the VMJ cells may act as sensors for an acquisition beacon laser operating at an adjacent wavelength to the main beam. Depending on the specific application, the cell design and semiconductor material may also be selected to maximize different design parameters such as high output voltages (high energy band-gaps) or high output currents (low energy band-gaps). These tests also demonstrate the highest output power density achieved thus far with an air-cooled receiver at 13.6 W/cm².

3.7 Beam Homogenization Optics

A different approach to the handling of the Gaussian beam issue is to employ conditioning optics stages that refocus the beam to create an even, or flat-top energy distribution across the beam profile at the receiver. This type of method will insure an even junction to junction illumination at the VMJ cell, but with the system cost of added hardware and complexity, with some efficiency losses. To quantify the potential performance gains with such a system, a comparison experiment was designed utilizing two stages of fly-eye optics to create a beam homogenizer, and a focusing stage to create a working field range. This optical arrangement can provide for an energy variation within 1% at the receiver, at total transmission efficiencies around 80%.

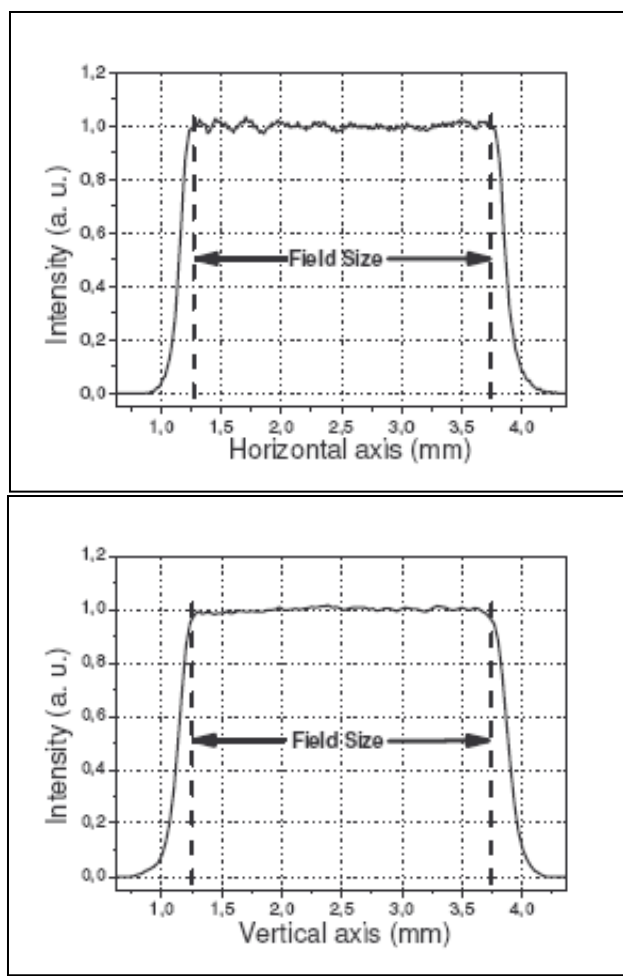


Figure 81: H and V profile cuts of the conditioned flat-top beam profile

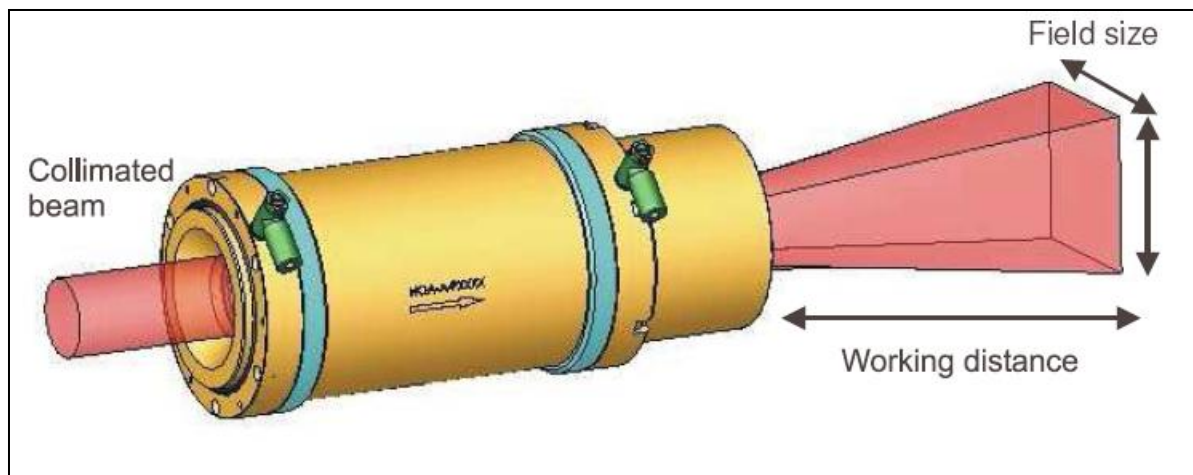


Figure 82: Mechanical illustration of the enclosed beam tube

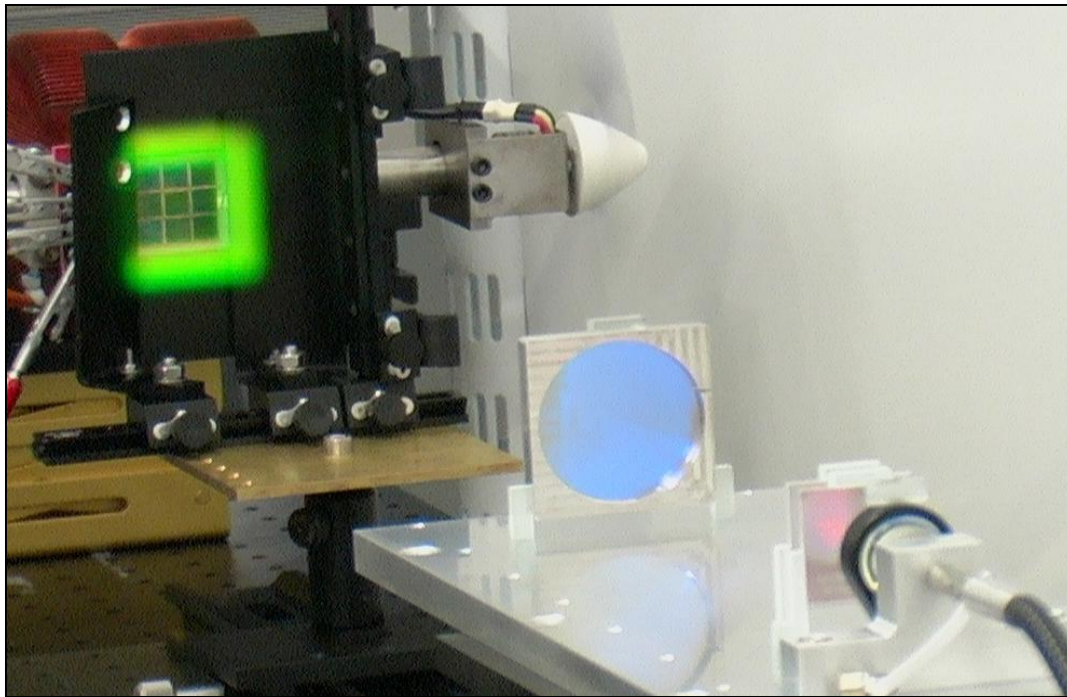


Figure 83: Picture of the unenclosed beam homogenization optic stages

With the addition of the extra optics stages, the resulting field of illumination could be imaged squarely on the target receiver, which coincides favorably with the naturally forming square VMJ arrays. The square beam facilitates the optimal geometric cell arrangement efficiency given the current square manufacturing of the VMJ cells, when compared with the wasted energy overfill regions when utilizing a round beam.

The receiver construction for this experiment is based on a water cooled design utilizing an anodized aluminum cold-block with machined internal recirculation channels. This type of receiver offers an increased controllability during experimentation, since the temperature at the face of the receiver may be closely regulated by adjusting the fluid flow to maintain a steady state temperature independent of radiated power.

When the conditioned flat-top beam was focused at 19.1 W/cm^2 on a 9-cell square array containing 5.85 cm^2 of convertible surface area, the receiver was able to perform at

an optical-to-electrical conversion rate of 41%, yielding a total of 44.6 W output power for a density of 7.62 W/cm^2 .

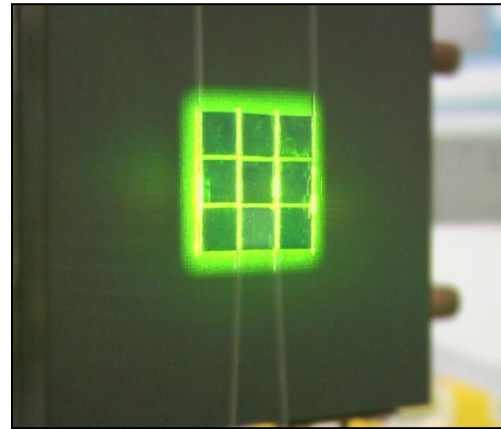


Figure 84: Nine cell water cooled receiver illuminated with a flat-top beam

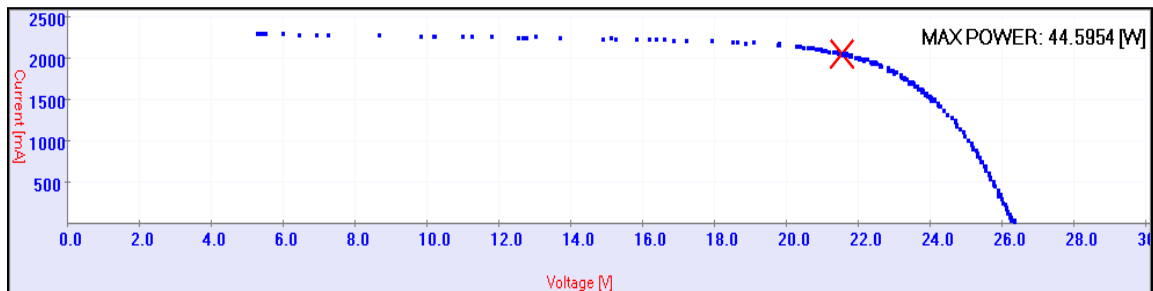


Figure 85: Results of the flat-top beam with a 9-cell parallel array

The same experiment was conducted minus the beam homogenization optics with the 9-cell parallel array. With an average 17.2 W/cm^2 input irradiance on the cells, the maximum output of the receiver using the Gaussian beam profile was 38.5 W at 6.58 W/cm^2 , which corresponds to 38% conversion efficiency. The data from these two experiments demonstrates an approximate 10% absolute improvement in the efficiency of the photovoltaic cells when employing a uniform profile beam versus a normal Gaussian beam.

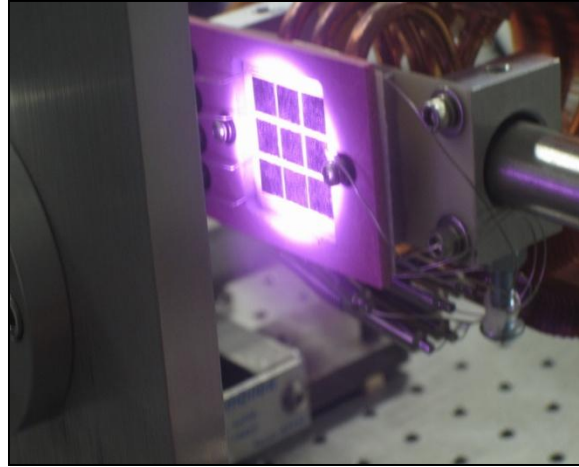


Figure 86: Nine cell receiver illuminated with a Gaussian beam

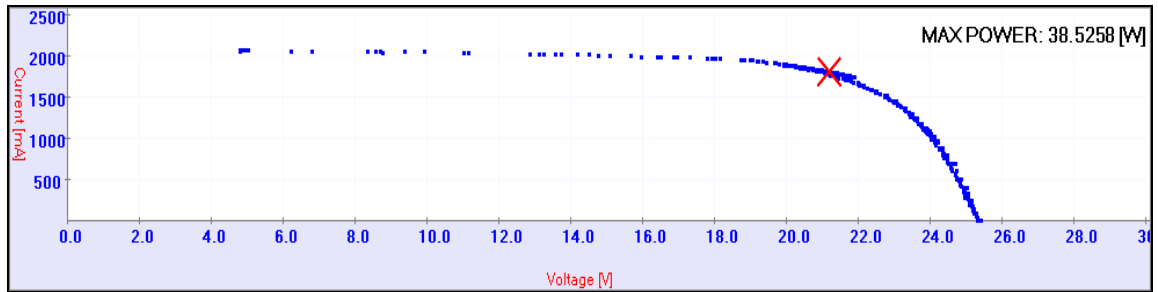


Figure 87: Results of the Gaussian beam with a 9-cell parallel array

Given the ability to precisely control the temperature of the new water-cooled receiver, an effort was made to determine the peak power density that a single 40-junction VMJ cell could produce. For this experiment, the active water cooling system was used behind the target to provide the maximum thermal transfer capacity of the system. In addition, forced air was drawn across the face of the receiver to prevent surface stagnation. The laser beam was focused down to illuminate a single VMJ cell, and at an input optical power density of 67.5 W/cm^2 , one 0.81 cm^2 cell was able to produce 12.7 W at 19.6 W/cm^2 for an optical-to-electrical conversion efficiency of 24%.

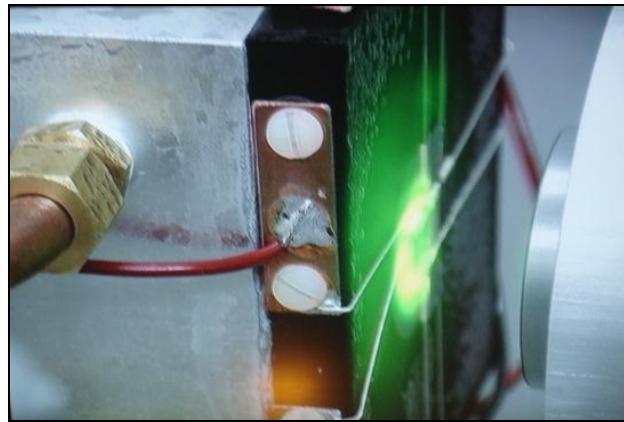


Figure 88: Peak power density test with a single VMJ cell

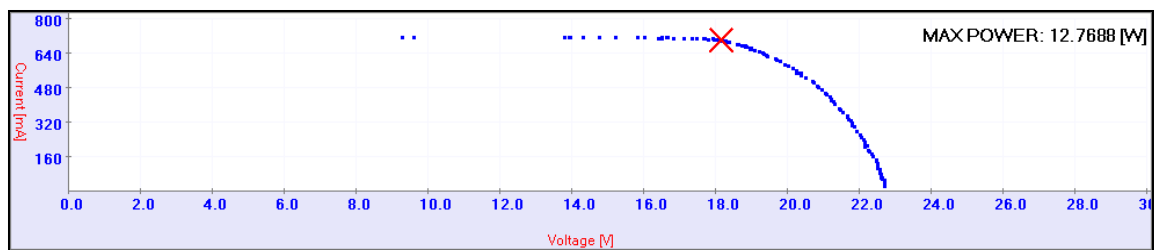


Figure 89: Peak power density I-V curve with a single VMJ cell

CHAPTER IV: EXPERIMENT PROCEDURE AND ANALYSIS

4.1 Beam Profile Characterization

The first experiment to be conducted is an empirical characterization of the beam profile for the current semiconductor fiber-coupled LIMO device in the HILPB laboratory at CSU. The laser system, as shown in *Figure 90*, is a digitally controlled continuous wave laser capable of delivering 368 watts of optical power at 977.2 nm, with a spectral bandwidth of 2.9 nm.



Figure 90: LIMO laser system and diode module

It is understood that the emitted wave-front is fundamentally Transverse Electro-Magnetic Gaussian (TEM₀₀) in profile [58], a model of which is shown in *Figure 91*:

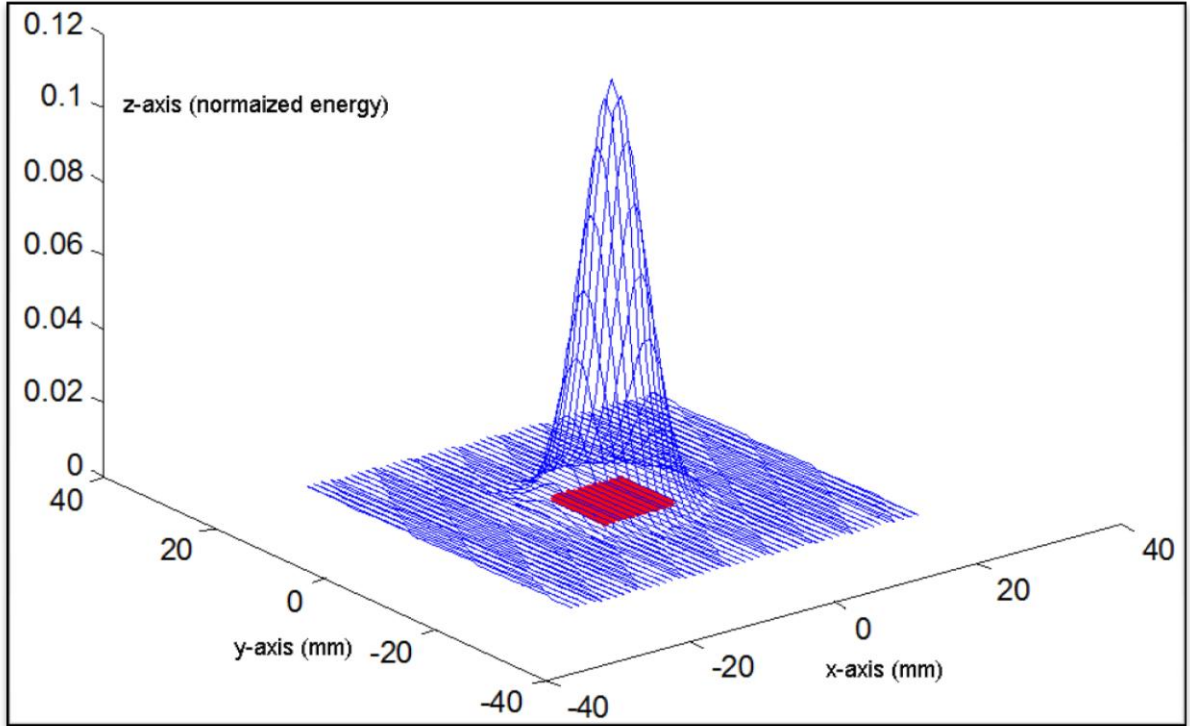


Figure 91: TEM₀₀ model of the beam profile

In order to better serve the ideas presented in this research, an empirical investigation is made into the characterization of the profile of the raw, unconditioned laser beam as it propagates in free space beyond the glass fiber. By taking a series of measurements across the x-y plane with a small translatable photovoltaic cell serving as a photo-detector, the piecewise spatial distribution of the profile may be found. An illustration of such an apparatus is shown in *Figure 92*.

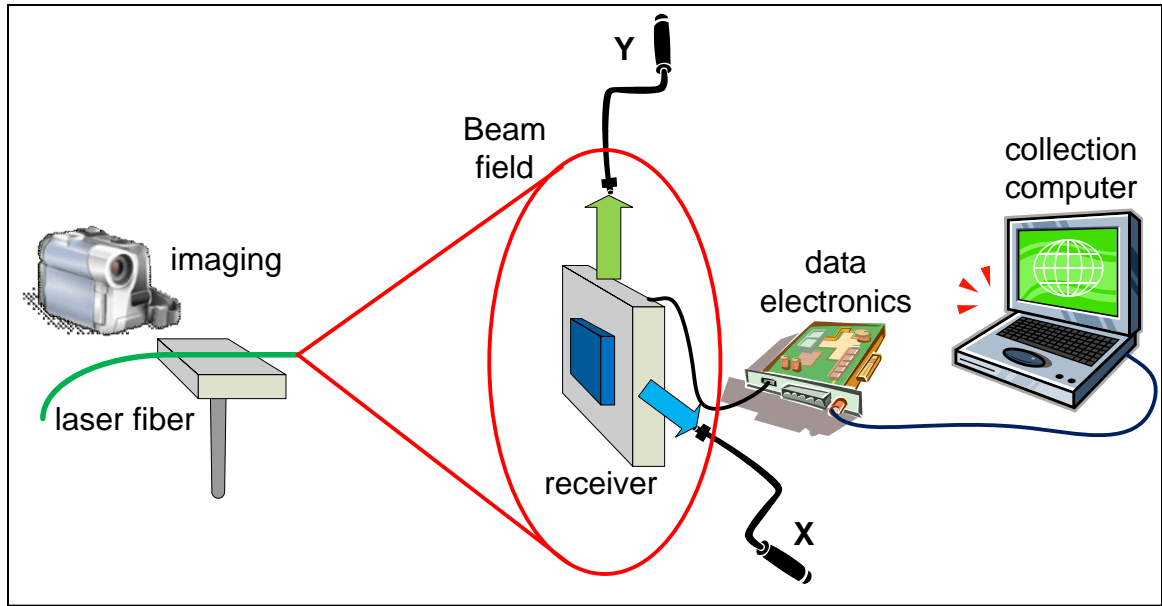


Figure 92: Beam profiling setup

The results from the beam characterization serves both beam acquisition, pointing & tracking and multiplexed communication purposes. For beam acquisition, pointing & tracking the profile data establishes a spatial limit in the tail of the distribution, beyond which the level of irradiance diminishes below the minimum amount to forward bias a VMJ cell. The geometry and energy of the tail can be used to design a perimeter photo-detection system that would serve as a way to fine tune the tracking performance of a vibrating or moving platform by providing limited differential feedback signals to a tracking control system.

In terms of optical communications, the profile data serves as the initial topology to begin subdividing the receiver design into separate regions for the purpose of multiplexing.

The test was performed as a way to characterize the profile of the beam, for the purpose of receiver array design to quantify the energy available in the tails of the

distribution. This energy may be used to provide beam tracking capabilities in an implemented system, when coupled with a perimeter array of photodetectors looking for either the full width half maximum (FWHM) or $1/e^2$ values of the beam waist. The test sequence was performed at an output laser radiant power (flux) of 200 watts. The beam was allowed to diverge naturally from its fiber termination, and a single VMJ cell was scanned across the field of illumination using two manual translation stages. The scanning was indexed in increments of 1 cm (4 turns), to construct a 19x19 array of measurements (total of 361 I-V curves traced). These measurements are made at a distance of 10 cm away from the laser fiber, and the receiver temperature was maintained between 7-9° C during the beam scanning process.

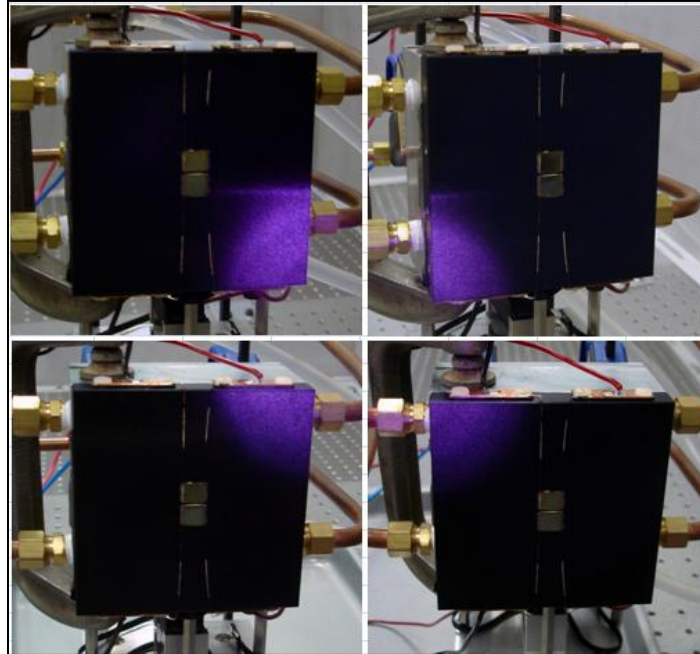


Figure 93: Scanning to the extents of the beam profile

The resulting measurements at each location index are used to create a surface plot of the energy available across the field of illumination. The total summed power converted across the field is 45.39 watts, for a bulk conversion efficiency of 40.5%.

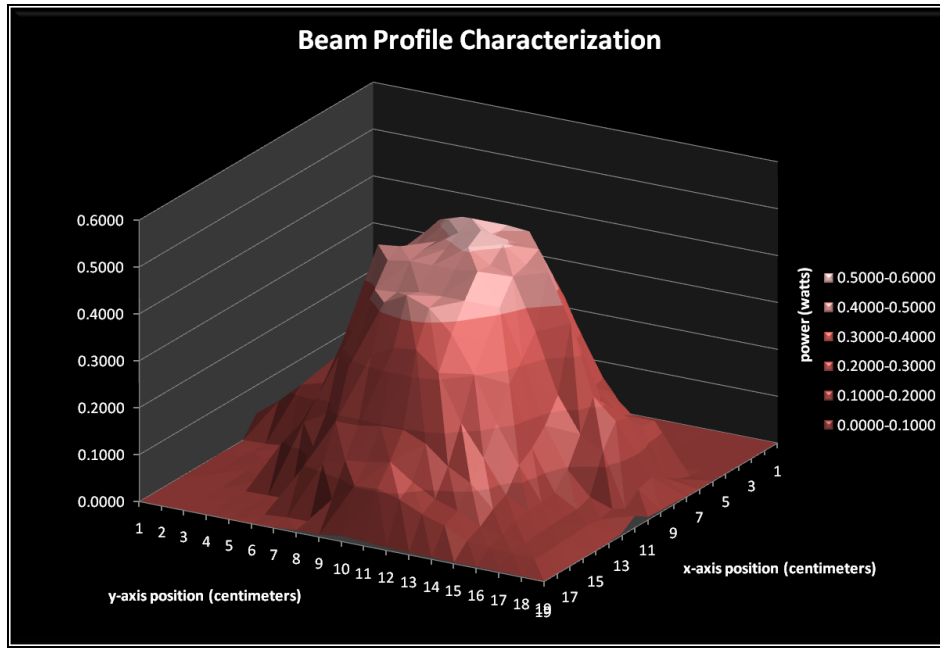


Figure 94: Surface plot of the beam at 200 W of radiant power

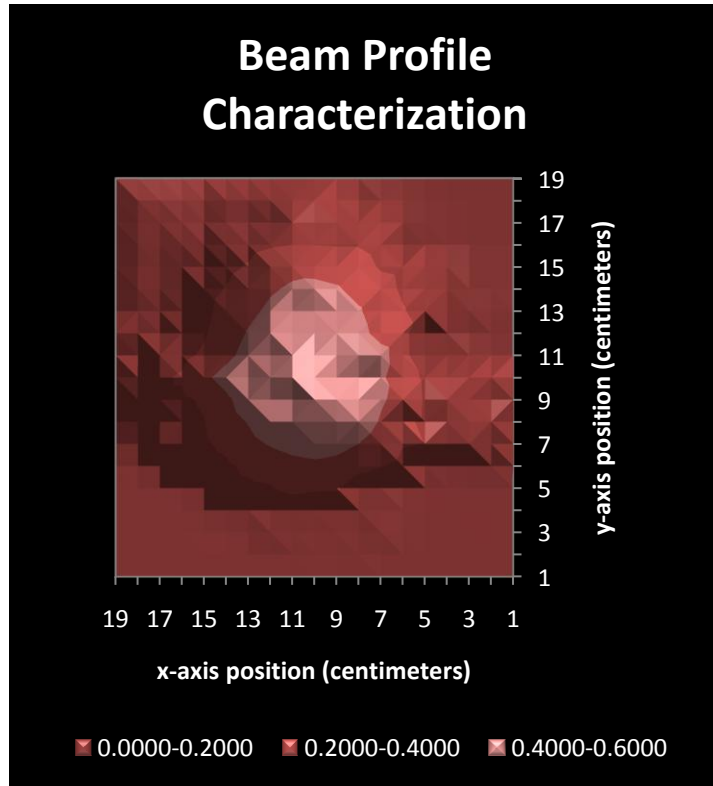


Figure 95: Contour plot of the beam at 200 W of radiant power

To generate the polynomial function for the beam distribution and the list of

coefficients to the i th degree (see order = 10 in this case), an automated fit process may be developed as shown in the Appendix. The general form of the equation is given as:

$$\begin{aligned}
 f(x, y) = & c_{00} + c_{01}y + c_{10}x + c_{02}xy + c_{11}x^2y + c_{20}x^2x + c_{03}y^2y + \\
 & c_{12}x^2y^2y + c_{21}x^2x^2y + c_{30}x^2x^2x + c_{04}y^3y^2y + c_{13}x^2y^3y^2y + c_{22}x^2x^2y^3y + \\
 & c_{31}x^2x^2x^2y + c_{40}x^2x^2x^2x + c_{05}y^4y^2y^2y + c_{14}x^2y^4y^2y^2y + c_{23}x^2x^2y^4y^2y + \\
 & c_{32}x^2x^2x^2y^2y + c_{41}x^2x^2x^2x^2y + c_{50}x^2x^2x^2x^2x + c_{06}y^5y^2y^2y^2y + \\
 & c_{15}x^2y^5y^2y^2y + c_{24}x^2x^2y^5y^2y^2y + c_{33}x^2x^2x^2y^5y^2y + c_{42}x^2x^2x^2x^2y^5y^2y + \\
 & c_{51}x^2x^2x^2x^2x^2y + c_{60}x^2x^2x^2x^2x^2x + c_{07}y^6y^2y^2y^2y^2y + c_{16}x^2y^6y^2y^2y^2y^2y + \\
 & c_{25}x^2x^2y^6y^2y^2y^2y + c_{34}x^2x^2x^2x^2y^6y^2y^2y + c_{43}x^2x^2x^2x^2x^2y^6y^2y^2y + c_{52}x^2x^2x^2x^2x^2y^6y^2y^2y + \\
 & c_{61}x^2x^2x^2x^2x^2y^6y^2y^2y + c_{70}x^2x^2x^2x^2x^2x + c_{08}y^7y^2y^2y^2y^2y^2y + \\
 & c_{17}x^2y^7y^2y^2y^2y^2y + c_{26}x^2x^2y^7y^2y^2y^2y^2y + c_{35}x^2x^2x^2y^7y^2y^2y^2y^2y + \\
 & c_{44}x^2x^2x^2x^2y^7y^2y^2y^2y + c_{53}x^2x^2x^2x^2x^2y^7y^2y^2y^2y + c_{62}x^2x^2x^2x^2x^2x^2y^7y^2y^2y^2y + \\
 & c_{71}x^2x^2x^2x^2x^2x^2y^7y^2y^2y^2y + c_{80}x^2x^2x^2x^2x^2x^2x + c_{09}y^8y^2y^2y^2y^2y^2y^2y + \\
 & c_{18}x^2y^8y^2y^2y^2y^2y^2y + c_{27}x^2x^2y^8y^2y^2y^2y^2y^2y + c_{36}x^2x^2x^2y^8y^2y^2y^2y^2y^2y + \\
 & c_{45}x^2x^2x^2x^2y^8y^2y^2y^2y^2y + c_{54}x^2x^2x^2x^2x^2y^8y^2y^2y^2y^2y + c_{63}x^2x^2x^2x^2x^2x^2y^8y^2y^2y^2y^2y + \\
 & c_{72}x^2x^2x^2x^2x^2x^2y^8y^2y^2y^2y^2y + c_{81}x^2x^2x^2x^2x^2x^2x^2y^8y^2y^2y^2y^2y + c_{90}x^2x^2x^2x^2x^2x^2x^2y^8y^2y^2y^2y^2y + \\
 & c_{010}y^9y^2y^2y^2y^2y^2y^2y + c_{19}x^2y^9y^2y^2y^2y^2y^2y^2y + c_{28}x^2x^2y^9y^2y^2y^2y^2y^2y^2y + \\
 & c_{37}x^2x^2x^2y^9y^2y^2y^2y^2y^2y + c_{46}x^2x^2x^2x^2y^9y^2y^2y^2y^2y^2y + c_{55}x^2x^2x^2x^2x^2y^9y^2y^2y^2y^2y + \\
 & c_{64}x^2x^2x^2x^2x^2x^2y^9y^2y^2y^2y^2y + c_{73}x^2x^2x^2x^2x^2x^2x^2y^9y^2y^2y^2y^2y + c_{82}x^2x^2x^2x^2x^2x^2x^2y^9y^2y^2y^2y^2y + \\
 & c_{91}x^2x^2x^2x^2x^2x^2x^2y^9y^2y^2y^2y^2y + c_{100}x^2x^2x^2x^2x^2x^2x^2x^2y^9y^2y^2y^2y^2y
 \end{aligned} \tag{69}$$

The coefficients are found after 23 iterations of convergence, with a final residual RMS value of 0.028981 (computations in Appendix). The convergence of the particular coefficients may be seen in the output file in the appendix, and result in the 10th order polynomial fit as shown in the *Figure 96* gnuplot.

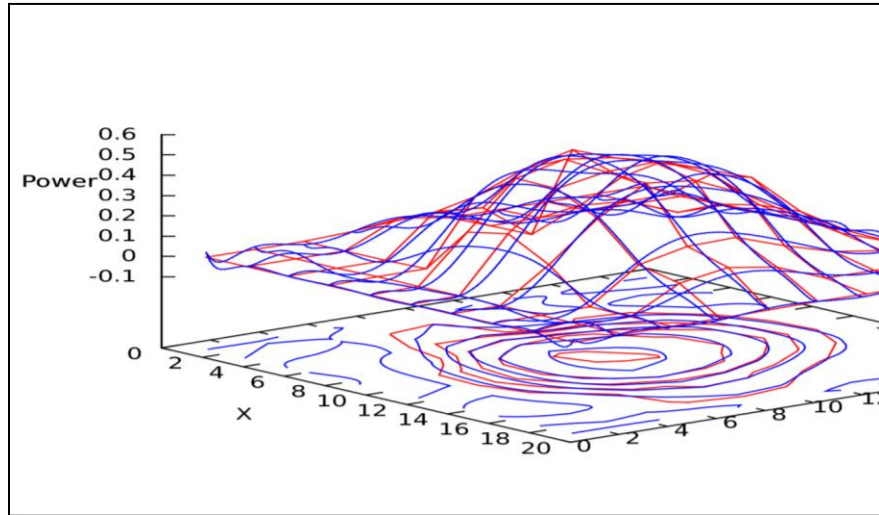


Figure 96: 10th order polynomial beam distribution

In a typical high energy laser system employing adaptive optics, 10th order

aberration correction is a reasonable for atmospheric induced aberration. Such a system would likely be able to correct for the Gaussian variances indicated here, which are likely introduced by imperfections in the cleaved fiber optic end.

This experiment also demonstrates the capability of the VMJ technology to be utilized as a direct measurement sensor for high power beam profiling, in a similar analog to RF far field scanning ranges.

4.2 Off-Axis Illumination

The second experiment conducted was to determine the performance of the VMJ cells under uneven illumination resulting from changes in the angle of beam incidence during simulated flight operations. This was accomplished through the gimbaled yoke hardware at the receiver as shown in *Figure 97*.



Figure 97: Experiment setup for the off axis tests

The gimbal system is able to rotate the receiver up to 60 degrees in two axes, and demonstrated in *Figures 98 and 99*.

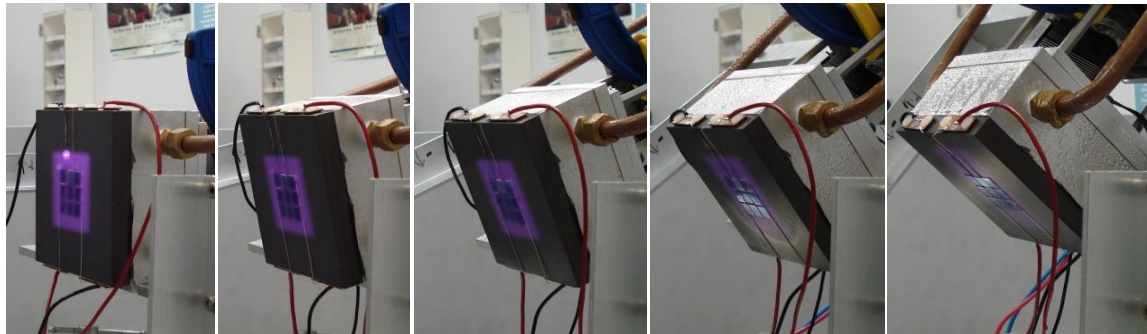


Figure 98: Progression of a horizontal axis rotation

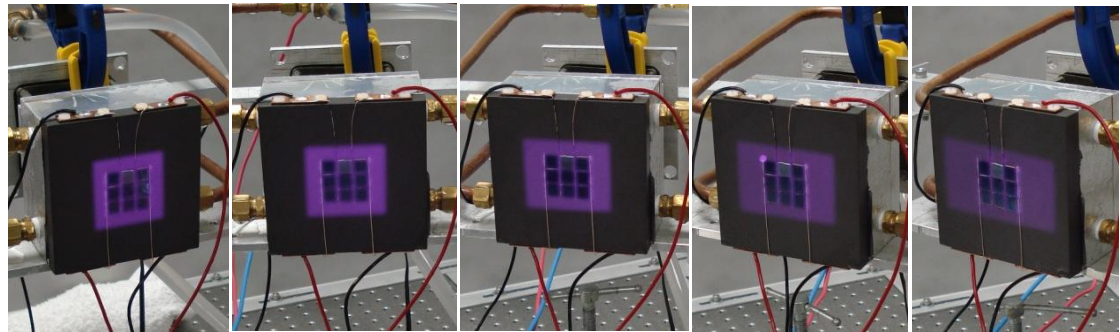


Figure 99: Progression of a vertical axis rotation

During a direct illumination test with orthogonal alignment and 200 watts of laser illumination, the receiver was observed to generate 25.41 W of power, which the temperature was maintained at 23 °C. This value establishes a baseline for comparisons across the two axes of rotation. With the same amount of radiant power, the receiver was incrementally tilted, and the resultant data is compiled in *Table X*.

TABLE X: Measured off-axis power generated by the receiver

Horizontal Axis Rotation (θ) °	Total Radiant Power (W)				
	150	200	250	300	350
0	11.2267	14.4593	17.2799	19.8647	22.0690
15	11.1667	14.3311	17.2298	19.7536	21.9559
30	10.5802	13.5921	16.3099	18.6517	20.8456
45	9.3802	11.9344	14.4754	16.5948	18.5797
60	7.8100	10.0007	12.1210	13.9915	15.6958
Vertical Axis Rotation (θ) °	Total Radiant Power (W)				
	150	200	250	300	350
0	11.2267	14.4593	17.2799	19.8647	22.0690
15	10.9278	14.0526	17.0027	19.6657	22.0601
30	9.3238	12.0850	14.6183	16.9224	18.9586
45	7.4762	9.6912	11.8106	13.7313	15.3878
60	5.9096	7.7255	9.3968	10.9618	12.3092

By plotting the off axis performance as a function of angle, the rate of performance degradation may be visualized as in *Figures 100-104*.

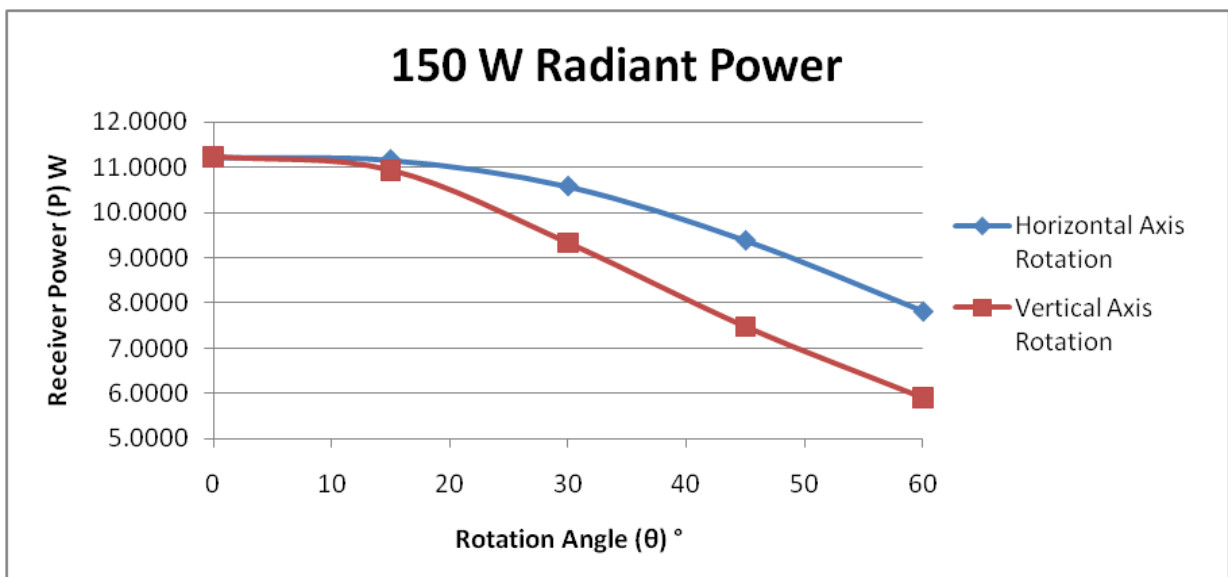


Figure 100: Horizontal and vertical off axis responses at 150 W radiant power

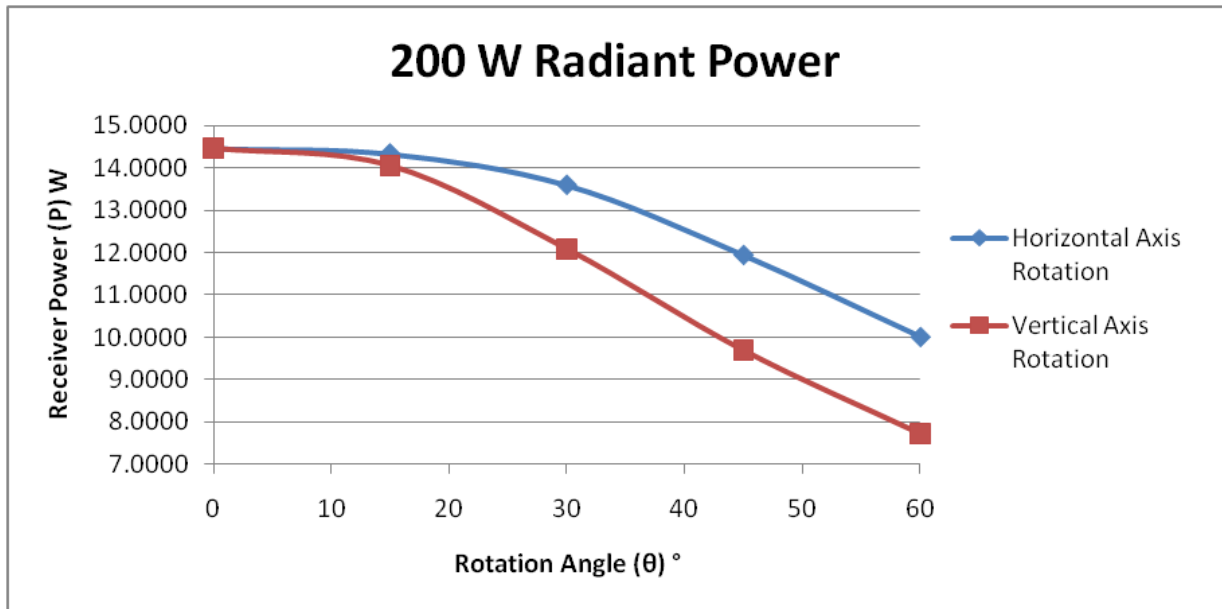


Figure 101: Horizontal and vertical off axis responses at 200 W radiant power

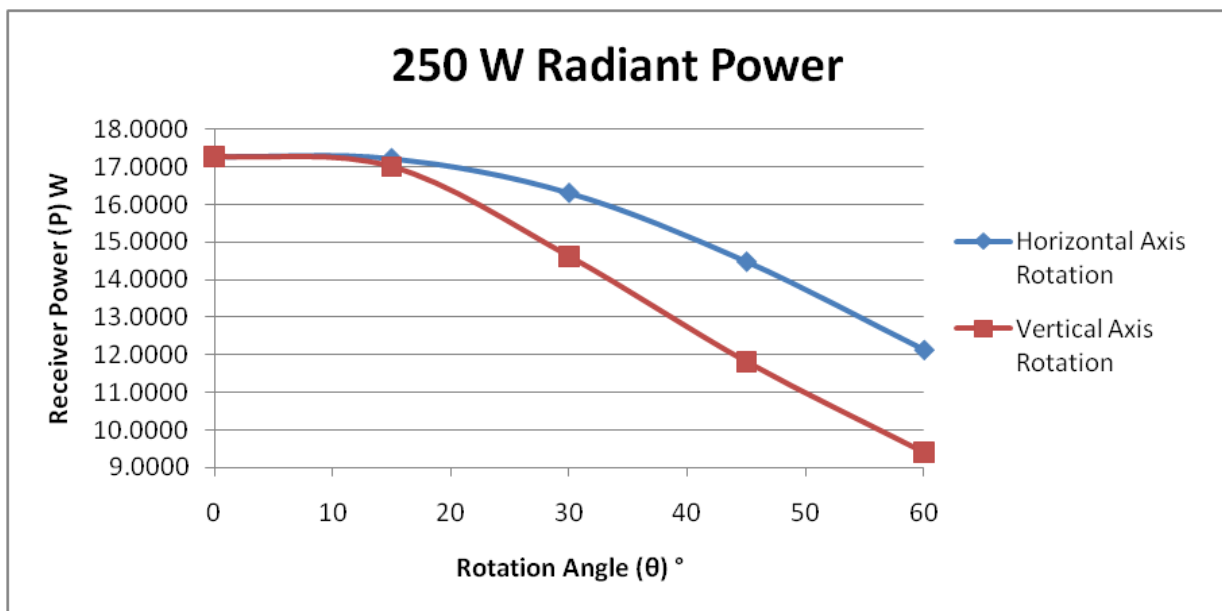


Figure 102: Horizontal and vertical off axis responses at 250 W radiant power

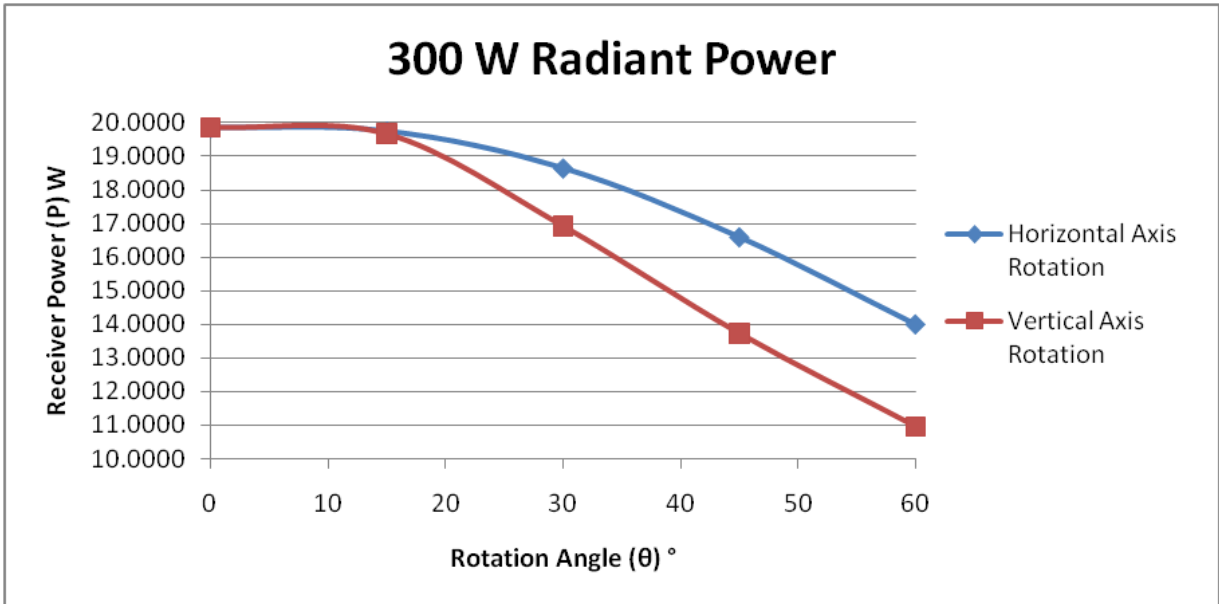


Figure 103: Horizontal and vertical off axis responses at 300 W radiant power

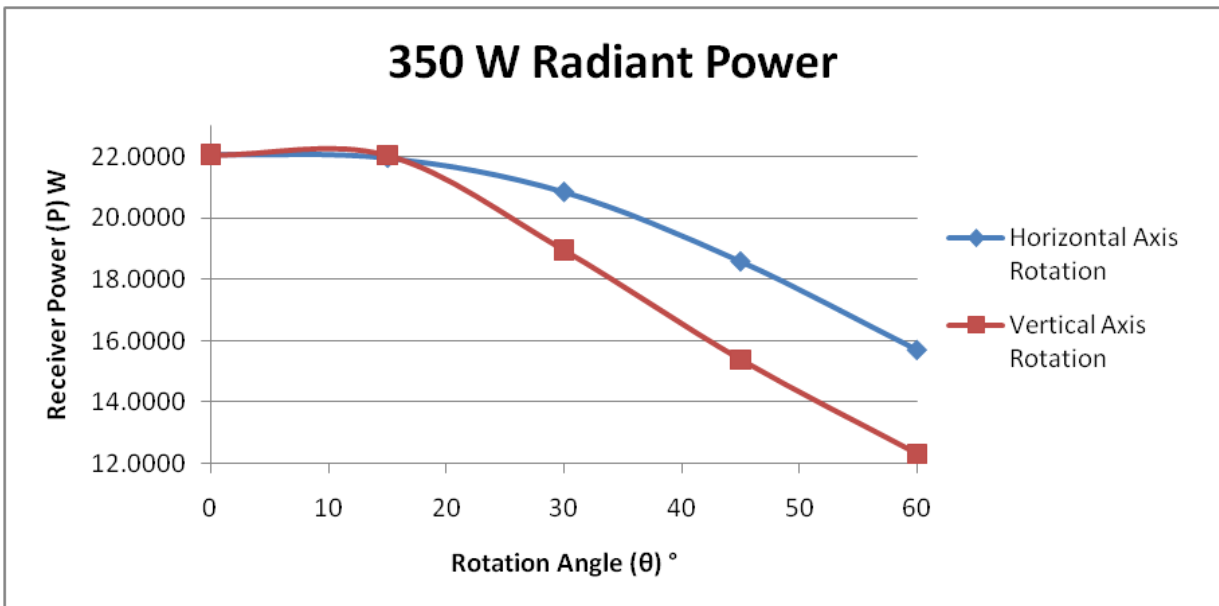


Figure 104: Horizontal and vertical off axis responses at 350 W radiant power

The off axis performance capability of the VMJ technology is very respectable, and a further examination into the data quantifies the result. *Figures 105-107* compare the initial baseline performance curve against the individual 45° rotations.

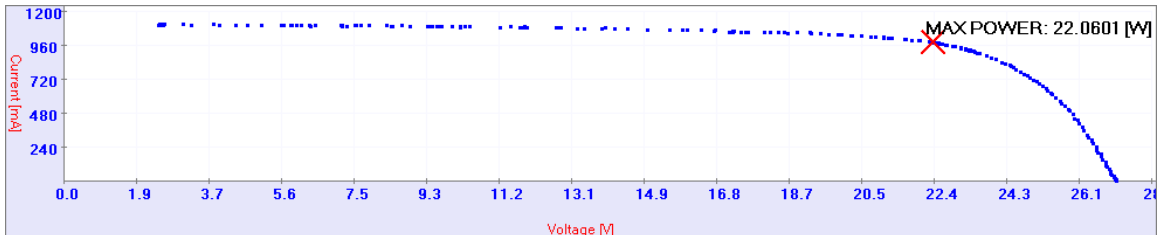


Figure 105: Direct illumination at 350 W

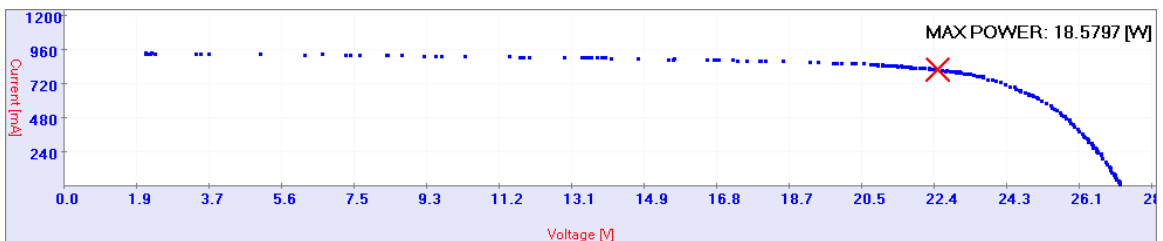


Figure 106: Horizontal axis rotation of 45 degrees

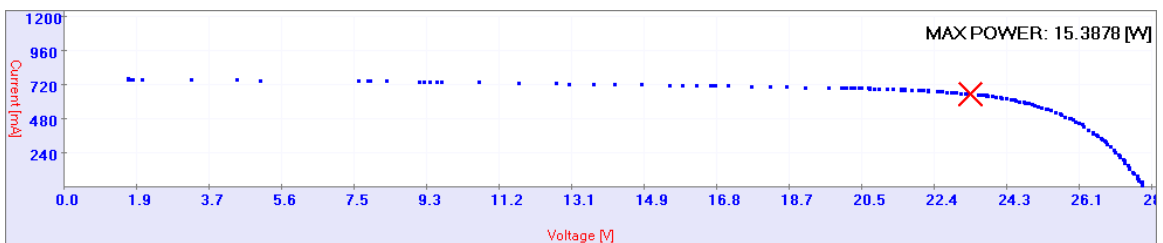


Figure 107: Vertical axis rotation of 45 degrees

During off-axis operation horizontally (45 degree off normal) the performance of the VMJ cells was observed to decrease by only 12% (3.49 W). This relatively minor drop in performance established a wide angle of acceptance when considering potential mission geometries and tracking system metrics.

The results of this test show a tremendous promise toward the potential tracking parameters in an implemented HILPB system, in that only a minimal amount of power is lost at significant levels of off-normal alignment.

4.3 Pulse Modulation

The purpose of this experiment is to investigate the ability for the VMJ cell to respond to a pulsed waveform across a range of intensities, from the low forward-biased threshold to a full 368 watts (the current maximum radiant capacity of the laser source). This is achieved by implementing a modulator into the beam path to provide binary-baseband on-off keying to encode information on the transmitted energy. The modulation is accomplished through active solid-state switching of the output section of the laser, as triggered by an external arbitrary waveform generator through the master digital control system. There are hardware limitations in the performance of the laser during this mode of operation since it is primarily a continuous wave device, and these are manifested in a maximum pulse repetition rate of just over 1 kHz.

To set up a comparison of cell topologies, a standard one sun mono-crystalline silicone photovoltaic cell was mounted to the water cooled receiver, and illuminated with the pulsed 980 nm source.

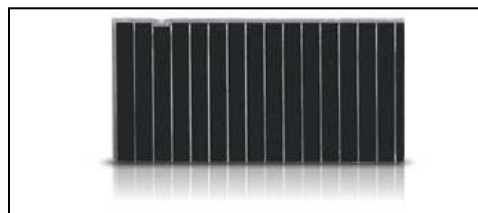


Figure 108: Single (mono) crystalline photovoltaic cell

Figure 109 depicts the external 1 kHz clocking signal, and the resultant laser diode current response as measured indirectly through magnetic induction. It can be seen that the laser diodes exhibit a slew rate in their response, which is measured to average a 2-3 μ s rise time in tracking the external signal.

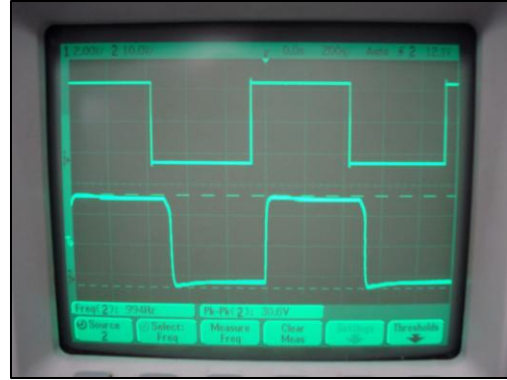


Figure 109: 1 kHz clocking (top) of the laser diodes (bottom)

In attempting to increase the repetition rate by clocking the laser at 10 kHz, it can be seen in *Figure 110* that the achievable output pulses peak at roughly 3 kHz.

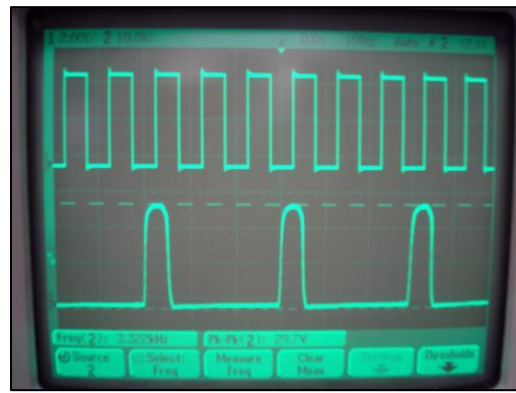


Figure 110: 10 kHz clocking (top) of the laser diodes (bottom)

The laser clocking rate is reduced back to 1 kHz, and the mono-crystalline silicone photovoltaic cell is illuminated with the laser. At intensities greater than 10 W of laser illumination, the cell is observed to rapidly decline in performance due to thermal effects, and so data is collected at this level of output radiance. *Figure 111* shows the zoomed in leading edge, typical output pulse train, and zoomed in trailing edge. It can be readily observed that the mono-crystalline silicone photovoltaic cell is capable of reproducing the 2-3 μ s rise and fall times of the laser pulse, but with a significant amount

of noise present and an output of approximately 500 mV.

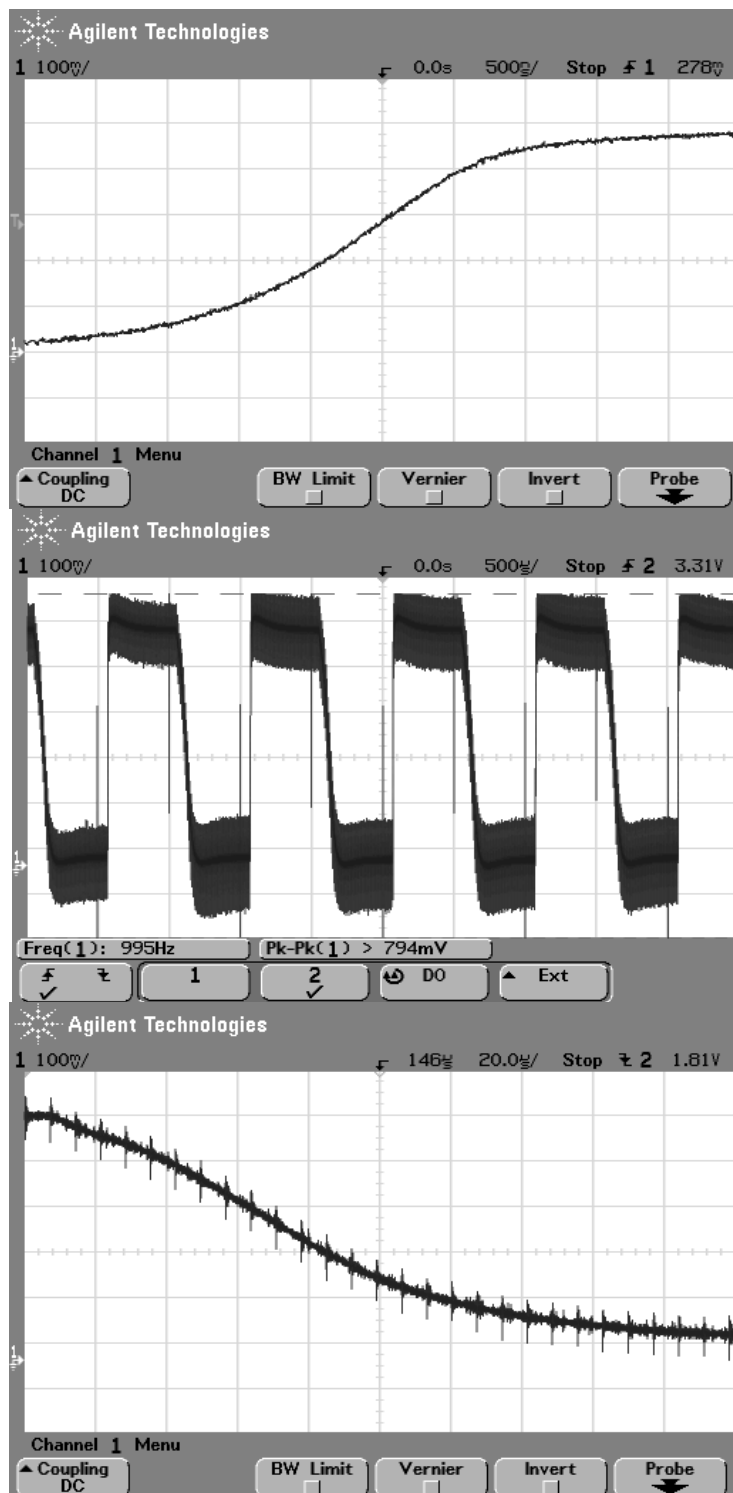


Figure 111: Mono-crystalline silicone photovoltaic cell output under 10 W illumination exhibiting significant noise but good transient responsivity

To get these results, every light in the room needed to be turned off and all bright equipment LEDs had to be covered up, otherwise the floor of the waveform would rise substantially. Also, the laser needed to be operated at a very low intensity, so as not to damage the cell. This leads to a unique benefit of using VMJ's for laser communications in practice since they require a relatively high energy density to become forward biased, and therefore they will offer a large improvement in signal to noise ratio even in bright environments, since these will register as relatively low dark current periods in the cell when compared to typical photovoltaic cells.

Next, a triple junction photovoltaic cell is similarly tested on a water-cooled receiver, as shown in *Figure 112*.

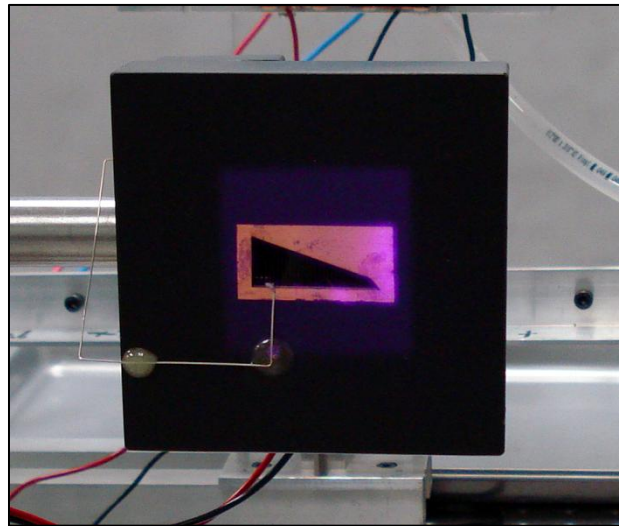


Figure 112: Triple Junction TASC under pulsed illumination

The triple junction cell was able to withstand up to 50 W of radiated power, but greatly distorted the input pulse shape by exhibiting an output rise time of 50 μs . Similar signal to noise performance can be observed, but now with an output voltage of 2.53 V.

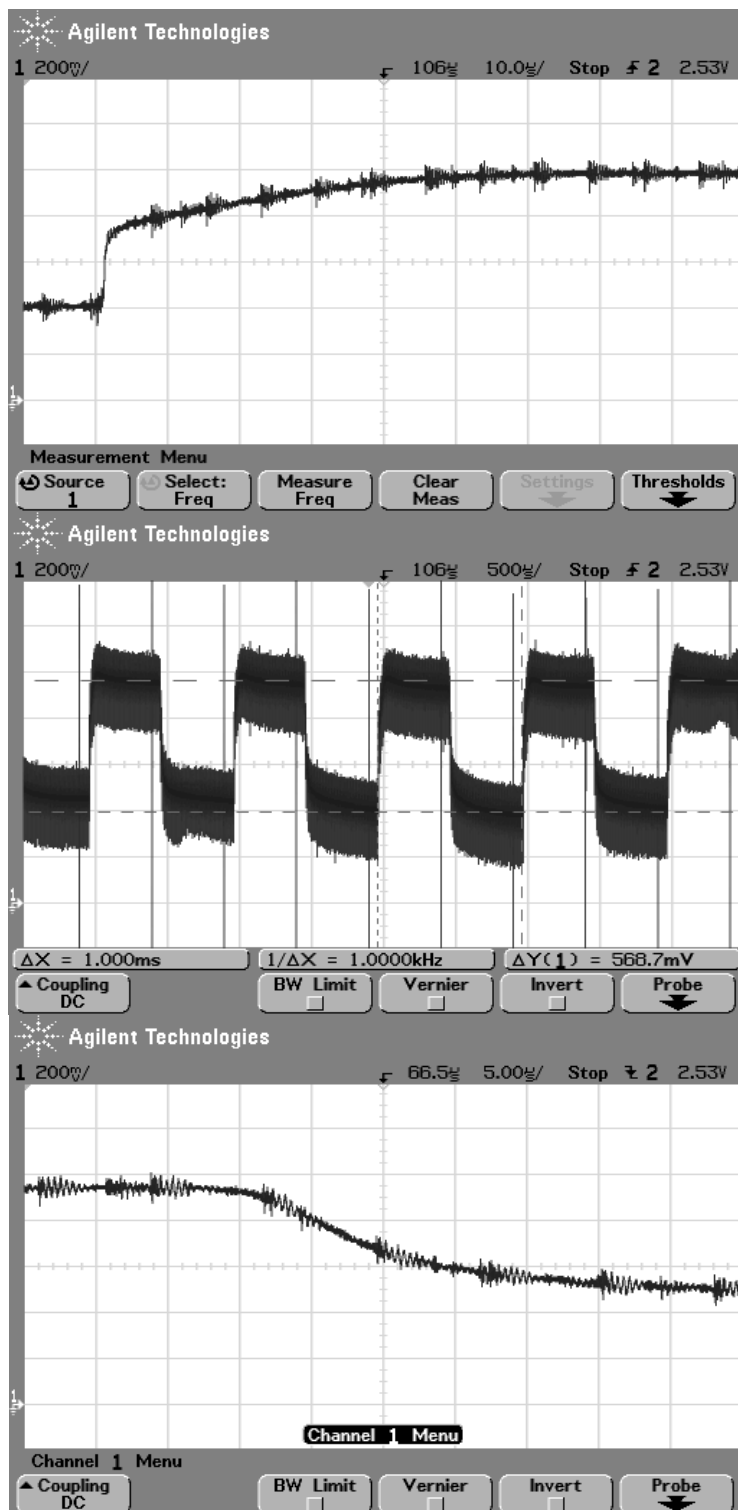


Figure 113: Triple junction photovoltaic cell output under 50 W illumination exhibiting significant signal distortion

During the triple junction test, only one of the three junctions would have been

forward biased from the laser source, and it is likely that the adjacent junctions contributed parasitic losses evident in the pulse distortions. Additionally, the extra junctions create a thermal barrier that limit the overall performance of the cell under conditions of high irradiance.

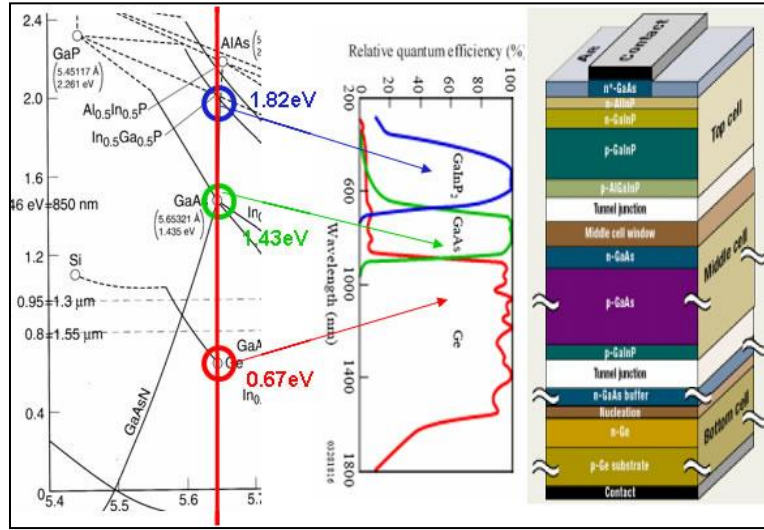


Figure 114: Quantum efficiency versus wavelength for a triple junction cell

For the last part of the test, a water-cooled VMJ receiver is similarly tested as the previous monocrystalline and triple junction cell, as shown in *Figure 115*.



Figure 115: VMJ photovoltaic cell under pulsed illumination

As demonstrated in many previous experiments, the VMJ cell is able to convert a wide range of irradiance levels, and so a series of tests were conducted at increasing

levels of radiated power in *Figures 116-123*.

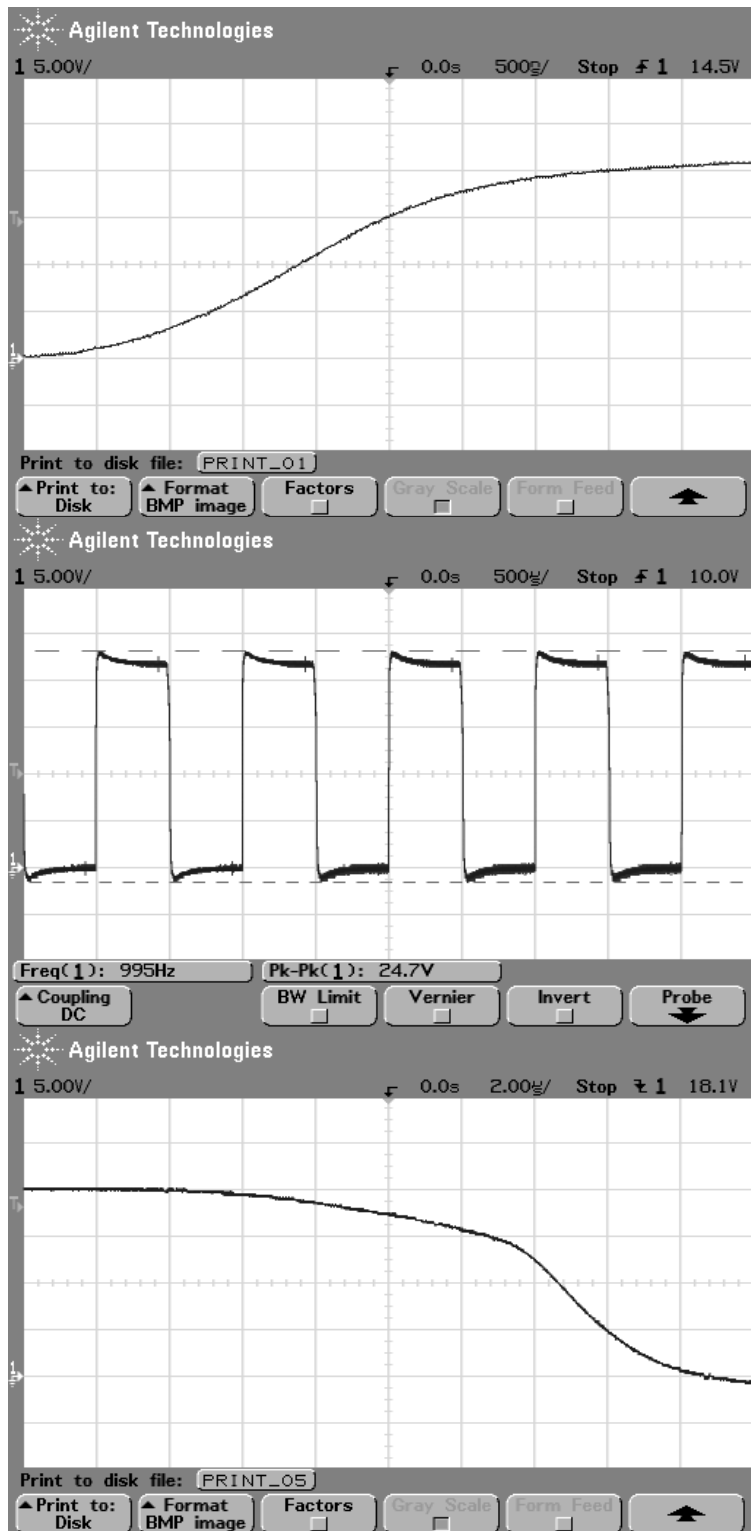


Figure 116: VMJ photovoltaic cell output under 30 W illumination

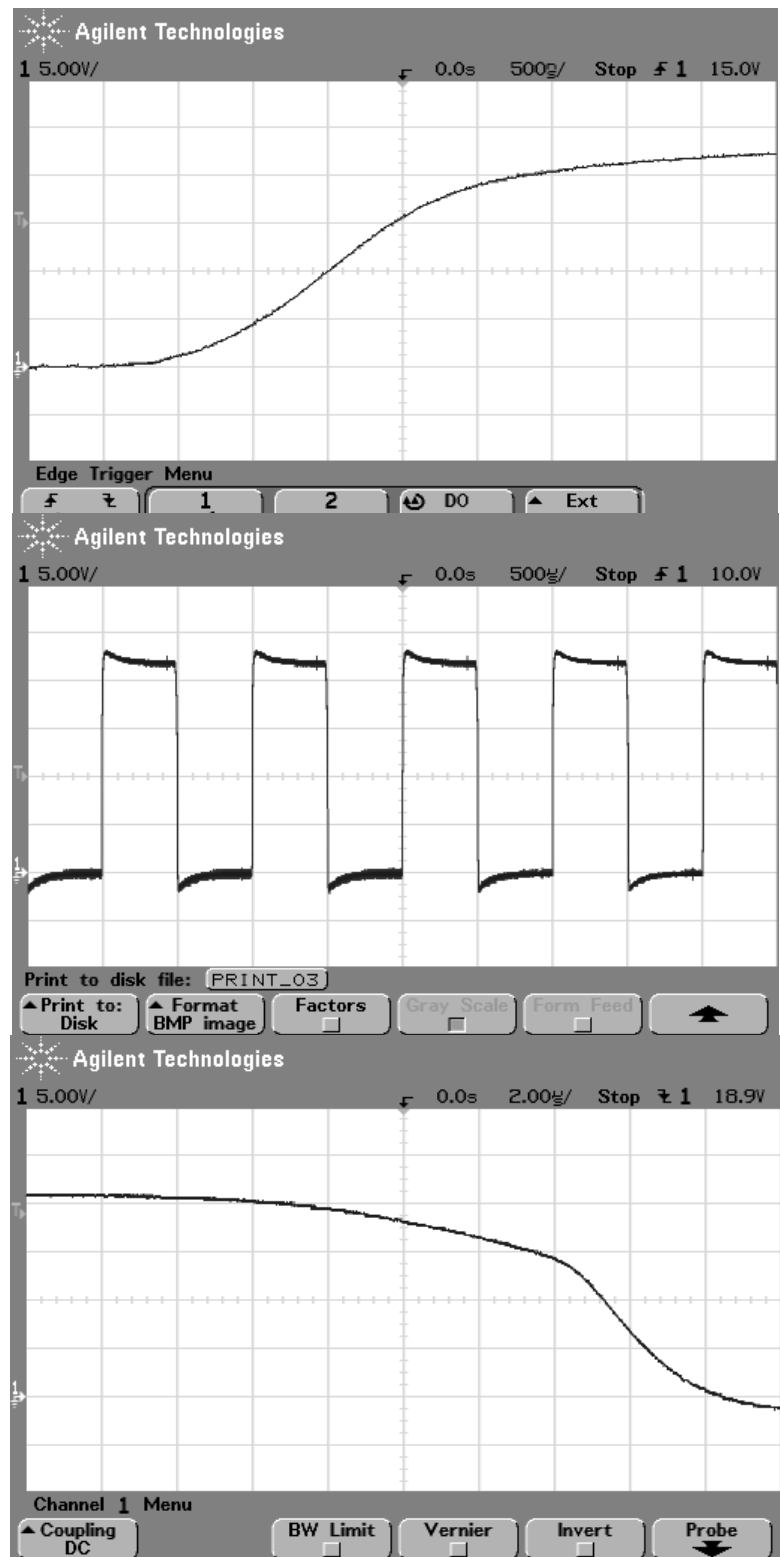


Figure 117: VMJ photovoltaic cell output under 75 W illumination

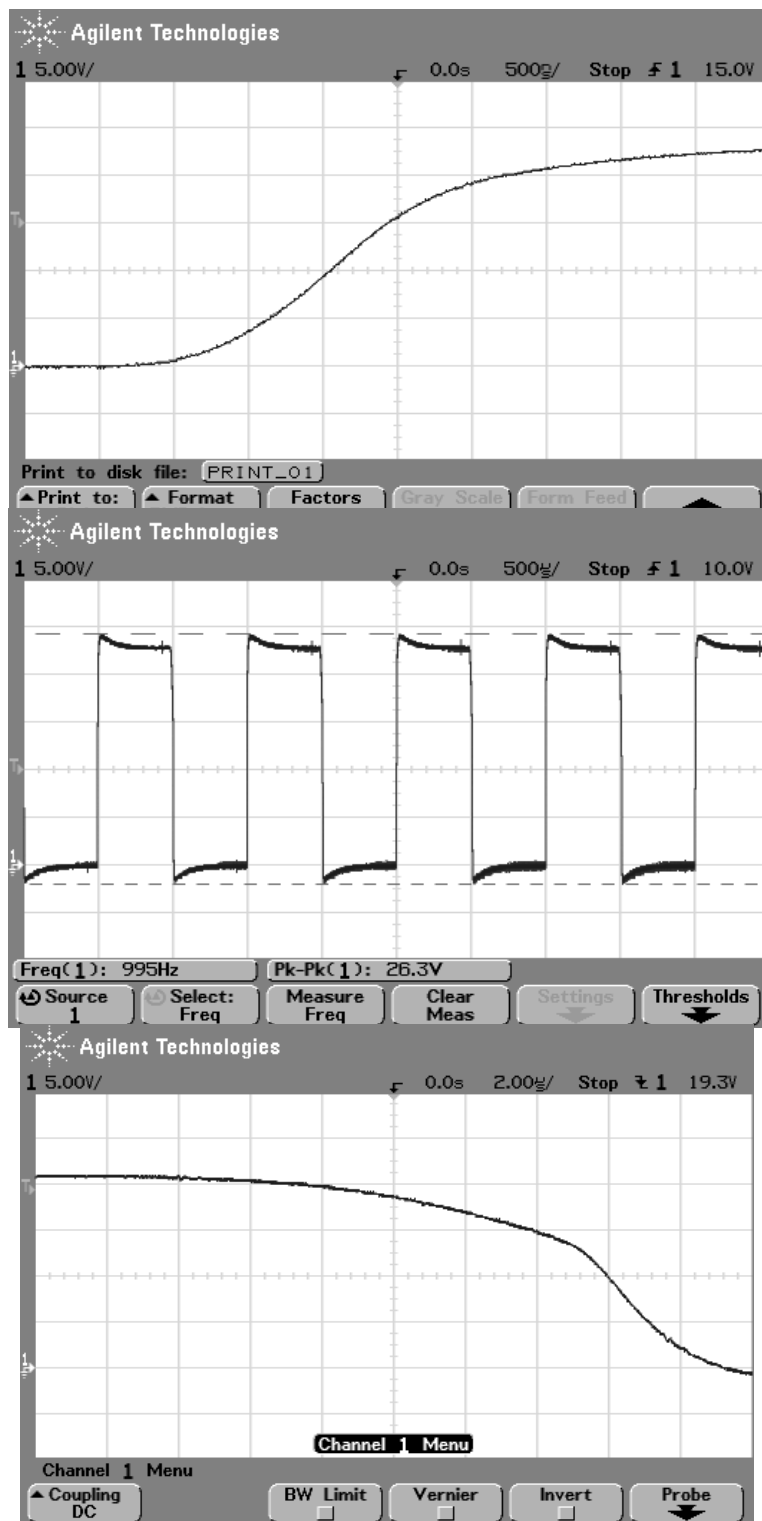


Figure 118: VMJ photovoltaic cell output under 120 W illumination

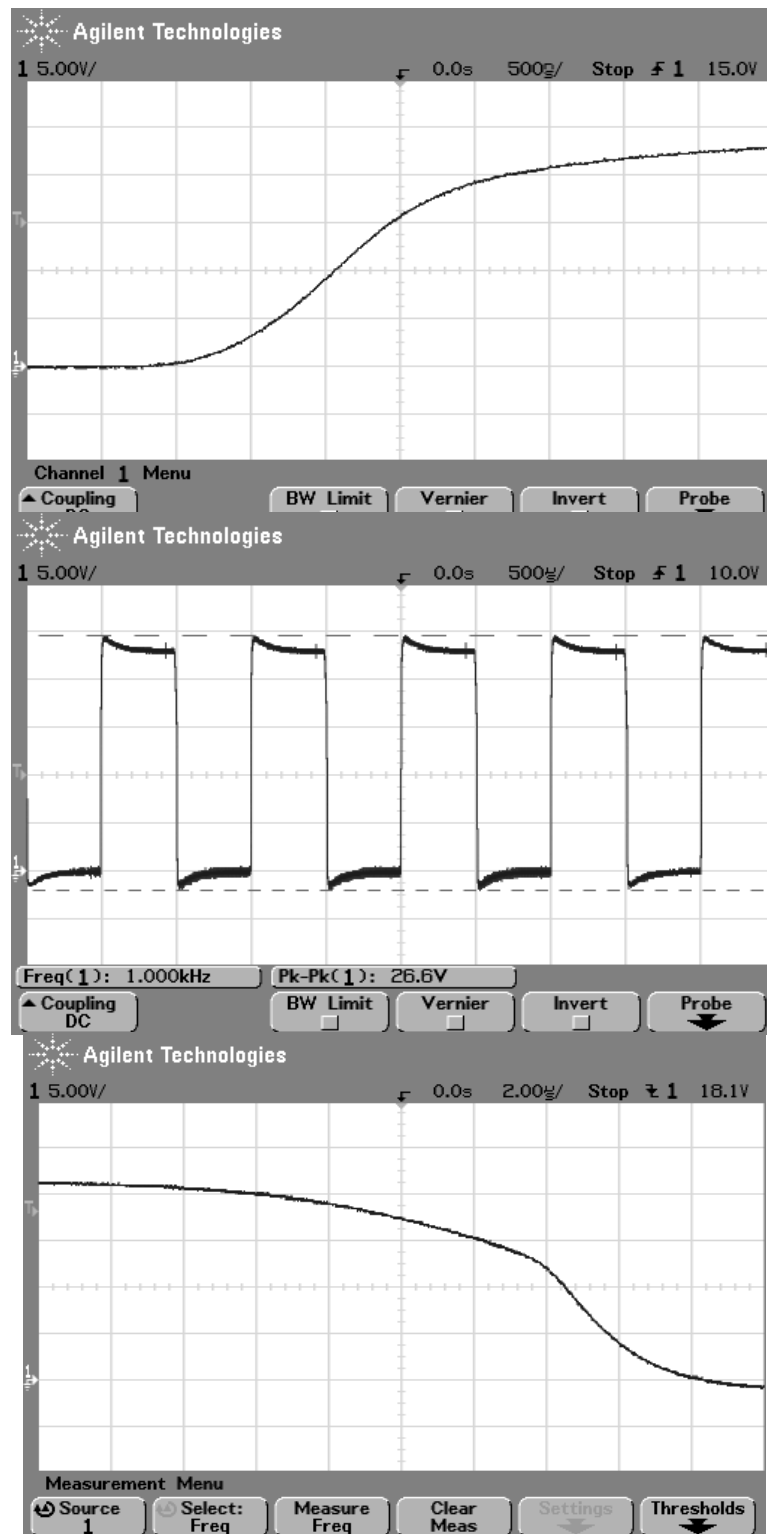


Figure 119: VMJ photovoltaic cell output under 165 W illumination

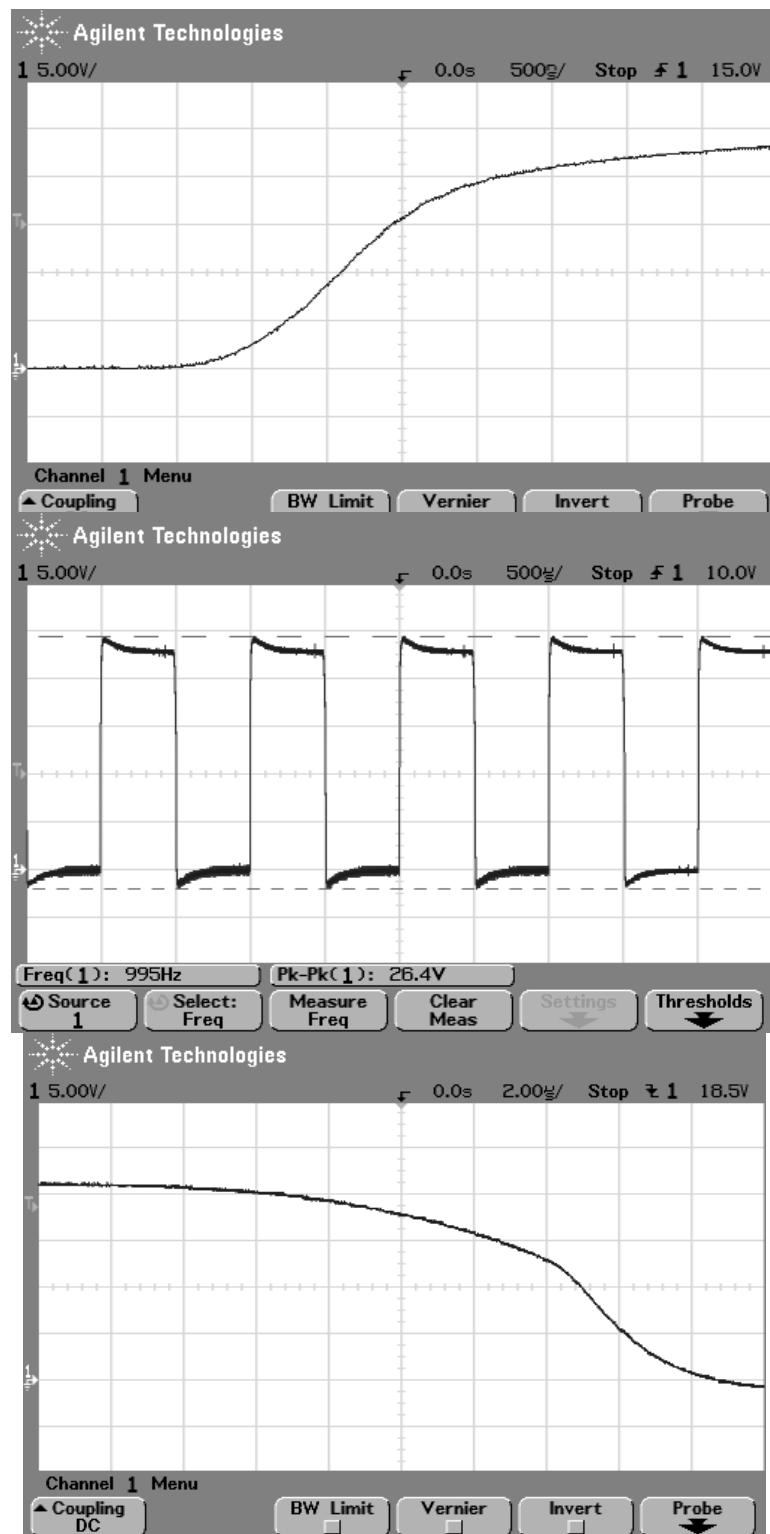


Figure 120: VMJ photovoltaic cell output under 210 W illumination

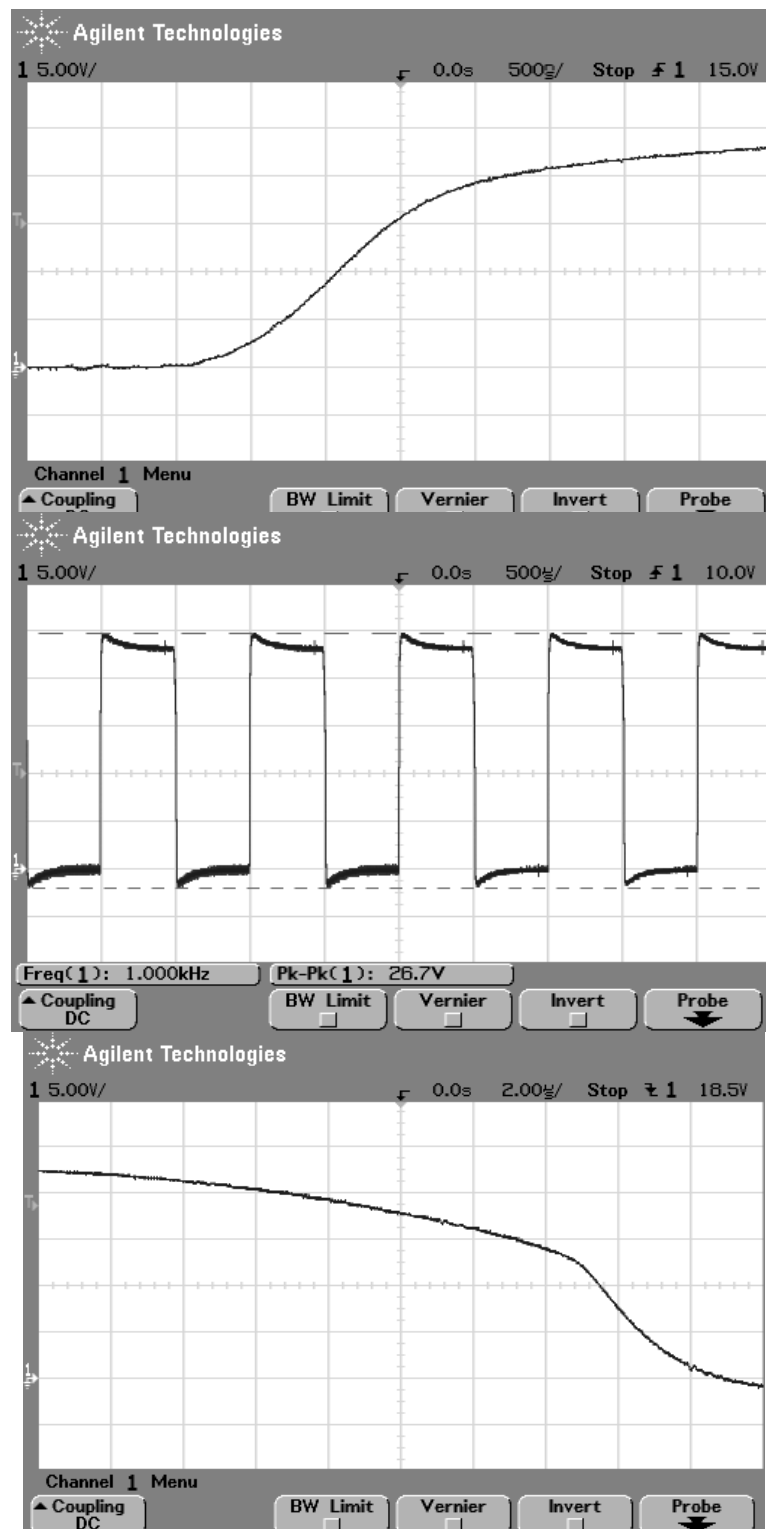


Figure 121: VMJ photovoltaic cell output under 255 W illumination

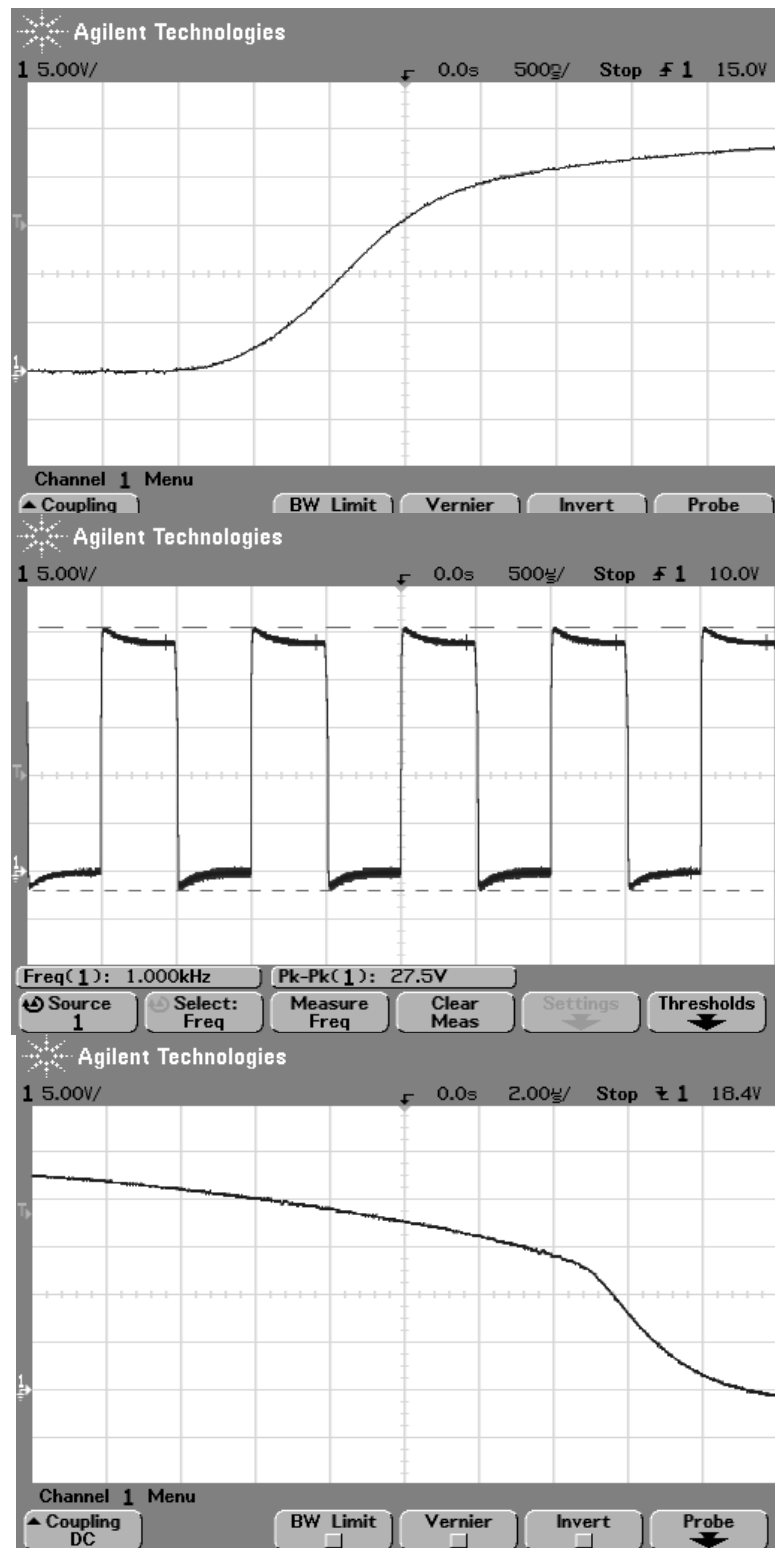


Figure 122: VMJ photovoltaic cell output under 300 W illumination

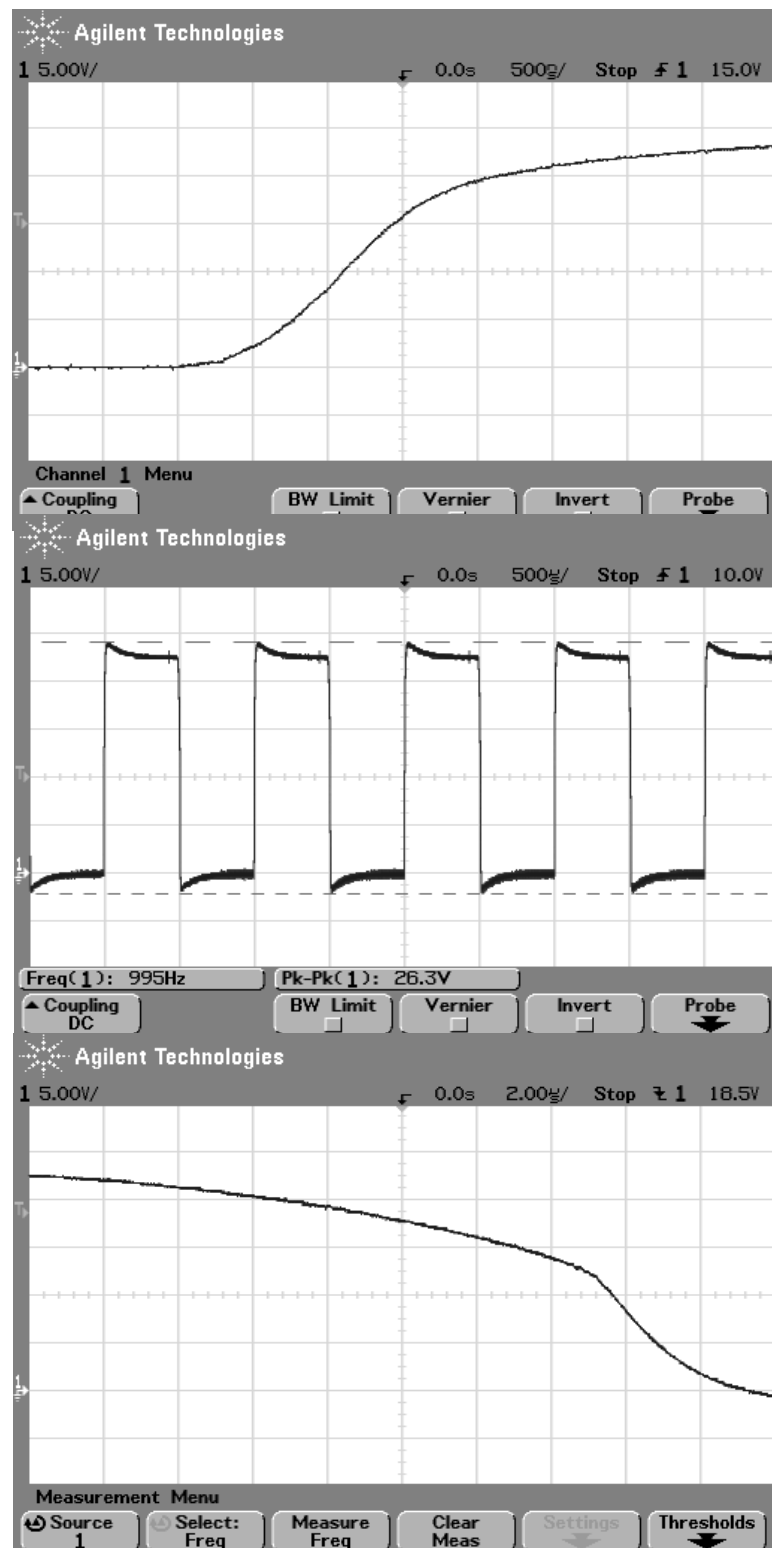
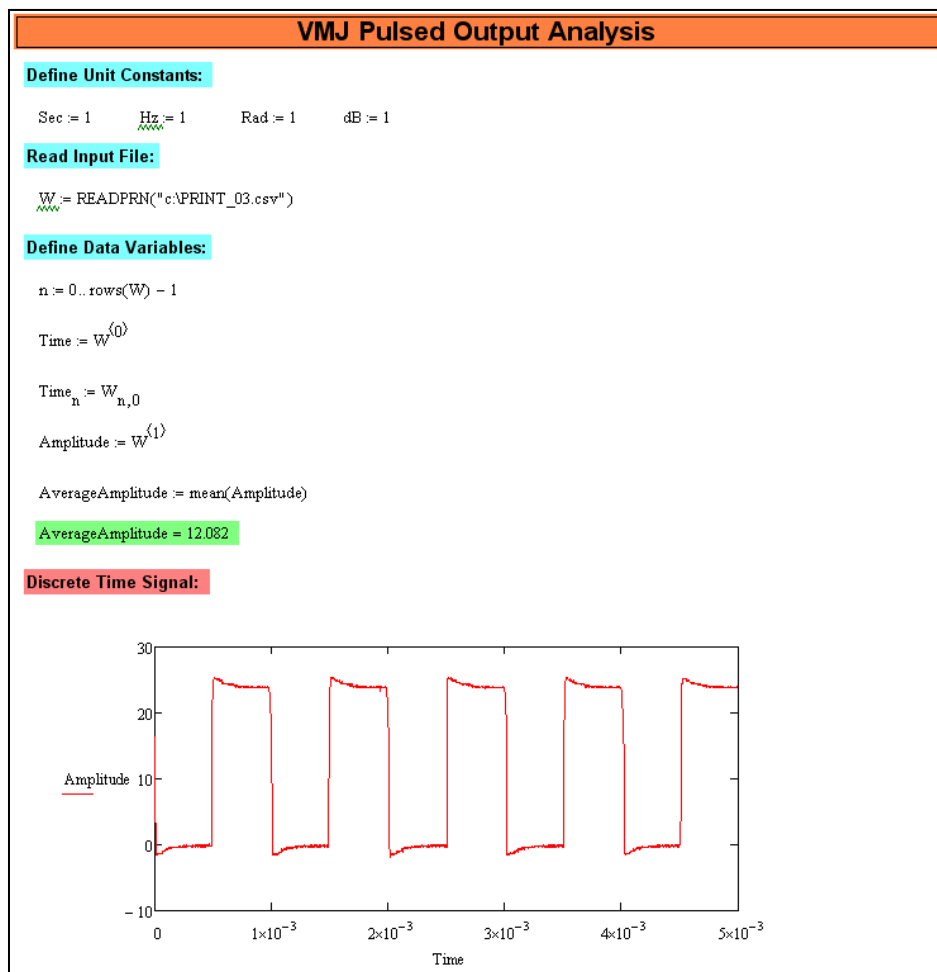


Figure 123: VMJ photovoltaic cell output under 345 W illumination

By analyzing the received pulse train at the receiver, critical aspects for the

feasibility of a HILPB communication system may be inferred. The VMJ cell was able to maintain the 2-3 μ s rise time across the entire operating range of the laser, while also delivering superior signal to noise due to the high voltage output.

To date the only data that exists on the performance of a VMJ cell has been collected during steady state operation with high intensities for the purpose of demonstrating a characteristic I-V curve during such conditions. The ability for the VMJ cell to accurately track a photonic transient serves as an indicator for practical bandwidth expectations for a HILPB communication system, which may also be examined in the frequency domain by computing a Fast Fourier Transformation (FFT) on the received signal in *Figure 124*.



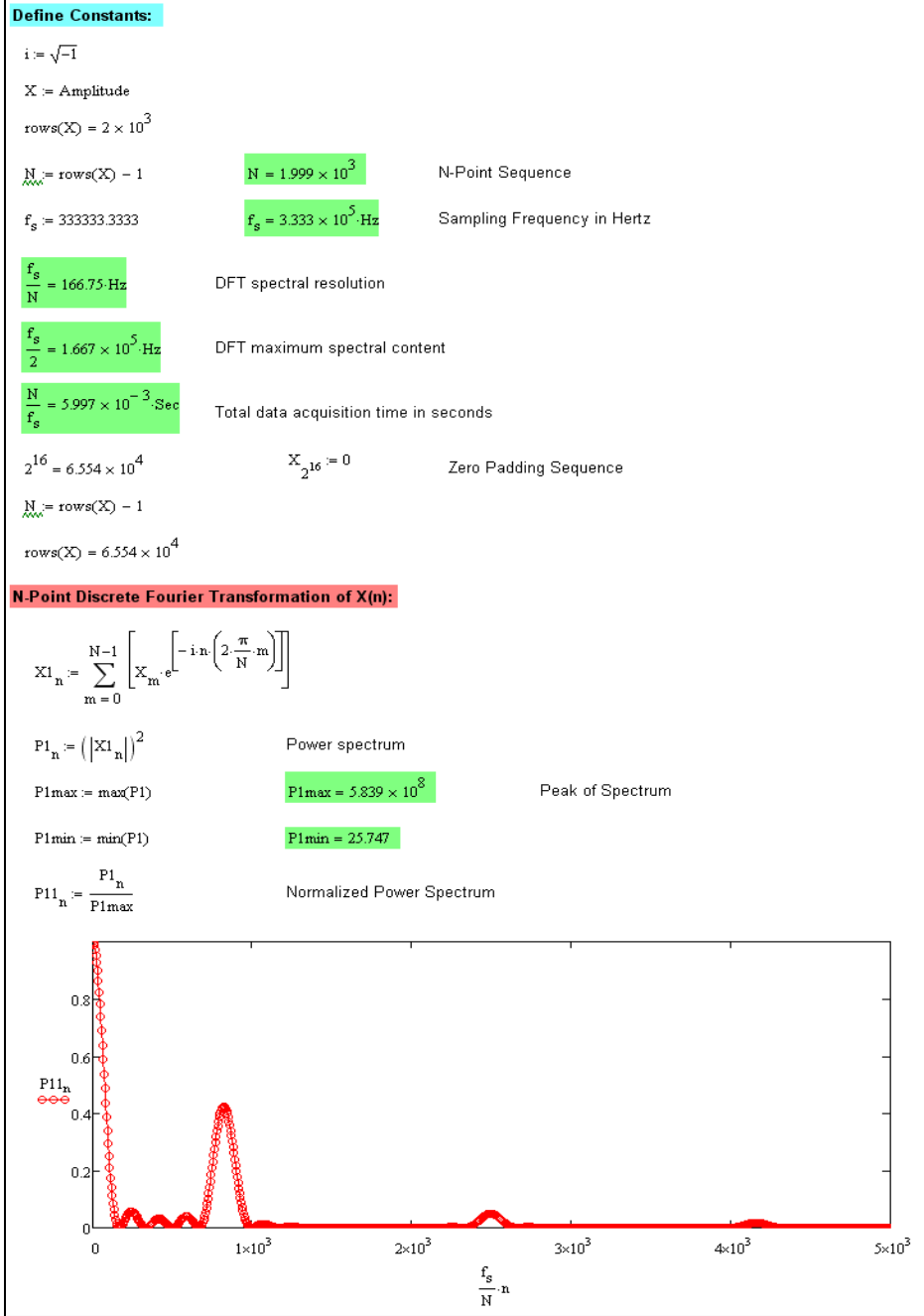


Figure 124: Discrete Fourier Transformation of the VMJ output

In the spectral plot, the DC power component of the VMJ cell delivered to the load may be observed, as well as the pulse train information at 1 kHz. In addition, spectral information representing the rise and fall time of the waveform and the harmonic series is represented.

From the various levels of irradiance, the responsivity (\mathcal{R}) of the VMJ cell may be calculated from the bulk current output and the per-junction illumination, as shown in *Table XI*. From the responsivity values, the external quantum efficiency may be calculated from the relation:

$$EQE = \frac{hv}{q} \times \mathcal{R} \quad (70)$$

Furthermore, the fraction of electron-hole pairs contributing to the photocurrent (ζ) may also be found by:

$$\zeta = \frac{EQE}{(1-\mathcal{R}) \times (1-e^{-\alpha\delta})} \quad (71)$$

Where: R = surface reflectivity (0.073)

α = absorption coefficient (100 cm^{-1})

δ = photodetector depth (0.04699 cm)

The calculated values are also shown in the table as a function of radiant flux. It should be noted that the receiver did experience a thermal increase during the experiment, which may partially influence the corresponding trend of decreased responsivity.

TABLE XI: VMJ Responsivity at increasing irradiance levels

Total Radiant Flux (Φ) W	Irradiance (I) W/cm ²	Flux per Cell (F_c) W	Flux per Junction (F_j) W	Output Current (i) A	Responsivity (R) A/W	External Quantum Efficiency (EQE)	Photonic Efficiency (ζ)	Receiver Temp (T) °C
30	2.5997	1.9279	0.0482	0.03190703	0.6620	0.8375	0.9089	5
45	3.8995	2.8919	0.0723	0.04823289	0.6672	0.8441	0.9159	5
60	5.1993	3.8558	0.0964	0.06455874	0.6697	0.8473	0.9195	5
75	6.4991	4.8198	0.1205	0.07743547	0.6427	0.8131	0.8823	5
90	7.7990	5.7837	0.1446	0.09261162	0.6405	0.8103	0.8793	6
105	9.0988	6.7477	0.1687	0.1085926	0.6437	0.8144	0.8838	7
120	10.3986	7.7116	0.1928	0.1219292	0.6324	0.8001	0.8683	7.5
135	11.6984	8.6756	0.2169	0.1361855	0.6279	0.7944	0.8620	8
150	12.9983	9.6395	0.2410	0.1481425	0.6147	0.7777	0.8439	8.5
165	14.2981	10.6035	0.2651	0.1607893	0.6066	0.7674	0.8327	9
180	15.5979	11.5674	0.2892	0.1761954	0.6093	0.7708	0.8365	10
195	16.8977	12.5314	0.3133	0.1884973	0.6017	0.7612	0.8260	9.3
210	18.1976	13.4953	0.3374	0.1997644	0.5921	0.7491	0.8129	9.7
225	19.4974	14.4593	0.3615	0.2136759	0.5911	0.7478	0.8115	10
240	20.7972	15.4232	0.3856	0.2268975	0.5885	0.7445	0.8079	10
255	22.0971	16.3872	0.4097	0.2404641	0.5870	0.7426	0.8058	10.25
270	23.3969	17.3511	0.4338	0.252421	0.5819	0.7362	0.7989	10.62
285	24.6967	18.3151	0.4579	0.2597792	0.5674	0.7178	0.7789	10
300	25.9965	19.2790	0.4820	0.2749553	0.5705	0.7217	0.7832	10
315	27.2964	20.2430	0.5061	0.2863374	0.5658	0.7158	0.7768	10.75
330	28.5962	21.2069	0.5302	0.2977195	0.5616	0.7104	0.7709	10
345	29.8960	22.1709	0.5543	0.3092166	0.5579	0.7058	0.7659	10
368	31.8891	23.6489	0.5912	0.3225532	0.5456	0.6902	0.7490	10

The transient responsivity of the VMJ cell has been demonstrated across the full available range of radiance levels to prove that there are not any substantial nonlinear signal distortions with the variable envelope. These results can be extended by comparing the VMJ cell transient performance to that of a single and triple-junction photovoltaic cell in the same environment. This comparison exploits the high voltage output of the VMJ cell, which allows for it to provide a better signal to noise ratio since stray photonic scattering would fall below the forward bias threshold. Additionally, the low parasitic loss characteristic of the VMJ cell allows for it to reproduce transients on the order of μ s. This demonstrates a unique superior applicability for a HILPB communications system in hostile environments requiring high SNR.

4.4 Pulsed Power

The final progression of the modulation development is to investigate the impact of power delivery with a HILPB communications system. Although the primary focus of this research is the communications feasibility of the HILPB system, a first-order look at the implications to power transmission is in order. One of the fundamental tasks at the receiver is to condition the impinging photonic energy into separate components: an information signal (or several) and usable energy for power distribution. The previous set of tests were conducted while varying the irradiance of the cells under pulsed conditions and recording any variations in performance. By pulsing the laser, the entire HILPB system may be abstractly modeled as an optically-coupled switched-mode DC/DC power convertor as shown in *Figure 125*, and these sets of data will give insight into its response linearity.

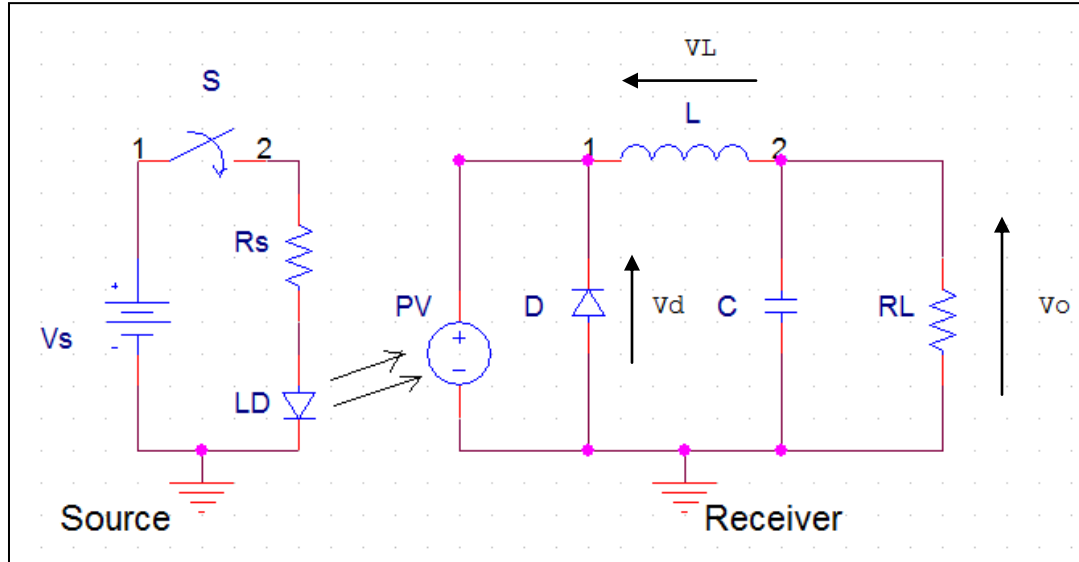


Figure 125: Optically-coupled switched-mode DC/DC power convertor abstraction for the HILPB communications system

For the general purpose of fundamental research, the output component filtering values were chosen to be sufficiently large at 10 mH and 1000 μ F so as to provide adequate signal stability to the data collection system under varying loads. For a specific point design, these values would need to be selected more critically based on the system criteria. *Figure 126* shows the breadboard convertor, data collection electronics and the active variable load.

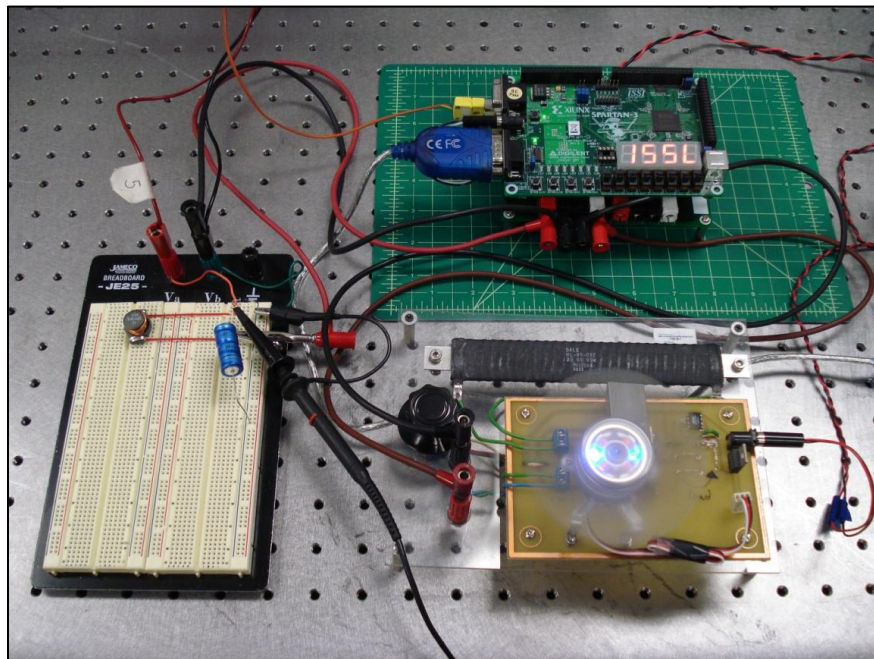


Figure 126: Clockwise from left: breadboard DC/DC convertor, data collection electronics and active variable load

For the first part of the experiment, data is recorded from the peak VMJ cell output across a variable 2-50 k Ω resistive load under laser off conditions. This is done to establish the output contributions (noise) from the broadband ambient light in the laser laboratory. The test was repeated five times, and the average taken of the results. Next, half of the overhead fluorescent lighting was turned off, and the tests repeated. Finally, all of the laboratory lighting was turned off, along with shielding the stray radiance from

the laser controller electronics and computer screens to get a series of dark measurements. These values are shown in *Table XII*.

TABLE XII: Ambient and Dark Current Measurements

Lab	Measurement	VMJ Output			TASC Output			Mono-Silicon Output		
		Current (I) mA	Voltage (E) V	Power (P) mW	Current (I) mA	Voltage (E) V	Power (P) mW	Current (I) mA	Voltage (E) V	Power (P) mW
Full Light	1	0.9718	5.5363	5.3800	9.3690	0.5230	4.9000	11.4504	0.1310	1.5000
	2	0.9258	5.9626	5.5200	8.3658	0.5140	4.3000	12.6866	0.1340	1.7000
	3	1.0178	5.0602	5.1500	9.2843	0.5170	4.8000	12.8788	0.1320	1.7000
	4	1.0408	5.7266	5.9600	9.0586	0.5630	5.1000	11.5702	0.1210	1.4000
	5	1.0178	6.3473	6.4600	9.6774	0.5270	5.1000	12.1212	0.1320	1.6000
	Average	0.9948	5.7266	5.6966	9.1510	0.5288	4.8400	12.1414	0.1300	1.5800
Half light	1	0.9488	5.5756	5.2900	8.3990	0.3810	3.2000	4.8193	0.0830	0.4000
	2	0.9028	6.4135	5.7900	8.8542	0.3840	3.4000	5.9172	0.0845	0.5000
	3	0.9373	5.4946	5.1500	9.9490	0.3920	3.9000	5.9524	0.0840	0.5000
	4	0.9488	6.2607	5.9400	8.5271	0.3870	3.3000	6.0241	0.0830	0.5000
	5	0.9718	4.4764	4.3500	8.6842	0.3800	3.3000	6.0241	0.0830	0.5000
	Average	0.9419	5.6442	5.3161	8.8827	0.3848	3.4200	5.7474	0.0835	0.4800
Dark	1	0.8146	4.1002	3.3400	3.5088	0.0570	0.2000	0.0000	0.0000	0.0000
	2	1.0195	4.1000	4.1800	3.3898	0.0590	0.2000	0.0000	0.0000	0.0000
	3	0.9243	4.1004	3.7900	3.5088	0.0570	0.2000	0.0000	0.0000	0.0000
	4	0.8658	4.1003	3.5500	3.5088	0.0570	0.2000	0.0000	0.0000	0.0000
	5	0.6439	4.1000	2.6400	3.5714	0.0560	0.2000	0.0000	0.0000	0.0000
	Average	0.8536	4.1002	3.5000	3.4975	0.0572	0.2000	0.0000	0.0000	0.0000

In addition to performing the measurements on VMJ cells, the same methodology was also applied to triple-junction TASC and mono-crystalline silicon photovoltaic devices to establish a baseline for low illuminations conditions.

Next, as with the previous experiment a 1 kHz switching frequency was used with the 980 nm laser source and the beam homogenizer at a range of 13 cm to illuminate the 9-cell receiver. Here, a variable duty cycle was employed, and the power output from the receiver was filtered to obtain average power measurements, at the expense of negligible parasitic losses. The first test used a full 100% duty cycle, and obtained a bulk receiver output of 11.3327 W as shown in *Figure 127*.

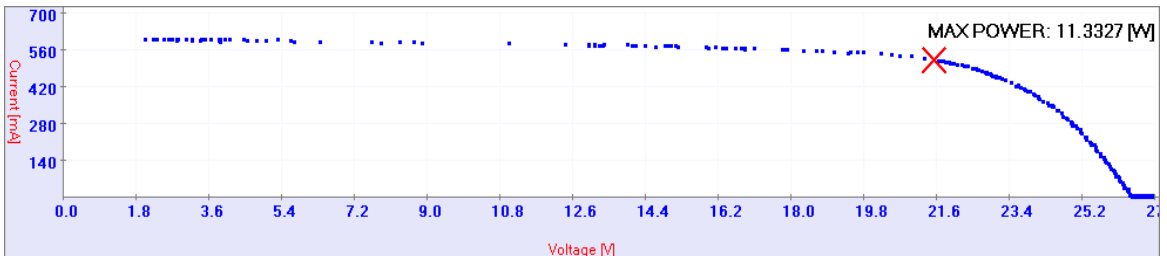


Figure 127: Full duty cycle with 11.3327 W output

The second test used a 50% duty cycle at 1 kHz switching the laser diodes, and obtained a bulk receiver output of 4.8078 W as shown in *Figure 128*.

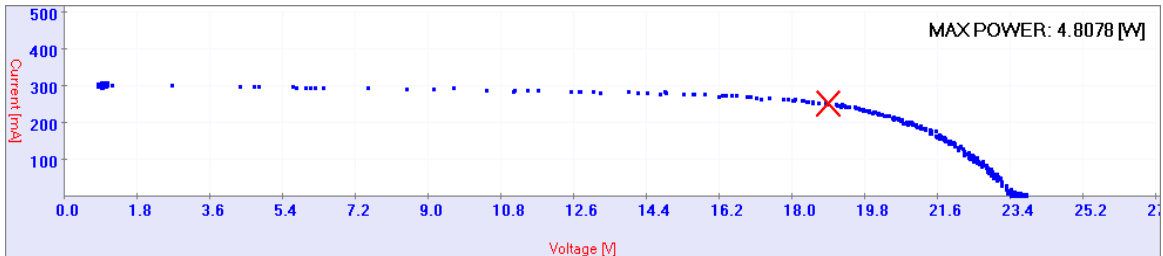


Figure 128: Half duty cycle with 4.8078 W output

The second test used a 25% duty cycle at 1 kHz switching the laser diodes, and obtained a bulk receiver output of 2.6789 W as shown in *Figure 129*.

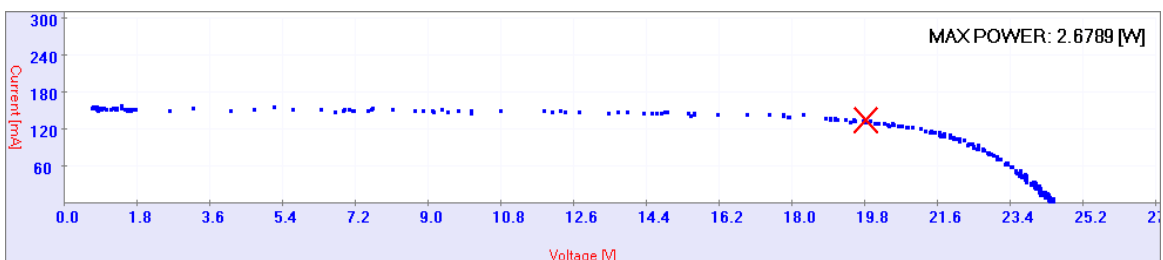


Figure 129: Quarter duty cycle with 2.6789 W output

Plotting these receiver output values against the duty cycle inputs shows a linear relationship, as shown in *Figure 130*.

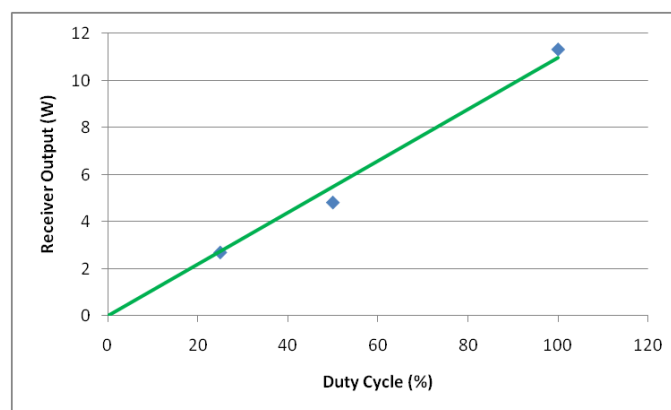


Figure 130: Receiver output versus duty cycle

Although this experiment involved full OOK of the laser diodes, it is important to note that this is not the only way to realize the communications functionality of the VMJ cells. From the dark information in *Table XII* (3.5 mW) and the peak single cell output achieved in *Figure 89* (12.7688), so far the maximum exhibited dynamic range of the photovoltaic device has been 35.6 dB. The maximum capability of this range has yet to be determined, as this is currently limited by the available source power, and could also be dramatically improved with narrowband optical filtering at the receiver.

Typical Pin-Photodiodes would enter their saturation regions with a few milliwatts of optical input power, and begin to slow up their response as they approach this limit. By comparison, the avalanche photodiode (APD) has an even smaller dynamic range, so neither device would be applicable for communications integration with a HILPB receiver unless it had a substantial filter, which would then reduce the low range sensitivity of the detector.

With such a substantial dynamic range available with the VMJ cell for communications, the average beam energy may be maintained sufficiently high to enable adequate power transmission by reducing the dynamic range. This could be accomplished by combining a high power steady-state laser with a lower power modulated source, which would be designed to deliver at least 3 dB of communication margin to the receiver over the specific system's link losses. When comparing this to the contemporary photovoltaic devices, the VMJ cells offer a far superior ability to compensate for background noise and channel losses, while concurrently delivering appreciable power to the receiver.

4.5 Multi-Channel Polarization Optics

The final experiment to be conducted is an investigation into the optical multiplexing capability of the HILPB communications system, by introducing polarization states. In the beam path, the laser is first slightly collimated to allow for a longer optical working field without a reduction in energy density, to accommodate the polarization stages. In general, semiconductor lasers exhibit a predominantly linear polarization state, and so for the purpose of this experiment linear polarization optics are employed. An 8.0 mm linear polarizer is introduced into the beam path at the source, approximately 18.0 mm from the cleaved fiber end, and slowly rotated to reveal the peak polarization axis of the beam while monitoring the average output intensity with a photovoltaic cell (*Figure 131 & 132*). This is done to provide for linearly polarized light at the highest intensity possible at the receiver.

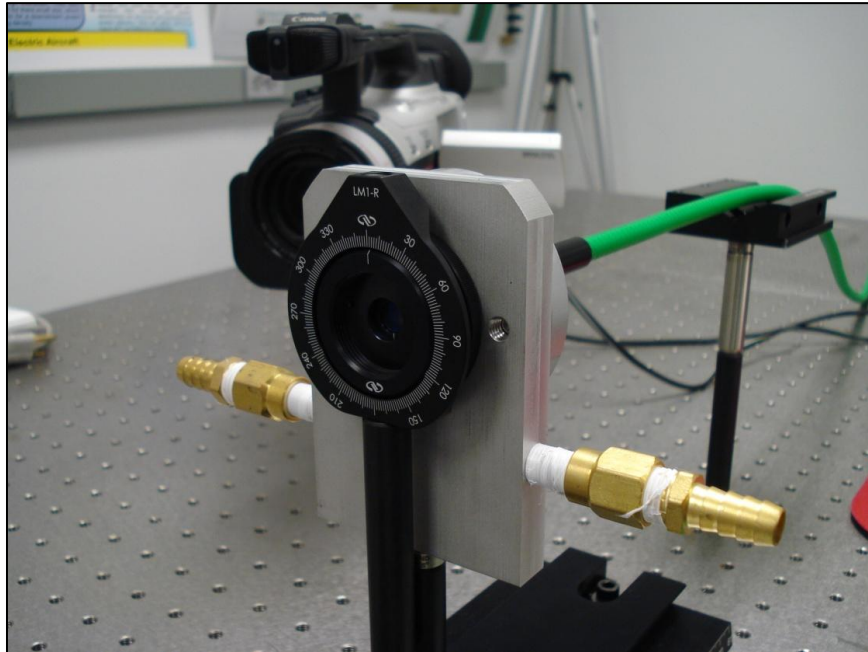


Figure 131: Source optics for the polarization experiment

In this test, the first polarizer may be thought of as an optical communications encoder at the physical layer on the transmitter side of the system. By rotating this optic stage through its full range and monitoring the output at the receiver, the dominant linear polarization axis of the laser may be identified as shown in (*Table XIII*).

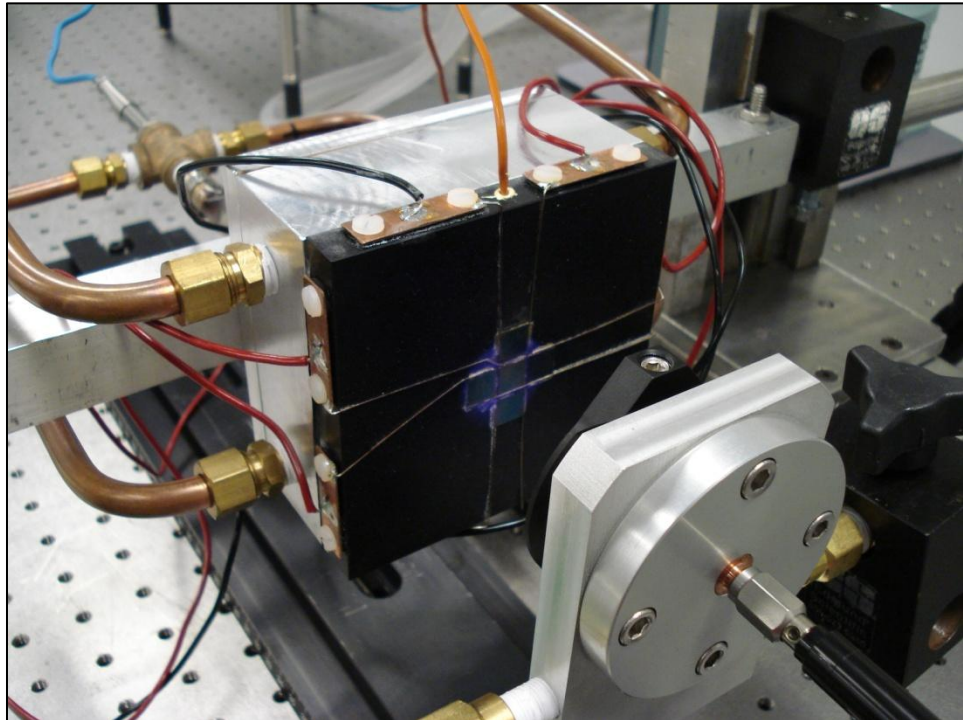


Figure 132: Rotating the linear source optic to characterize the dominant linear beam polarization angle

Next, a second 21.0 mm linear polarizer is placed in front of the receiver, and this optical stage may be thought of as a physical layer optical decoder at the receiver side of the system, as shown in *Figure 133*.

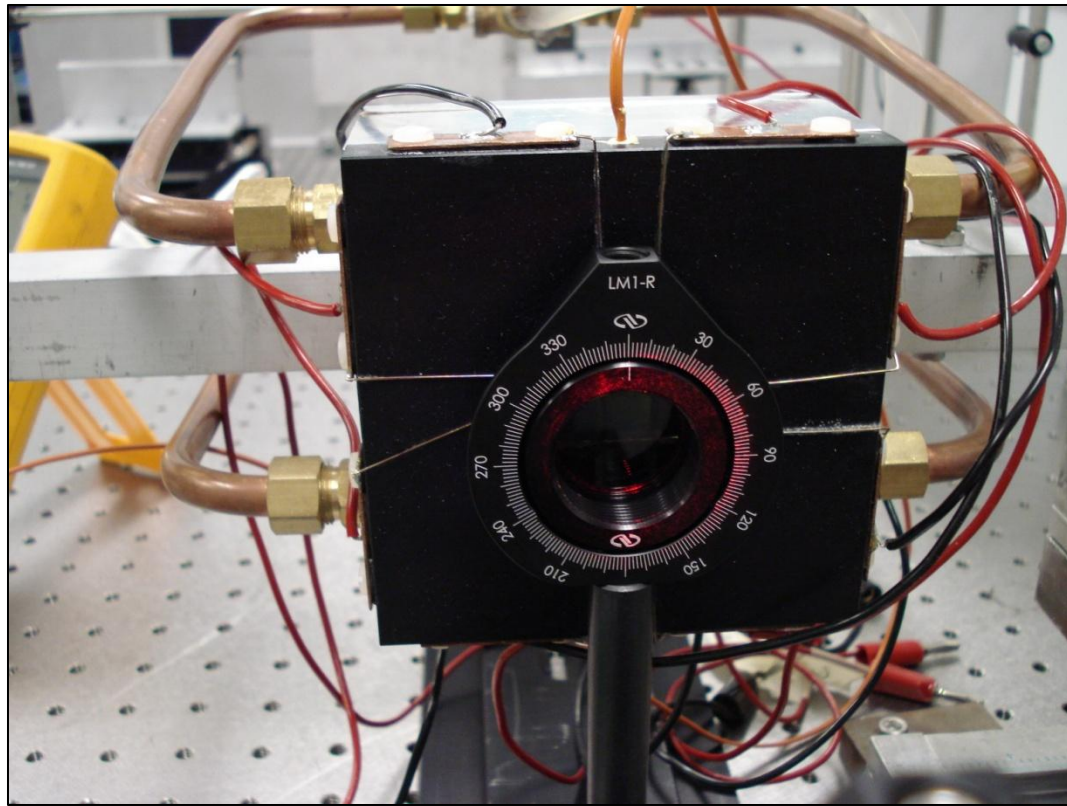


Figure 133: Introduction of the receiver optic for the polarization experiment

By varying the angle of polarization of the second lens the ability for the receiver to successfully decode the signal will vary as per Malus' law, also shown in *Table XIII*. During this experiment, the receiver was maintained at a constant temperature of 23 °C, and under a resistive load of 10 MΩ. The transmittance of the polarizing stages was empirically measured to be 87.9%, which contributes a slight systems loss in implementing this approach.

TABLE XIII: Polarization rotation at both optic stages

Clamp Position (θ) °	Stage 1 Optic			Stage 2 Optic		
	Voltage (E) V	Power (P) μW	Power (P) dBm	Voltage (E) V	Power (P) μW	Power (P) dBm
0	3.83	0.3830	-34.17	5.91	0.5910	-32.28
10	3.91	0.3910	-34.08	6.07	0.6070	-32.17
20	4.51	0.4510	-33.46	6.19	0.6190	-32.08
30	5.01	0.5010	-33.00	6.13	0.6130	-32.13
40	5.11	0.5110	-32.92	5.91	0.5910	-32.28
50	5.47	0.5470	-32.62	5.43	0.5430	-32.65
60	5.94	0.5940	-32.26	4.89	0.4890	-33.11
70	6.06	0.6060	-32.18	4.22	0.4220	-33.75
80	6.25	0.6250	-32.04	3.45	0.3450	-34.62
90	6.54	0.6540	-31.84	2.43	0.2430	-36.14
100	6.52	0.6520	-31.86	1.28	0.1280	-38.93
110	6.40	0.6400	-31.94	0.62	0.0620	-42.08
120	6.33	0.6330	-31.99	0.89	0.0890	-40.51
130	6.05	0.6050	-32.18	1.94	0.1940	-37.12
140	5.66	0.5660	-32.47	3.02	0.3020	-35.20
150	5.17	0.5170	-32.87	4.04	0.4040	-33.94
160	4.76	0.4760	-33.22	5.02	0.5020	-32.99
170	4.32	0.4320	-33.65	5.61	0.5610	-32.51
180	4.40	0.4400	-33.57	5.88	0.5880	-32.31
190	4.23	0.4230	-33.74	6.12	0.6120	-32.13
200	4.36	0.4360	-33.61	6.32	0.6320	-31.99
210	4.57	0.4570	-33.40	6.22	0.6220	-32.06
220	4.93	0.4930	-33.07	5.97	0.5970	-32.24
230	5.43	0.5430	-32.65	5.59	0.5590	-32.53
240	5.74	0.5740	-32.41	4.96	0.4960	-33.05
250	6.12	0.6120	-32.13	4.43	0.4430	-33.54
260	6.29	0.6290	-32.01	3.38	0.3380	-34.71
270	6.49	0.6490	-31.88	2.47	0.2470	-36.07
280	6.41	0.6410	-31.93	1.29	0.1290	-38.89
290	6.28	0.6280	-32.02	0.57	0.0570	-42.44
300	5.96	0.5960	-32.25	0.86	0.0860	-40.66
310	5.73	0.5730	-32.42	1.85	0.1850	-37.33
320	5.36	0.5360	-32.71	3.24	0.3240	-34.89
330	5.14	0.5140	-32.89	4.13	0.4130	-33.84
340	4.94	0.4940	-33.06	5.05	0.5050	-32.97
350	4.51	0.4510	-33.46	5.57	0.5570	-32.54
360	3.93	0.3930	-34.06	5.95	0.5950	-32.25

In *Table XIII*, the first stage was found to be aligned with the predominant axis of the beam at a linear angle of 90° (270° compliment). The peak and minimum values are indicated in boldface, and a plot of the measurements taken at 10° increments may be seen in *Figure 134*.

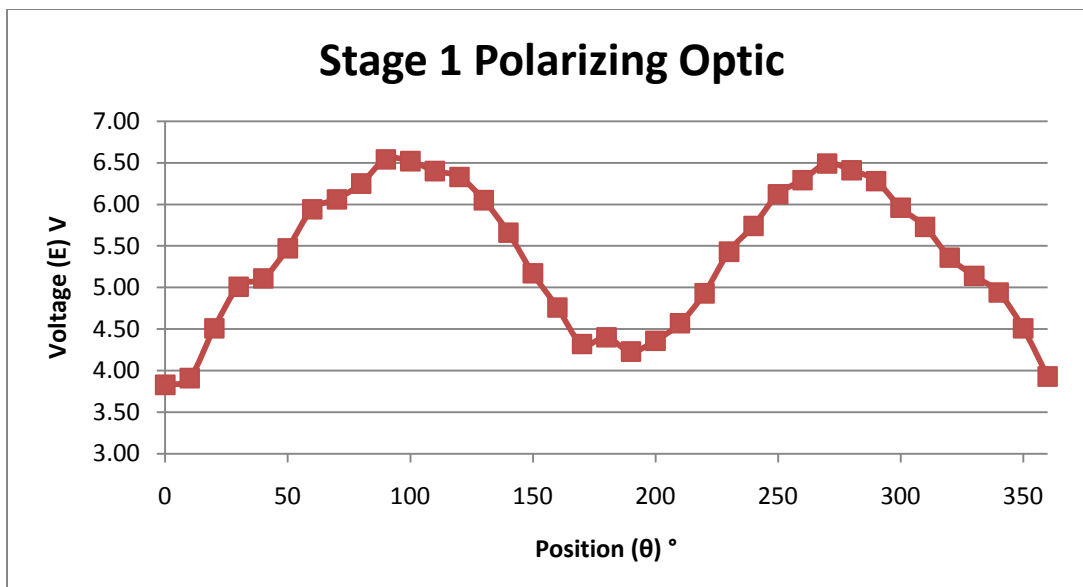


Figure 134: Stage 1 (source) linear polarization rotation

In the second half of the experiment, the first stage was reset and held to the predominant optical polarization axis to peak the output of the laser, and the second (receiver) stage was rotated through its extents. The peak and minimum values are indicated in boldface, and a plot of the measurements taken at 10° increments may be seen in *Figure 135*.

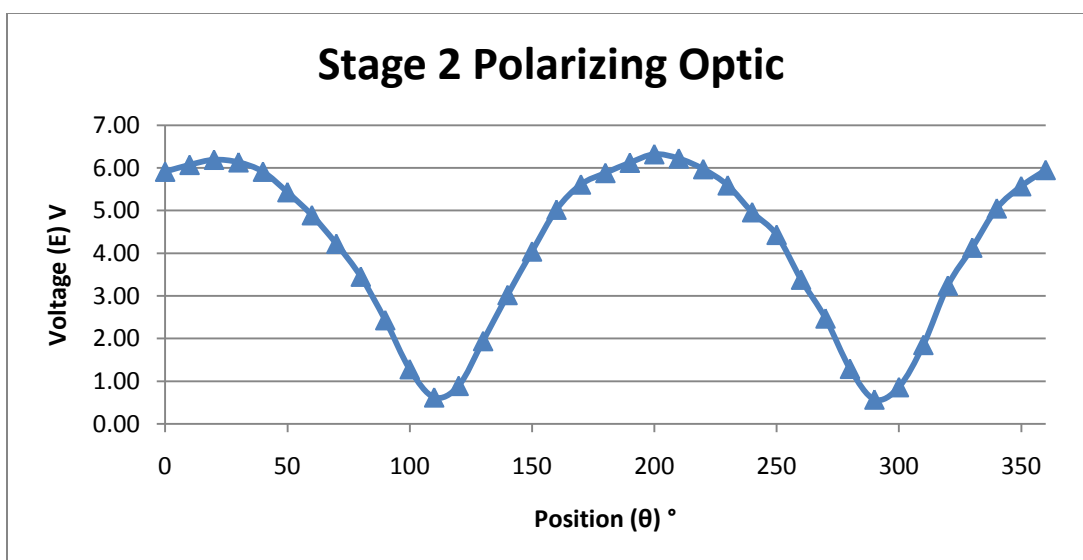


Figure 135: Stage 2 (receiver) linear polarization rotation

By examining the peak and minimum values of the second stage, the polarization extinction ratio (ER) may be calculated by:

$$ER = 10 \times \log \frac{P_{max}}{P_{min}} \quad (72)$$

In this case the ER=10.448 dB, and this generous amount of dynamic range demonstrates the feasibility of employing polarization states into the system. Extending this idea further, the receiver may be partitioned into multiple detection regions, each handling a different alignment of polarization with minimal crosstalk between them. At the transmission side, the laser source may be delivered by multiple separate polarization states, and each state could handle a unique message to be transmitted. These states could traverse down their respective optical paths and combined together in free space as they reach the surface of the receiver. In this way the average received energy could remain high, while also increasing the bandwidth of the system by the number of states employed. Alternatively, polarization states may be used to accomplish PPBM as another way to keep the average power high. Furthermore, the introduction of polarization states adds a further physical layer of privacy and security to the communications system.

In practice it may be preferable to utilize circular polarization states rather than linear, in a similar manner to that of many RF communications systems. In doing so, the orientation constraint between the terminals would be eliminated, and the system would be less sensitive to induced polarization distortions, although it was noted during the SILEX experiment that the atmospheric polarization errors at the Canary Islands were less than what was induced from the system optics.

4.6 Link Budget and Applicable Systems

By utilizing variations of Frii's transmission equation [59] and geometric optics, an embedded link budget worksheet may be constructed for a GEO to ground transmission. In this example system, a one micron source is utilized to return scientific data to a ground based 0.5 m telescope. This case-study system depicts the typical atmospheric loss and background radiance parameters that are encountered with such a link, and also employs a PPM scheme to gain approximately overall 6 dB, leaving a healthy available link margin of 8.5 dB.

Optical Communications Link Budget					
Parameter	Expression	Value	Units	Gain	Units
Optical Space Flight Transceiver Characteristics					
Wavelength (λ)		1064	nm		
Laser Transmitter Average Optical Power (P_T)		0.5	W	-3.01	dBW
Transceiver Aperture Diameter (D_T)		10	cm		
Transceiver Aperture Far-Field On-Axis Gain (G_T)	$G_T = \frac{4\pi A}{\lambda^2}$			109.40	dB
Beamwidth (Θ_s)	$\Theta_s = \frac{2.24\lambda}{D_T}$	23.83	μrad		
Transceiver Efficiency (coupling, reflection, refraction, scattering) (L_T)				-3.46	dB
Pointing Loss (uncompensated jitter and pointing bias) ($L_{p,T}$)				-0.19	dB
Equivalent Isotropically Radiated Power (EIRP)	$EIRP = G_T + L_T + L_{p,T}$			102.7394604	(dBW)
Optical Channel					
Range Between Transmitter and Receiver (R)		35,786	km		
Range Between Transmitter and Receiver (R)		0.000239215	AU		
Range (l_m)	$l_m = 8.317R$	0.00	light minute		
Illuminated Footprint Diameter (d_{beam})	$d_{beam} = 2R \tan(0.5\theta_s)$	0.85	km		
Illuminated Footprint Area (a_{beam})	$a_{beam} = \pi(0.5d_{beam})^2$	571051.4841	m ²		
Total Signal Power at Earth distance (P_{beam})	$P_{beam} = P_T + L_p + L_A$	0.41	W	-3.92	dB
Signal Irradiance at Ground Receiver (E)	$E = \frac{P_{beam}}{a_{beam}}$	710059.50	pW/m ²		
Free-Space Loss (L_s)	$L_s = \frac{\lambda}{4\pi R^2}$			-292.5152234	dB
Space Plasma Attenuation Due to Compton Scattering (L_p)				0	dB
Earth's Atmospheric Attenuation (L_A) within 30° zenith				-0.91	dB
Earth Transceiver(s) System Characteristics					
Ground Receiver Diameter (D_R)		50	cm		
Ground Receiver Obscuration (b)		12	cm		
Obscuration Ratio (g)	$\gamma = \frac{\pi(0.5D_R)^2}{\pi(0.5b)^2}$	0.0576			
Ground Receiver Aperture Gain (G_R)	$G_R = \frac{4\pi A}{\lambda^2} + (1 - \gamma^2)$			123.36	dB
Ground Receiver Efficiency (L_R)				-2.14	dB
Focal Plane Loss (spatial filtering & tilt/tip compensation) (L_{WF})				-0.91	dB
Total Collected Optical Signal Power at Detector (P_R)	$P_R = EIRP + L_s + L_p + L_A + G_R + L_R + L_{WF}$	91.81137149	nW	-70.37	(dBW)
Detection					
Photon Flux Incident on Detector (I_s)	$A_s = \frac{\lambda P_R}{hc}$			116.91	dB-ph/sec
Photon Detection Efficiency (PDE) (β)		74.99	%	-1.25	dB
Detected Average Signal Power (P_{RD})	$P_{RD} = P_R + \beta$	68.84881583	nW	-71.62103525	(dBW)
Detected Average Signal Photons (n_s)	$n_s = \lambda_s + \beta$			115.66	dB-ph/sec
Background Parameters Within Field of View (FOV)					
Sky Radiance (W/cm ² /sr/um)		2.70E-03	W/cm ² /sr/um		
Mars Radiance (W/cm ² /sr/um)		1.46E-03	W/cm ² /sr/um		
Stray and Scattered Light Radiance (W/cm ² /sr/um)		9.65E-04	W/cm ² /sr/um		
Nominal Fried parameter-atmospheric coherence diameter (r_o)		21.5	cm		
Filter Noise Equivalent Bandwidth (NEB)		0.2	nm		
Detector Dark Noise (cps)		4.00E+04	cps		
Incident Noise Photons (I_b)		9.59E-05	W	57.1032	dB-ph/sec
Detected Average Noise Photons (n_b)	$n_b = \lambda_b + \beta$			54.96322113	dB-ph/sec
Signaling Efficiency					
Desired Data Rate (D_{rate})		112500	Mbps		
PPM slots per frame (M-ary)		32	slots		
Duty Cycle (D)	$D = 1/M$	0.03125			
bits per frame (k)	$k = \log_2(M)$	5	bits		
Turbo code Forward Error Correction (FEC) rate		0.5			
Code Overhead (periodic symbol insertion)		3.5	%		
Slot Width (T_s)	$T_s = \frac{\log_2 M}{D_{rate} M}$	0.00	ns		
Average Detected Signal Photons per Pulse/Slot (n_s)	$n_s = \beta \lambda_s T_s$			-6.073697635	dB-ph/pulse
Average Detected noise per slot time (n_b)	$n_b = \beta \lambda_b T_s$			-66.77513066	dB-ph/slot
Max Theoretical Channel Efficiency for 64-ary PPM (C)	$C = \log_2(M)$			6.989700043	dB bits/ph
Performance loss due to Additive Noise (dB)				-0.78	dB
Performance loss due to code rate (dB)				-1.38	dB
Code Gap Distance from Capacity (dB)				-0.3	dB
Receiver/Decoder Implementation Loss (dB)				-1.02	dB
Required signal (p)	$P = \frac{1}{C - L_{other}}$			-3.509700043	dB-cts/bit
Detected signal (p_D)				4.998402061	dB-cts/bit
Link Margin (M)	$M = p_D - p$			8.508102105	dB

Figure 136: Optical communications link budget

It is important to note that in estimating such systems, nominal loss values are used that usually represent a cumulative distribution function (CDF) generated from empirical data, such as a atmospheric opacity value for a 95% clear sky. Such values are in general sufficient for scientific data return, especially when spatial diversity is an architectural option. For critical systems involving control and/or tactical time sensitive information, the robustness of the link will become a primary performance metric.

Referring to the MODTRAN results, it is shown that during periods of fog, rain or snow the atmospheric attenuation value may range from 0.9-6.9 dB per km, and cumulous clouds would present another 17-156 dB of attenuation depending on their thickness which would quickly eliminate the available margin and break the downlink. Dependable terrestrial crosslinks through these conditions would be impossible unless sufficient radiated power was available alone with detectors that could handle the large dynamic fluctuations in irradiance. The VMJ technology, with its demonstrated dynamic range of 35.6 dB under modulated conditions would be able to greatly enhance the operating envelope of a forward link optical communications system under significant and varying channel disturbances.

By employing a return sensor at the remote platform, asymmetrical bidirectional communications may also be achieved using only one laser and telescope. Modulating Retro-reflector (MRR) devices can be employed to enable high speed free space optical communication links between the source and other potential resource constrained remote platforms. This technology promises to eliminate the laser terminal and associated gimbaled pointing and tracking system at the payload end of the link, thus reduces the SWaP requirements without sacrificing performance and greatly reduces the tracking

requirements at the source station.

The MRR devices redirect an incoming CW beam back to the source within an acceptance angle of roughly 60° , modulating the return beam with an electro-optic shutter at rates exceeding 10 Mbps. The MRR devices feature a small size (<10 cm), low mass (<10 gm) and are energy efficient (<500 mW). Such a device could easily be powered by harvesting energy from the interrogating HILPB system. Because of the round trip distance of the photonic energy, systems utilizing the MRR technology experience a range-to-the-fourth loss back at the source platform detectors. In the high radiant power scenarios such as with HILPB, these losses would not pose a problem.

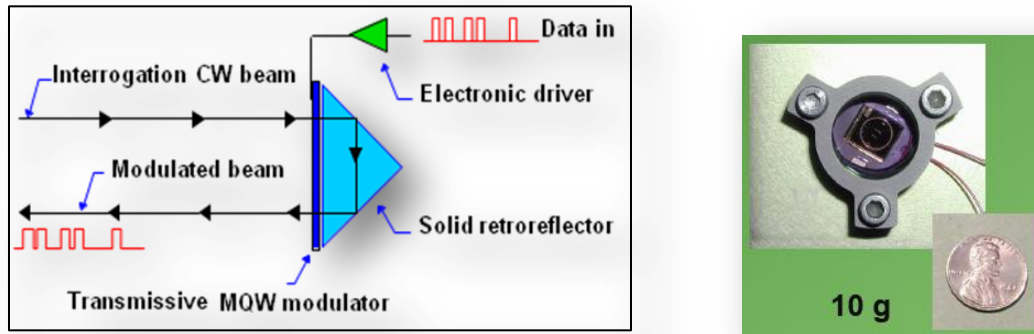


Figure 137: Modulating retro reflector

Such a system could be used to provide retro-directive beam control for the transmitting station, by sending remote ephemeris data back to the source through the MRR in a fully-cooperative target fashion. This information may contain differential fine steering data from perimeter VMJ sensors at the receiver looking for the FWHM points of the beam, or local control information of the remote receiver. In return, the source terminal could use this information in a feed forward controller for point ahead tracking, and the real time feedback is only limited by the round trip time (RTT) of the speed of

light. A block diagram of such a system is illustrated in *Figure 138*, including the central HILPB power receiver and the enabled forward and return optical communication paths.

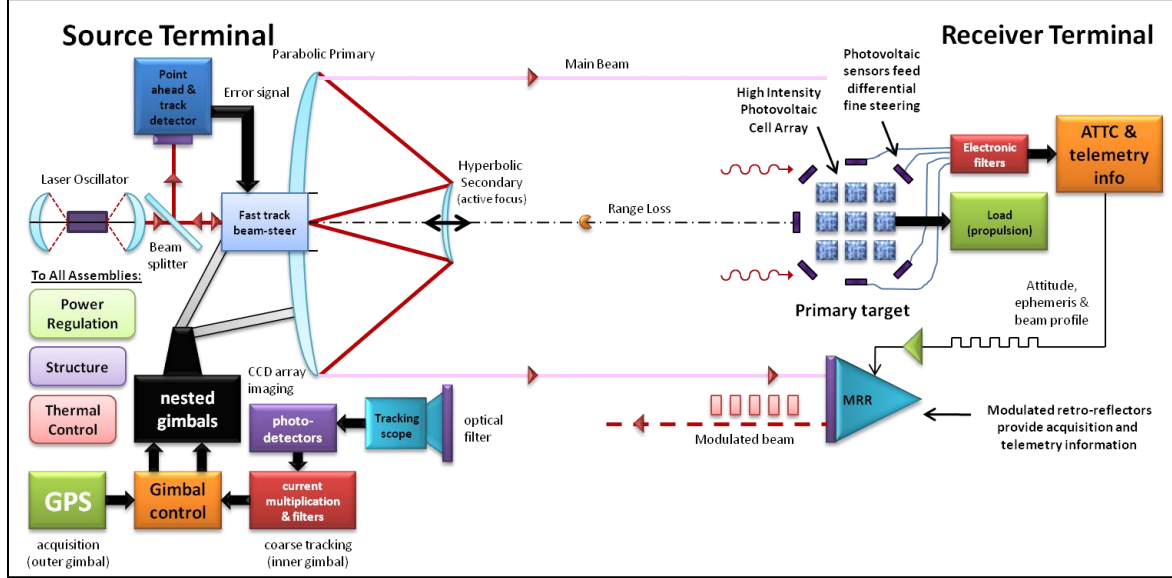


Figure 138: Optical multi-function architecture schematic

In this general architecture, the pointing gimbal begins with GPS-based position knowledge to project a cone of uncertainty in the direction of the target. An acquisition sequence is initiated to scan for the receiver, utilizing the coarse gimbal control. During this scan, the main beam may be regulated at a lower power and defocused to cover a larger region, or a separate low pilot guidance beam may be used. Once an MRR return is achieved, the link is established, and the relative platform pose may be determined from the detected signals. From the ephemeris information transmitted to source terminal, attitude correction may be applied to normalize the pose, and the acquisition beam may be progressively focused to enable tracking & range determination. From here the point ahead and fast beam steer tracking mirror systems are activated, achieving transmitter-to-tracker pointing calibration where the beam is fully captured on the primary receiving aperture. The differential photovoltaic sensors at the receiver capture

the beam waist and then feedback the profile information to the transmitter through the MRR devices to center the beam on the target. At this point the high energy beam is activated enabling power transmission, during which time the feedback signals from MRR's serve beam tracking and interlocking by continuing to transmit navigation and beam quality information throughout the engagement. A loss of beam lock would shut down the high energy laser and reinitialize the acquisition sequence.

In general, the utilization of VMJ technology for optical communications is most applicable to architectures enabling high speed secure communication through scenarios featuring considerable and/or varying channel losses, where the source is not power constrained. This would exclude architectures such as deep space trunk lines and dedicated inter-satellite links, since a great deal of work is being performed by researchers at JPL in cryogenic nanowire single photon detectors and highly efficient pulse position modulation (PPM) schemes to close links under these conditions [60]. However, one major limitation to space based optical communications is with small sun pointing angles when the sun-probe-Earth angle approaches 3-5°, where the background radiance greatly exceeds that of the emitted signal, and the receiver risks thermal damage. An example of such a mission maximizing this geometry would be a solar probe, and it is conceivable that VMJ technology could be utilized to enable high speed optical communication data return from the probe to a GEO relay satellite, where a conventional RF-band could then link down to the ground.

Finally, the military has been pursuing a multitude of technologies to enable optical communications with submerged submarines from airborne platforms [61, 62]. Such a system would reduce the reliance on deployable towed surface buoys, which

diminish the covert nature submarine operations. The considerable challenges encountered include multivariable nonlinear dynamics such as the sea-spray, air-to-water interface, biological matter present in the water, and the salinity. These properties are regionally specific, vary between coastal and open waters and are subject to local weather conditions, requiring a potential prototype system to handle a wide range of channel losses. In general, such a system would employ a blue-green laser source with a wide field of view to maximize propagation and handle refractive scattering. The detectors in such a system may also need to accommodate Doppler effects due to Rayleigh scattering from the bulk molecular motion in the turbulent medium [63]. The current silicon-based VMJ technology has an appreciable responsivity in the visible range, and may offer the necessary dynamic range to enable such submersible links.

CHAPTER V: RESULTS AND CONCLUSIONS

The results presented in this work serve as a technical extension and enhancement to the High Intensity Laser Power Beaming (HILPB) for wireless power transmission research endeavor. The feasibility of utilizing the VMJ technology for free-space optical communications has been demonstrated, by modulating information signals onto the transmitted photonic energy. The system level implications and variations of potential applications including beamwidth and directivity, signal-to-noise-ratio, spectrum constraints, signal power budget, bit-error-rate, information bandwidth, privacy, modulation and detection schemes, transmission channel attenuation and disturbances (atmospheric turbulence, scintillation from index of refraction fluctuations, absorption and scattering from thermal and moisture variation) and beam acquisition tracking and pointing influence on the performance metrics of optical transmission technologies have been investigated.

The high energy laser laboratory at Cleveland State University was also employed to conduct experiments to investigate the feasibility of utilizing the VMJ technology for optical communications, including:

- Beam profiling (Gaussian beam waist may be detected for fine tracking)
- Off axis performance (7% output decrease at 45° off-normal)

- Modulation (ability to track 1 kHz square OOK at 350 W, high SNR)
- Dynamic range (35.6 dB, linear concurrent WPT and communications)
- Polarization (multi-channel demonstrated with ER=10.448 dB)
- Applications (challenging atmospheric/oceanographic environments)
- Integration (multi-use beamed energy capability)

Beam profiling: The results from the beam profile characterization demonstrates that the variances induced from the cleaved fiber optic end are minimal, and that the Gaussian profile may be used in conjunction with VMJ sensors in order to enable a fine tracking control system. The geometry and energy of the tail may be used to design a perimeter photo-detection system that would serve as a way to fine tune the tracking performance of a vibrating or moving platform by providing limited differential feedback signals to a tracking control system by looking for either the full width half maximum (FWHM) or $1/e^2$ values of the beam waist. The capability of the VMJ technology was also demonstrated as a direct measurement sensor for high power beam profiling, in a similar analog to RF far field scanning ranges.

Off axis performance: During off-axis operation horizontally (45 degree off normal) the performance of the VMJ cells was observed to decrease by only 7% (1.77W). This relatively minor drop in performance established a wide angle of acceptance when considering potential mission geometries and tracking system metrics. The results of this test show a tremendous promise toward the potential tracking parameters in an implemented HILPB system, in that only a minimal amount of power is lost at significant levels of off-normal alignment.

Modulation: A laser modulator was implemented to exhibit the transient response of the VMJ technology, and was demonstrated across the full available range of radiance levels to prove that there are not any substantial nonlinear signal distortions with the variable envelope. These results can be extended by comparing the VMJ cell transient performance to that of a single and triple-junction photovoltaic cell in the same environment. This comparison exploits the high voltage output of the VMJ cell, which allows for it to provide a superior signal to noise ratio since stray photonic scattering would generally fall below the forward bias threshold, when compared with single or triple junction photovoltaic technologies. Additionally, the low parasitic loss characteristic of the VMJ cell allows for it to reproduce transients on the order of μ s or better. This demonstrates a unique applicability for a HILPB communications system in hostile environments requiring high SNR. For these types of applications, the simpler OOK modulation techniques would be applicable, given the high average radiated energy.

Dynamic range: The maximum exhibited dynamic range of the photovoltaic device has been 35.6 dB, as limited by the available source power, and could also be additionally improved with narrowband optical filtering at the receiver. With such a substantial dynamic range available for communications, the average beam energy may be maintained sufficiently high to enable adequate power transmission by reducing the dynamic range. This could be accomplished by combining a high power steady-state laser with a lower power modulated source, which would be designed to deliver at least 3 dB of communication margin to the receiver over the specific system's link losses. When comparing this to the contemporary photovoltaic devices, the VMJ cells offer a far

superior ability to compensate for background noise and channel losses, while concurrently delivering appreciable power to the receiver.

Polarization: Further studies were also made into techniques for extending the information bandwidth and security of a HILPB communication system through employing polarization stages to demonstrate a secure multi-channel multiplexing scheme with the VMJ cells. In this case the ER=10.448 dB, and this generous amount of dynamic range demonstrates the feasibility of employing multiple polarization states into the system. Extending this idea further, the receiver may be partitioned into multiple detection regions, each handling a different alignment of polarization with minimal crosstalk between them. At the transmission side, the laser source may be delivered by multiple separate polarization states, and each state could handle a unique message to be transmitted. These states could traverse down their respective optical paths and combined together in free space as they reach the surface of the receiver. In this way the average received energy could remain high, while also increasing the bandwidth of the system by the number of states employed. Alternatively, polarization states may be used to accomplish PPBM as another way to keep the average power high. Furthermore, the introduction of polarization states adds a further physical layer of privacy and security to the communications system.

Applications: In general, the utilization of VMJ technology for optical communications is most applicable to architectures enabling high speed secure communication through scenarios featuring considerable and/or varying channel losses, where the source is not power constrained. Architectures including considerable atmospheric or oceanographic challenges such as up/down links during theater of war

operations, and submarine communications may be enabled with the VMJ technology. Additionally, space missions requiring small sun pointing angles or systems requiring concurrent WPT and optical communications capability are applicable.

Integration: The integration of the HILPB system with optical communications has been demonstrated, and such a system may be used to enable a multi-use directed energy system. By using the communications capability to send ephemeris data and perform ranging, an integrated beamed energy (IBE) system may be realized. This type of system could enable power and propulsion to a remote platform, while sending forward control and navigation information over the communications channel. The IBE system would maintain the power, sensing and computationally intensive operations at the source, and therefore reducing the burden on the resource-constrained remote platform.

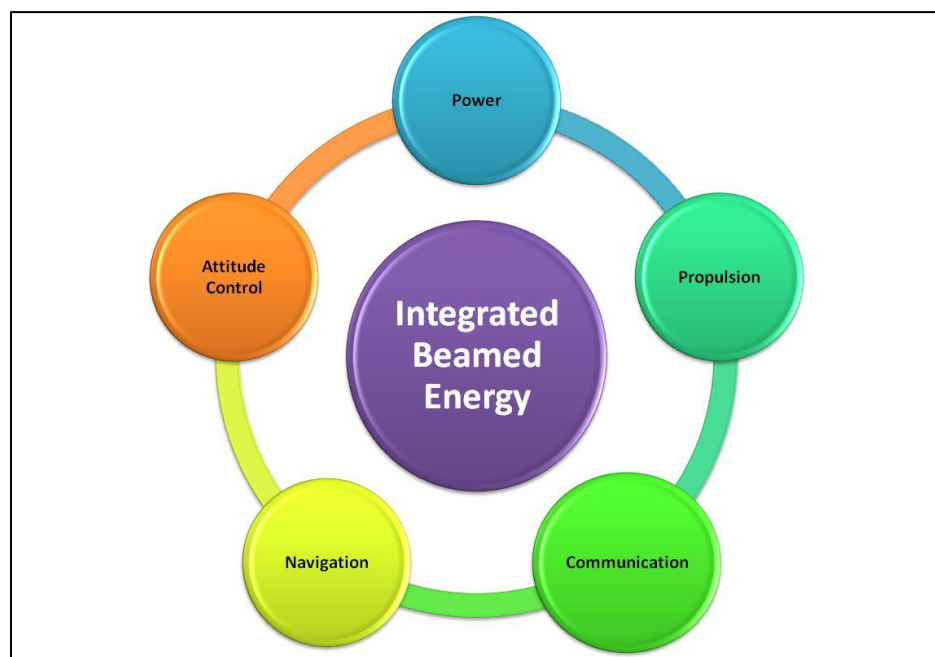


Figure 139: Potential integrated beamed energy representation

The result of this research demonstrates the feasibility of, and serves as a comprehensive design guide for the implementation of a HILPB communication system. In addition, the developed mathematical models and empirical data support the ongoing wireless power transmission effort by expanding the fundamental knowledge base of the HILPB technology.

CHAPTER VI: RECOMMENDATIONS

Several avenues have been highlighted for follow-on work that is beyond the original scope of this research. In considering the VMJ technology, there are 3 primary areas of improvement for continuing research, including the development of a lower-loss AR coating for the cells, optimizing the cell thickness for the fundamental operating wavelength, and adjusting the cell chemistry to shift up to the “eye-safer” region of 1550 nm or beyond.

Currently, there is an estimated 20% back-reflection from the cells. This may be reduced down to 5% through the proper application of AR coatings. This improvement will influence the overall HILPB end-to-end system efficiency.

By adjusting the thickness of the VMJ cells during the manufacturing stage, an improvement in performance may be obtained by tuning the penetration depth to the operating wavelength of the laser. Determining this optimal thickness will present a tradeoff against the induced thermal impedance of the excess material, and this must be optimized around a desired system operating point.

Finally, a significant amount of laser energy is wasted due to the fact that the active area of the photocells does not fully cover the aperture of the receiver. This in part is due to the construction of the cells and their geometric layout on the surface of the receiver. Future work in manufacturing chevron-shaped VMJ cells will have further

potential improvements on array performance, by increasing the packing density in a radial array. A different approach may be to investigate the possibility of manufacturing curved junctions within the cell, to inversely match the profile of the impinging beam.

REFERENCES

- [1] “Signal Lamp,” Wikipedia, 2011, Wikipedia Foundation, Inc.,
http://en.wikipedia.org/wiki/Signal_lamp.
- [2] “Aeronautical Lighting and Other Airport Visual Aids,” 2011, FAA Aeronautical Information Manual, FAA Aeronautical Information Manual, Chapter 2 (Aeronautical Lighting and Other Airport Visual Aids), Section 1 (Airport Lighting Aids).
- [3] Katzman, M. *Laser Satellite Communications*, Englewood Cliffs, NJ: Prentice Hall, 1987, pp. 56-67.
- [4] Boronson, D. M. “An overview of Lincoln Lab Development of Lasercom Technologies for Space,” *SPIE OE-LASE '93*, Vol. 1866, Los Angeles, CA, Jan. 20-21, 1993.
- [5] Pillsbury, A. D. “LITE Engineering Model-II: the Flight Qualified Subsystem,” *SPIE OE-LASE '93*, Vol. 1866, Los Angeles, CA, Jan. 20-21, 1993.
- [6] Boronson, D. M. “LITE Engineering Model-I: Operation and Performance of the Communications and Beam Control Subsystems,” *SPIE OE-LASE '93*, Vol. 1866, Los Angeles, CA, Jan. 20-21, 1993.
- [7] “Optical Communications Group,” 2011, Jet Propulsion Laboratory,
<http://lasers.jpl.nasa.gov/PAGES/about.html>.
- [8] Ruiz, D., R. Czichy, J. Bara, A. Cameron, A. Belmonte, P. Menendez-Valdes, F. Blanco, and C. Pedreira, “Inter-Mountain Laser Communication Tests,” *Free-Space Laser Communication Technologies II*, SPIE, Vol. 1218, 1990, pp. 419-430.

- [9] Wilks, S. C., J. R. Morris, J. M. Brase, S. S. Olivier, J. R. Henderson, C. Thompson, M. Kartz, and A. J. Ruggiero, "Modeling of Adaptive Optics-Based Free Space Communications Systems," *Proc. Of SPIE*, Vol. 4281, 2002.
- [10] "Optical Inter-orbit Communications Engineering Test Satellite "KIRARI"," 2009, Japanese Aerospace Exploration Agency, http://www.jaxa.jp/projects/sat/oicets/index_e.html.
- [11] "Record Set for Space Laser Communication," 2006, Space, http://www.space.com/missionlaunches/060104_laser_comm.html.
- [12] "Mars Telecommunications Orbiter," Wikipedia, 2011, Wikipedia Foundation, Inc., http://en.wikipedia.org/wiki/Mars_Telecommunications_Orbiter.
- [13] Moore, C.I.; Burris, H.R.; Rabinovich, W.S.; Suite, M.; Wasiczko, L.; Jaremko, J.; Ibanez, J.; Georges, E.S.; Uecke, S.; Mock, J.; Sender, J.; Muth, J.F.; Wood, T.S.; "Lasercomm demonstration during US navy trident warrior 06 forcenet exercise," Antennas and Propagation Society International Symposium, 2007 IEEE, US Naval Res. Lab., Washington.
- [14] Roguski, Randy,"Solar power 'concentrator' could revolutionize industry, Cleveland inventors say", The Plain Dealer, Sunday, November 16, 2008.
http://blog.cleveland.com/business/2008/11/greenfield_solargreenfield_sol.html.
- [15] Cook, J. R.; Cusumano, S. J.; Whiteley, M. R., "Potential use of CW high energy laser on an airborne platform," AIP Conference Proceedings Fourth International Symposium on Beamed Energy Propulsion n 830 2006 p.400-10.
- [16] "Navy's Drone Death Ray Takes Out Targets at Sea," 2010, Wired,

<http://www.wired.com/dangerroom/2010/05/navys-drone-death-ray-takes-out-targets-at-sea/>.

- [17] Hochstetler, Ron, "Airships for the 21st Century," IEEE Spectrum, October, 2010.http://spectrum.ieee.org/aerospace/aviation/airships-for-the-21st-century/?utm_source=techalert&utm_medium=email&utm_campaign=100710.
- [18] Gilbreath, G. C. ; Rabinovich, W. S. ; Meehan, T. J. ; Vilcheck, M. J. ; Mahon, R. ; Burris, Ray ; Ferraro, M. ; Sokolsky, I. ; Vasquez, J. A. ; Cochrell, K., "Large-Aperture Multiple Quantum Well Modulating Retroreflector for Free-Space Optical Data Transfer on Unmanned Aerial Vehicles," SPIE Optical Engineering, 40(7) 1348–1356, July, 2001.
- [19] Leik N. Myrabo, John S. Lewis, "Lightcraft Flight Handbook," Apogee Books, 2009.
- [20] Schawlow et al., "Masers and Maser Communications System," U.S. Patent No. 2929922, Mar 1960.
- [21] O'Shea, D., Callen, W., Rhodes, W., *An Introduction to Lasers and Their Applications*, Reading, Massachusetts: Addison-Wesley Publishing Company, 1977, Chapter 8.
- [22] "Defense Satellite Communications System," Wikipedia, 2011, Wikipedia Foundation, http://en.wikipedia.org/wiki/Defense_Satellite_Communications_System.
- [23] Aviv, David G., "Laser Space Communications", Artech House Publishing, Norword, MA, 2006, pg. 3.
- [24] "Solar Energy in Earth's Atmosphere," 2011, Windows to the Universe, http://www.windows2universe.org/earth/Atmosphere/earth_atmosph_radiation_budget.htm

ml.

- [25] Saleh, B. E. A., Teich, M. C., “Fundamentals of Photonics”, Wiley-Interscience; 2nd edition, March 9, 2007.
- [26] “Polarizer,” Wikipedia, 2011, Wikipedia Foundation, <http://en.wikipedia.org/wiki/Polarizer>.
- [27] “Wave plate,” Wikipedia, 2011, Wikipedia Foundation, <http://en.wikipedia.org/wiki/Waveplate>.
- [28] “Input Light Intensity,” 2011 OSI Optoelectronics, <http://www.osiopptoelectronics.com/technology-corner/frequently-asked-questions/input-light-intensity.aspx>.
- [29] P. Holenarsipur, “I'm OOK. You're OOK?,” Maxim Application Note 4439, April 08, 2009.
- [30] Biswas, A., and S. Piazzola, “Deep-Space Optical Communications Downlink Budget from Mars: System Parameters,” *JPL-IPN Progress Report*, 42-154, 2003.
- [31] Hufnagle, R. E., and N. R. Stanley, “Modulation Transfer Function Associated with Image Transmission Through Turbulent Media,” *Journal of the Optical Society of America*, Vol. 54, Jan. 1964, pp. 52-61.
- [32] J. W. Goodman, *Statistical Optics*, John Wiley & Sons, 1985.
- [33] Weichel, H., *Laser Beam Propagation in the Atmosphere*, Volume TT-3, Bellingham, WA: SPIE Optical Engineering Press, 1990.
- [34] Chu, T. S., and D. C. Hogg, “Effects of Precipitation on Propagation at 0.53, 3.5,

and 10.6 micron,” *Bell System Technical Journal*, Vol. 47, May-June 1968, pp 723-759.

[35] Hudson, R. D., *Infrared Systems Engineering*, New York: John Wiley and Sons, 1969.

[36] Subramanian, M., “Atmospheric Limitations for Laser Communications,” *EASCON Record*, 1968.

[37] RCA Labs, *Research Program on the Utilization of Coherent Light*, AD 276526, April 20, 1962.

[38] “MODTRAN 4 Software,” Kirtland Air Force Base, AFRL Space Vehicles Directorate Public Affairs, Library Fact Sheets, 2007,
<http://www.kirtland.af.mil/library/factsheets/factsheet.asp?id=7915>.

[39] Ross, M., P. Freedman, J. Abernathy, G. Matassou, J. Wolf, and J.D. Barry,”Spatial Optical Communications with the Nd:YAG Laser, Proc. IEEE Vol. 66, No. 3, March 1978.

[40] Pratt, W. K., *Laser Space Communications*, New York: John Wiley & Sons 1971.

[41] Eugene Hecht: “Optics Fundamentals”, Addison Wesley; 4th edition, August 12, 2001, Chapter 5.6 Fiberoptics.

[42] Phillip Sprangle, Antonio Ting, Joseph Peñano, Richard Fischer, And Bahman Hafizi, ”Beam Combining: High-power fiber-laser beams are combined incoherently” OptoIQ, 2008.

http://www.laserfocusworld.com/display_article/331428/12/none/none/WebX/BEAM-COMBINING:-High-power-fiber-laser-beams-are-combined-incoherentl.

- [43] “Fiber Optic Beam Delivery Systems,” US Laser Corporation Tech Note, 2011.
<http://www.uslasercorp.com/envoy/fobd.html>.
- [44] Chen, C. C., and C. S. Gardner, “ Impact of Random Pointing and Tracking Error on the Design of Coherent and Non Coherent Optical Intersatellite Communications,” *IEEE Trans. On Communication*, Vol. 37, 1981, pp. 252-260.
- [45] Barry, J. D., and G. S. Mecherle, “Beam Pointing Error Significant Design Parameters for Satellite-born, Free Space Optimal Communications Systems,” *Optical Engineering*, Vol. 24, pp. 1049-1054.
- [46] Toyoshina, M, T. Jono, K. Nakagawa, and A. Yamamoto, “Optimum Divergence Angles of a Gaussian Beam Wave in the Presence of Random Jitter in Free Space Communication Systems, *Journal of the Optical Society of America*, Vol. A19, 2002, pp.567-571.
- [47] Polishuk, A., and S. Arnon, “Optimization of a Laser Satellite Communication System with an Optical Preamplifier,” *Journal of the Optical Society of America*, Vol. 21, No. 7, 2004.
- [48] Arnon, S., S. R. Rotman, and N. S. Kopeika, “Performance Limitations of Free-Space Optical Communication Satellite Networks Due to Vibrations: Direct Detection Digital Mode,” *SPIE/Optical Engineering*, Vol. 36, No. 11, 1997, pp. 3148-3157.
- [49] Arnon, S., S. R. Rotman, and N. S. Kopeika, “Beamwidth and Transmitter Power Adaptive to Tracking System Performance for Free-Space Optical Communication,” *Applied Optics*, Vol. 36, 1997, pp. 605-610.
- [50] Arnon, S., S. R. Rotman, and N. S. Kopeika, “Bandwidth Maximization for

Satellite Laser Communication," *IEEE Trans. On Aerospace and Electronic Systems*, Vol. 35, No. 2, 1999.

[51] Lee, S., G. G. Ortiz, J. W. Alexander, A. Portillo, and C. Jeppesen, "Accelerometer-Assisted Tracking and Pointing for Deep Space Optical Communications: Concept, Analysis, and Implementation," IEEE Aerospace Conference, Big Sky, MT, 2001.

[52] Bujard, P., "Thermal conductivity of boron nitride filled epoxy resins:temperature dependence and influence of sample preparation ,," Ciba-Geigy Ltd., Fribourg; Thermal Phenomena in the Fabrication and Operation of Electronic Components: I-THERM '88, InterSociety Conference on; 11-13 May 1988.

[53] Liu, G; Cui, B; Chen, R J., "Thermal Expansion Behavior of Copper/Kovar Alloy Composite ,," Northeast Univ. Technol. (China). Vol. 9, no. 4, pp. 498-501. Dec. 1988.

[54] SPI Silver Paste Plus datasheet, 2011, SPI,
http://www.2spi.com/catalog/spec_prep/plus_prop.html.

[55] D. E. Raible, "High intensity laser power beaming for wireless power transmission," Master's Thesis, Department of Electrical and Computer Engineering, Cleveland State University, Cleveland, OH, May, 2008.

[56] S. Noor Mohammad, S. Abidi, "Theory of saturation photocurrent and photovoltage in p-n junction solar cells, "Journal of Applied Physics. Vol. 61, pp.4909-4919. 15 May, 1987.

[57] E. D. Palik, " Handbook of Optical Constants of Solids," Academic Press, NY, 1985.

- [58] Alda, Javier, "Laser and Gaussian beam propagation and transformation," University Complutense of Madrid, Madrid, Spain, Encyclopedia of Optical Engineering, 2003.
- [59] Bernard J. Klein, John J. Degnan, "Optical Antenna Gain 1: Transmitting Antennas," Applied Optics, Vol. 13, No. 9, September 1974.
- [60] Abhijit Biswas, Hamid Hemmati, Sabino Piazolla, Bruce Moision, Kevin Birnbaum, Kevin Quirk, "Deep-space optical terminals (DOT) systems engineering," IPN Progress Report 42-183, November 15, 2010.
- [61] "Darpa Pushes Submarine Laser Communications Technology for ASW Operations," 2011, Military & Aerospace Electronics,
<http://www.militaryaerospace.com/index/display/article-display/372765/articles/military-aerospace-electronics/online-news-2/2010/01/darpa-pushes-submarine-laser-communications-technology-for-asw-operations.html>.
- [62] "QinetiQ to demonstrate submarine laser communications system during RIMPAC exercise in June 2012," 2011, Military & Aerospace Electronics,
http://www.militaryaerospace.com/index/display/article-display/9230722242/articles/military-aerospace-electronics/online-news-2/2010/9/qinetiq-to_demonstrate.html?sms_ss=email&at_xt=4ca38bf0720ab839,0.
- [63] "Rayleigh Scattering," 2011, Optical Instrumentation and Nondestructive Evaluation Branch, <http://www.grc.nasa.gov/WWW/OptInstr/rayleigh.html>.

APPENDICES

The following C code is used to generate the general form polynomial and the list of coefficients to the ith degree (see order = 10 in this case):

```
#include <stdio.h>

void main()
{
    FILE *f;

    f = fopen("lol.txt", "w");
    int order = 10;
    int i, j, k, l;

    for (i = 0; i <= order; i++)
    {
        for(j = 0; j <= i; j++)
        {
            fprintf(f, "c%i%i", j, i-j);
            for(k = 0; k < j; k++)
            {
                fprintf(f, "*x");
            }
            for(l = k; l < i; l++)
            {
                fprintf(f, "*y");
            }
            if(j < i || i != order)
                fprintf(f, " + ");
        }
        fprintf(f, "\n\n");
    }

    for(i = 0; i <= order; i++)
    {
        for(j = 0; j <= i; j++)
        {
            fprintf(f, "c%i%i", j, i-j);
            if(i < order || j < i)
                fprintf(f, ",");
        }
    }

    fprintf(f, "\n\n");
    fclose(f);
}
```

The following code generates the 10th order coefficients and the gnuplot:

Lastly, the output iterations from the coefficient computational process are given:

```

After 23 iterations the fit converged.
final sum of squares of residuals : 0.24777
rel. change during last iteration : 0

degrees of freedom      (FIT_NDF)          : 295
rms of residuals        (FIT_STDFIT) = sqrt(WSSR/ndf)   : 0.028981
variance of residuals  (reduced chisquare) = WSSR/ndf    : 0.000839898

Final set of parameters            Asymptotic Standard Error
=====                      =====
c00      = 2.35554      +/- 0.4838      (20.54%)
c01      = -2.64328     +/- 0.6553      (24.79%)
c10      = -2.78066     +/- 0.6553      (23.57%)
c02      = 1.67979      +/- 0.4667      (27.78%)
c11      = 1.31206      +/- 0.2637      (20.1%)
c20      = 1.75502      +/- 0.4667      (26.59%)
c03      = -0.573947    +/- 0.1817      (31.66%)
c12      = -0.560686    +/- 0.09591     (17.11%)
c21      = -0.328353    +/- 0.09591     (29.21%)
c30      = -0.66403     +/- 0.1817      (27.36%)
c04      = 0.114384     +/- 0.04288     (37.49%)
c13      = 0.143737     +/- 0.0228      (15.86%)
c22      = 0.0788841    +/- 0.0193      (24.46%)
c31      = 0.0579267    +/- 0.0228      (39.36%)
c40      = 0.156539     +/- 0.04288     (27.39%)
c05      = -0.0139738   +/- 0.006476     (46.35%)
c14      = -0.0219248   +/- 0.00353     (16.1%)
c23      = -0.0140876   +/- 0.002803     (19.9%)
c32      = -0.00731975  +/- 0.002803     (38.29%)
c41      = -0.00712405  +/- 0.00353     (49.55%)
c50      = -0.023798    +/- 0.006476     (27.21%)
c06      = 0.00106355   +/- 0.00064     (60.18%)
c15      = 0.00204976   +/- 0.0003612    (17.62%)
c24      = 0.00162128   +/- 0.0002784    (17.17%)
c33      = 0.000786305  +/- 0.0002574    (32.73%)
c42      = 0.000527319  +/- 0.0002784    (52.79%)
c51      = 0.00057951   +/- 0.0003612    (62.32%)
c60      = 0.00237009   +/- 0.00064     (27%)
c07      = -4.94652e-05  +/- 4.118e-05   (83.25%)
c16      = -0.000118815 +/- 2.432e-05   (20.47%)
c25      = -0.000113955 +/- 1.851e-05   (16.24%)
c34      = -6.32413e-05  +/- 1.637e-05   (25.88%)
c43      = -2.77411e-05  +/- 1.637e-05   (59.01%)
c52      = -3.07293e-05  +/- 1.851e-05   (60.22%)
c61      = -2.92362e-05  +/- 2.432e-05   (83.18%)
c70      = -0.000153528  +/- 4.118e-05   (26.82%)
c08      = 1.30867e-06   +/- 1.661e-06   (127%)
c17      = 4.15136e-06   +/- 1.041e-06   (25.07%)
c26      = 4.79565e-06   +/- 7.962e-07   (16.6%)
c35      = 2.94809e-06   +/- 6.847e-07   (23.22%)
c44      = 1.55146e-06   +/- 6.524e-07   (42.05%)
c53      = 5.31753e-07   +/- 6.847e-07   (128.8%)
c62      = 1.36108e-06   +/- 7.962e-07   (58.5%)
c71      = 8.09287e-07   +/- 1.041e-06   (128.6%)

```

c80	= 6.22511e-06	+/- 1.661e-06	(26.69%)
c09	= -1.62601e-08	+/- 3.815e-08	(234.6%)
c18	= -7.92923e-08	+/- 2.574e-08	(32.46%)
c27	= -1.13285e-07	+/- 2.04e-08	(18%)
c36	= -6.91627e-08	+/- 1.743e-08	(25.2%)
c45	= -4.86458e-08	+/- 1.607e-08	(33.03%)
c54	= -1.95973e-08	+/- 1.607e-08	(81.99%)
c63	= -1.81445e-09	+/- 1.743e-08	(960.7%)
c72	= -3.90972e-08	+/- 2.04e-08	(52.17%)
c81	= -8.43074e-09	+/- 2.574e-08	(305.3%)
c90	= -1.43397e-07	+/- 3.815e-08	(26.6%)
c010	= 4.46935e-11	+/- 3.801e-10	(850.5%)
c19	= 6.20246e-10	+/- 2.807e-10	(45.25%)
c28	= 1.21033e-09	+/- 2.41e-10	(19.91%)
c37	= 4.6609e-10	+/- 2.187e-10	(46.93%)
c46	= 9.47676e-10	+/- 2.069e-10	(21.83%)
c55	= -1.5371e-10	+/- 2.032e-10	(132.2%)
c64	= 4.40915e-10	+/- 2.069e-10	(46.93%)
c73	= -2.3252e-10	+/- 2.187e-10	(94.07%)
c82	= 5.51599e-10	+/- 2.41e-10	(43.7%)
c91	= -4.0046e-11	+/- 2.807e-10	(700.8%)
c100	= 1.43145e-09	+/- 3.801e-10	(26.56%)

Iteration 0
WSSR : 3.46733e+028 delta(WSSR)/WSSR : 0
delta(WSSR) : 0 limit for stopping : 1e-016
lambda : 4.36613e+011

initial set of free parameter values

c00	= 1
c01	= 1
c10	= 1
c02	= 1
c11	= 1
c20	= 1
c03	= 1
c12	= 1
c21	= 1
c30	= 1
c04	= 1
c13	= 1
c22	= 1
c31	= 1
c40	= 1
c05	= 1
c14	= 1
c23	= 1
c32	= 1
c41	= 1
c50	= 1
c06	= 1
c15	= 1
c24	= 1
c33	= 1
c42	= 1
c51	= 1
c60	= 1
c07	= 1
c16	= 1
c25	= 1
c34	= 1

```

c43      = 1
c52      = 1
c61      = 1
c70      = 1
c08      = 1
c17      = 1
c26      = 1
c35      = 1
c44      = 1
c53      = 1
c62      = 1
c71      = 1
c80      = 1
c09      = 1
c18      = 1
c27      = 1
c36      = 1
c45      = 1
c54      = 1
c63      = 1
c72      = 1
c81      = 1
c90      = 1
c010     = 1
c19      = 1
c28      = 1
c37      = 1
c46      = 1
c55      = 1
c64      = 1
c73      = 1
c82      = 1
c91      = 1
c100     = 1
/

```

Iteration 1
 WSSR : 1.72225e+023 delta(WSSR)/WSSR : -201325
 delta(WSSR) : -3.46731e+028 limit for stopping : 1e-016
 lambda : 4.36613e+010

resultant parameter values

```

c00      = 1
c01      = 1
c10      = 1
c02      = 1
c11      = 1
c20      = 1
c03      = 1
c12      = 1
c21      = 1
c30      = 1
c04      = 0.999999
c13      = 1
c22      = 1
c31      = 1
c40      = 0.999999
c05      = 0.999992
c14      = 0.999993
c23      = 0.999994
c32      = 0.999994
c41      = 0.999993
c50      = 0.999992
c06      = 0.999892
c15      = 0.99991
c24      = 0.999915
c33      = 0.999916
c42      = 0.999915
c51      = 0.99991

```

```

c60      = 0.999892
c07      = 0.998579
c16      = 0.998813
c25      = 0.998887
c34      = 0.998917
c43      = 0.998917
c52      = 0.998887
c61      = 0.998813
c70      = 0.998579
c08      = 0.982655
c17      = 0.985435
c26      = 0.98628
c35      = 0.986748
c44      = 0.986911
c53      = 0.986748
c62      = 0.98628
c71      = 0.985435
c80      = 0.982655
c09      = 0.820557
c18      = 0.845579
c27      = 0.851657
c36      = 0.857204
c45      = 0.860737
c54      = 0.860737
c63      = 0.857204
c72      = 0.851657
c81      = 0.845579
c90      = 0.820557
c100     = -0.0475349
c19      = -0.0345137
c28      = -0.0957286
c37      = -0.0632466
c46      = -0.0116794
c55      = 0.0103841
c64      = -0.0116794
c73      = -0.0632466
c82      = -0.0957286
c91      = -0.0345137
c100     = -0.0475349
/

```

Iteration 2
WSSR : 1.53749e+021 delta(WSSR)/WSSR : -111.017
delta(WSSR) : -1.70687e+023 limit for stopping : 1e-016
lambda : 4.36613e+009

resultant parameter values

```

c00      = 1
c01      = 1
c10      = 1
c02      = 1
c11      = 1
c20      = 1
c03      = 1
c12      = 1
c21      = 1
c30      = 1
c04      = 0.999995
c13      = 0.999995
c22      = 0.999996
c31      = 0.999995
c40      = 0.999995
c05      = 0.999933
c14      = 0.999938
c23      = 0.99994
c32      = 0.99994
c41      = 0.999938
c50      = 0.999933
c06      = 0.999102

```

```

c15      = 0.999177
c24      = 0.999215
c33      = 0.999225
c42      = 0.999215
c51      = 0.999177
c60      = 0.999102
c07      = 0.988613
c16      = 0.989632
c25      = 0.990176
c34      = 0.99039
c43      = 0.99039
c52      = 0.990176
c61      = 0.989632
c70      = 0.988613
c08      = 0.869977
c17      = 0.882111
c26      = 0.888917
c35      = 0.891958
c44      = 0.892894
c53      = 0.891958
c62      = 0.888917
c71      = 0.882111
c80      = 0.869977
c09      = -0.141494
c18      = -0.0333335
c27      = 0.0297186
c36      = 0.0586657
c45      = 0.0734535
c54      = 0.0734535
c63      = 0.0586657
c72      = 0.0297186
c81      = -0.0333335
c90      = -0.141494
c010     = 0.00474348
c19      = -0.000620472
c28      = 0.00960827
c37      = -0.0510975
c46      = 0.0031682
c55      = 0.0441814
c64      = 0.0031682
c73      = -0.0510975
c82      = 0.00960827
c91      = -0.000620472
c100     = 0.00474348
/

```

```

Iteration 3
WSSR    : 6.29329e+018   delta(WSSR)/WSSR : -243.306
delta(WSSR) : -1.53119e+021   limit for stopping : 1e-016
lambda   : 4.36613e+008

```

resultant parameter values

```

c00      = 1
c01      = 1
c10      = 1
c02      = 1
c11      = 1
c20      = 1
c03      = 0.999999
c12      = 0.999999
c21      = 0.999999
c30      = 0.999999
c04      = 0.999984
c13      = 0.999986
c22      = 0.999986
c31      = 0.999986
c40      = 0.999984
c05      = 0.999824
c14      = 0.999839

```

```

c23      = 0.999843
c32      = 0.999843
c41      = 0.999839
c50      = 0.999824
c06      = 0.998092
c15      = 0.998229
c24      = 0.998292
c33      = 0.998314
c42      = 0.998292
c51      = 0.998229
c60      = 0.998092
c07      = 0.980777
c16      = 0.981766
c25      = 0.982422
c34      = 0.982826
c43      = 0.982826
c52      = 0.982422
c61      = 0.981766
c70      = 0.980777
c08      = 0.830673
c17      = 0.83355
c26      = 0.83896
c35      = 0.84403
c44      = 0.845956
c53      = 0.84403
c62      = 0.83896
c71      = 0.83355
c80      = 0.830673
c09      = -0.0993558
c18      = -0.143865
c27      = -0.117384
c36      = -0.0748079
c45      = -0.0480214
c54      = -0.0480214
c63      = -0.0748079
c72      = -0.117384
c81      = -0.143865
c90      = -0.0993558
c010     = 0.00279729
c19      = 0.00464952
c28      = 0.0068827
c37      = -0.00511263
c46      = 0.00061948
c55      = 0.00924664
c64      = 0.00061948
c73      = -0.00511263
c82      = 0.0068827
c91      = 0.00464952
c100     = 0.00279729
/

```

```

Iteration 4
WSSR    : 3.02374e+017   delta(WSSR)/WSSR : -19.8129
delta(WSSR) : -5.99091e+018   limit for stopping : 1e-016
lambda   : 4.36613e+007

```

resultant parameter values

```

c00      = 1
c01      = 1
c10      = 1
c02      = 0.999998
c11      = 0.999998
c20      = 0.999998
c03      = 0.999977
c12      = 0.99998
c21      = 0.99998
c30      = 0.999977
c04      = 0.999757
c13      = 0.999786

```

```

c22      = 0.999793
c31      = 0.999786
c40      = 0.999757
c05      = 0.997504
c14      = 0.997831
c23      = 0.99793
c32      = 0.99793
c41      = 0.997831
c50      = 0.997504
c06      = 0.976413
c15      = 0.979668
c24      = 0.98077
c33      = 0.981072
c42      = 0.98077
c51      = 0.979668
c60      = 0.976413
c07      = 0.809669
c16      = 0.836713
c25      = 0.846178
c34      = 0.850092
c43      = 0.850092
c52      = 0.846178
c61      = 0.836713
c70      = 0.809669
c08      = -0.0767577
c17      = 0.073849
c26      = 0.123057
c35      = 0.152227
c44      = 0.162687
c53      = 0.152227
c62      = 0.123057
c71      = 0.073849
c80      = -0.0767577
c09      = -0.00163482
c18      = 0.00722741
c27      = -0.0898362
c36      = -0.0328748
c45      = 0.0384455
c54      = 0.0384455
c63      = -0.0328748
c72      = -0.0898362
c81      = 0.00722741
c90      = -0.00163482
c010     = 0.000175178
c19      = -0.000695369
c28      = 0.00319148
c37      = 0.00967725
c46      = -0.0305682
c55      = 0.0417574
c64      = -0.0305682
c73      = 0.00967725
c82      = 0.00319148
c91      = -0.000695369
c100     = 0.000175178
/

```

Iteration 5
WSSR : 6.41706e+014 delta(WSSR)/WSSR : -470.204
delta(WSSR) : -3.01732e+017 limit for stopping : 1e-016
lambda : 4.36613e+006

resultant parameter values

```

c00      = 1
c01      = 0.999999
c10      = 0.999999
c02      = 0.999993
c11      = 0.999993
c20      = 0.999993
c03      = 0.999935

```

```

c12      = 0.999938
c21      = 0.999938
c30      = 0.999935
c04      = 0.999417
c13      = 0.999446
c22      = 0.999458
c31      = 0.999446
c40      = 0.999417
c05      = 0.995025
c14      = 0.995226
c23      = 0.995398
c32      = 0.995398
c41      = 0.995226
c50      = 0.995025
c06      = 0.961253
c15      = 0.962158
c24      = 0.963893
c33      = 0.964517
c42      = 0.963893
c51      = 0.962158
c60      = 0.961253
c07      = 0.745064
c16      = 0.744245
c25      = 0.757601
c34      = 0.765275
c43      = 0.765275
c52      = 0.757601
c61      = 0.744245
c70      = 0.745064
c08      = -0.162528
c17      = -0.208867
c26      = -0.143713
c35      = -0.0956068
c44      = -0.0770818
c53      = -0.0956068
c62      = -0.143713
c71      = -0.208867
c80      = -0.162528
c09      = 0.0104167
c18      = 0.0159456
c27      = 0.010663
c36      = -0.011641
c45      = 0.01651
c54      = 0.01651
c63      = -0.011641
c72      = 0.010663
c81      = 0.0159456
c90      = 0.0104167
c010     = -0.000214625
c19      = -0.000371147
c28      = -0.000367191
c37      = 0.00131138
c46      = -0.00267103
c55      = 0.00287881
c64      = -0.00267103
c73      = 0.00131138
c82      = -0.000367191
c91      = -0.000371147
c100     = -0.000214625
/

```

Iteration 6
WSSR : 2.48151e+013 delta(WSSR)/WSSR : -24.8594
delta(WSSR) : -6.16891e+014 limit for stopping : 1e-016
lambda : 436613

resultant parameter values

```

c00      = 0.999999
c01      = 0.999988

```

```

c10      = 0.999988
c02      = 0.9999
c11      = 0.999908
c20      = 0.9999
c03      = 0.999164
c12      = 0.999253
c21      = 0.999253
c30      = 0.999164
c04      = 0.993377
c13      = 0.994182
c22      = 0.994335
c31      = 0.994182
c40      = 0.993377
c05      = 0.952512
c14      = 0.958699
c23      = 0.960278
c32      = 0.960278
c41      = 0.958699
c50      = 0.952512
c06      = 0.717118
c15      = 0.755023
c24      = 0.765504
c33      = 0.769004
c42      = 0.765504
c51      = 0.755023
c60      = 0.717118
c07      = -0.136824
c16      = 0.0077492
c25      = 0.0438448
c34      = 0.072696
c43      = 0.072696
c52      = 0.0438448
c61      = 0.00774921
c70      = -0.136824
c08      = 0.00761364
c17      = -0.0134038
c26      = -0.0960861
c35      = 0.00331389
c44      = 0.06204
c53      = 0.00331389
c62      = -0.0960861
c71      = -0.0134038
c80      = 0.00761364
c09      = -8.89457e-005
c18      = -2.15307e-005
c27      = 0.016236
c36      = -0.0203328
c45      = 0.00990908
c54      = 0.00990908
c63      = -0.0203328
c72      = 0.016236
c81      = -2.15308e-005
c90      = -8.89456e-005
c010     = -2.49969e-006
c19      = 3.56179e-005
c28      = -0.000660689
c37      = 0.0014202
c46      = -0.00204697
c55      = 0.00224348
c64      = -0.00204697
c73      = 0.0014202
c82      = -0.000660689
c91      = 3.56179e-005
c100     = -2.49969e-006
/

```

Iteration 7
 WSSR : 1.44048e+011 delta(WSSR)/WSSR : -171.27
 delta(WSSR) : -2.46711e+013 limit for stopping : 1e-016
 lambda : 43661.3

resultant parameter values

c00	= 0.99999
c01	= 0.999932
c10	= 0.999932
c02	= 0.999547
c11	= 0.999566
c20	= 0.999547
c03	= 0.997029
c12	= 0.9972
c21	= 0.9972
c30	= 0.997029
c04	= 0.981754
c13	= 0.982799
c22	= 0.98331
c31	= 0.982799
c40	= 0.981754
c05	= 0.900941
c14	= 0.905225
c23	= 0.91022
c32	= 0.91022
c41	= 0.905225
c50	= 0.900941
c06	= 0.569419
c15	= 0.57423
c24	= 0.604833
c33	= 0.616823
c42	= 0.604833
c51	= 0.57423
c60	= 0.569419
c07	= -0.202533
c16	= -0.258961
c25	= -0.154236
c34	= -0.0837496
c43	= -0.0837496
c52	= -0.154236
c61	= -0.258961
c70	= -0.202533
c08	= 0.0216501
c17	= 0.0359873
c26	= -0.00241398
c35	= 0.00838834
c44	= 0.0226256
c53	= 0.0083883
c62	= -0.00241395
c71	= 0.0359873
c80	= 0.0216501
c09	= -0.000964763
c18	= -0.00208442
c27	= 0.0016129
c36	= -0.00207223
c45	= 0.000112246
c54	= 0.000112244
c63	= -0.00207222
c72	= 0.00161289
c81	= -0.00208442
c90	= -0.000964764
c010	= 1.55773e-005
c19	= 4.2997e-005
c28	= -6.11585e-005
c37	= 9.85624e-005
c46	= -9.8591e-005
c55	= 0.000117735
c64	= -9.8591e-005
c73	= 9.85623e-005
c82	= -6.11584e-005
c91	= 4.29969e-005
c100	= 1.55773e-005
/	

Iteration 8
 WSSR : 9.44905e+008 delta(WSSR)/WSSR : -151.447
 delta(WSSR) : -1.43103e+011 limit for stopping : 1e-016
 lambda : 4366.13

resultant parameter values

c00	= 0.999907
c01	= 0.999461
c10	= 0.999461
c02	= 0.996741
c11	= 0.996961
c20	= 0.996741
c03	= 0.980917
c12	= 0.982708
c21	= 0.982708
c30	= 0.980917
c04	= 0.898533
c13	= 0.909289
c22	= 0.911702
c31	= 0.909289
c40	= 0.898533
c05	= 0.555426
c14	= 0.604113
c23	= 0.61939
c32	= 0.619389
c41	= 0.604113
c50	= 0.555425
c06	= -0.294591
c15	= -0.166746
c24	= -0.11894
c33	= -0.101575
c42	= -0.11894
c51	= -0.166746
c60	= -0.294593
c07	= 0.0493688
c16	= -0.00316809
c25	= -0.00686547
c34	= 0.0320629
c43	= 0.0320629
c52	= -0.00686548
c61	= -0.00316793
c70	= 0.0493692
c08	= -0.00394496
c17	= 0.00321298
c26	= 0.000535919
c35	= -0.00611861
c44	= 0.005567
c53	= -0.00611861
c62	= 0.00053593
c71	= 0.00321296
c80	= -0.003945
c09	= 0.000154069
c18	= -0.000254951
c27	= 0.000143501
c36	= 2.68545e-005
c45	= 2.25315e-006
c54	= 2.25468e-006
c63	= 2.68544e-005
c72	= 0.0001435
c81	= -0.000254949
c90	= 0.00015407
c010	= -2.362e-006
c19	= 5.96471e-006
c28	= -7.0152e-006
c37	= 9.35954e-006
c46	= -1.48836e-005
c55	= 1.7215e-005
c64	= -1.48836e-005

```

c73      = 9.35955e-006
c82      = -7.01518e-006
c91      = 5.96468e-006
c100     = -2.36202e-006
/

```

```

Iteration 9
WSSR      : 2.98429e+007    delta(WSSR)/WSSR : -30.6627
delta(WSSR) : -9.15063e+008   limit for stopping : 1e-016
lambda     : 436.613

```

resultant parameter values

```

c00      = 0.998814
c01      = 0.994724
c10      = 0.994724
c02      = 0.97613
c11      = 0.977614
c20      = 0.976129
c03      = 0.899487
c12      = 0.907977
c21      = 0.907976
c30      = 0.899485
c04      = 0.642475
c13      = 0.672507
c22      = 0.685478
c31      = 0.672503
c40      = 0.642467
c05      = 0.0914632
c14      = 0.138545
c23      = 0.203879
c32      = 0.203877
c41      = 0.138534
c50      = 0.0914443
c06      = -0.0985805
c15      = -0.197731
c24      = -0.0512448
c33      = 0.0207219
c42      = -0.0512367
c51      = -0.19773
c60      = -0.0985759
c07      = 0.0173075
c16      = 0.0438263
c25      = -0.0197344
c34      = 0.0171985
c43      = 0.0171997
c52      = -0.0197362
c61      = 0.0438264
c70      = 0.0173072
c08      = -0.00132836
c17      = -0.00392023
c26      = 0.00347813
c35      = -0.00407905
c44      = 0.00260876
c53      = -0.00407909
c62      = 0.00347826
c71      = -0.00392025
c80      = -0.00132836
c09      = 4.83889e-005
c18      = 0.000155102
c27      = -0.000164212
c36      = 0.000160529
c45      = -3.24519e-005
c54      = -3.24457e-005
c63      = 0.000160526
c72      = -0.000164215
c81      = 0.000155103
c90      = 4.83893e-005
c010     = -6.85262e-007
c19      = -2.26335e-006

```

```

c28      = 2.40551e-006
c37      = -1.50942e-006
c46      = -1.28939e-006
c55      = 1.91102e-006
c64      = -1.2895e-006
c73      = -1.50932e-006
c82      = 2.40552e-006
c91      = -2.26336e-006
c100     = -6.85274e-007
/

```

Iteration 10
WSSR : 143401 delta(WSSR)/WSSR : -207.108
delta(WSSR) : -2.96995e+007 limit for stopping : 1e-016
lambda : 43.6613

resultant parameter values

```

c00      = 0.992014
c01      = 0.973293
c10      = 0.973297
c02      = 0.909058
c11      = 0.914567
c20      = 0.909071
c03      = 0.713249
c12      = 0.739095
c21      = 0.739095
c30      = 0.713281
c04      = 0.252399
c13      = 0.326503
c22      = 0.357592
c31      = 0.326471
c40      = 0.252428
c05      = -0.315875
c14      = -0.211506
c23      = -0.122532
c32      = -0.122555
c41      = -0.211618
c50      = -0.315958
c06      = 0.0825262
c15      = 0.0265234
c24      = 0.0182136
c33      = 0.0468584
c42      = 0.0182218
c51      = 0.0265535
c60      = 0.0825531
c07      = -0.00994614
c16      = -0.000156739
c25      = -0.00384829
c34      = -0.00285677
c43      = -0.00285639
c52      = -0.00385043
c61      = -0.000159424
c70      = -0.00994977
c08      = 0.000626668
c17      = -0.000151784
c26      = 0.000396726
c35      = -5.9851e-005
c44      = 0.000377561
c53      = -5.98781e-005
c62      = 0.000396939
c71      = -0.000151696
c80      = 0.000626915
c09      = -2.00519e-005
c18      = 9.01557e-006
c27      = -1.65579e-005
c36      = 4.97679e-006
c45      = -8.04696e-006
c54      = -8.04387e-006
c63      = 4.97583e-006

```

```

c72      = -1.65665e-005
c81      = 9.01549e-006
c90      = -2.00603e-005
c010     = 2.57633e-007
c19      = -1.57552e-007
c28      = 2.4146e-007
c37      = -5.26577e-008
c46      = 1.39791e-008
c55      = 1.56548e-007
c64      = 1.39165e-008
c73      = -5.26088e-008
c82      = 2.41584e-007
c91      = -1.57585e-007
c100     = 2.57746e-007
/

```

Iteration 11
WSSR : 967.419 delta(WSSR)/WSSR : -147.23
delta(WSSR) : -142433 limit for stopping : 1e-016
lambda : 4.36613

resultant parameter values

```

c00      = 0.935436
c01      = 0.843572
c10      = 0.843652
c02      = 0.612021
c11      = 0.649691
c20      = 0.612352
c03      = 0.149001
c12      = 0.265231
c21      = 0.265092
c30      = 0.149846
c04      = -0.328158
c13      = -0.172512
c22      = -0.104451
c31      = -0.173265
c40      = -0.327034
c05      = 0.110034
c14      = 0.00693912
c23      = 0.0546943
c32      = 0.0556867
c41      = 0.00699349
c50      = 0.109388
c06      = -0.0170982
c15      = 0.00418062
c24      = -0.013049
c33      = -0.000143364
c42      = -0.0131955
c51      = 0.00426116
c60      = -0.0169632
c07      = 0.0014576
c16      = -0.00061343
c25      = 0.00113161
c34      = 0.000240391
c43      = 0.000250031
c52      = 0.00113846
c61      = -0.000621375
c70      = 0.00144316
c08      = -7.03212e-005
c17      = 3.52866e-005
c26      = -4.32183e-005
c35      = -3.5182e-005
c44      = 9.86914e-006
c53      = -3.58234e-005
c62      = -4.32116e-005
c71      = 3.56332e-005
c80      = -6.94781e-005
c09      = 1.80548e-006
c18      = -9.34115e-007

```

```

c27      = 6.71031e-007
c36      = 1.37715e-006
c45      = -6.76034e-008
c54      = -5.62e-008
c63      = 1.39236e-006
c72      = 6.62287e-007
c81      = -9.40373e-007
c90      = 1.77987e-006
c010     = -1.92083e-008
c19      = 9.37971e-009
c28      = -1.9478e-009
c37      = -1.74069e-008
c46      = -4.4143e-009
c55      = 4.56914e-009
c64      = -4.61772e-009
c73      = -1.75135e-008
c82      = -1.77131e-009
c91      = 9.404e-009
c100     = -1.88912e-008
/

```

Iteration 12
WSSR : 7.63694 delta(WSSR)/WSSR : -125.676
delta(WSSR) : -959.782 limit for stopping : 1e-016
lambda : 0.436613

resultant parameter values

```

c00      = 0.612165
c01      = 0.382617
c10      = 0.379951
c02      = 0.0405578
c11      = 0.125506
c20      = 0.037303
c03      = -0.198618
c12      = -0.0814025
c21      = -0.0802712
c30      = -0.198053
c04      = 0.0633145
c13      = 0.0287255
c22      = 0.049954
c31      = 0.0197205
c40      = 0.068794
c05      = -0.0074514
c14      = -0.00862782
c23      = -0.00683538
c32      = -0.0065353
c41      = -0.00572259
c50      = -0.00987458
c06      = 0.000200447
c15      = 0.00146716
c24      = 0.000298111
c33      = 0.00115746
c42      = 0.000190773
c51      = 0.00106057
c60      = 0.000643316
c07      = 3.32111e-005
c16      = -0.000135686
c25      = -1.15092e-006
c34      = -6.75018e-005
c43      = -6.11577e-005
c52      = 9.00782e-006
c61      = -0.000103789
c70      = -9.65541e-006
c08      = -3.37077e-006
c17      = 6.93045e-006
c26      = -1.1391e-007
c35      = 1.56255e-006
c44      = 3.56769e-006
c53      = 1.04674e-006

```

```

c62      = -5.24283e-007
c71      = 5.44887e-006
c80      = -1.05841e-006
c09      = 1.23371e-007
c18      = -1.84672e-007
c27      = -6.82579e-009
c36      = -3.27184e-009
c45      = -7.92653e-008
c54      = -6.93488e-008
c63      = 1.11917e-008
c72      = 2.46297e-010
c81      = -1.46281e-007
c90      = 5.75459e-008
c010     = -1.65395e-009
c19      = 2.00404e-009
c28      = 3.06897e-010
c37      = -4.40642e-010
c46      = 9.67998e-010
c55      = 4.1577e-010
c64      = 7.77769e-010
c73      = -5.69105e-010
c82      = 2.72022e-010
c91      = 1.57515e-009
c100     = -8.81835e-010
/

```

Iteration 13
WSSR : 0.293495 delta(WSSR)/WSSR : -25.0207
delta(WSSR) : -7.34344 limit for stopping : 1e-016
lambda : 0.0436613

resultant parameter values

```

c00      = 0.0407811
c01      = 0.0229523
c10      = -0.0119654
c02      = 0.0179133
c11      = 0.0682198
c20      = -0.0154791
c03      = -0.0142766
c12      = -0.0928267
c21      = 0.0496685
c30      = -0.0248191
c04      = 0.000822869
c13      = 0.0369077
c22      = -0.00264965
c31      = -0.0205187
c40      = 0.0162902
c05      = 0.000767166
c14      = -0.00679076
c23      = -0.00179684
c32      = 0.002421
c41      = 0.0039088
c50      = -0.00416597
c06      = -0.000191357
c15      = 0.000675965
c24      = 0.000430309
c33      = -0.000155138
c42      = -0.000283858
c51      = -0.00045954
c60      = 0.000577731
c07      = 2.03458e-005
c16      = -3.8598e-005
c25      = -4.05806e-005
c34      = -3.01389e-006
c43      = 2.08919e-005
c52      = 1.53902e-005
c61      = 3.49554e-005
c70      = -4.72053e-005
c08      = -1.13708e-006

```

```

c17      = 1.23359e-006
c26      = 2.00975e-006
c35      = 5.68878e-007
c44      = -3.84816e-007
c53      = -1.10211e-006
c62      = -3.37183e-007
c71      = -1.67981e-006
c80      = 2.2741e-006
c09      = 3.27333e-008
c18      = -1.90792e-008
c27      = -5.37636e-008
c36      = -1.65421e-008
c45      = -4.75331e-009
c54      = 1.662e-008
c63      = 3.04607e-008
c72      = -2.75426e-009
c81      = 4.64239e-008
c90      = -5.98357e-008
c010     = -3.83328e-010
c19      = 8.14187e-011
c28      = 6.62301e-010
c37      = -3.27368e-011
c46      = 5.20696e-010
c55      = -5.09238e-010
c64      = 1.39862e-010
c73      = -5.16866e-010
c82      = 2.096e-010
c91      = -5.63688e-010
c100     = 6.63851e-010
/

```

```

Iteration 14
WSSR    : 0.259229      delta(WSSR)/WSSR : -0.132183
delta(WSSR) : -0.0342657   limit for stopping : 1e-016
lambda    : 0.00436613

```

resultant parameter values

```

c00      = 0.584592
c01      = -0.791879
c10      = -0.861258
c02      = 0.531963
c11      = 0.613324
c20      = 0.552605
c03      = -0.169754
c12      = -0.338154
c21      = -0.102036
c30      = -0.238322
c04      = 0.0273131
c13      = 0.0951943
c22      = 0.0401762
c31      = 0.00810182
c40      = 0.0644966
c05      = -0.00193339
c14      = -0.014961
c23      = -0.00904527
c32      = -0.00223139
c41      = 7.00052e-005
c50      = -0.011035
c06      = -2.75607e-005
c15      = 0.00139332
c24      = 0.00116335
c33      = 0.00038011
c42      = 6.23124e-005
c51      = -0.000102079
c60      = 0.001211
c07      = 1.49998e-005
c16      = -7.8581e-005
c25      = -8.62349e-005
c34      = -4.02923e-005

```

```

c43      = -4.66448e-006
c52      = -2.43864e-006
c61      = 1.27123e-005
c70      = -8.49253e-005
c08      = -1.08315e-006
c17      = 2.60877e-006
c26      = 3.73433e-006
c35      = 2.10251e-006
c44      = 7.65434e-007
c53      = -3.22092e-007
c62      = 2.73149e-007
c71      = -8.04602e-007
c80      = 3.67607e-006
c09      = 3.43341e-008
c18      = -4.57027e-008
c27      = -9.00874e-008
c36      = -5.10834e-008
c45      = -3.26462e-008
c54      = -3.53928e-009
c63      = 1.65077e-008
c72      = -1.52259e-008
c81      = 2.68145e-008
c90      = -8.94109e-008
c010     = -4.20714e-010
c19      = 3.03268e-010
c28      = 9.90071e-010
c37      = 2.96612e-010
c46      = 8.02406e-010
c55      = -2.92012e-010
c64      = 2.94696e-010
c73      = -4.04844e-010
c82      = 3.24159e-010
c91      = -3.73483e-010
c100     = 9.34322e-010
/

```

Iteration 15
WSSR : 0.247776 delta(WSSR)/WSSR : -0.0462256
delta(WSSR) : -0.0114536 limit for stopping : 1e-016
lambda : 0.000436613

resultant parameter values

```

c00      = 2.31528
c01      = -2.60092
c10      = -2.73738
c02      = 1.65326
c11      = 1.29665
c20      = 1.72777
c03      = -0.564543
c12      = -0.555767
c21      = -0.32337
c30      = -0.654346
c04      = 0.112349
c13      = 0.142653
c22      = 0.0780443
c31      = 0.0568218
c40      = 0.15444
c05      = -0.0136914
c14      = -0.0217678
c23      = -0.0139782
c32      = -0.0072094
c41      = -0.00696341
c50      = -0.0235065
c06      = 0.00103789
c15      = 0.00203484
c24      = 0.00161129
c33      = 0.00077758
c42      = 0.000517178
c51      = 0.000564205

```

```

c60      = 0.0023436
c07      = -4.79461e-005
c16      = -0.000117894
c25      = -0.000113345
c34      = -6.27489e-005
c43      = -2.72454e-005
c52      = -3.01081e-005
c61      = -2.82901e-005
c70      = -0.000151958
c08      = 1.25222e-006
c17      = 4.11586e-006
c26      = 4.77212e-006
c35      = 2.92988e-006
c44      = 1.53469e-006
c53      = 5.13336e-007
c62      = 1.33704e-006
c71      = 7.72762e-007
c80      = 6.16677e-006
c09      = -1.50644e-008
c18      = -7.85156e-008
c27      = -1.12767e-007
c36      = -6.87714e-008
c45      = -4.83049e-008
c54      = -1.92547e-008
c63      = -1.41707e-009
c72      = -3.85669e-008
c81      = -7.63092e-009
c90      = -1.42161e-007
c010     = 3.3683e-011
c19      = 6.12887e-010
c28      = 1.20538e-009
c37      = 4.62401e-010
c46      = 9.44574e-010
c55      = -1.56644e-010
c64      = 4.37786e-010
c73      = -2.36279e-010
c82      = 5.46524e-010
c91      = -4.76291e-011
c100     = 1.42007e-009
/

```

Iteration 16

```

WSSR      : 0.24777      delta(WSSR)/WSSR  : -2.38677e-005
delta(WSSR) : -5.91371e-006  limit for stopping : 1e-016
lambda    : 4.36613e-005

```

resultant parameter values

```

c00      = 2.35553
c01      = -2.64327
c10      = -2.78065
c02      = 1.67978
c11      = 1.31206
c20      = 1.75502
c03      = -0.573944
c12      = -0.560685
c21      = -0.328353
c30      = -0.664028
c04      = 0.114383
c13      = 0.143736
c22      = 0.0788839
c31      = 0.0579265
c40      = 0.156538
c05      = -0.0139738
c14      = -0.0219247
c23      = -0.0140875
c32      = -0.00731974
c41      = -0.00712403
c50      = -0.023798
c06      = 0.00106354

```

```

c15      = 0.00204975
c24      = 0.00162128
c33      = 0.000786303
c42      = 0.000527318
c51      = 0.000579508
c60      = 0.00237009
c07      = -4.94648e-005
c16      = -0.000118815
c25      = -0.000113954
c34      = -6.32412e-005
c43      = -2.7741e-005
c52      = -3.07292e-005
c61      = -2.92361e-005
c70      = -0.000153527
c08      = 1.30866e-006
c17      = 4.15135e-006
c26      = 4.79565e-006
c35      = 2.94809e-006
c44      = 1.55145e-006
c53      = 5.31751e-007
c62      = 1.36108e-006
c71      = 8.09281e-007
c80      = 6.2251e-006
c09      = -1.62597e-008
c18      = -7.92921e-008
c27      = -1.13285e-007
c36      = -6.91626e-008
c45      = -4.86457e-008
c54      = -1.95973e-008
c63      = -1.81442e-009
c72      = -3.90972e-008
c81      = -8.43061e-009
c90      = -1.43397e-007
c010     = 4.46902e-011
c19      = 6.20244e-010
c28      = 1.21033e-009
c37      = 4.66089e-010
c46      = 9.47675e-010
c55      = -1.53711e-010
c64      = 4.40914e-010
c73      = -2.32521e-010
c82      = 5.51599e-010
c91      = -4.00474e-011
c100     = 1.43145e-009
/

```

Iteration 17

```

WSSR      : 0.24777      delta(WSSR)/WSSR  : -1.42513e-011
delta(WSSR) : -3.53104e-012  limit for stopping : 1e-016
lambda    : 4.36613e-006

```

resultant parameter values

```

c00      = 2.35554
c01      = -2.64329
c10      = -2.78066
c02      = 1.67979
c11      = 1.31207
c20      = 1.75503
c03      = -0.573949
c12      = -0.560687
c21      = -0.328354
c30      = -0.664031
c04      = 0.114384
c13      = 0.143737
c22      = 0.0788842
c31      = 0.0579268
c40      = 0.156539
c05      = -0.0139739
c14      = -0.0219248

```

```

c23      = -0.0140876
c32      = -0.00731977
c41      = -0.00712407
c50      = -0.023798
c06      = 0.00106355
c15      = 0.00204976
c24      = 0.00162129
c33      = 0.000786306
c42      = 0.000527321
c51      = 0.000579512
c60      = 0.0023701
c07      = -4.94656e-005
c16      = -0.000118815
c25      = -0.000113955
c34      = -6.32414e-005
c43      = -2.77412e-005
c52      = -3.07294e-005
c61      = -2.92363e-005
c70      = -0.000153528
c08      = 1.30869e-006
c17      = 4.15137e-006
c26      = 4.79566e-006
c35      = 2.94809e-006
c44      = 1.55146e-006
c53      = 5.31755e-007
c62      = 1.36108e-006
c71      = 8.09291e-007
c80      = 6.22512e-006
c09      = -1.62604e-008
c18      = -7.92924e-008
c27      = -1.13285e-007
c36      = -6.91627e-008
c45      = -4.86459e-008
c54      = -1.95974e-008
c63      = -1.81449e-009
c72      = -3.90973e-008
c81      = -8.43083e-009
c90      = -1.43397e-007
c010     = 4.46965e-011
c19      = 6.20247e-010
c28      = 1.21033e-009
c37      = 4.66091e-010
c46      = 9.47676e-010
c55      = -1.53709e-010
c64      = 4.40915e-010
c73      = -2.3252e-010
c82      = 5.516e-010
c91      = -4.00453e-011
c100     = 1.43145e-009
/

```

Iteration 18
WSSR : 0.24777 delta(WSSR)/WSSR : -4.33265e-011
delta(WSSR) : -1.0735e-011 limit for stopping : 1e-016
lambda : 4.36613e-007

resultant parameter values

```

c00      = 2.35554
c01      = -2.64329
c10      = -2.78067
c02      = 1.67979
c11      = 1.31207
c20      = 1.75503
c03      = -0.573948
c12      = -0.560687
c21      = -0.328355
c30      = -0.664032
c04      = 0.114384
c13      = 0.143737

```

```

c22      = 0.0788843
c31      = 0.057927
c40      = 0.156539
c05      = -0.0139739
c14      = -0.0219248
c23      = -0.0140876
c32      = -0.00731979
c41      = -0.0071241
c50      = -0.0237981
c06      = 0.00106355
c15      = 0.00204976
c24      = 0.00162129
c33      = 0.000786307
c42      = 0.000527323
c51      = 0.000579514
c60      = 0.0023701
c07      = -4.94655e-005
c16      = -0.000118815
c25      = -0.000113955
c34      = -6.32414e-005
c43      = -2.77413e-005
c52      = -3.07295e-005
c61      = -2.92365e-005
c70      = -0.000153528
c08      = 1.30868e-006
c17      = 4.15136e-006
c26      = 4.79566e-006
c35      = 2.94809e-006
c44      = 1.55146e-006
c53      = 5.3176e-007
c62      = 1.36109e-006
c71      = 8.09296e-007
c80      = 6.22512e-006
c09      = -1.62603e-008
c18      = -7.92924e-008
c27      = -1.13285e-007
c36      = -6.91628e-008
c45      = -4.86459e-008
c54      = -1.95974e-008
c63      = -1.8146e-009
c72      = -3.90974e-008
c81      = -8.43092e-009
c90      = -1.43397e-007
c010     = 4.46954e-011
c19      = 6.20246e-010
c28      = 1.21033e-009
c37      = 4.66091e-010
c46      = 9.47677e-010
c55      = -1.53709e-010
c64      = 4.40916e-010
c73      = -2.32519e-010
c82      = 5.51601e-010
c91      = -4.00444e-011
c100     = 1.43145e-009
***** */

```

Iteration 19

```

WSSR      : 0.24777      delta(WSSR)/WSSR  : -6.70897e-013
delta(WSSR) : -1.66228e-013   limit for stopping : 1e-016
lambda    : 43661.3

```

resultant parameter values

```

c00      = 2.35554
c01      = -2.64329
c10      = -2.78067
c02      = 1.67979
c11      = 1.31207
c20      = 1.75503
c03      = -0.573948

```

```

c12      = -0.560687
c21      = -0.328355
c30      = -0.664032
c04      = 0.114384
c13      = 0.143737
c22      = 0.0788843
c31      = 0.057927
c40      = 0.156539
c05      = -0.0139739
c14      = -0.0219248
c23      = -0.0140876
c32      = -0.00731979
c41      = -0.0071241
c50      = -0.0237981
c06      = 0.00106355
c15      = 0.00204976
c24      = 0.00162129
c33      = 0.000786307
c42      = 0.000527323
c51      = 0.000579514
c60      = 0.0023701
c07      = -4.94655e-005
c16      = -0.000118815
c25      = -0.000113955
c34      = -6.32414e-005
c43      = -2.77413e-005
c52      = -3.07295e-005
c61      = -2.92365e-005
c70      = -0.000153528
c08      = 1.30868e-006
c17      = 4.15136e-006
c26      = 4.79566e-006
c35      = 2.94809e-006
c44      = 1.55146e-006
c53      = 5.3176e-007
c62      = 1.36109e-006
c71      = 8.09296e-007
c80      = 6.22512e-006
c09      = -1.62603e-008
c18      = -7.92924e-008
c27      = -1.13285e-007
c36      = -6.91628e-008
c45      = -4.86459e-008
c54      = -1.95974e-008
c63      = -1.8146e-009
c72      = -3.90974e-008
c81      = -8.43092e-009
c90      = -1.43397e-007
c010     = 4.46954e-011
c19      = 6.20246e-010
c28      = 1.21033e-009
c37      = 4.66091e-010
c46      = 9.47677e-010
c55      = -1.53709e-010
c64      = 4.40916e-010
c73      = -2.32519e-010
c82      = 5.51601e-010
c91      = -4.00444e-011
c100     = 1.43145e-009
***** */

```

```

Iteration 20
WSSR      : 0.24777      delta(WSSR)/WSSR  : -1.71852e-012
delta(WSSR) : -4.25798e-013  limit for stopping : 1e-016
lambda    : 4.36613e+011

```

resultant parameter values

```

c00      = 2.35554
c01      = -2.64329

```

```

c10      = -2.78067
c02      = 1.67979
c11      = 1.31207
c20      = 1.75503
c03      = -0.573948
c12      = -0.560687
c21      = -0.328355
c30      = -0.664032
c04      = 0.114384
c13      = 0.143737
c22      = 0.0788843
c31      = 0.057927
c40      = 0.156539
c05      = -0.0139739
c14      = -0.0219248
c23      = -0.0140876
c32      = -0.00731979
c41      = -0.0071241
c50      = -0.0237981
c06      = 0.00106355
c15      = 0.00204976
c24      = 0.00162129
c33      = 0.000786307
c42      = 0.000527323
c51      = 0.000579514
c60      = 0.0023701
c07      = -4.94655e-005
c16      = -0.000118815
c25      = -0.000113955
c34      = -6.32414e-005
c43      = -2.77413e-005
c52      = -3.07295e-005
c61      = -2.92365e-005
c70      = -0.000153528
c08      = 1.30868e-006
c17      = 4.15136e-006
c26      = 4.79566e-006
c35      = 2.94809e-006
c44      = 1.55146e-006
c53      = 5.3176e-007
c62      = 1.36109e-006
c71      = 8.09296e-007
c80      = 6.22512e-006
c09      = -1.62603e-008
c18      = -7.92924e-008
c27      = -1.13285e-007
c36      = -6.91628e-008
c45      = -4.86459e-008
c54      = -1.95974e-008
c63      = -1.8146e-009
c72      = -3.90974e-008
c81      = -8.43092e-009
c90      = -1.43397e-007
c010     = 4.46954e-011
c19      = 6.20246e-010
c28      = 1.21033e-009
c37      = 4.66091e-010
c46      = 9.47677e-010
c55      = -1.53709e-010
c64      = 4.40916e-010
c73      = -2.32519e-010
c82      = 5.51601e-010
c91      = -4.00444e-011
c100     = 1.43145e-009
*/

```

```

Iteration 21
WSSR      : 0.24777      delta(WSSR)/WSSR : -3.20494e-013
delta(WSSR) : -7.94087e-014    limit for stopping : 1e-016
lambda    : 4.36613e+011

```

resultant parameter values

c00	= 2.35554
c01	= -2.64329
c10	= -2.78067
c02	= 1.67979
c11	= 1.31207
c20	= 1.75503
c03	= -0.573948
c12	= -0.560687
c21	= -0.328355
c30	= -0.664032
c04	= 0.114384
c13	= 0.143737
c22	= 0.0788843
c31	= 0.057927
c40	= 0.156539
c05	= -0.0139739
c14	= -0.0219248
c23	= -0.0140876
c32	= -0.00731979
c41	= -0.0071241
c50	= -0.0237981
c06	= 0.00106355
c15	= 0.00204976
c24	= 0.00162129
c33	= 0.000786307
c42	= 0.000527323
c51	= 0.000579514
c60	= 0.0023701
c07	= -4.94655e-005
c16	= -0.000118815
c25	= -0.000113955
c34	= -6.32414e-005
c43	= -2.77413e-005
c52	= -3.07295e-005
c61	= -2.92365e-005
c70	= -0.000153528
c08	= 1.30868e-006
c17	= 4.15136e-006
c26	= 4.79566e-006
c35	= 2.94809e-006
c44	= 1.55146e-006
c53	= 5.3176e-007
c62	= 1.36109e-006
c71	= 8.09296e-007
c80	= 6.22512e-006
c09	= -1.62603e-008
c18	= -7.92924e-008
c27	= -1.13285e-007
c36	= -6.91628e-008
c45	= -4.86459e-008
c54	= -1.95974e-008
c63	= -1.8146e-009
c72	= -3.90974e-008
c81	= -8.43092e-009
c90	= -1.43397e-007
c010	= 4.46954e-011
c19	= 6.20246e-010
c28	= 1.21033e-009
c37	= 4.66091e-010
c46	= 9.47677e-010
c55	= -1.53709e-010
c64	= 4.40916e-010
c73	= -2.32519e-010
c82	= 5.51601e-010
c91	= -4.00444e-011
c100	= 1.43145e-009

After 22 iterations the fit converged.
final sum of squares of residuals : 0.24777
rel. change during last iteration : 0

degrees of freedom (FIT_NDF) : 295
rms of residuals (FIT_STDFIT) = sqrt(WSSR/ndf) : 0.028981
variance of residuals (reduced chisquare) = WSSR/ndf : 0.000839898

	Final set of parameters	Asymptotic Standard Error
c00	= 2.35554	+/- 0.4838 (20.54%)
c01	= -2.64329	+/- 0.6553 (24.79%)
c10	= -2.78067	+/- 0.6553 (23.57%)
c02	= 1.67979	+/- 0.4667 (27.78%)
c11	= 1.31207	+/- 0.2637 (20.1%)
c20	= 1.75503	+/- 0.4667 (26.59%)
c03	= -0.573948	+/- 0.1817 (31.66%)
c12	= -0.560687	+/- 0.09591 (17.11%)
c21	= -0.328355	+/- 0.09591 (29.21%)
c30	= -0.664032	+/- 0.1817 (27.36%)
c04	= 0.114384	+/- 0.04288 (37.49%)
c13	= 0.143737	+/- 0.0228 (15.86%)
c22	= 0.0788843	+/- 0.0193 (24.46%)
c31	= 0.057927	+/- 0.0228 (39.36%)
c40	= 0.156539	+/- 0.04288 (27.39%)
c05	= -0.0139739	+/- 0.006476 (46.35%)
c14	= -0.0219248	+/- 0.00353 (16.1%)
c23	= -0.0140876	+/- 0.002803 (19.9%)
c32	= -0.00731979	+/- 0.002803 (38.29%)
c41	= -0.0071241	+/- 0.00353 (49.55%)
c50	= -0.0237981	+/- 0.006476 (27.21%)
c06	= 0.00106355	+/- 0.00064 (60.18%)
c15	= 0.00204976	+/- 0.0003612 (17.62%)
c24	= 0.00162129	+/- 0.0002784 (17.17%)
c33	= 0.000786307	+/- 0.0002574 (32.73%)
c42	= 0.000527323	+/- 0.0002784 (52.79%)
c51	= 0.000579514	+/- 0.0003612 (62.32%)
c60	= 0.0023701	+/- 0.00064 (27%)
c07	= -4.94655e-005	+/- 4.118e-005 (83.25%)
c16	= -0.000118815	+/- 2.432e-005 (20.47%)
c25	= -0.000113955	+/- 1.851e-005 (16.24%)
c34	= -6.32414e-005	+/- 1.637e-005 (25.88%)
c43	= -2.77413e-005	+/- 1.637e-005 (59.01%)
c52	= -3.07295e-005	+/- 1.851e-005 (60.22%)
c61	= -2.92365e-005	+/- 2.432e-005 (83.18%)
c70	= -0.000153528	+/- 4.118e-005 (26.82%)
c08	= 1.30868e-006	+/- 1.661e-006 (127%)
c17	= 4.15136e-006	+/- 1.041e-006 (25.07%)
c26	= 4.79566e-006	+/- 7.962e-007 (16.6%)
c35	= 2.94809e-006	+/- 6.847e-007 (23.22%)
c44	= 1.55146e-006	+/- 6.524e-007 (42.05%)
c53	= 5.3176e-007	+/- 6.847e-007 (128.8%)
c62	= 1.36109e-006	+/- 7.962e-007 (58.5%)
c71	= 8.09296e-007	+/- 1.041e-006 (128.6%)
c80	= 6.22512e-006	+/- 1.661e-006 (26.69%)
c09	= -1.62603e-008	+/- 3.815e-008 (234.6%)
c18	= -7.92924e-008	+/- 2.574e-008 (32.46%)
c27	= -1.13285e-007	+/- 2.04e-008 (18%)
c36	= -6.91628e-008	+/- 1.743e-008 (25.2%)
c45	= -4.86459e-008	+/- 1.607e-008 (33.03%)
c54	= -1.95974e-008	+/- 1.607e-008 (81.99%)
c63	= -1.8146e-009	+/- 1.743e-008 (960.7%)
c72	= -3.90974e-008	+/- 2.04e-008 (52.17%)
c81	= -8.43092e-009	+/- 2.574e-008 (305.3%)
c90	= -1.43397e-007	+/- 3.815e-008 (26.6%)
c010	= 4.46954e-011	+/- 3.801e-010 (850.5%)
c19	= 6.20246e-010	+/- 2.807e-010 (45.25%)
c28	= 1.21033e-009	+/- 2.41e-010 (19.91%)
c37	= 4.66091e-010	+/- 2.187e-010 (46.93%)

c46	= 9.47677e-010	+/- 2.069e-010	(21.83%)
c55	= -1.53709e-010	+/- 2.032e-010	(132.2%)
c64	= 4.40916e-010	+/- 2.069e-010	(46.93%)
c73	= -2.32519e-010	+/- 2.187e-010	(94.07%)
c82	= 5.51601e-010	+/- 2.41e-010	(43.7%)
c91	= -4.00444e-011	+/- 2.807e-010	(700.9%)
c100	= 1.43145e-009	+/- 3.801e-010	(26.56%)

correlation matrix of the fit parameters:

c41	c50	c06	c15	c24	c33	c42	c51	c60	c07	c16	c25	c34	c43	c52	c61	c70	c08	c17	c26	c35	c44	
c53	c62	c71	c80	c09	c18	c27	c36	c45	c54	c63	c72	c81	c90	c010	c19	c28	c37	c46	c55	c64	c73	
c82	c91	c100																				
c00																						
c01	1.000																					
c10	-0.774	1.000																				
c02	-0.774	0.215	1.000																			
c11	0.663	-0.966	-0.096	1.000																		
c20	0.722	-0.557	-0.557	0.348	1.000																	
c03	0.663	-0.096	-0.966	0.023	0.348	1.000																
c12	-0.592	0.908	0.053	-0.983	-0.224	-0.008	1.000															
c21	-0.630	0.681	0.301	-0.515	-0.865	-0.118	0.371	1.000														
c30	-0.592	0.053	0.908	-0.008	-0.224	-0.983	0.002	0.050	0.371	1.000												
c04	0.535	-0.846	-0.032	0.944	0.147	0.003	-0.988	-0.261	-0.022	-0.000	1.000											
c13	0.575	-0.718	-0.189	0.608	0.676	0.048	-0.476	-0.935	-0.281	-0.013	0.357	1.000										
c22	0.533	-0.419	-0.419	0.224	0.930	0.224	-0.114	-0.804	-0.804	-0.114	0.056	0.556	1.000									
c31	0.575	-0.189	-0.718	0.048	0.676	0.608	-0.013	-0.281	-0.935	-0.476	0.004	0.105	0.556	1.000								
c40	0.535	-0.032	-0.846	0.003	0.147	0.944	-0.000	-0.022	-0.261	-0.988	0.000	0.004	0.056	0.357	1.000							
c05	-0.485	0.784	0.020	-0.896	-0.096	-0.001	0.959	0.180	0.010	0.000	-0.991	-0.257	-0.027	-0.001	-0.000	1.000						
c14	-0.531	0.716	0.128	-0.653	-0.519	-0.022	0.543	0.809	0.151	0.004	-0.428	-0.958	-0.353	-0.038	-0.001	0.322						
1.000																						
c23	-0.476	0.474	0.280	-0.305	-0.830	-0.107	0.178	0.911	0.537	0.038	-0.098	-0.756	-0.892	-0.270	-0.013	0.050						
0.550	1.000																					
c32	-0.476	0.280	0.474	-0.107	-0.830	-0.305	0.038	0.537	0.911	0.178	-0.013	-0.270	-0.892	-0.756	-0.098	0.004						
0.120	0.605	1.000																				
c41	-0.531	0.128	0.716	-0.022	-0.519	-0.653	0.004	0.151	0.809	0.543	-0.001	-0.038	-0.353	-0.958	-0.428	0.000						
0.009	0.120	0.550	1.000																			
c50	-0.485	0.020	0.784	-0.001	-0.096	-0.896	0.000	0.010	0.180	0.959	-0.000	-0.001	-0.027	-0.257	-0.991	0.000						
0.000	0.004	0.050	0.322	1.000																		
c06	0.441	-0.724	-0.012	0.843	0.061	0.000	-0.920	-0.120	-0.004	-0.000	0.968	0.178	0.012	0.000	0.000	-0.993						
0.230	-0.023	-0.001	-0.000	-0.000	1.000																	
c15	0.487	-0.691	-0.090	0.663	0.395	0.010	-0.579	-0.671	-0.080	-0.001	0.476	0.862	0.210	0.013	0.000	-0.371						
0.968	-0.365	-0.048	-0.002	-0.000	0.273	1.000																
c24	0.435	-0.493	-0.199	0.359	0.698	0.055	-0.232	-0.901	-0.340	-0.013	0.138	0.858	0.692	0.121	0.003	-0.076						
0.701	-0.926	-0.345	-0.036	-0.001	0.037	0.512	1.000															
c33	0.411	-0.328	-0.328	0.161	0.807	0.161	-0.069	-0.698	-0.698	-0.069	0.027	0.440	0.957	0.440	0.027	-0.009						
0.234	-0.852	-0.852	-0.234	-0.009	0.003	0.106	0.602	1.000														
c42	0.435	-0.199	-0.493	0.055	0.698	0.359	-0.013	-0.340	-0.901	-0.232	0.003	0.121	0.692	0.858	0.138	-0.001						
0.036	-0.345	-0.926	-0.701	-0.076	0.000	0.009	0.136	0.602	1.000													
c51	0.487	-0.090	-0.691	0.010	0.395	0.663	-0.001	-0.080	-0.671	-0.579	0.000	0.013	0.210	0.862	0.476	-0.000						
0.002	-0.048	-0.365	-0.968	-0.371	-0.000	0.000	0.009	0.106	0.512	1.000												
c60	0.441	-0.012	-0.724	0.000	0.061	0.843	-0.000	-0.004	-0.120	-0.920	0.000	0.000	0.012	0.178	0.968	-0.000						
0.000	-0.001	-0.023	-0.230	-0.993	0.000	0.000	0.000	0.003	0.037	0.273	1.000											
c07	-0.402	0.668	0.007	-0.791	-0.037	-0.000	0.877	0.075	0.001	0.000	-0.936	-0.115	-0.004	-0.000	-0.000	0.974						
0.154	0.009	0.000	0.000	-0.994	-0.187	-0.015	-0.000	-0.000	0.000	0.000	-0.116	-0.004	-0.000	0.401								
c16	-0.442	0.648	0.064	-0.647	-0.297	-0.005	0.587	0.541	0.040	0.000	-0.499	-0.743	-0.116	-0.004	-0.000	0.401						
0.888	0.220	0.016	0.000	0.000	-0.304	-0.973	-0.334	-0.039	-0.001	-0.000	-0.000	0.213	1.000									
c25	-0.396	0.487	0.145	-0.387	-0.569	-0.029	0.270	0.825	0.208	0.005	-0.172	-0.876	-0.493	-0.051	-0.001	0.099						
0.787	0.763	0.173	0.009	0.000	-0.051	-0.625	-0.941	-0.358	-0.042	-0.001	-0.000	0.022	0.439	1.000								
c34	-0.364	0.346	0.237	-0.201	-0.717	-0.089	0.099	0.758	0.490	0.028	-0.043	-0.569	-0.853	-0.230	-0.007	0.016						
0.349	0.940	0.586	0.085	0.001	-0.005	-0.180	-0.801	-0.890	-0.297	-0.024	-0.000	0.001	0.073	0.559	1.000							
c43	-0.364	0.237	0.346	-0.089	-0.717	-0.201	0.028	0.490	0.758	0.099	-0.007	-0.230	-0.853	-0.569	-0.043	0.001						
0.085	0.586	0.940	0.349	0.016	-0.000	-0.024	-0.297	-0.890	-0.801	-0.180	-0.005	0.000	0.004	0.112	0.594	1.000						
c52	-0.396	0.145	0.487	-0.029	-0.569	-0.387	0.005	0.208	0.825	0.270	-0.001	-0.051	-0.493	-0.876	-0.172	0.000						
0.009	0.173	0.763	0.787	0.099	-0.000	-0.001	-0.042	-0.358	-0.941	-0.625	-0.051	0.000	0.000	0.006	0.112	0.559	1.000					
c61	-0.442	0.064	0.648	-0.005	-0.297	-0.647	0.000	0.040	0.541	0.587	-0.000	-0.004	-0.116	-0.743	-0.499	-0.000						
0.000	0.016	0.220	0.888	0.401	0.000	0.000	-0.001	-0.039	-0.334	-0.973	-0.304	-0.000	-0.000	-0.000	0.004	0.073	0.439	1.000				
c70	-0.402	0.007	0.668	-0.000	-0.037	-0.791	0.000	0.001	0.075	0.877	-0.000	-0.000	-0.004	-0.115	-0.936	0.000						

0.000	0.000	0.009	0.154	0.974	-0.000	-0.000	-0.000	-0.015	-0.187	-0.994	0.000	0.000	0.000	0.000	0.001	0.022	0.213	
1.000																		
c08	0.368	-0.617	-0.004	0.739	0.020	0.000	-0.831	-0.042	-0.000	-0.000	0.899	0.066	0.001	0.000	0.000	-0.948	-0.000	
0.091	-0.002	-0.000	-0.000	-0.000	0.979	0.113	0.004	0.000	0.000	-0.000	0.000	-0.995	-0.132	-0.006	-0.000	-0.000	0.000	-0.000
1.000																		
c17	0.395	-0.594	-0.045	0.611	0.221	0.002	-0.572	-0.425	-0.018	-0.000	0.500	0.618	0.056	0.001	0.000	-0.413	-0.782	
-0.114	-0.003	-0.000	-0.000	0.320	0.903	0.187	0.009	0.000	0.000	-0.000	-0.230	-0.976	-0.262	-0.019	-0.000	-0.000	-0.000	
0.000	0.145	1.000																
c26	0.353	-0.459	-0.106	0.388	0.449	0.016	-0.288	-0.712	-0.123	-0.002	0.193	0.824	0.327	0.019	0.000	-0.117	-0.804	
-0.571	-0.073	-0.002	-0.000	0.063	0.687	0.793	0.174	0.008	-0.000	0.000	-0.028	-0.517	-0.946	-0.314	-0.026	0.000	0.000	
0.000	0.008	0.328	1.000															
c35	0.320	-0.341	-0.174	0.223	0.602	0.050	-0.123	-0.737	-0.326	-0.011	0.059	0.633	0.678	0.111	0.002	-0.024	-0.440	
-0.888	-0.348	-0.026	-0.000	0.008	0.252	0.889	0.653	0.114	0.003	-0.000	-0.002	-0.113	-0.720	-0.904	-0.292	-0.021	0.000	
0.000	0.000	0.032	0.463	1.000														
c44	0.308	-0.249	-0.249	0.115	0.654	0.115	-0.043	-0.566	-0.566	-0.043	0.013	0.329	0.835	0.329	0.013	-0.003	-0.145	
-0.740	-0.740	-0.145	-0.003	0.000	0.047	0.470	0.947	0.470	0.047	0.000	-0.000	-0.009	-0.216	-0.838	-0.838	-0.216	-0.009	
0.000	0.000	0.060	0.530	1.000														
c53	0.320	-0.174	-0.341	0.050	0.602	0.223	-0.011	-0.326	-0.737	-0.123	0.002	0.111	0.678	0.633	0.059	-0.000	-0.026	
-0.348	-0.888	-0.440	-0.024	0.000	0.003	0.114	0.653	0.889	0.252	0.008	-0.000	-0.000	-0.021	-0.292	-0.904	-0.720	-0.113	
0.002	0.000	0.000	0.072	0.530	1.000													
c62	0.353	-0.106	-0.459	0.016	0.449	0.388	-0.002	-0.123	-0.712	-0.288	0.000	0.019	0.327	0.824	0.193	-0.000	-0.002	
-0.073	-0.571	-0.804	-0.117	0.000	0.000	0.008	0.174	0.793	0.687	0.063	-0.000	-0.000	0.000	-0.026	-0.314	-0.946	-0.517	
0.028	0.000	0.000	-0.000	-0.000	0.060	0.463	1.000											
c71	0.395	-0.045	-0.594	0.002	0.221	0.611	-0.000	-0.018	-0.425	-0.572	-0.000	0.001	0.056	0.618	0.500	0.000	-0.003	
-0.114	-0.782	-0.413	-0.000	-0.000	0.009	0.187	0.903	0.320	0.000	0.000	0.000	0.000	-0.019	-0.262	-0.976	-0.230	-0.000	
0.000	0.000	0.000	0.032	0.328	1.000													
c80	0.368	-0.004	-0.617	0.000	0.020	0.739	-0.000	-0.000	-0.042	-0.831	0.000	0.000	0.001	0.066	0.899	-0.000	-0.000	
-0.000	-0.000	-0.002	-0.091	-0.948	0.000	0.000	0.000	0.004	0.113	0.979	-0.000	-0.000	-0.000	-0.000	-0.006	-0.132	-0.995	
0.000	0.000	0.000	-0.000	-0.000	0.000	0.000	0.008	0.145	1.000									
c09	-0.337	0.570	0.002	-0.690	-0.009	-0.000	0.785	0.018	0.000	0.000	-0.860	-0.029	-0.000	-0.000	-0.000	0.916	0.040	
0.000	-0.996	-0.068	-0.000	-0.000	-0.000	-0.000	0.000	0.000	0.000	0.000	0.982	0.061	0.000	0.000	0.000	0.000	-0.000	
c18	-0.347	0.532	0.032	-0.561	-0.161	-0.001	0.538	0.326	0.006	0.000	-0.483	-0.499	-0.020	-0.000	-0.000	0.408	0.664	
0.044	0.000	0.000	-0.323	-0.806	-0.076	-0.000	-0.000	-0.000	-0.000	0.236	0.914	0.113	0.000	0.000	0.000	-0.000	-0.151	
-0.979	-0.150	-0.000	-0.000	-0.000	0.000	0.000	0.000	0.072	1.000									
c27	-0.302	0.409	0.075	-0.362	-0.339	-0.008	0.282	0.576	0.067	0.000	-0.198	-0.718	-0.199	-0.005	-0.000	0.125	0.751	
0.388	0.022	0.000	0.000	-0.070	-0.686	-0.601	-0.059	-0.000	-0.000	0.032	0.548	0.801	0.120	0.000	0.000	0.000	-0.010	
0.000	-0.368	-0.946	-0.201	-0.000	-0.000	0.000	-0.000	0.000	0.177	1.000								
c36	-0.269	0.310	0.124	-0.221	-0.472	-0.028	0.132	0.645	0.202	0.004	-0.068	-0.618	-0.483	-0.047	-0.000	0.030	0.475	
0.731	0.175	0.005	-0.000	-0.010	-0.299	-0.843	-0.396	-0.029	0.000	0.000	0.002	0.147	0.782	0.665	0.091	-0.000	-0.000	
0.000	-0.000	-0.045	-0.573	-0.899	-0.208	-0.000	0.000	0.000	0.000	0.000	0.283	1.000						
c45	-0.254	0.236	0.176	-0.127	-0.542	-0.065	0.054	0.558	0.385	0.018	-0.019	-0.383	-0.696	-0.169	-0.004	0.005	0.197	
0.755	0.483	0.050	0.000	-0.001	-0.074	-0.583	-0.791	-0.211	-0.008	0.000	0.000	0.016	0.322	0.900	0.505	0.049	-0.000	
0.197	0.000	-0.105	-0.733	-0.835	-0.169	0.000	0.000	0.000	0.000	0.000	0.367	1.000						
c54	-0.254	0.176	0.236	-0.065	-0.542	-0.127	0.018	0.385	0.558	0.054	-0.004	-0.169	-0.696	-0.383	-0.019	0.000	0.050	
0.483	0.755	0.197	0.005	-0.000	-0.008	-0.211	-0.791	-0.583	-0.074	-0.001	0.000	0.000	0.049	0.505	0.900	0.322	0.016	
0.000	-0.000	-0.000	-0.169	-0.835	-0.733	-0.105	-0.000	0.000	0.000	0.000	0.000	0.400	1.000					
c63	-0.269	0.124	0.310	-0.028	-0.472	-0.221	0.004	0.202	0.645	0.132	-0.000	-0.047	-0.483	-0.618	-0.068	0.000	0.005	
0.175	0.731	0.475	0.030	-0.000	-0.000	-0.029	-0.396	-0.843	-0.299	-0.010	0.000	0.000	0.091	0.665	0.782	0.147	-0.000	
0.002	-0.000	-0.000	0.000	0.000	-0.208	-0.899	-0.573	-0.045	-0.000	0.000	0.000	0.000	-0.000	0.367	1.000			
c72	-0.302	0.075	0.409	-0.008	-0.339	-0.362	0.000	0.067	0.576	0.282	0.000	-0.005	-0.199	-0.718	-0.198	-0.000	0.022	
0.388	0.751	0.125	0.000	0.000	-0.059	-0.601	-0.686	-0.070	-0.000	-0.000	0.000	0.000	0.283	1.000				
0.032	0.000	-0.000	0.000	0.000	-0.201	-0.946	-0.368	-0.010	-0.000	0.000	0.000	0.000	0.000	0.000	0.000	0.000	0.548	
c81	-0.347	0.032	0.532	-0.001	-0.161	-0.561	-0.000	0.006	0.326	0.538	0.000	0.000	-0.020	-0.499	-0.483	-0.000	-0.000	
0.044	0.664	0.408	0.000	0.000	0.000	0.000	-0.076	-0.806	-0.323	-0.000	-0.000	-0.000	0.000	0.113	0.914			
0.236	0.000	0.000	0.000	0.000	-0.150	-0.979	-0.151	-0.000	-0.000	0.000	0.000	0.000	0.000	0.000	0.177	1.000		
c90	-0.337	0.002	0.570	-0.000	-0.009	-0.690	0.000	0.000	0.018	0.785	-0.000	-0.000	-0.000	-0.029	-0.860	0.000	0.000	
0.000	0.000	0.040	0.916	-0.000	-0.000	-0.000	-0.000	-0.051	-0.956	0.000	0.000	0.000	0.000	0.000	0.000	0.000	0.061	
0.982	-0.000	-0.000	0.000	-0.000	-0.000	0.000	-0.068	-0.996	0.000	0.000	0.000	-0.000	0.000	0.000	0.000	0.000	0.072	
1.000																		
c010	0.309	-0.527	-0.000	0.645	0.000	0.000	-0.741	-0.000	-0.000	-0.000	0.820	0.000	0.000	0.000	0.000	-0.882	0.000	
0.000	-0.000	-0.000	-0.000	0.930	-0.000	0.000	0.000	-0.000	0.000	-0.000	0.963	0.000	-0.000	-0.000	-0.000	0.000	0.000	
0.000	0.985	-0.000	0.000	0.000	0.000	0.000	-0.000	0.000	-0.996	0.000	-0.000	-0.000	-0.000	-0.000	0.000	0.000	0.000	
0.000	1.000																	
c19	0.299	-0.466	-0.022	0.502	0.116	0.000	-0.492	-0.244	-0.000	-0.000	0.451	0.392	0.000	0.000	0.000	-0.388	0.547	
0.000	-0.000	-0.000	-0.000	0.314	0.696	0.000	0.000	0.000	-0.233	-0.825	0.000	-0.000	-0.000	-0.000	0.000	0.000	0.000	
0.000	0.152	0.923	-0.000	0.000	0.000	0.000	-0.000	0.000	-0.074	-0.981	0.000	-0.000	-0.000	-0.000	0.000	0.000	0.000	
0.000	-0.000	1.000																
c28	0.243	-0.339	-0.051	0.312	0.241	0.004	-0.253	-0.434	-0.033	-0.000	0.184	0.575	0.108	0.000	0.000	-0.121	0.640	
-0.234	-0.000	-0.000	-0.000	0.070	0.620	0.406	0.000	0.000	0.000	-0.033	-0.523	-0.605	-0.000	-0.000	-0.000	-0.000	0.000	

```

0.000 0.010 0.371 0.799 0.000 0.000 0.000 0.000 0.000 -0.000 -0.187 -0.945 -0.000 -0.000 -0.000 -0.000 -0.000 -
0.000 0.000 -0.000 1.000
    c37      0.202 -0.246 -0.079 0.187 0.326 0.014 -0.120 -0.486 -0.109 -0.001 0.066 0.509 0.294 0.015 -0.000 -0.031 -
0.427 -0.505 -0.067 0.000 0.000 0.011 0.292 0.660 0.183 0.000 -0.000 0.000 -0.002 -0.155 -0.695 -0.374 -0.000 0.000 0.000 -
0.000 0.000 0.052 0.577 0.626 0.000 0.000 -0.000 -0.000 0.000 -0.000 -0.322 -0.878 -0.000 -0.000 0.000 0.000 0.000 -
0.000 0.000 0.000 0.000 1.000
    c46      0.179 -0.183 -0.108 0.110 0.371 0.032 -0.053 -0.436 -0.216 -0.006 0.020 0.341 0.459 0.069 0.001 -0.006 -
0.200 -0.588 -0.241 -0.011 0.000 0.001 0.085 0.537 0.489 0.061 -0.000 -0.000 -0.000 -0.021 -0.351 -0.698 -0.192 0.000 0.000 -
0.000 0.000 -0.000 0.136 0.725 0.438 -0.000 -0.000 -0.000 0.000 -0.000 -0.000 -0.475 -0.773 -0.000 0.000 0.000 0.000 0.000 -
0.000 0.000 -0.000 0.000 0.000 1.000
    c55      0.172 -0.140 -0.140 0.062 0.385 0.062 -0.020 -0.334 -0.334 -0.020 0.005 0.180 0.523 0.180 0.005 -0.001 -
0.064 -0.461 -0.461 -0.064 -0.001 0.000 0.013 0.257 0.642 0.257 0.013 0.000 -0.000 -0.000 -0.077 -0.560 -0.560 -0.077 -0.000 -
0.000 0.000 0.000 0.268 0.779 0.268 -0.000 0.000 0.000 -0.000 -0.000 -0.000 -0.632 -0.632 0.000 0.000 0.000 -0.000 -
0.000 0.000 0.000 0.000 0.000 1.000
    c64      0.179 -0.108 -0.183 0.032 0.371 0.110 -0.006 -0.216 -0.436 -0.053 0.001 0.069 0.459 0.341 0.020 -0.000 -
0.011 -0.241 -0.588 -0.200 -0.006 0.000 0.000 0.061 0.489 0.537 0.085 0.001 -0.000 -0.000 -0.000 -0.192 -0.698 -0.351 -0.021 -
0.000 0.000 0.000 0.000 0.438 0.725 0.136 0.000 0.000 -0.000 -0.000 -0.000 -0.773 -0.475 -0.000 -0.000 -0.000 -
0.000 0.000 0.000 0.000 0.000 -0.000 1.000
    c73      0.202 -0.079 -0.246 0.014 0.326 0.187 -0.001 -0.109 -0.486 -0.120 0.000 0.015 0.294 0.509 0.066 -0.000 -
0.000 -0.067 -0.505 -0.427 -0.031 0.000 0.000 -0.000 0.183 0.660 0.292 0.011 -0.000 -0.000 0.000 0.000 -0.374 -0.695 -0.155 -
0.002 0.000 0.000 -0.000 -0.000 -0.000 0.626 0.577 0.052 -0.000 -0.000 0.000 0.000 0.000 0.000 -0.878 -0.322 0.000 -
0.000 0.000 -0.000 -0.000 -0.000 -0.000 1.000
    c82      0.243 -0.051 -0.339 0.004 0.241 0.312 0.000 -0.033 -0.434 -0.253 -0.000 -0.000 0.108 0.575 0.184 0.000 -
0.000 0.000 -0.234 -0.640 -0.121 -0.000 -0.000 -0.000 0.406 0.620 0.070 0.000 0.000 0.000 0.000 -0.000 -0.605 -0.523 -
0.033 -0.000 -0.000 -0.000 -0.000 0.000 0.799 0.371 0.010 0.000 0.000 0.000 0.000 0.000 -0.000 -0.000 -0.945 -0.187 -
0.000 -0.000 -0.000 0.000 -0.000 -0.000 0.000 0.000 -0.000 -0.000 1.000
    c91      0.299 -0.022 -0.466 -0.000 0.116 0.502 0.000 0.000 -0.244 -0.492 -0.000 -0.000 -0.000 0.392 0.451 0.000 -
0.000 0.000 -0.547 -0.388 -0.000 -0.000 -0.000 -0.000 0.696 0.314 0.000 0.000 0.000 0.000 0.000 0.000 -0.825 -
0.233 -0.000 -0.000 -0.000 -0.000 0.000 0.923 0.152 0.000 0.000 -0.000 0.000 0.000 0.000 -0.000 0.000 0.000 -0.981 -
0.074 -0.000 -0.000 0.000 -0.000 -0.000 0.000 0.000 -0.000 -0.000 1.000
    c100     0.309 -0.000 -0.527 0.000 0.000 0.645 -0.000 -0.000 -0.000 -0.741 0.000 0.000 0.000 0.000 -0.000 0.820 -0.000 -
-0.000 -0.000 -0.000 0.000 -0.882 0.000 0.000 0.000 0.000 0.000 0.930 -0.000 -0.000 -0.000 -0.000 -0.000 0.000 -
0.963 0.000 0.000 0.000 0.000 0.000 -0.000 -0.000 0.985 -0.000 -0.000 -0.000 -0.000 -0.000 -0.000 -0.000 0.000 0.000 -
0.996 0.000 0.000 0.000 -0.000 0.000 0.000 0.000 -0.000 -0.000 1.000
gnuplot> quit

```